
Metamorphic events during the formation of the East African Orogen: case studies from Madagascar and Tanzania

Dissertation
zur Erlangung des Doktorgrades
der Mathematisch–Naturwissenschaftlichen Fakultät
der Christian–Albrechts–Universität
zu Kiel

vorgelegt von
Niels Jöns



Kiel
2006

Metamorphic events during the formation of the East African Orogen: case studies from Madagascar and Tanzania

Dissertation
zur Erlangung des Doktorgrades
der Mathematisch–Naturwissenschaftlichen Fakultät
der Christian–Albrechts–Universität
zu Kiel

vorgelegt von
Niels Jöns



Kiel
2006

Referent: *Prof. Dr. Volker Schenk*

Korreferent/in:

Tag der mündlichen Prüfung:

Zum Druck genehmigt: *Kiel*,

Der Dekan

Vorwort

Die vorliegende Arbeit stellt zwar eine monographische Dissertation dar, die einzelnen Kapitel, denen eine Einleitung vorangestellt ist, sind jedoch bezüglich ihres Aufbaues so konzipiert, daß sie unabhängig voneinander publiziert werden können bzw. bereits publiziert sind. Durch diesen Umstand ist es zu erklären, daß jedes Kapitel nochmals eine eigene Einleitung, Diskussion und ein Literaturverzeichnis enthält. Auch beim Schreibstil, dem Umfang, der Verwendung von Abkürzungen sowie der Formatierung von Abbildungen und Tabellen wurde bereits den Anforderungen unterschiedlicher Fachzeitschriften Rechnung getragen. Diesen Umstand möge der Leser berücksichtigen.

Kiel, September 2006

Niels Jöns

Table of Contents

Zusammenfassung	xi
Abstract	xiii
1 Introduction	1
1.1 The formation of the East African Orogen in the context of the Gondwana assembly	1
1.2 The Madagascar–Tanzania connection	2
1.3 Of granulites and whiteschists	3
1.4 Study approach and analytical techniques	3
1.5 Outline of this study	4
References	6
2 Metamorphic evolution of northern Madagascar	9
2.1 Abstract	9
2.2 Introduction	10
2.3 Geological setting	12
2.4 Analytical procedure and data processing	13
2.5 Petrography and mineral chemistry	15
2.5.1 Northern (Série de Daraina-Milanoa) and central Bemarivo Belt . .	15
2.5.2 Southern Bemarivo Belt (Série de Sahantaha)	15
2.6 Mineral reaction history	24
2.7 Conventional geothermobarometry	26
2.8 Geochronology	28
2.8.1 Monazite textures and chemistry	28
2.8.2 Geochronological results	32
2.9 Discussion and conclusions	33
2.9.1 <i>P-T</i> path and geodynamic interpretation	33
2.9.2 Interpretation of the geochronological results	35
2.9.3 The Bemarivo Belt and its relation to the formation of Gondwana .	35
2.10 Acknowledgements	36
References	36

3	The Vohibory Block: Relics of the Mozambique Ocean	43
3.1	Abstract	43
3.2	Introduction	43
3.3	Geological setting	44
3.4	Petrography and mineral chemistry	46
3.5	Geothermobarometry and pressure-temperature evolution	46
3.6	Geochemistry	47
3.7	Geochronology	50
3.8	Discussion and conclusions	52
3.9	Acknowledgements	52
	References	53
4	Metamorphic evolution of southern Madagascar	57
4.1	Abstract	57
4.2	Introduction	58
4.3	Previous work and geological setting	59
4.4	Analytical procedures	62
4.4.1	Sampling	62
4.4.2	Electron microprobe analyses and U-Th-total Pb dating	63
4.4.3	Sensitive high-mass resolution ion microprobe (SHRIMP)	63
4.5	Petrography and mineral chemistry	64
4.5.1	Felsic and intermediate gneisses	64
4.5.2	Metabasites	65
4.5.3	Metapelites	66
4.5.4	Calcsilicates	86
4.5.5	Marbles	88
4.5.6	Anorthosites	88
4.6	Thermobarometric estimates and P - T evolution	90
4.6.1	Qualitative estimates from reaction textures	90
4.6.2	Conventional geothermobarometry	91
4.7	Geochronology	94
4.7.1	U-Th-total Pb dating of monazite	94
4.7.2	U-Pb dating of zircon	104
4.8	Discussion and conclusions	105
4.8.1	Pressure-temperature evolution	105
4.8.2	Timing of metamorphic events	106
4.8.3	Implications for the Gondwana formation	108
4.9	Acknowledgements	108
	References	108

5	Petrology of whiteschists from Mautia Hill	119
5.1	Abstract	119
5.2	Introduction	120
5.3	Previous work and geological setting	121
5.4	Petrography and mineral chemistry	123
5.4.1	Analytical procedure	123
5.4.2	Metapelites	123
5.4.3	Metabasites	124
5.4.4	Other rock types	124
5.4.5	Whiteschists and chlorite schists	126
5.5	Thermobarometry	139
5.5.1	Metapelites	139
5.5.2	Metabasites	140
5.5.3	Hornblende-kyanite-talc-quartz schists	142
5.6	Reaction history	142
5.6.1	CMASH-CO ₂ -Fe ₂ O ₃ system	143
5.6.2	MASH-Fe ₂ O ₃ system	145
5.7	Discussion and conclusions	146
5.7.1	<i>P-T</i> evolution	146
5.7.2	Influence of water activity and oxygen fugacity	147
5.7.3	Metasomatism and precursor rock of whiteschists	147
5.7.4	Geodynamic setting	148
5.8	Acknowledgements	149
	References	149
	List of Figures	157
	List of Tables	159
A	Bemarivo Belt: SHRIMP zircon data of metapelitic samples	161
B	Vohibory & Betsimisaraka: Mineral chemistry and geochemistry	165
C	Southern Madagascar: CL images of zircon used for U-Pb dating	169
D	Mautia Hill: Mineral analyses for thermobarometry	175
	Publications related to this thesis	179
	Danksagung	181

Zusammenfassung

Die Bildung des Großkontinentes Gondwana wurde am Übergang vom Proterozoikum zum Phanerozoikum mit der Schließung des Mozambique-Ozeans und nachfolgender Kollision zwischen Kontinentalblöcken Ost- und Westgondwanas abgeschlossen. Das größte bei dieser sogenannten Panafrikanischen Orogenese entstandene Gebirge ist das Ostafrikanische Orogen („East African Orogen“), welches sich von Arabien durch Ostafrika bis in die Antarktis erstreckt. Die geodynamische Entwicklung dieses zentralen Gebirges ist trotz seiner wichtigen Lage in vielerlei Hinsicht noch unverstanden. So ist es nach wie vor unklar, zu welchem Zeitpunkt die Kontinent-Kollisionen stattfanden. Auch die Möglichkeit, daß das Ostafrikanische Orogen ein akkretionäres Gebirge darstellt, wird noch diskutiert. Datierungen von Metamorphoseereignissen zeigen eine deutlich bimodale Verteilung mit Hauptphasen vor ca. 630 Millionen und vor ca. 535 Millionen Jahren (Ma). Die geodynamische Signifikanz beider Alter ist jedoch in vielen Fällen unklar. Auch Relikte des postulierten Mozambique-Ozeans, welcher einstmals die Fragmente West- und Ostgondwanas bzw. den Mikrokontinent Azania getrennt haben soll, wurden im zentralen Teil des Ostafrikanischen Orogens bisher nicht nachgewiesen, und die Lage der Suturzone ist daher nicht bekannt. Madagaskar und Tansania haben aufgrund ihrer zentralen Lage eine Schlüsselstellung bei der Klärung dieser Fragen. Die vorliegende Arbeit untersucht metamorphe Gesteine aus beiden Ländern, um ein besseres Verständnis der Geodynamik zur Zeit der Gondwanabildung zu erlangen.

Die Gesteinsproben wurden petrographisch und mineralchemisch (EPMA) untersucht. Reaktionstexturen und geothermobarometrische Berechnungen dienen zur Herleitung der Druck-Temperatur-Entwicklung der Gesteinsmetamorphose. Die Metamorphoseereignisse wurden durch isotopische U-Pb SHRIMP-Analysen von Zirkonen sowie chemische *in situ* U-Th-Pb-Altersdatierung von Monazit zeitlich eingeordnet. Zudem wurde die Gesamtgesteinschemie ausgewählter Metabasite mittels RFA und ICP-MS untersucht. Auf Grundlage dieser Daten wurden Rückschlüsse auf die geodynamische Entwicklung des Ostafrikanischen Orogens gezogen.

Die metabasischen Gesteine des Vohibory Blocks in Südmadagaskar zeigen geochemische Charakteristika von Basalten, welche an mittelozeanischen Rücken und im Bereich von Inselbögen gebildet wurden. Aufgrund ihres Bildungsalters von 700–850 Ma können sie dem Mittelneoproterozoischen Mozambique-Ozean zugeordnet werden. Das hauptsächliche Metamorphosestadium des Vohibory Blocks vor ca. 610 Ma markiert die Schließung eines Backarc-Beckens und Akkretion eines Inselbogens an den Kontinent Azania.

Dieses Metamorphoseereignis kann im gesamten Südteil Madagaskars, südlich der Rano-tsara-Scherzone, durch Monazit- und Zirkonatdatierungen nachgewiesen werden. Im Gegensatz zum Vohibory Block kam es in der Androyan-Gruppe Südmadagaskars jedoch vor ca. 535 Ma zu einer hochgradig metamorphen Überprägung, welche in großen Bereichen unter „ultrahohen“ Temperaturen stattfand. Dieses Ereignis, welches mit der Ausbildung von Mineralparagenesen wie Sapphirin + Quarz, Orthopyroxen + Sillimanit + Quarz und Osumilith + Granat einhergeht, markiert die die Gondwanabildung abschließende Kollision des kontinentalen Blockes Azania mit dem Tansania-Kraton.

Der Bemarivo Belt von Nordmadagaskar kollidierte zu gleicher Zeit (vor ca. 535–540 Ma) mit Azania. Die Kollision wurde gefolgt von magmatischen Intrusionen, die die Kruste noch bis vor ca. 510 Ma aufheizten. Das 630 Ma-Ereignis konnte nicht nachgewiesen werden. Es gibt aber Monazit mit einem Alter von ungefähr 740 Ma, welcher als detritisch gedeutet wird und darauf hindeutet, daß diese nördlichste tektonische Einheit Madagaskars einst im Bereich der Seychellen lag, von wo ähnliche Alter bekannt sind.

In Tansania kam es vor ca. 535 Ma zur Bildung der Weißschiefer von Mautia Hill, welche ebenfalls die Kollision des Tansania-Kratons mit Azania im späten Neoproterozoikum markieren. Diese unter einem niedrigen geothermischen Gradienten und einem im Uhrzeigersinn verlaufenden Druck-Temperatur-Pfad gebildeten Gesteine weisen eine sehr ungewöhnliche Mineralogie auf, welche sich unter dem Einfluß von Fluidinfiltration und stark oxidierenden Bedingungen ausbildete.

Abstract

The formation of the supercontinent Gondwana at the transition from the Proterozoic to the Phanerozoic ended with the closure of the Mozambique Ocean and the subsequent collision of continental blocks belonging to East and West Gondwana. As a result of the so-called Pan-African Orogeny, the huge East African Orogen formed, which extends from Arabia through eastern Africa into Antarctica. Although it holds a key position for understanding the formation of Gondwana, many aspects of its geodynamic evolution are still not well understood. The exact timing of continental collisions is not known and the possibility that the East African Orogen represents an accretionary orogen is still a matter of debate. Age dating of metamorphic events revealed two main episodes of metamorphism: at ca. 630 Ma and at ca. 535 Ma. However, the geodynamic significance of these ages is mostly unknown. Another problem is that relics of the Mozambique Ocean, which is thought to have separated East and West Gondwana and the microcontinent Azania, have not yet been found in the central East African Orogen, leading to uncertainty about the position of suture zones. Due to their central position, Madagascar and Tanzania are of importance to answer these questions. Against this background, the present thesis investigates metamorphic rocks from both countries in order to get a better understanding of the formation of the East African Orogen.

The rock samples were petrographically examined and the mineral chemistry was determined using the electron microprobe. Observations on reaction textures and geothermobarometric calculations helped to deduce the metamorphic pressure-temperature evolution. The metamorphic events were dated by means of isotopic U-Pb SHRIMP analyses of zircon and chemical U-Th-total Pb dating of monazite. The whole-rock chemistry of selected samples was analysed using XRF and ICP-MS techniques. Based on these data, an interpretation of the geodynamic evolution of the East African Orogen is proposed.

The metabasic rocks of the Vohibory block of southern Madagascar have chemical compositions similar to those of basalts from mid-ocean ridge and island-arc settings. Their formation age of 700–850 Ma indicates that they are related to the middle Neoproterozoic Mozambique Ocean. The main metamorphism of the Vohibory block has been dated at ca. 610 Ma, marking the closure of a back-arc basin and the accretion of an island arc to the margin of the Azania continent.

This metamorphic event can be determined in monazite and zircon from whole southern Madagascar, south of the Ranotsara shear zone. Unlike the Vohibory block, the Androyan group of southern Madagascar experienced a high-grade metamorphic overprinting

at ca. 535 Ma, which locally reached ultrahigh temperature conditions. This metamorphic event, which is characterised by mineral assemblages like sapphirine + quartz, orthopyroxene + sillimanite + quartz, and osumilite + garnet, marks the collision of Azania with the Tanzania Craton.

At the same time (ca. 535–540 Ma), the Bemarivo Belt of northern Madagascar collided with Gondwana. This collision was followed by magmatic intrusions that heated the crust until ca. 510 Ma. The 630 Ma event has not been detected here. However, there is monazite with an age of ca. 740 Ma, which is interpreted to be of detrital origin. This points to a former connection of the Bemarivo Belt with the Seychelles, from where similar ages are known.

In Tanzania, the formation of whiteschists at Mautia Hill is attributed to the late Neoproterozoic (ca. 535 Ma) collision between the Tanzania Craton and Azania. These rocks, which have been formed under low geothermal gradients, feature an uncommon mineralogy, resulting from fluid infiltration and highly oxidising conditions.

Chapter 1

Introduction

1.1 The formation of the East African Orogen in the context of the Gondwana assembly

The transition from the Proterozoic to the Phanerozoic was a period of rapid global change. Several large-scale glaciation events (“Snowball Earth”; Hoffman *et al.*, 1998) have been found as well as the evolution of increasingly complex life, from single-celled to complex multicellular organisms (e.g., Knoll, 2003). Another important observation is that the formation of the Gondwana supercontinent does also fall into this period. For obvious reasons one might speculate that these observations are somehow linked. It may be possible that the existence of large continental masses is a prerequisite for global glaciations and that the subsequent breakoff into smaller continents is triggering the biodiversity. Furthermore, the existence of supercontinents may have an influence on mantle convection processes, possibly triggering superplume formation and extensive volcanism, which, in turn, affects the biodiversity by changing the climate and the timing of orogenic events. Therefore, the understanding of the tectonic configuration during the Gondwana formation contributes to a better understanding of the whole System Earth.

The East African Orogen seems to play a key role in the final amalgamation of the Gondwana supercontinent. It is one of the largest orogenic belts on Earth, stretching from Arabia through whole eastern Africa into Antarctica. Former workers attributed the formation of this orogen to the collision of the already consolidated parts of Eastern Gondwana (Australia, Antarctic, India) and Western Gondwana (Africa, America), leading to the closure of a huge oceanic basin, commonly referred to as the Mozambique Ocean, and a subsequent final orogenic event (i.e. the Pan-African; McWilliams, 1981; Stern, 1994). Recent advances in analytical techniques have led to more precise geochronological data, which point to a prolonged period of metamorphic activity from ca. 650 to ca. 480 Ma, which is much longer than any Phanerozoic orogeny. Therefore, it is still a matter of debate, whether the East African Orogen has to be seen as an accretionary orogen with a continued series of metamorphic events resulting from accretion of microcontinental blocks in the timeframe of 650 to 480 Ma, or if there are just two discrete metamorphic events, at

650–600 Ma and at 550–520 Ma, respectively (e. g., Meert *et al.*, 1995; Meert, 2003; John *et al.*, 2004a,b). The controversy is mainly due to the application of different scientific approaches and techniques in deciphering the orogenic history: some studies put the main emphasis on palaeomagnetism, others on geochronology, however, geochronological studies in combination with detailed petrological work are just rarely performed. The latter approach is a particular powerful one if it combines detailed reconstructions of petrological pressure-temperature paths with texturally controlled *in situ* dating of metamorphic minerals, providing not just information about the timing but also the geodynamic setting of metamorphism. Results thus obtained, allow for making statements about the character *and* timing of processes at active continental margins, e. g. distinguishing between subduction, continent collision or advective heat input above a subduction zone prior to collision.

1.2 The Madagascar–Tanzania connection

A marked change in metamorphic grade and lithologic character is found within the East African Orogen. In the north, the Arabian-Nubian Shield consists of juvenile magmatic terranes, with oceanic suture zones marked by frequent outcrops of ophiolitic sequences. Here, the metamorphic grade is generally low, which contrasts to the central and southern part of the East African Orogen, where high-grade metamorphic gneisses, mainly of granulite-facies grade, are found. For reconstructing the thermal and tectonic history of orogenic events, the high-grade rocks are of particular importance, because they provide insights into the geodynamic evolution of the lower continental crust during the Gondwana formation. However, the prolonged and intense thermo-tectonic overprint complicates the decipherment of some other important features, e. g. locating the position of former suture zones or determining polymetamorphism.

The present work focuses on two study areas, Madagascar and Tanzania. Together they preserve a section through the whole East African Orogen, from the Tanzania Craton in the West to the Antongil Block (part of the Indian Dharwar Craton) in the East. Most of the studied rocks are metapelitic gneisses that are suitable for applying conventional geothermobarometry. Furthermore, they have the potential to preserve a variety of reaction textures, providing qualitative information about the *P-T* history. Finally, the common occurrence of metamorphic monazite in different textural settings allows for a precise correlation of the age and character of metamorphism, often even in case of a polymetamorphic history. An additional problem is that the location of the suture of the Mozambique Ocean in the central East African Orogen is not known. In Madagascar there are a few lithological units that are rich in metabasic rocks and may represent such ancient suture zones. However, their Mid-Ocean Ridge chemistry indicating its oceanic origin has not yet been proven.

1.3 Of granulites and whiteschists

Apart from this large-scale regional geological questions, the study area is also of interest to investigate problems of metamorphic processes in general. Ultrahigh temperature (UHT) metamorphism marks lower crustal metamorphism at temperatures of over 900 °C (Harley, 1998a). Such metamorphic conditions were originally thought to be exceptional, however, during the past two decades several occurrences of UHT rocks have been reported, mostly due to improvements in recognizing and documenting it. These occurrences range from outcrop-scale phenomena to vast areas of tens of thousands square-kilometres (e. g., Sandiford *et al.*, 1987; Ouzegane & Boumaza, 1996; Raith *et al.*, 1997; Harley, 1998b; Goncalves *et al.*, 2004; Das *et al.*, 2006), thus UHT turns out to be rather a major form of metamorphism than an exceptional phenomenon. Therefore, ultrahigh temperature metamorphic rocks may contribute to estimate the transfer of heat during orogenic processes, to get information about the response of the lower crust to deformation, and, finally to answer the question: what is the geodynamic cause of UHT metamorphism?

Whiteschists (talc–kyanite schists; Schreyer, 1973) are less frequent than granulites, but they provide important geodynamic information as well. Their evolution is generally characterised by a clockwise pressure-temperature evolution under relatively low geothermal gradients and may indicate the sites of palaeo-collision zones. The mineralogy of these rocks can be described in comparatively simple chemical systems (e. g., MASH-Fe₂O₃), most likely as a result of intense metasomatic alteration. Therefore, whiteschists may also provide insights into processes of fluid-rock interaction during an orogeny.

Madagascar is famous for its occurrence of UHT-metamorphic mineral assemblages (e. g., Nicollet, 1990; Waters, 1991), and Mautia Hill in Tanzania is one of the most famous whiteschist occurrences (McKie, 1959), making this area of the East African Orogen not just a rewarding study object concerning the Gondwana formation, but also for solving fundamental petrological questions.

1.4 Study approach and analytical techniques

To approach the above-mentioned problems, we first did extensive field work in whole Madagascar. The main focus lay on sampling the different tectonic units. Metapelites were preferentially taken, because they have the highest potential to preserve the metamorphic history by reaction textures and mineral zonations. Furthermore, they contain monazite and zircon, which can be dated to constrain the timing of metamorphic events. Metabasic rocks from potential suture zones were sampled to carry out major and trace element geochemistry as well as zircon dating. Field work in Tanzania was restricted to the location of Mautia Hill, a small outcrop of whiteschists with unusual mineralogy, associated with metabasites and metapelites. Thin sections of all rock samples were produced and examined using polarising microscopy. Observations on reaction textures gave first ideas about the metamorphic history. The mineral chemistry of selected samples was determined in polished sections using the electron microprobe. With these data, geo-

thermobarometric calculations were performed to get more detailed information about the pressure and temperature evolution of the rocks, which, in turn, are necessary for a geodynamic interpretation.

Geochronological techniques were applied to unravel the timing of metamorphic events. We used two different approaches: U–Th–total Pb dating of monazite using the electron microprobe and isotopic U–Pb dating of zircon by means of SHRIMP (Sensitive High-Mass Resolution Ion Microprobe). The first method was applied to Pb-free polished thin sections, resulting in texturally controlled *in situ* age data with a high spatial resolution (spot size is ca. 2 μm in diameter). For SHRIMP dating samples were crushed and separated zircons were mounted in epoxy resin. Though the analyses are not done *in situ* (i. e. not texturally controlled in a thin section) and the spot size is larger (ca. 20 μm), this method provides more precise age data.

Whole rock geochemical techniques have been used to determine the geodynamic setting of melt formation, leading to the magmatic protoliths of metabasic samples from possible suture zones. X-ray fluorescence (XRF) was used to determine the major elements. For analysing trace elements, samples were dissolved using acid digestion bombs and subsequently analysed by means of Inductively Coupled Plasma Mass Spectrometry (ICP-MS).

1.5 Outline of this study

There are quite many yet unresolved problems concerning the petrology and mineralogy of the rocks of Madagascar and Tanzania, however, the present study focuses on a few key-points.

Chapter 2 is a detailed petrological study of high-grade metamorphic metapelites from the Bemarivo Belt of northern Madagascar. This tectonic unit was accreted to the Gondwana supercontinent during the latest stages of the Pan-African orogeny. *In situ* dating of monazite has been combined with detailed petrological work to unravel the geodynamic setting and the duration of collision with Gondwana.

This chapter is already published:

Jöns, N., Schenk, V., Appel, P. & Razakamanana, T. (2006): Two-stage metamorphic evolution of the Bemarivo Belt of northern Madagascar: constraints from reaction textures and in-situ monazite dating. *Journal of metamorphic Geology* **24**, 329-347.

Chapter 3 deals with the geochemistry, geochronology, and petrology of metabasic rocks of the Vohibory Block of southern Madagascar. The results demonstrate that the Vohibory Block is a remnant of the ancient Mozambique Ocean, representing an island arc/back-arc succession. In the early stages of the Pan-African orogeny, fragments of this arc terrane have been incorporated into the forming supercontinent, as evidenced by high-pressure amphibolite-facies metamorphism. This tectono-thermal event does not mark the final

closure of the Mozambique Ocean, but witnesses a period of convergence. Furthermore, it marks the position of a suture zone, the direct evidence of which was, up to now, missing in the high-grade rocks of the central East African Orogen.

This chapter is submitted and currently in review:

Jöns, N. & Schenk, V. (in review): Relics of the Mozambique Ocean in the central East African Orogen: evidence from the Vohibory Block of southern Madagascar. Submitted to *Geology*.

Chapter 4 describes UHT mineral assemblages in southern Madagascar. It has long been known that the rocks from this huge area experienced metamorphism under high temperatures, but the regional distribution of specific assemblages indicating ultrahigh-temperature conditions (e.g., spinel + quartz, osumilite + garnet, sapphirine + quartz, orthopyroxene + sillimanite + quartz) has up to now not been reported. Furthermore, the high-MgAl gneisses, which show such assemblages, feature complex reaction textures that allow for a detailed reconstruction of retrograde P - T conditions. The results are combined with monazite and zircon geochronology, showing that the high-temperature event was in the late stage of the Pan-African orogeny (ca. 535 Ma), preceded by an earlier metamorphism at ca. 630 Ma.

This chapter will be submitted to *Journal of Petrology*:

Jöns, N. & Schenk, V. (to be submitted): The ultra-high temperature granulites of southern Madagascar in a polymetamorphic context: implications for the amalgamation of the Gondwana supercontinent. *Journal of Petrology*.

Chapter 5 is a phase petrological and mineral chemical study of whiteschists and associated rocks from Mautia Hill in Tanzania. This locality is well known for its mineralogical variety (e.g., purple and green yoderite, yellow sapphirine, högbomite, kornerupine, pseudobrookite), but the clockwise P - T evolution of the whiteschists gives also indications for the final collision between East and West Gondwana and closure of the Mozambique Ocean. We combined conventional geothermobarometry on “normal” metapelites and metabasites with phase equilibria of the uncommon Mn-bearing whiteschists to constrain the geodynamic setting of metamorphism.

This chapter is published:

Jöns, N. & Schenk, V. (2004): Petrology of whiteschists and associated rocks at Mautia Hill (Tanzania): Fluid infiltration during high-grade metamorphism? *Journal of Petrology* **45**, 1959-1981.

The results presented in this thesis contribute to a better understanding of orogenic processes during the Gondwana formation. Geochronological and petrological data from Madagascar as well as Tanzania point to crustal thickening at ca. 535 Ma, representing the final collision between East and West Gondwana. In southern Madagascar, this period is characterised by widespread UHT metamorphism, at Mautia Hill whiteschists are

evidence for the collision. Our findings contrast with the interpretation of many former workers (e. g., Stern, 1994; Meert *et al.*, 1995; Collins & Pisarevsky, 2005), who propose that the main collision occurred at 650–600 Ma, followed by post-collisional extension and escape tectonics in the period of 600–500 Ma. However, an older metamorphic event at ca. 630 Ma is present in Tanzania (Appel *et al.*, 1998) as well as southern Madagascar (this work, chapter 4), preceding the final amalgamation of Gondwana.

References

- Appel, P., Möller, A. & Schenk, V., 1998. High-pressure granulite facies metamorphism in the Pan-African belt of eastern Tanzania: P-T-t evidence against granulite formation by continent collision. *Journal of metamorphic Geology*, **16**, 491–509.
- Collins, A. S. & Pisarevsky, S. A., 2005. Amalgamating eastern Gondwana: The evolution of the Circum-Indian Orogens. *Earth-Science Reviews*, **71**, 229–270.
- Das, S., Bhattacharya, A., Raith, M. M., Bhadra, S. & Banerjee, M., 2006. Aluminous sapphirine granulites from the Eastern Ghats Belt (India): Phase relations and relevance to counterclockwise P-T history. *European Journal of Mineralogy*, **18**, 35–48.
- Goncalves, P., Nicollet, C. & Montel, J.-M., 2004. Petrology and in situ U-Th-Pb monazite geochronology of ultrahigh-temperature metamorphism from the Andriamena mafic unit, North-Central Madagascar. Significance of a petrographical P-T path in a polymetamorphic context. *Journal of Petrology*, **45**, 1923–1957.
- Harley, S., 1998a. On the occurrence and characterization of ultrahigh-temperature crustal metamorphism. In: *What Drives Metamorphism and Metamorphic Reactions?* (eds. Treloar, P. & O'Brien, P.), Geological Society, London. 81–107.
- Harley, S. L., 1998b. Ultrahigh temperature granulite metamorphism (1050 °C, 12 kbar) and decompression in garnet (Mg70)–orthopyroxene–sillimanite gneisses from the Rauer Group, East Antarctica. *Journal of metamorphic Geology*, **16**, 541–562.
- Hoffman, P. F., Kaufman, A. J., Halverson, G. P. & Schrag, D. P., 1998. A Neoproterozoic Snowball Earth. *Science*, **281**, 1342–1346.
- John, T., Schenk, V., Mezger, K. & Tembo, F., 2004a. Timing and P-T evolution of whiteschist metamorphism in the Lufilian Arc - Zambesi Belt orogen (Zambia): implications for the assembly of Gondwana. *Journal of Geology*, **112**, 71–90.
- John, T., Scherer, E. E., Haase, K. & Schenk, V., 2004b. Trace element fractionation during fluid-induced eclogitization in a subducting slab: trace element and Lu–Hf–Sm–Nd isotope systematics. *Earth and Planetary Science Letters*, **227**, 441–456.

- Knoll, A. H., 2003. *Life on a young planet: the first three billion years of evolution on Earth*. Princeton Science Library. Princeton University Press.
- McKie, D., 1959. Yoderite, a new hydrous magnesium iron aluminosilicate from Mautia Hill, Tanganyika. *Mineralogical Magazine*, **32**, 282–307.
- McWilliams, M. O., 1981. Palaeomagnetism and Precambrian tectonic evolution of Gondwana. In: *Precambrian Plate Tectonics* (ed. Kröner, A.), Elsevier, Amsterdam, Developments in Precambrian Geology. 649–687.
- Meert, J. G., 2003. A synopsis of events related to the assembly of eastern Gondwana. *Tectonophysics*, **362**, 1–40.
- Meert, J. G., van der Voo, R. & Ayub, S., 1995. Paleomagnetic investigation of the Neoproterozoic Gagwe lavas and Mbozi Complex, Tanzania and the assembly of Gondwana. *Precambrian Research*, **74**, 225–244.
- Nicollet, C., 1990. Crustal evolution of the granulites of Madagascar. In: *Granulites and Crustal Evolution* (eds. Vielzeuf, D. & Vidal, P.), Kluwer Academic Publishers. 291–310.
- Ouzegane, K. & Boumaza, S., 1996. An example of ultrahigh-temperature metamorphism: orthopyroxene–sillimanite–garnet, sapphirine–quartz and spinel–quartz parageneses in Al-Mg granulites from In Hihaou, In Ouzzal, Hoggar. *Journal of metamorphic Geology*, **14**, 693–708.
- Raith, M., Karmakar, S. & Brown, M., 1997. Ultra-high temperature metamorphism and multistage decompressional evolution of sapphirine granulites from the Palni Hills Ranges, southern India. *Journal of metamorphic Geology*, **15**, 379–399.
- Sandiford, M., Neall, F. B. & Powell, R., 1987. Metamorphic evolution of aluminous granulites from Labwor Hills, Uganda. *Contributions to Mineralogy and Petrology*, **95**, 217–225.
- Schreyer, W., 1973. Whiteschists: A high-pressure rock and its geologic significance. *Journal of Geology*, **81**, 735–739.
- Stern, R. J., 1994. Arc assembly and continental collision in the Neoproterozoic East African Orogen: Implications for the consolidation of Gondwanaland. *Annual Reviews of Earth and Planetary Sciences*, **22**, 319–351.
- Waters, D. J., 1991. Hercynite-quartz granulites: phase relations, and implications for crustal processes. *European Journal of Mineralogy*, **3**, 367–386.

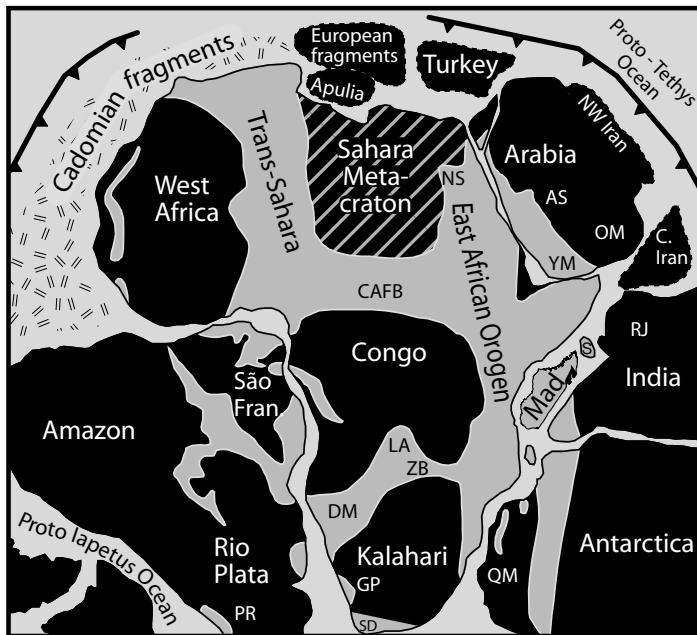
Chapter 2

Two-stage metamorphic evolution of the Bemarivo Belt of northern Madagascar: constraints from reaction textures and *in situ* monazite dating

2.1 Abstract

New results on the pressure-temperature-time evolution, deduced from conventional geothermobarometry and *in-situ* U-Th-total Pb dating of monazite, are presented for the Bemarivo Belt in northern Madagascar. The belt is subdivided into a northern part consisting of low-grade metamorphic epicontinental series and a southern part made up of granulite-facies metapelites. The prograde metamorphic stage of the latter unit is preserved by kyanite inclusions in garnet, which is in agreement with results of the garnet (core)–alumosilicate–quartz–plagioclase (inclusions in garnet; GASP) equilibrium. The peak-metamorphic stage is characterised by ultrahigh temperatures of $\sim 900\text{--}950\text{ }^\circ\text{C}$ and pressures of $\sim 9\text{ kbar}$, deduced from GASP equilibria and feldspar thermometry. In proximity to charnockite bodies, garnet-sillimanite-bearing metapelites contain aluminous orthopyroxene (max. 8.0 wt.% Al_2O_3) pointing to even higher temperatures of $\sim 970\text{ }^\circ\text{C}$. Peak-metamorphism is followed by near-isothermal decompression to pressures of 5–7 kbar and subsequent near-isobaric cooling, which is demonstrated by the extensive late-stage formation of cordierite around garnet. Internal textures and differences in chemistry of metapelitic monazite point to a polyphase growth history. Monazite with magmatically zoned cores is rarely preserved, and gives an age of ca. $737 \pm 19\text{ Ma}$, interpreted as the maximum age of sedimentation. Two metamorphic stages are dated: M_1 monazite cores range from $563 \pm 28\text{ Ma}$ to $532 \pm 23\text{ Ma}$, representing the collisional event, and M_2 monazite rims ($521 \pm 25\text{ Ma}$ to $513 \pm 14\text{ Ma}$), interpreted as grown during peak-metamorphic temperatures. These are among the youngest ages reported for high-grade metamorphism in Madagascar, and are supposed to reflect the Pan-African attachment of the Bemarivo Belt to the Gondwana supercontinent during its final amalgamation stage. In the course of this, the southern Bemarivo Belt was buried to a depth of $> 25\text{ km}$. Approximately 25–30 Ma later, the rocks underwent heating, in-

Figure 2.1: Reconstruction of a part of the Gondwana supercontinent, approximately 544 Ma ago (modified after Kusky *et al.*, 2003, and references therein), showing the relationship between Madagascar and the surrounding areas. Pan-African orogens are marked in grey, cratons in black. AS, Arabian Shield; CAFB, Central African Fold Belt; GP, Gariep; DM, Damara; LA, Lufilian Arc; Mad, Madagascar; OM, Oman; PR, Pampean Ranges; PS, Paterson; QM, Queen Maud Land; RJ, Rajasthan; São Fran., São Francisco; SD, Saldania; S, Seychelles; YM, Yemen; NS, Nubian Shield; ZB, Zambezi Belt.



terpreted to be due to magmatic underplating, and uplift. Presumably, the northern part of the Belt was also affected by this tectonism, but buried to lower depth, and therefore metamorphosed to lower grades.

2.2 Introduction

A fundamental method of reconstructing former geodynamic processes is by the determination of pressure-temperature-time paths of metamorphism. In polymetamorphic terranes additional accurate *in-situ* dating of metamorphic textures is particularly important to understand the often complicated tectono-thermal history. By integrating chronological and pressure-temperature information better constraints on the timing of burial and exhumation during orogenic processes can be obtained.

The Neoproterozoic East African Orogen is one of the largest orogenic belts on Earth, extending from Arabia through whole Eastern Africa into Antarctica (Fig. 2.1). It has been formed during the Pan-African orogeny, which is considered to have caused the final assembly of the supercontinent Gondwana (McWilliams, 1981; Stern, 1994). In recent years, advances in dating techniques have led to more precise geochronological results, which show that the formerly considered final collision between East and West Gondwana cannot be attributed to a single tectonic event (Meert *et al.*, 1995; Meert, 2003). In fact, it has to be assumed that the Pan-African orogeny consists of a series of discrete events, the exact timing and local distribution of which is not always well known. Madagascar holds a central position in the East African Orogen (Fig. 2.1), because it preserves a section from an Archaean craton, i.e. the Antongil Block (Fig. 2.2a), to the western orogenic hinterland. A tectonic subdivision has just recently been proposed (Collins *et al.*, 2000b;

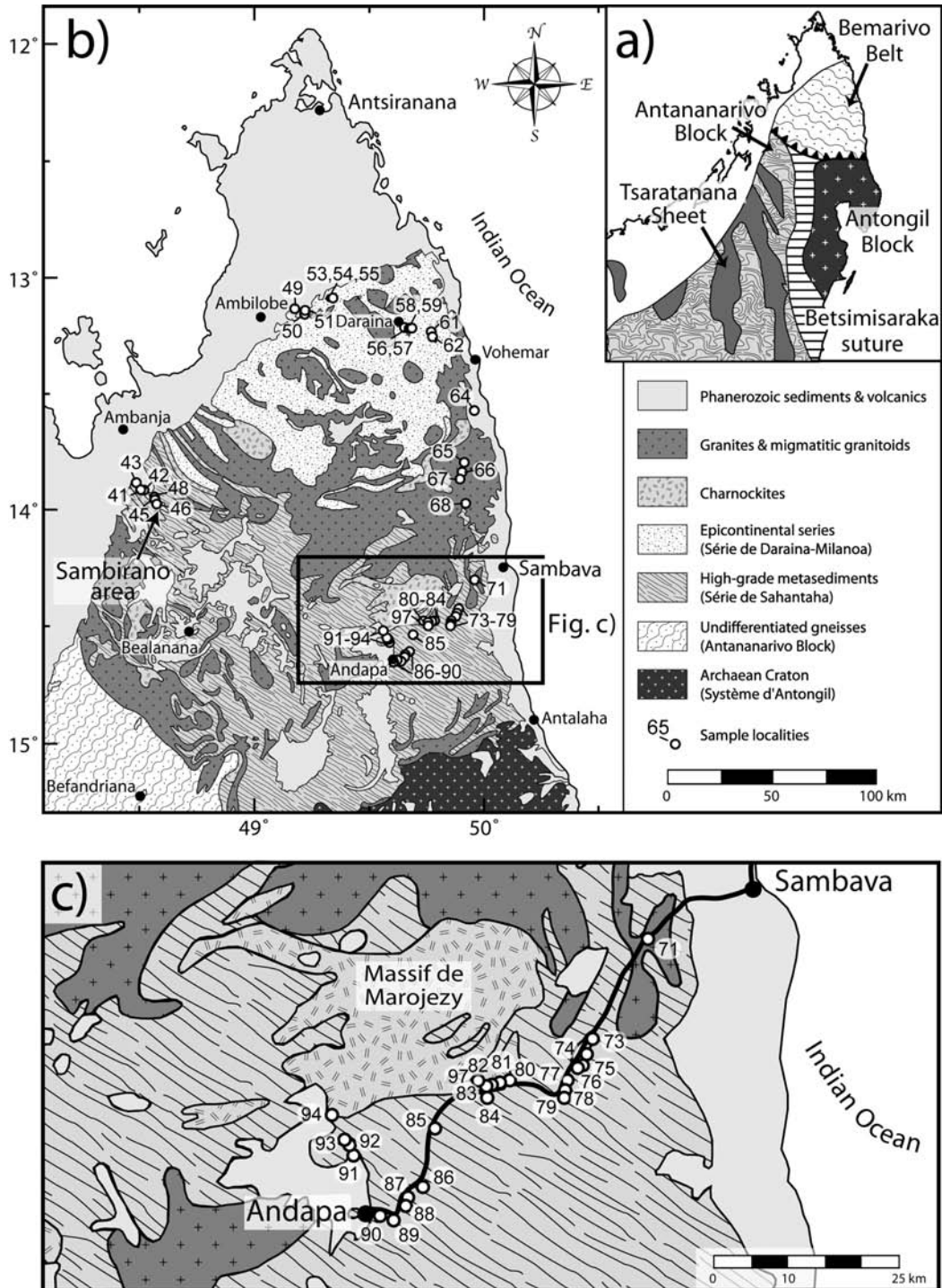


Figure 2.2: Simplified geological map of Northern Madagascar, modified after Besairie (1970) and Hottin (1976). (a) Overview over the main tectonic units of northern Madagascar (modified after Collins & Windley, 2002). To the west, the Archaean Antongil Block is rimmed by the proposed Betsimisaraka suture zone. The Bemarivo Belt is crosscutting both units. (b) Map of the Bemarivo Belt, showing our sample localities. (c) Cutout of panel (b), showing the geology and sample locations of the area between Andapa and Sambava, as well as the position of the Massif de Marojezy.

Collins & Windley, 2002), but reliable data on the pressure-temperature-time evolution of the different units, especially in northern and central Madagascar, are mostly lacking. The Antongil Block (Fig. 2.2a) is believed to represent a part of the Indian Dharwar Craton. West of the Antongil Block, there is the ca. 2.5 Ga old Antananarivo Block. Both are separated from each other by a 30 to 60 km wide region, consisting of metasediments with enclosed basic and ultrabasic rocks. This zone is interpreted as an oceanic suture, named Betsimisaraka suture (Fig. 2.2a; Collins *et al.*, 2000b; Kröner *et al.*, 2000).

Up to now, not much attention has been paid to the role of the Bemarivo Belt for the Gondwana formation. It is situated in northern Madagascar, just north of the cratonic Archaean Antongil Block (Fig. 2.2a). On the basis of geochronology, as well as palaeogeographic continental reconstructions of Gondwana, it is correlated with the Seychelles and the Rajasthan region of India (Tucker *et al.*, 1999a; Torsvik *et al.*, 2001). Large areas within the Bemarivo Belt consist of metasedimentary rocks, which are suitable for applying conventional geothermobarometry. Here, we present new data and observations on the petrology of these rocks, in order to deduce the pressure and temperature conditions during the Pan-African orogeny. In addition, chemical U-Th-total Pb dating was undertaken on polyphase monazite to unravel the geodynamic evolution of this central part of Gondwana.

2.3 Geological setting

The Bemarivo Belt is the northernmost basement unit of Madagascar. It strikes WNW—ESE and truncates structures in the Antananarivo Block, the Antongil Block, and the Betsimisaraka suture zone (Fig. 2.2a). It can be subdivided into three distinct regions (Fig. 2.2b). The southern region is 50–150 km wide, extends from the area around Antalaha (in the east) to the Sambirano river (in the west) and consists of high-grade metapelitic rocks. It is bordered to the north by a 50- to 80-km-broad region, dominated by metagranitoids and granites. The northernmost part consists of lower-grade metamorphic epicontinental series. Following the established nomenclature for lithologies in southern Madagascar, Besairie (1970) attributed the southern area to the ‘Système du Graphite’, whereas the northern part belongs to the ‘Système du Vohibory’. According to the geological synthesis of Madagascar after Hottin (1976), this southern area is termed the ‘Séries de Sahantaha’ and consists of kyanite- and sillimanite-bearing quartzites, mica-schists, granites, conglomerates, paragneisses, marbles, and minor amphibolites. Within this series, Hottin (1976) noted an increasing metamorphic grade from the Antongil Block (‘Système d’Antongil’) towards the north and the west. The northern part is termed the ‘Série de Daraina-Milanoa’. It consists of muscovite-bearing paragneisses, conglomerates, metavolcanics, quartzites, marbles, amphibolites, and mica-schists containing kyanite or garnet–staurolite. The grade of metamorphism is greenschist- to epidote-amphibolite facies.

The Bemarivo Belt is thought to represent a part of a Neoproterozoic continental arc terrane (Tucker *et al.*, 1999a; Buchwaldt & Tucker, 2001). A rhyolite of the Série de Daraina-Milanoa has been dated at ca. 715 Ma (Tucker *et al.*, 1999a). A granitic intrusion

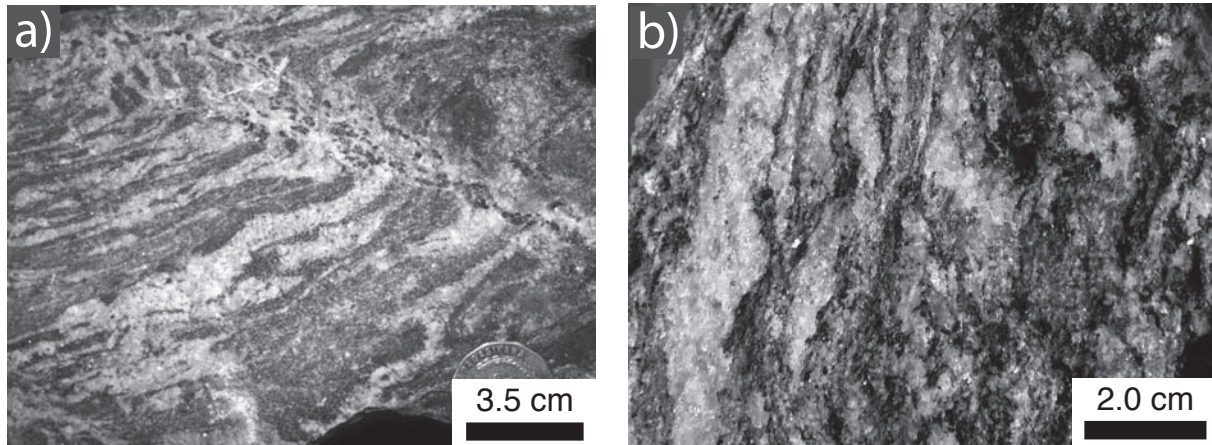


Figure 2.3: (a) Enderbitic gneiss showing intense migmatisation (Central Bemarivo Belt, Md65). (b) Metapelite containing leucosomes as well as biotite- and sillimanite-rich bands (Southern Bemarivo Belt, Md83).

in the migmatites of the central part formed at 753.8 ± 1.7 Ma (Tucker *et al.* in Ashwal, 1997). Collins *et al.* (2000a) postulate an overthrusting of the Bemarivo Belt to the south after closure of the Betsimisaraka suture. Syntectonic metamorphism in the southern part of the Bemarivo Belt reached granulite facies grade at 520–510 Ma (Tucker *et al.*, 1999a; Buchwaldt *et al.*, 2003). Afterwards, extensional collapse is thought to have occurred (Collins *et al.*, 2000a). Conventional geothermobarometry has been applied by Buchwaldt *et al.* (2003) to rocks of the southern Bemarivo Belt. They determined metamorphic conditions of $T=750\text{--}930$ °C and $P=6\text{--}10$ kbar. However, their thermometric estimates are based only on Fe-Mg exchange between minerals, which is problematic for constraining conditions of high-temperature metamorphic rocks because of re-equilibration on cooling (e.g., Fitzsimons & Harley, 1994).

In the southern part of the Bemarivo Belt, garnet-free enderbitic and charnockitic gneisses, which frequently show migmatisation, are found (Fig. 2.3a). Other rock types, such as calcisilicates, marbles, quartzites, and metabasites, occur just in small amounts. In the area between Sambava and Andapa (Fig. 2.2b,c), migmatitic metapelites (Fig. 2.3b) commonly occur, which are mostly lacking in the Sambirano area. In the northern part of the Bemarivo Belt, we took samples along the roadside from Ambilobe via Daraina and Vohémar to Sambava (Fig. 2.2b). Samples are generally epidote-bearing amphibolites, but in minor amounts also quartzites and muscovite-bearing micaschists occur. Between Vohémar and Sambava, granitic and granodioritic gneisses are predominant.

2.4 Analytical procedure and data processing

Measurements were performed on a JEOL Superprobe JXA-8900R electron microprobe at the University of Kiel, equipped with five wavelength-dispersive spectrometers. The accelerating voltage was generally 15 kV for a probe current of 20 nA. Yttrium in garnet

Table 2.1: Measurement conditions for U-Th-totalPb dating of monazite. Background measurement time is given for one background.

Element	Crystal	Line	Measurement time	
			(peak)	(background)
U	PETH	M β	50 s	30 s
Th	PETH	M α	20 s	10 s
Pb	PETH	M β	220 s	100 s
P	PETJ	K α	15 s	7 s
Ca	PETH	K α	15 s	5 s
Si	TAP	K α	40 s	20 s
Y	PETJ	L α	30 s	10 s
Al	TAP	K α	20 s	10 s
Sm	LIF	L β	60 s	30 s
La	LIF	L α	60 s	30 s
Eu	LIF	L β	30 s	10 s
Ce	LIF	L α	15 s	7 s
Dy	LIF	L α	100 s	30 s
Nd	LIF	L α	20 s	10 s
Gd	LIF	L β	40 s	20 s
Pr	LIF	L β	80 s	20 s
Er	LIF	L α	80 s	20 s

was measured with 20 kV and 300 nA; for apatite measurements (needed for Grt-Mnz thermometry) 10 kV and 10 nA were used. Synthetic and natural minerals were used as the standards. Sample spot sizes were 1–7 μm in diameter. The raw data were corrected using the CITZAF method of Armstrong (1995).

For feldspar thermometry, the composition of mesoperthitic grains was reintegrated from measurements of plagioclase and alkali-feldspar. The proportions of host and lamellae were determined from backscattered electron images using an image analysis software. The textural context of the grains was carefully checked to account for possible exsolution-free or recrystallised rims.

For monazite measurements, the accelerating voltage was 20 kV with a probe current of 80 nA. The following standard materials were used: synthetic orthophosphates (Jarosewich & Boatner, 1991) for P, Y, and REE; synthetic uranium-bearing glass for U; natural wolastonite for Ca and Si; thorianite for Th; crocoite for Pb; corundum for Al. X-ray lines, measurement crystals and counting times are listed in Table 2.1. Matrix correction for monazite analyses was done using the JEOL ZAF program. The interference of Th M γ on U M β was corrected with an experimentally derived correction factor.

All monazite was analysed *in-situ* to have textural control over the mineral inclusion relationships. For control over internal zoning, backscattered electron images as well as

X-ray maps of Y, Th, U and Pb were obtained. The samples were polished on Pb-free polishing discs. As an internal laboratory standard during measurements, the homogeneous monazite F6 from the Anosyan Massif (Manangotry Pass) in SE Madagascar (kindly provided by M. Raith, Bonn) was repetitively analysed. It was dated with the U-Pb method of cogenetic zircon and by a Sm-Nd monazite-biotite-garnet-zircon isochron at 545 ± 2 and 542 ± 11 Ma, respectively (Paquette *et al.*, 1994). Analytical errors for each analysis were calculated from the counting statistics using the program 'CombError' of P. Appel (can be downloaded from <http://www.min.uni-kiel.de/epma/sw.html>). The age was calculated after the isochron method of Suzuki & Adachi (1991, 1994), using the software of Kato *et al.* (1999) with decay constants from Steiger & Jäger (1977). A York-regression isochron (York, 1966) was forced through the origin (Cocherie *et al.*, 1998) with an error of 150 ppm at the point of zero ThO_2^* and PbO.

2.5 Petrography and mineral chemistry

2.5.1 Northern (Série de Daraina-Milanoa) and central Bemarivo Belt

The northern Bemarivo Belt is dominated by metabasic rocks, which are interpreted as metamorphosed volcanoclastic sediments (Hottin, 1976). Coarse-grained titanite-, epidote- and garnet-bearing amphibolites are common, and locally they show a strong metasomatic overprint. Granodioritic and granitic gneisses, as well as muscovite-bearing quartzites and micaschists do also occur. Kyanite is reported from quartzites (Lacroix, 1922), and Hottin (1976) describes garnet–staurolite parageneses from micaschists. The central part of the belt is made up largely of granites and gabbros, as well as enderbitic and charnockitic gneisses. The gneisses show intensive migmatization (Fig. 2.3a) and are generally garnet-free (only one sample contains late-stage garnet). This either points to high temperatures or low pressures during metamorphism. Porphyritic hornblende–biotite gneisses are subordinate.

2.5.2 Southern Bemarivo Belt (Série de Sahantaha)

Metapelites

Metapelitic rocks, which commonly show migmatitic textures (Fig. 2.3b), occur in the Andapa-Sambava region of the southern Bemarivo Belt (Fig. 2.2c), and have also been reported to occur near Bealanana (Besairie, 1970; Fig. 2.2b). The sample locations are shown in Fig. 2.2 and the equilibrium mineral assemblages of the samples are given in Table 2.2. According to their mineral content, three main types can be distinguished. The most common metapelites contain kyanite, sillimanite, garnet, K-feldspar, quartz, biotite, and late-stage cordierite (no. [1] in Table 2.2). Other assemblages lack either garnet or plagioclase or cordierite or aluminosilicate (no. [2], [3] & [4] in Table 2.2). A second group of rocks contains additional orthopyroxene and locally spinel (no. [5] & [6] in Table 2.2).

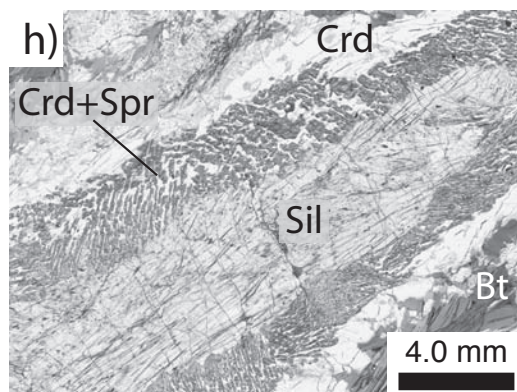
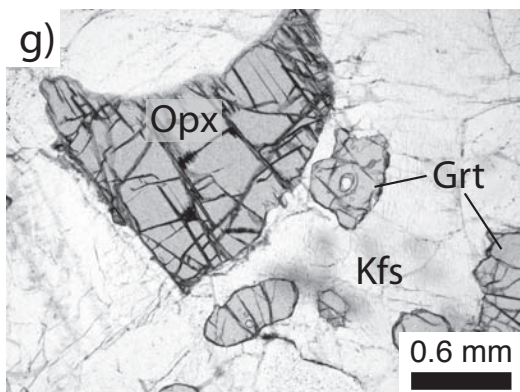
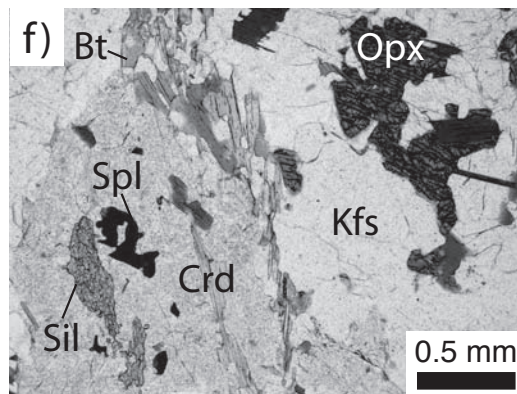
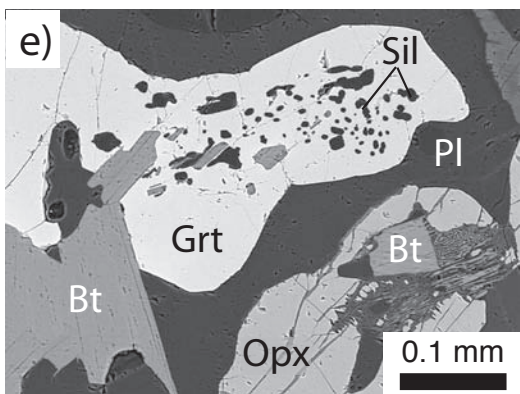
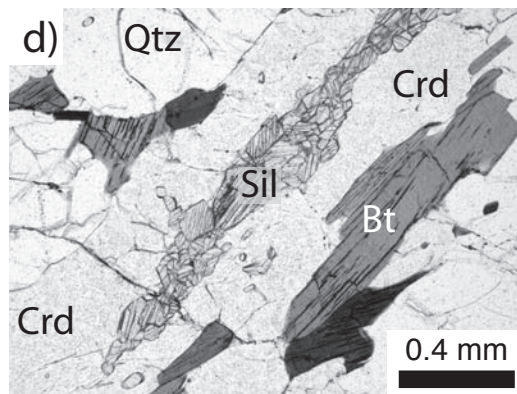
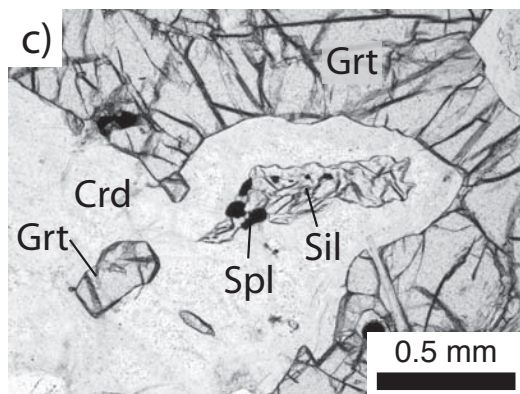
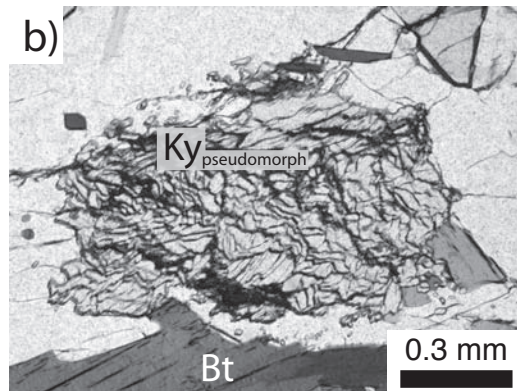
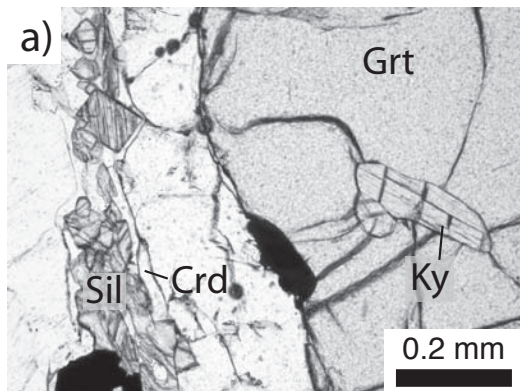
Table 2.2: Mineral assemblages in metapelitic and semipelitic rocks. [1]–[4] are typical metapelitic rocks, [5]–[6] are rare Opx-bearing assemblages, and [7] are silica-undersaturated metapelites. Sample numbers are given without prefix ‘Md’.

[1]	Ky/Sil	Grt	Kfs	Qtz	±Pl	Bt	—	(Crd)	(±Spl)
[2]	Ky/Sil	—	Kfs	Qtz	Pl	Bt	—	—	—
[3]	Ky/Sil	—	Kfs	Qtz	—	Bt	—	(Crd)	—
[4]	—	Grt	Kfs	Qtz	Pl	Bt	—	—	—
[5]	Ky/Sil	Grt	Kfs	Qtz	Pl	Bt	Opx	(Crd)	(Spl)
[6]	—	Grt	Kfs	Qtz	Pl	Bt	Opx	—	—
[7]	Ky/Sil	—	Kfs	—	Pl	Bt	—	Crd/(Crd)	(±Spr)
Common accessory minerals: Ap, Mnz, Ilm, Rt, & Spl; in (7) also Crn									
[1]	73-1-03, 73-3-03, 75-1-03, 76-1-03, 82-2-03, 83-1-03, 83-9-03, 83-10-03, 83-12-03, 83-14-03, 83-15-03, 84-1-03, 86-1-03, 87-1-03, 87-2-03, 88-1-03, 88-2-03, 88-3-03, 89-1-03, 90-1-03, 93-1-03, 93-2-03, 93-4-03								
[2]	78-2-03								
[3]	89-2-03								
[4]	48-1-03, 80-1-03, 92-1-03								
[5]	83-13-03								
[6]	81-1-03, 81-2-03								
[7]	83-2-03, 83-3-03, 83-4-03, 83-5-03, 83-6-03, 83-7-03, 83-8-03, M97-12-2								

Some samples lack sillimanite (no. [4] & [6] in Table 2.2) and are of semipelitic composition. Finally, in minor amounts silica-undersaturated high Mg-Al metapelites were found close to the Massif de Marojezy (Fig. 2.2c), closely associated with other metapelitic rocks. They contain corundum and sapphirine, but are quartz-free (no. [7] in Table 2.2).

The metapelites of the first type are porphyroblastic, medium-grained, and show a well-developed schistosity made up of bands of sillimanite and biotite. Concordant as well as discordant leucosomes are frequently present (Fig. 2.3b). Garnet locally contains inclusions of kyanite near the core (Fig. 2.4a) and sillimanite needles close to the rim. Sillimanite in the matrix forms euhedral crystals (Fig. 2.4a), but large aggregates that are fine-fibrous

Figure 2.4 (following page): Microphotographs showing reaction textures in metapelites (mineral abbreviations after Kretz, 1983). Pictures are taken under plane-polarised light, except for panel e, which is a backscattered-electron image. (a) Garnet porphyroblast including kyanite, and sillimanite growing in the rock matrix (Md90-1-03). (b) Aggregate of sillimanite, interpreted as a pseudomorph after kyanite (Md75-1-03). (c) Garnet breakdown and late-stage formation of cordierite. Small relics of garnet are situated in the cordierite (Md83-14-03). (d) Cordierite rim separating biotite and sillimanite (Md88-3-03). (e) Coexisting garnet and orthopyroxene in a metapelite. Garnet contains inclusions of sillimanite (Md83-13-03). (f) Orthopyroxene porphyroblasts and sillimanite in a metapelitic rock. Sillimanite is surrounded by late-stage cordierite and spinel (Md83-13-03). (g) Orthopyroxene and garnet in the leucosome of a metapelitic gneiss (Md81-1-03). (h) Sillimanite mantled by a symplectite of cordierite and sapphirine (Md83-2-03).



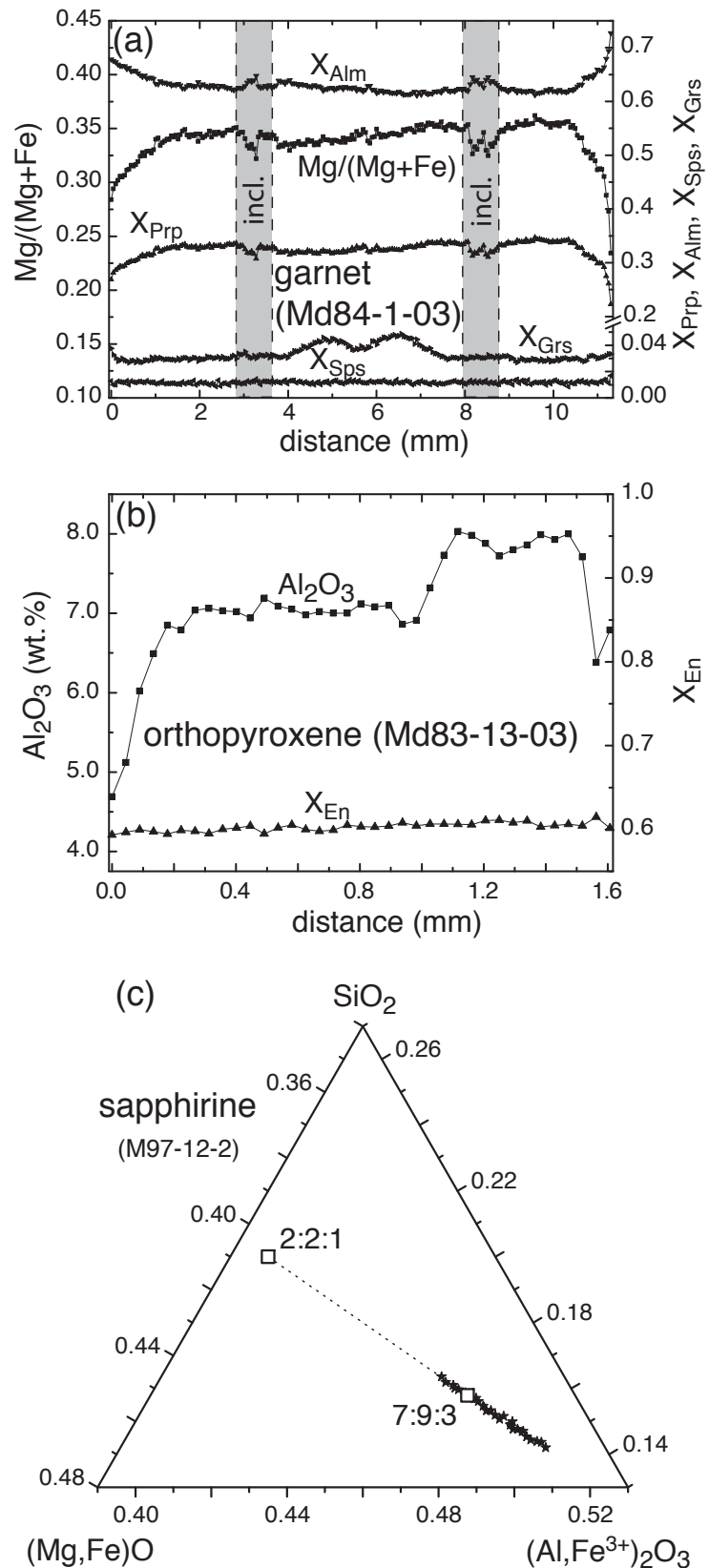


Figure 2.5: (a) Chemical profile of a metapelitic garnet from a Grt-Sil-Bt-Crd gneiss, showing a weak zonation. The shaded areas are inclusion-rich (Bt, Kfs). (b) Profile through a metamorphic orthopyroxene (coexisting with Grt and Sil). A zonation in the alumina content is preserved, whereas the Mg-Fe is completely reequilibrated. (c) Sapphire analyses in the diagram $(\text{Mg,Fe})\text{O}$ - $(\text{Al,Fe}^{3+})_2\text{O}_3$ - SiO_2 . For comparison 7:9:3 and 2:2:1 compositions are shown (cf. Higgins *et al.*, 1979).

Table 2.3: Representative electron microprobe analyses of metapelitic garnet.

Sample No.	90-1 40*	90-1 12*	90-1 334*	90-1 336*	90-1 411†	90-1 412†	83-13 39†	83-13 40†	83-13 89*	83-13 96*	82-2 29†	84-1 774‡	84-1 776‡
SiO ₂	38.88	38.97	38.81	38.77	38.73	39.08	38.34	38.79	38.52	38.78	37.94	38.27	38.02
TiO ₂	0.04	0.03	0.01	0.04	0.03	0.01	0.02	0.00	0.00	0.02	0.00	0.04	0.00
Al ₂ O ₃	21.87	21.81	21.87	21.94	21.78	21.93	21.91	21.87	21.92	22.08	21.54	21.20	21.11
Cr ₂ O ₃	0.03	0.04	0.03	0.03	0.02	0.04	0.03	0.02	0.02	0.04	0.11	0.01	0.03
FeO	28.36	28.88	27.76	27.97	29.10	28.60	31.72	30.88	30.81	29.99	34.48	32.63	32.50
MgO	9.06	9.06	8.09	8.18	9.08	9.00	6.81	7.70	7.73	7.79	5.67	6.31	6.11
MnO	0.35	0.32	0.30	0.29	0.36	0.31	1.29	1.29	1.15	1.18	0.26	0.68	0.77
CaO	1.26	1.16	3.05	2.81	0.89	0.82	0.56	0.58	0.57	0.55	0.60	1.09	1.20
Na ₂ O	n.d.	n.d.	n.d.	n.d.	n.d.	n.d.	n.d.	n.d.	n.d.	n.d.	n.d.	0.02	0.05
Y ₂ O ₃	0.02	0.03	n.d.	n.d.	n.d.	n.d.	n.d.	n.d.	n.d.	n.d.	n.d.	0.02	0.05
Total	99.87	100.30	99.92	100.03	99.99	99.79	100.68	101.13	100.72	100.43	100.60	100.25	99.79
Si	3.00	3.00	3.00	3.00	3.00	3.02	2.99	3.00	2.99	3.00	2.99	3.01	3.01
Ti	0.00	0.00	0.00	0.00	0.00	0.00	0.00	0.00	0.00	0.00	0.00	0.00	0.00
Al	1.99	1.98	1.99	2.00	1.99	2.00	2.01	1.99	2.00	2.02	2.00	1.97	1.97
Cr	0.00	0.00	0.00	0.00	0.00	0.00	0.00	0.00	0.00	0.00	0.01	0.00	0.00
Fe	1.83	1.86	1.80	1.81	1.88	1.85	2.07	2.00	2.00	1.94	2.27	2.15	2.15
Mg	1.04	1.04	0.93	0.94	1.05	1.04	0.79	0.89	0.89	0.90	0.67	0.74	0.72
Mn	0.02	0.02	0.02	0.02	0.02	0.02	0.09	0.08	0.08	0.08	0.02	0.05	0.05
Ca	0.10	0.10	0.25	0.23	0.07	0.07	0.05	0.05	0.05	0.05	0.05	0.09	0.10
Na	n.d.	n.d.	n.d.	n.d.	n.d.	n.d.	n.d.	n.d.	n.d.	n.d.	n.d.	0.00	0.01
Y	0.00	0.00	n.d.	n.d.	n.d.	n.d.	n.d.	n.d.	n.d.	n.d.	n.d.	0.00	0.01
Total	7.98	8.00	7.99	8.00	8.01	8.00	8.00	8.01	8.01	7.99	8.01	8.01	8.02
X _{Mg}	0.36	0.36	0.34	0.34	0.36	0.36	0.28	0.31	0.31	0.32	0.23	0.26	0.25
X _{Prp}	0.35	0.34	0.31	0.31	0.35	0.35	0.26	0.29	0.30	0.30	0.22	0.24	0.24
X _{Alm}	0.61	0.62	0.60	0.60	0.62	0.62	0.69	0.66	0.66	0.66	0.76	0.71	0.71
X _{Spss}	0.01	0.01	0.01	0.01	0.01	0.01	0.03	0.03	0.03	0.03	0.01	0.02	0.02
X _{Grs}	0.03	0.03	0.08	0.08	0.02	0.02	0.02	0.02	0.01	0.01	0.01	0.03	0.03

cations calculated on the basis of 12 oxygens; * core analysis; † outer zone analysis; ‡ rim analysis

Table 2.4: Representative electron microprobe analyses of metapelitic biotite, sapphirine, and cordierite.

Sample No.	81-1 Bt(602)	90-1 Bt(40)	48-1 Bt(5)	93-2 Bt(14)	M97/12 Bt(645)	M97/12 Spr(449)	M97/12 Spr(454)	82-2 Crd(20)*	84-1 Crd(826)*	84-1 Crd(819)†	84-1 Crd(823)†	M97/12 Crd(304)
SiO ₂	35.84	35.58	36.19	36.30	39.61	11.96	12.31	49.39	48.59	49.04	49.16	50.72
TiO ₂	5.04	5.62	5.19	5.82	2.52	0.01	0.08	0.00	0.00	0.02	0.00	0.02
Al ₂ O ₃	16.53	15.72	14.73	15.44	17.76	65.67	65.36	32.48	32.36	32.31	32.27	32.59
Cr ₂ O ₃	0.06	0.00	0.00	0.00	0.05	0.03	0.03	0.00	0.02	0.00	0.04	0.00
FeO	15.12	16.85	19.35	15.04	5.80	3.97	4.39	6.08	5.92	5.48	5.73	2.01
Fe ₂ O ₃	n.c.	n.c.	n.c.	n.c.	n.c.	0.91	0.46	n.c.	n.c.	n.c.	n.c.	n.c.
MgO	12.73	11.26	10.03	12.62	20.24	17.06	17.16	9.64	9.88	10.09	9.94	12.50
MnO	0.06	0.00	0.10	0.00	0.00	0.11	0.11	0.03	0.05	0.09	0.03	0.08
CaO	0.00	0.00	0.11	0.00	0.00	0.02	0.01	0.00	0.00	0.02	0.00	0.00
Na ₂ O	0.06	0.09	0.16	0.17	0.14	0.02	0.02	0.08	0.11	0.08	0.07	0.13
K ₂ O	10.20	10.09	10.03	10.11	9.81	0.01	0.00	0.00	0.00	0.00	0.01	0.01
BaO	n.d.	n.d.	0.11	n.d.	n.d.	0.00	0.00	n.d.	n.d.	n.d.	n.d.	n.d.
P ₂ O ₅	n.d.	n.d.	n.d.	n.d.	n.d.	0.01	0.05	n.d.	n.d.	n.d.	n.d.	n.d.
Total	95.64	95.21	96.00	95.50	95.93	99.78	99.98	97.70	96.93	97.13	97.25	98.06
Si	5.37	5.41	5.52	5.45	5.59	1.41	1.45	5.06	5.02	5.04	5.05	5.08
Ti	0.57	0.64	0.60	0.66	0.27	0.00	0.01	0.00	0.00	0.00	0.00	0.00
Al	2.92	2.82	2.65	2.73	2.96	9.11	9.05	3.92	3.94	3.92	3.91	3.85
Cr	0.01	0.00	0.00	0.00	0.01	0.00	0.00	0.00	0.00	0.00	0.00	0.00
Fe ²⁺	1.90	2.14	2.47	1.89	0.69	0.39	0.43	0.52	0.51	0.47	0.49	0.17
Fe ³⁺	n.c.	n.c.	n.c.	n.c.	n.c.	0.08	0.04	n.c.	n.c.	n.c.	n.c.	n.c.
Mg	2.84	2.55	2.28	2.82	4.26	2.99	3.00	1.47	1.52	1.55	1.52	1.87
Mn	0.01	0.00	0.01	0.00	0.00	0.01	0.01	0.00	0.00	0.01	0.00	0.01
Ca	0.00	0.00	0.02	0.00	0.00	0.00	0.00	0.00	0.00	0.00	0.00	0.00
Na	0.02	0.03	0.05	0.05	0.04	0.01	0.01	0.02	0.02	0.02	0.02	0.03
K	1.95	1.96	1.95	1.94	1.77	0.00	0.00	0.00	0.00	0.00	0.00	0.00
Ba	n.d.	n.d.	0.01	n.d.	n.d.	0.00	0.00	n.d.	n.d.	n.d.	n.d.	n.d.
P	n.d.	n.d.	n.d.	n.d.	n.d.	0.00	0.00	n.d.	n.d.	n.d.	n.d.	n.d.
Total	15.59	15.55	15.56	15.54	15.59	14.00	14.00	10.99	11.01	11.01	10.99	11.01
Oxygens	22	22	22	22	22	20	20	18	18	18	18	18
X _{Mg}	0.60	0.54	0.48	0.60	0.86	0.88	0.87	0.74	0.75	0.77	0.76	0.92

Fe³⁺ calculated assuming stoichiometry; n.c., not calculated; n.d., not determined; * core analysis; † rim analysis

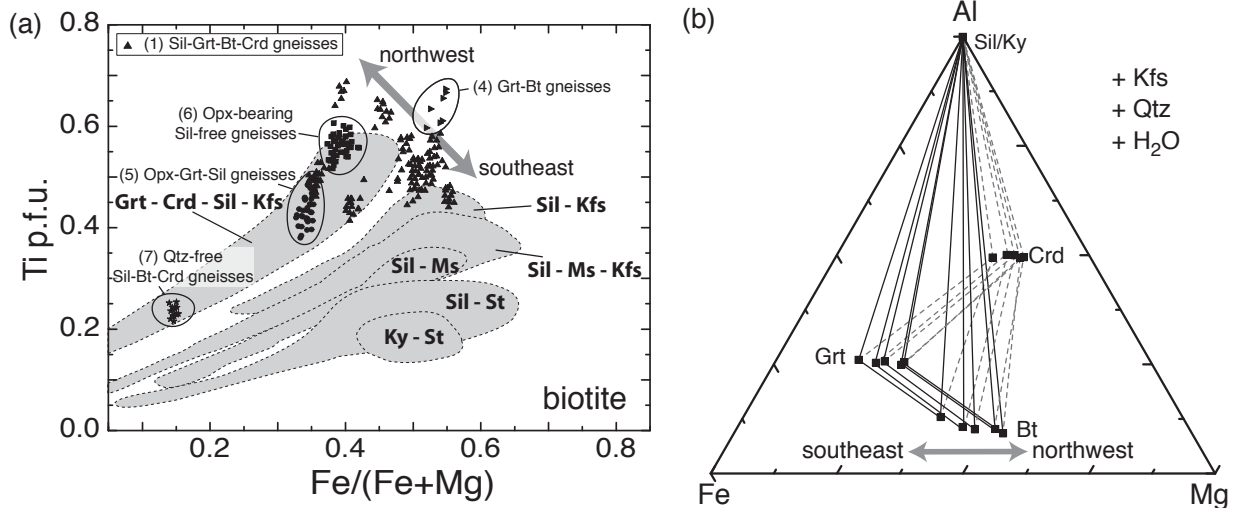


Figure 2.6: (a) Compositions of metapelitic biotites from rocks of the southern Bemarivo Belt in the X_{Fe} vs. Tip.f.u. diagram (formula units calculated on the basis of 22 oxygens; coexisting with ilmenite or ilmenite + rutile). Most biotite (triangular symbols) is from Grt-Sil-Bt-Crd gneisses and shows a systematic change in chemical composition from southeast to northwest. Biotite analyses from other metapelitic mineral assemblages are also shown (numbers refer to Table 2.2). Shaded fields: compositional ranges of biotite from metamorphic zones in New England (Robinson *et al.*, 1982). (b) AFM diagram (projection from Kfs, Qtz, and H₂O) showing mineral compositions of Grt-Sil-Bt-Crd gneisses from the Andapa area. The gradual increase of Mg contents towards the northwest points to increasing metamorphic conditions.

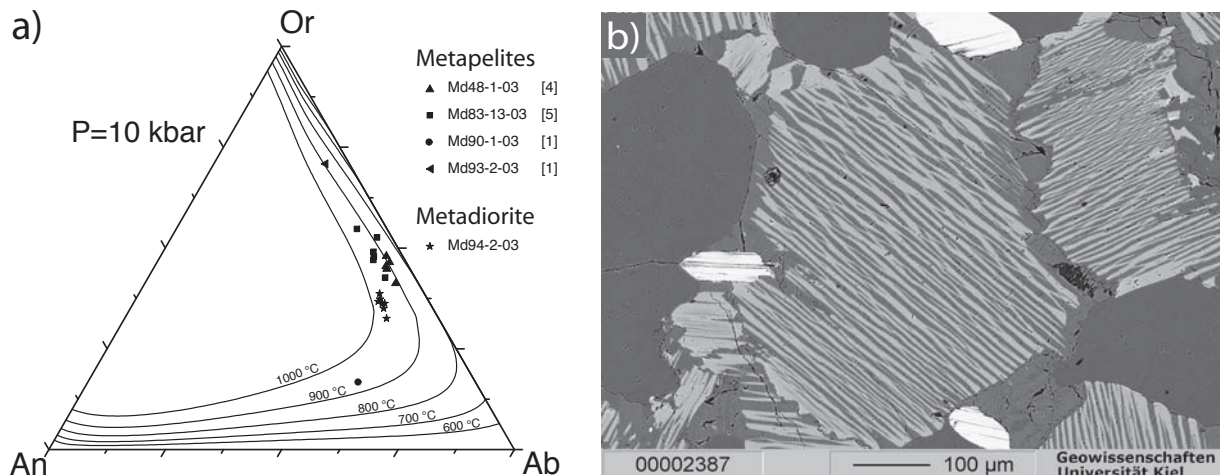


Figure 2.7: (a) Results of the feldspar thermometry. Most re-integrated compositions of mesoperthites give temperatures in the range of 900 to 1000 °C. Isoleths after Fuhrmann & Lindsley (1988). Bracketed numbers correspond to mineral assemblages in Table 2.2. (b) Typical rock texture showing large mesoperthitic feldspars (backscattered electron image).

Table 2.5: Representative electron microprobe analyses of metapelitic orthopyroxene, plagioclase, and alkali feldspar.

Sample No.	83-13	83-13	83-13	83-13	81-1	90-1	90-1	90-1	90-1	90-1	90-1	90-1	90-1	90-1
	OpX(268)*	OpX(270)*	OpX(45)†	OpX(31)‡	OpX(536)	Pl(442)¶	Pl(444)¶	Pl(461)§	Pl(462)§	Pl(456)¶	Kfs(468)	Kfs(468)	Kfs(495)	
SiO ₂	48.81	48.21	49.45	49.11	50.01	57.42	58.04	60.17	60.38	56.25	64.06	64.44	64.44	
TiO ₂	0.00	0.00	0.11	0.10	0.11	n.d.	n.d.	n.d.	n.d.	n.d.	n.d.	n.d.	n.d.	
Al ₂ O ₃	7.32	8.03	6.25	6.61	4.89	26.08	25.70	24.41	24.47	27.67	18.43	18.43	18.67	
Cr ₂ O ₃	0.00	0.00	0.06	0.07	0.01	n.d.	n.d.	n.d.	n.d.	n.d.	n.d.	n.d.	n.d.	
FeO	22.80	22.72	23.48	23.52	25.05	n.c.	n.c.	n.c.	n.c.	n.c.	n.c.	n.c.	n.c.	
Fe ₂ O ₃	n.c.	n.c.	n.c.	n.c.	n.c.	0.32	0.60	0.26	0.27	0.42	0.05	0.05	0.00	
MgO	20.06	19.90	20.19	20.10	19.18	n.d.	n.d.	n.d.	n.d.	n.d.	n.d.	n.d.	n.d.	
MnO	0.36	0.31	0.27	0.27	0.59	n.d.	n.d.	n.d.	n.d.	n.d.	n.d.	n.d.	n.d.	
CaO	0.05	0.03	0.02	0.06	0.04	8.36	8.14	6.41	6.42	9.84	0.04	0.04	0.14	
Na ₂ O	0.00	0.00	0.04	0.04	0.00	6.46	6.57	7.70	7.80	5.58	1.30	1.30	1.87	
K ₂ O	0.00	0.00	0.01	0.01	0.00	0.60	0.41	0.23	0.21	0.28	15.36	14.15	14.15	
BaO	n.d.	n.d.	n.d.	n.d.	n.d.	0.00	0.01	0.05	0.00	0.00	0.48	0.53	0.53	
Total	99.40	99.20	99.88	99.89	99.88	99.24	99.47	99.23	99.55	100.04	99.72	99.80	99.80	
Si	1.83	1.81	1.85	1.84	1.89	2.60	2.62	2.70	2.70	2.53	2.98	2.98	2.98	
Ti	0.00	0.00	0.00	0.00	0.00	n.d.	n.d.	n.d.	n.d.	n.d.	n.d.	n.d.	n.d.	
Al	0.32	0.36	0.28	0.29	0.22	1.39	1.37	1.29	1.29	1.47	1.01	1.01	1.02	
Cr	0.00	0.00	0.00	0.00	0.00	n.d.	n.d.	n.d.	n.d.	n.d.	n.d.	n.d.	n.d.	
Fe ²⁺	0.72	0.71	0.74	0.74	0.79	n.c.	n.c.	n.c.	n.c.	n.c.	n.c.	n.c.	n.c.	
Fe ³⁺	n.c.	n.c.	n.c.	n.c.	n.c.	0.01	0.02	0.01	0.01	0.01	0.00	0.00	0.00	
Mg	1.12	1.12	1.13	1.12	1.08	n.d.	n.d.	n.d.	n.d.	n.d.	n.d.	n.d.	n.d.	
Mn	0.01	0.01	0.01	0.01	0.02	n.d.	n.d.	n.d.	n.d.	n.d.	n.d.	n.d.	n.d.	
Ca	0.00	0.00	0.00	0.00	0.00	0.41	0.39	0.31	0.31	0.47	0.00	0.01	0.01	
Na	0.00	0.00	0.00	0.00	0.00	0.57	0.57	0.67	0.68	0.49	0.12	0.12	0.17	
K	0.00	0.00	0.00	0.00	0.00	0.04	0.02	0.01	0.01	0.02	0.91	0.84	0.84	
Ba	n.d.	n.d.	n.d.	n.d.	n.d.	0.00	0.00	0.00	0.00	0.00	0.01	0.01	0.01	
Total	4.00	4.01	4.01	4.00	4.00	5.02	4.99	4.99	5.00	4.99	5.03	5.03	5.03	
Oxygens	6	6	6	6	6	8	8	8	8	8	8	8	8	
X _{Mg}	0.61	0.61	0.60	0.60	0.58	—	—	—	—	—	—	—	—	
X _{Al}	—	—	—	—	—	0.56	0.58	0.68	0.68	0.50	0.11	0.11	0.16	
X _{Aln}	—	—	—	—	—	0.40	0.40	0.31	0.31	0.48	0.00	0.01	0.01	
X _{Or}	—	—	—	—	—	0.04	0.02	0.01	0.01	0.02	0.89	0.83	0.83	

in feldspars all iron as Fe³⁺; n.c., not calculated; n.d., not determined; * core analysis; † rim analysis; ¶ inclusion in Grt; § matrix

and undulously extinguishing are also very common (Fig. 2.4b). Due to this texture, we interpret them as pseudomorphs formed after kyanite. Apart from a narrow retrograde re-equilibrated rim, even large garnet porphyroblasts are just weakly zoned (Fig. 2.5a), whereas smaller ones are unzoned. They have an X_{Mg} [= $Mg/(Mg + Fe^{2+})$] of 0.25–0.35, $X_{Prp} = 0.15$ –0.35, $X_{Alm} = 0.55$ –0.80, $X_{Sps} = 0.00$ –0.01, and $X_{Grs} = 0.02$ –0.03. Garnet cores have slightly higher grossular contents (ca. 0.05) and lower X_{Mg} . Representative garnet analyses are given in Table 2.3. Brownish biotite forms hypidiomorphic flakes in the rock matrix (Fig. 2.4b,d). Coexisting with ilmenite or ilmenite + rutile, it has variable X_{Mg} values of 0.35–0.60 and Ti contents of 0.4–0.7 p.f.u. (calculation based on 22 oxygens; Fig. 2.6a; Table 2.4). Some grains of green late-stage biotite have much lower Ti contents (ca. 0.2–0.3 p.f.u.). Cordierite forms rims around garnet (Fig. 2.4c) and is separating biotite and sillimanite (Fig. 2.4d). Its X_{Mg} varies in the range of 0.6–0.8 (Table 2.4). All cordierite seems to have formed during retrograde metamorphism, and no inclusions of cordierite in garnet have been found. The large regional variation in composition of garnet, biotite, and cordierite is correlated with a systematic shift to the more Mg-rich side (Fig. 2.6b) from the southeast to the northwest of the Andapa area. Beside quartz, the matrix of the rock is mainly made up of alkalifeldspar ($X_{Or} = 0.8$ –0.9). Plagioclase is inversely zoned and has a composition of $X_{An} = 0.2$ –0.3 in the core and $X_{An} = 0.3$ –0.4 at the rim (Table 2.5). Some metapelites contain plagioclase with $X_{An} = 0.55$ –0.60 and inclusions in garnet with even higher X_{An} of 0.65–0.70. Reintegrated compositions of mesoperthitic feldspars are shown in Fig. 2.7. Common accessory minerals are monazite and zircon, which occur in the rock matrix as well as inclusions in garnet. Apatite has just been found to be included in garnet. Cordierite- and sillimanite-free garnet-biotite gneisses (no. [4] in Table 2.2) occur in the whole southern Bemarivo Belt. Garnet and biotite form porphyroblasts in a rock matrix consisting of quartz and mesoperthitic feldspar (Fig. 2.7). A sample from the Sambirano area (Md48-1-03) contains garnet with $X_{Mg} = 0.22$ –0.26, $X_{Prp} = 0.21$ –0.24, $X_{Alm} = 0.68$ –0.71, $X_{Sps} = 0.05$ –0.06, and $X_{Grs} = 0.02$ –0.04. Biotite is characterised by $X_{Mg} = 0.45$ –0.48 and Ti contents of 0.60–0.67 p.f.u. (calculation based on 22 oxygens).

Garnet–orthopyroxene–sillimanite-bearing gneisses (no. [5] in Table 2.2) have just been found close to the Massif de Marojezy. Garnet porphyroblasts are strongly resorbed, and, in few cases, inclusions of sillimanite are present (Fig. 2.4e). Garnet is unzoned with $X_{Mg} = 0.25$ –0.30, $X_{Prp} = 0.25$ –0.35, $X_{Alm} = 0.65$ –0.70, $X_{Sps} < 0.05$, and $X_{Grs} < 0.05$. The coexisting orthopyroxene (Fig. 2.4e, f) is up to 2 mm in diameter and has a constant X_{Mg} of 0.60–0.65. It shows variation in the alumina content from 8 wt.% in the core to 4.5 wt.% near the rim (Fig. 2.5b; Table 2.5). Sillimanite is also preserved as aggregates, which are surrounded by late-stage cordierite ($X_{Mg} = 0.79$ –0.82; Fig. 2.4f). Furthermore, biotite ($X_{Mg} = 0.65$ –0.67; Ti = 0.38–0.46 p.f.u., based on 22 oxygens), quartz, mesoperthitic feldspar, and late-stage spinel occur. Spinel has an X_{Mg} of 0.29–0.34 (containing some Fe^{3+}) and is Zn-bearing (1.7–2.1 wt.% ZnO). In sillimanite-free rocks (no. [6] in Table 2.2) garnet and orthopyroxene occur in leucosomes (Fig. 2.4g). Here, the pyroxene is unzoned with $X_{Mg} = 0.59$ –0.60 and $Al_2O_3 = 4.2$ –5.5 wt.%. Garnet has a composition of $X_{Mg} = 0.30$ –0.45, $X_{Prp} = 0.30$ –0.37, $X_{Alm} = 0.48$ –0.64, $X_{Sps} = 0.03$ –0.04, and $X_{Grs} = 0.00$ –0.03. Further minerals are quartz, plagioclase, alkalifeldspar, and biotite (Fig. 2.6).

The matrix of the quartz-free high Mg-Al gneisses (no. [7] in Table 2.2) is composed of biotite ($X_{Mg} = 0.85$; Ti = 0.20–0.28 p.f.u.; Fig. 2.6a; Table 2.4), perthitic K-feldspar, and euhedral cordierite ($X_{Mg} = 0.90$ –0.92; Table 2.4). Cordierite of the same composition and mostly peraluminous sapphirine (Fig. 2.4h and 2.5c; Table 2.4; $X_{Mg} = 0.86$ –0.89 with ca. 5–15 % of the total iron as Fe_2O_3) constitute symplectitic intergrowths, which separate sillimanite from the rock matrix (Fig. 2.4h). Fibrous fine-grained sillimanite forms large aggregates (up to 5 cm), which locally recrystallised to form a second generation of idiomorphic sillimanite. Some small grains of plagioclase are obviously derived from exsolution of perthites. Corundum is also present (not shown in Fig. 2.4h), either as fine needles included in sillimanite or as larger prismatic grains in cordierite of the matrix. In domains containing no sapphirine, the amount of corundum is higher.

Enderbitic and charnockitic gneisses

Charnockitic gneisses form large complexes in the northern Sambirano as well as in the Andapa region. Their gneissic texture indicates deformation and metamorphism subsequent to emplacement. They are generally garnet-free and contain orthopyroxene. Locally orthopyroxene is surrounded by late-stage clinopyroxene and biotite, the formation of which is attributed to cooling. Just in one charnockitic sample from the central Bemarivo Belt, late-stage spongy garnet has been found, most likely also grown during cooling. Common accessory minerals are apatite, monazite, and zircon. Enderbitic gneisses consist of hornblende, orthopyroxene, clinopyroxene, plagioclase, and accessory apatite, but do not contain garnet.

Further rock types

Marbles, calcsilicates, ultrabasites, and quartzites are subordinate in volume. Marbles consist of calcite, dolomite, and minor amounts of phlogopite. Some small grains of forsterite are rimmed by diopside or tremolite. Calcsilicates are rich in titanite. Further minerals are plagioclase, amphibole, diopside, and scapolite. Ultrabasites occur as small lenses embedded in charnockites. They consist of amphibole, spinel, orthopyroxene, and some plagioclase. Quartzites are nearly pure, except for some sillimanite and biotite.

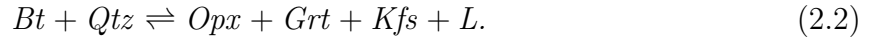
2.6 Mineral reaction history

Information about the pressure-temperature conditions during the prograde history of metapelites of the Bemarivo Belt is well documented by kyanite inclusions in garnet (Fig. 2.4a). Aggregates of near-coaxial sillimanite prisms in the rock matrix, which are clearly distinct from late euhedral crystals, are interpreted to be a pseudomorphic replacement after kyanite (Fig. 2.4b). Due to the large amount of these fine-grained pseudomorphs in the matrix of the rocks, we conclude that at one stage of the evolution the rocks were well equilibrated in the kyanite stability field. Another common texture is the dehydra-

tion of biotite and formation of omnipresent leucosomes, which can be explained by the dehydration reaction



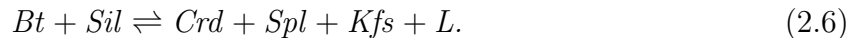
In orthopyroxene-bearing rocks (no. [5] & [6] in Table 2.2), the dehydration was due to the reaction



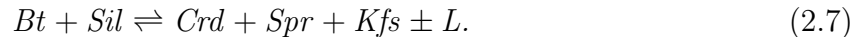
explaining the garnet- and orthopyroxene-bearing leucosomes (Fig. 2.4g). As a result of a decompressional stage, broad and well equilibrated cordierite rims have formed around garnet (Fig. 2.4c; no. [1] in Table 2.2), locally leading to complete consumption of the garnet via the reactions



The formation of cordierite is much more pronounced than in other areas that also show decompressional textures, such as Calabria or Sri Lanka (Schenk, 1984; Raase & Schenk, 1994). This indicates a decompressional stage either at higher temperatures or of longer duration than in other areas. In orthopyroxene + sillimanite-bearing rocks (no. [5] in Table 2.2) as well as orthopyroxene-free metapelites (no. [1] in Table 2.2), the formation of late-stage spinel and cordierite (Fig. 2.4f) is reflecting the reactions

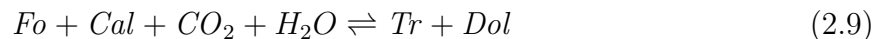
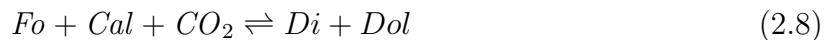


In the rocks containing sapphirine (no. [7] in Table 2.2), the formation of cordierite most likely resulted from the breakdown of sillimanite + biotite:



Sapphirine–cordierite intergrowths are a typical texture in silica-undersaturated rocks and are interpreted to form during decompression (Kelsey *et al.*, 2005, and references therein). Finally, subsequent rehydration and cooling is texturally evidenced by the late-stage formation of greenish biotite and biotite–quartz intergrowths replacing cordierite. The fluid for this rehydration may be either of external origin or derives from crystallising anatectic melts.

In olivine-bearing marbles, forsterite is rimmed by diopside or tremolite, interpreted as due to the reactions



The occurrence of both reactions reflects lowering of the X_{CO_2} during cooling to $T < 700^\circ\text{C}$ (Käse & Metz, 1980).

2.7 Conventional geothermobarometry

The petrographic textures and mineral chemical data described above represent a robust frame for the clockwise character of the P - T evolution and the ultrahigh temperatures of metamorphism: kyanite inclusions in the core of garnet are the oldest relics of the metamorphic evolution in the metapelites. Thus, garnet growth started within the stability field of kyanite and proceeded in the sillimanite stability field. The omnipresence of pseudomorphic aggregates of sillimanite replacing former kyanite is evidence for an early metamorphic stage that formed rocks, which were well equilibrated in the kyanite stability field. The ubiquitous occurrence of mesoperthitic feldspars in the southern Bemarivo Belt and the local occurrence of aluminous orthopyroxene coexisting with garnet and sillimanite point to peak-metamorphic temperatures exceeding 900 °C. The Ti-rich composition of biotite from all rock types confirms the suggestion of high-grade metamorphic conditions in the southern Bemarivo Belt. The extensive development of late-stage cordierite rims around garnet supports the interpretation of decompression under high temperatures.

In the following, results of conventional thermobarometry are presented to better constrain the P - T conditions during the different metamorphic stages. Geothermobarometric calculations have been performed on metapelites of the southern Bemarivo Belt, especially on rocks from the area around Andapa. Mineral analyses used for P - T calculations are given in Tables 2.3–2.5; results are shown in Table 2.6, 2.7, and Fig. 2.8.

Garnet–monazite thermometry (Pyle *et al.*, 2001) using Y-rich garnet cores (200–300 ppm) and inclusions of monazite ($X_{YPO_4} = 0.010$ – 0.035), Ca-rich plagioclase ($X_{An} = 0.3$ – 0.5), and fluorine-rich apatite ($X_F = 0.70$ – 0.85 ; $X_{OH} = 0.10$ – 0.25 ; $X_{Cl} \approx 0.05$) gives prograde temperature estimates in the range of 560–585 °C (at 6.0 kbar, assumed $f_{H_2O} = 1600$ bar). Garnet contains also inclusions of kyanite, therefore the garnet–alumosilicate–quartz–plagioclase (GASP) geobarometer has been applied for pressure estimates. Using the calibration of Koziol (1989), analyses of garnet cores and Ca-rich plagioclase inclusions in garnet ($X_{An} = 0.40$) give prograde pressure results in the stability field of kyanite (ca. 6 kbar at 550 °C). If the Ca content in garnet cores is not the one that formed during garnet growth but is lower due to partial re-equilibration by intracrystalline diffusion during peak temperatures, the obtained prograde GASP pressures may represent only minimum pressures for the early metamorphic stage. Outer zone analyses of garnet and matrix plagioclase ($X_{An} = 0.31$) give estimates for peak-metamorphic pressures of ca. 8.5 kbar (at 950 °C), in agreement with the omnipresence of matrix sillimanite. Peak-temperatures are calculated from orthopyroxene-bearing metapelites using the Al-in-Opx thermometer of Harley & Green (1982). Results for orthopyroxene cores (up to 8 wt.% Al_2O_3) and garnet are in the range of 950–1000 °C (at 8.5 kbar), which is in agreement with Al-isopleths of Harley & Motoyoshi (2000; Fig. 2.8). The combination of GASP (outer garnet zone/matrix plagioclase) with feldspar thermometry of metapelitic rocks yields estimates for the peak of metamorphism of ca. 950 °C at 9 kbar, which is at slightly lower temperatures than the results from orthopyroxene-bearing samples. However, just one alumosilicate-bearing metapelitic sample contains orthopyroxene, and this sample occurs close to the Massif de Marojezy. Therefore, temperature estimates on this sample may reflect just local

Table 2.6: Summary of representative P - T calculations. All samples are metapelites from the area around Andapa. Pressures and temperatures in brackets are assumed values for calculation.

	Sample	Combination		Temp. [°C]	Press. [kbar]
progr.	Md90-1-03	Grt334*/P1442¶	GASP	(550)	6.1
		Grt336*/P1444¶	GASP	(550)	6.0
	Md90-1-03	Grt40*/P1456¶/Mnz265/Ap23	Grt-Mnz	582	(6.0)
		Grt12*/P1456¶/Mnz265/Ap23	Grt-Mnz	563	(6.0)
peak	Md90-1-03	Grt411†/P1462§	GASP	(950)	9.3
		Grt412†/P1461§	GASP	(950)	8.9
	Md83-13-03	Grt89*/Opx268*	Al-in-Opx	989	(9.0)
		Grt96*/Opx270*	Al-in-Opx	1009	(9.0)
retro. 1	Md82-2-03	Grt29†/Crd20§	Grt-Crd-Sil-Qtz	(850)	5.8
		Grt774†/Crd826§	Grt-Crd-Sil-Qtz	(850)	6.4
	Md83-13-03	Grt39†/Opx45‡	Al-in-Opx	823	(6.0)
		Grt49†/Opx31‡	Al-in-Opx	883	(6.0)
retro. 2	Md84-1-03	Grt776‡/Crd819‡	Grt-Crd (Fe-Mg)	643	(6.0)
		Grt774‡/Crd823‡	Grt-Crd (Fe-Mg)	663	(6.0)

GASP: Koziol (1989); Grt-Mnz: Pyle *et al.* (2001); Al-in-Opx: Harley & Green (1982); Grt-Crd-Sil-Qtz & Grt-Crd (Fe-Mg): Berman (1991) with Berman & Aranovich (1996); * core analysis; † outer zone analysis; ‡ rim analysis; ¶ inclusion in Grt; § matrix

conditions. But widespread high temperatures are supported by feldspar thermometry. Mesoperthites in an orthopyroxene-bearing metapelite (Md83-13-03) yield minimum temperatures of approximately 940 °C, which is in fair agreement with results of Al-in-Opx thermometry applied to the same sample. To avoid determining a magmatic rather than a metamorphic temperature, ternary feldspars of metapelitic rocks were examined. Reintegrated compositions of these mesoperthites point to minimum metamorphic temperatures of ca. 900–950 °C (Fig. 2.7a, Table 2.7). Feldspars in a meta-igneous sample (Md94-2-03) taken close to the Marojezy massif yield slightly higher temperatures of ca. 980 °C. A decompression to ca. 6 kbar (at 850 °C) following a near-isothermal path is deduced from Al-in-Opx using garnet and orthopyroxene rims (coexisting with sillimanite) and from garnet-cordierite-sillimanite-quartz equilibria (Berman & Aranovich, 1996, with Berman, 1991). Using the outermost reequilibrated rims of garnet and the neighbouring cordierite, Grt-Crd Fe-Mg exchange thermometry (Berman & Aranovich, 1996, with Berman, 1991) leads to ca. 650 °C (Table 2.6; Fig. 2.8). This temperature has to be interpreted as the closing temperature of the Fe-Mg exchange between both minerals. Further evidence for the cooling stage is given by the formation of late-stage garnet in one charnockitic gneiss sample. However, this sample is from the central part of the Bemarivo Belt, and a correlation with the metamorphic conditions of the metapelites in the southern part of the belt is not unequivocal.

Table 2.7: Examples of reintegrated feldspar compositions as well as compositions and proportions of hosts and exsolution lamellae from four metapelitic and one meta-igneous sample.

Sample	Rock type*	Vol.%	Pl composition	Vol.%	Kfs composition	integrated composition
Md48-1-03	metapelite [4]	48.3	Ab _{0.92} An _{0.07} Or _{0.01}	51.7	Ab _{0.07} An _{0.00} Or _{0.93}	Ab _{0.49} An _{0.04} Or _{0.47}
Md83-13-03	metapelite [5]	39.3	Ab _{0.83} An _{0.16} Or _{0.01}	60.7	Ab _{0.22} An _{0.01} Or _{0.77}	Ab _{0.46} An _{0.07} Or _{0.47}
Md90-1-03	metapelite [1]	18.1	Ab _{0.68} An _{0.31} Or _{0.01}	81.9	Ab _{0.11} An _{0.00} Or _{0.89}	Ab _{0.58} An _{0.25} Or _{0.17}
Md93-2-03	metapelite [1]	21.4	Ab _{0.76} An _{0.23} Or _{0.01}	78.6	Ab _{0.10} An _{0.00} Or _{0.90}	Ab _{0.24} An _{0.05} Or _{0.71}
Md94-2-03	metadiorite	61.1	Ab _{0.82} An _{0.17} Or _{0.01}	38.9	Ab _{0.10} An _{0.00} Or _{0.90}	Ab _{0.54} An _{0.11} Or _{0.35}

* bracketed number corresponds to assemblage number in Table 2.2

2.8 Geochronology

For the geodynamic interpretation of the evolution of metamorphic rocks, it is of particular importance to correlate metamorphic reaction textures with the ages of the corresponding metamorphic events. Monazite is the best mineral for dating metamorphism in pelitic lithologies, because it occurs frequently and nearly all included lead is radiogenic (Montel *et al.*, 1994; Parrish, 1990). In addition, internal zoning can record significant details of the metamorphic history, e. g., several distinct growth events. Here, the method of chemical dating of monazite from electron microprobe analyses (U-Th-total Pb dating) was used. Although the precision is lower compared to conventional isotopic dating techniques, the advantages of the method are a high spatial resolution (the diameter of measurement points is less than 5 μm) and the possibility to perform texturally controlled *in-situ* analyses. Compared to conventional analyses, this approach, in combination with careful studies of backscattered electron images and X-ray maps of the analysed monazites, can avoid the danger of determining geological meaningless mixed ages between different metamorphic events.

2.8.1 Monazite textures and chemistry

Monazite in metapelitic rocks occurs evenly distributed. It is typically between 10 and 250 μm in size, and in backscattered electron image, it generally shows a homogeneous core (M_1) and a narrow rim (M_2 ; Fig. 2.9a, b). In rare cases, a distinct part of the core shows an additional magmatic zonation pattern (M_0 ; Fig. 9c). Monazite included in garnet often has more irregular shapes than matrix monazite and shows no distinguishable rim (Fig. 2.9d). Patchy zonation patterns are just rarely observed. Monazite shows the characteristic LREE enrichment over HREE (Fig. 2.10; representative analyses in Table 2.8), as it is typical in garnet-bearing rocks (Zhu & O’Nions, 1999).

As regards end-members, monazite is chemically characterised as $X_{LREE} = 0.67\text{--}0.95$, $X_{Hut} = 0.00\text{--}0.07$, $X_{HREE} = 0.00\text{--}0.06$, $X_{Brb} = 0.00\text{--}0.17$, and $X_{YPO_4} = 0.00\text{--}0.35$ (calculation described in Pyle *et al.*, 2001). Maximum Y_2O_3 contents are 5.5 wt.%, and ThO_2 is in the range from 3 to 18 wt.%. The rims are antithetically composed, i. e. higher amounts of Th are correlated with lower amounts of Y. The Y-poor rims point to previous extensive

Sample No.	83-13 195	83-12 78	90-1 265	83-12 72
P ₂ O ₅	30.75	29.85	29.45	29.92
SiO ₂	0.21	0.27	0.53	0.61
CaO	0.53	0.85	1.58	1.35
Y ₂ O ₃	1.73	1.61	1.65	0.40
La ₂ O ₃	18.79	14.39	13.14	13.26
Ce ₂ O ₃	32.12	28.64	26.30	27.26
Pr ₂ O ₃	2.74	3.16	2.85	3.02
Nd ₂ O ₃	8.45	11.97	11.23	11.87
Sm ₂ O ₃	0.77	2.10	1.83	2.55
Eu ₂ O ₃	0.02	0.11	0.00	b.d.l.
Gd ₂ O ₃	0.58	1.75	1.53	2.12
Dy ₂ O ₃	0.18	0.46	0.46	0.15
Er ₂ O ₃	0.11	0.05	0.09	b.d.l.
PbO	0.12	0.13	0.22	0.25
ThO ₂	2.77	4.02	8.66	6.54
UO ₂	0.20	0.40	0.25	1.42
Al ₂ O ₃	b.d.l.	0.01	0.01	0.02
Total	100.07	99.77	99.78	99.74
P	1.004	0.991	0.979	0.973
Si	0.008	0.010	0.021	0.024
Ca	0.022	0.036	0.067	0.057
Y	0.036	0.034	0.035	0.008
La	0.267	0.208	0.190	0.194
Ce	0.454	0.411	0.378	0.397
Pr	0.038	0.045	0.041	0.044
Nd	0.116	0.168	0.158	0.168
Sm	0.010	0.028	0.025	0.035
Eu	0.000	0.002	0.000	b.d.l.
Gd	0.007	0.023	0.020	0.028
Dy	0.002	0.006	0.006	0.002
Er	0.001	0.001	0.001	b.d.l.
Pb	0.001	0.001	0.002	0.003
Th	0.024	0.036	0.077	0.059
U	0.002	0.004	0.002	0.013
Al	b.d.l.	0.000	0.001	0.001
Total	1.992	2.004	2.002	2.005
X _{LREE}	0.902	0.859	0.790	0.831
X _{HREE}	0.011	0.029	0.027	0.030
X _{Hut}	0.006	0.006	0.016	0.017
X _{Brb}	0.045	0.072	0.133	0.114
X _{YPO₄}	0.036	0.034	0.034	0.008
app. age	817 ± 29	563 ± 19	545 ± 12	514 ± 10

Table 2.8: Representative electron microprobe analyses of monazites of all three generations: magmatic (No. 195), M₁ (No. 78 and 265), and M₂ (No. 72). The apparent age is given in Ma with 2σ error.

cations calculated on the basis of 4 oxygens

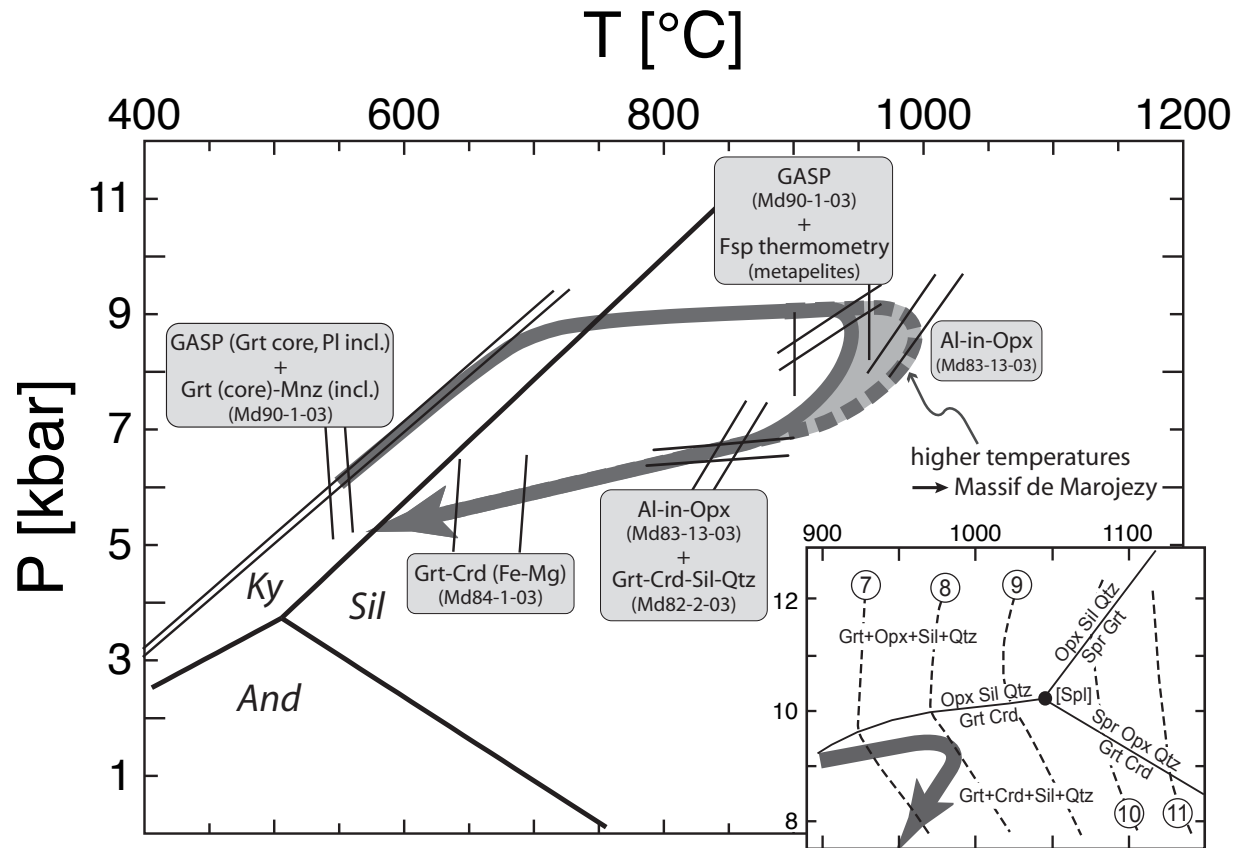


Figure 2.8: Pressure-temperature diagram depicting the metamorphic evolution of the southern Bemarivo Belt, as deduced from conventional geothermobarometry of metapelitic rocks. The inset shows the isopleths of Al_2O_3 in orthopyroxene (wt.%, encircled numbers) in the assemblages Grt-Opx-Sil-Qtz and Grt-Crd-Sil-Qtz (after Harley & Motoyoshi, 2000). Orthopyroxene with 8 wt.% Al_2O_3 corresponds to temperatures of ca. 970 °C.

garnet crystallisation, which has a strong influence over Y and HREE contents of monazite. Differences in Th content may be related to coexisting zircon (Pyle *et al.*, 2001), which has been found to occur as well. Rims also show a high variation in the amount of lead (0.1–0.4 wt.% PbO). The chondrite-normalised REE+Y distribution patterns are mostly similar, and a negative Eu anomaly is always present (Fig. 2.10). Comparing all monazite analyses, magmatically zoned cores (M_0) have chondrite-normalised elemental ratios $(\text{La}/\text{Nd})_N$ of 4.0–4.6, whereas other analyses give lower values (M_1 : 2.1–3.75; M_2 : 1.5–2.7). Also $(\text{La}/\text{Sm})_N$ differs significantly from magmatic cores (11.2–17.7) to M_1 (5.8–9.8) and M_2 (3.5–7.8). The Eu/Eu^* (i.e. $\text{Eu}_N/\sqrt{\text{Sm}_N \cdot \text{Gd}_N}$) shows just a slight variation from 0.02–0.18 in magmatic and M_1 monazite, but M_2 rims mostly have Eu contents below the detection limit (Fig. 2.10a, b, c). Aside from these general observations, the chemical characteristics of monazite are to some degree also influenced by local mineral equilibria.

The observations that the rims have a slightly different chemistry and that monazite inclusions in garnet do not show this rim, let us conclude that metamorphic growth took

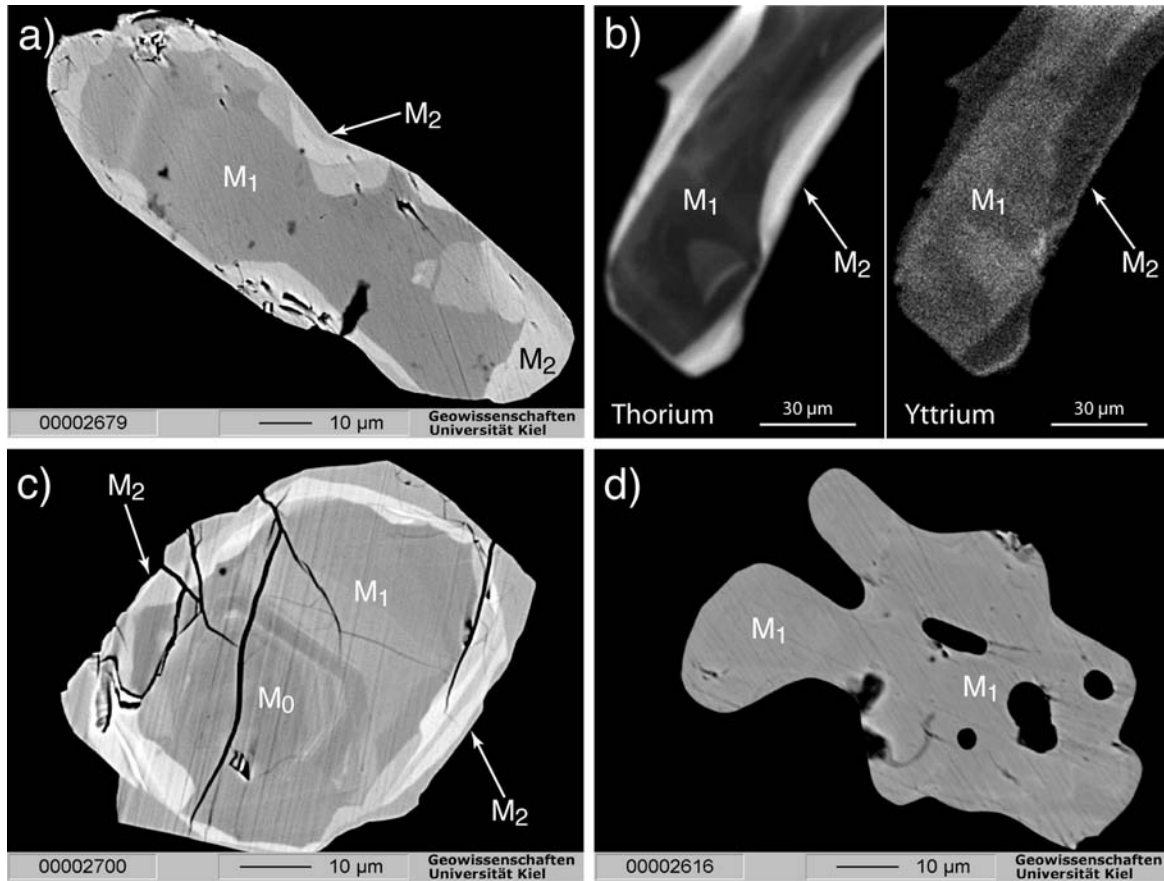


Figure 2.9: Monazite from metapelites of the southern Bemarivo Belt, and the correlation of growth zones with magmatic (M_0) as well as two metamorphic stages (M_1 and M_2). (a) Monazite with a homogeneous core (M_1) and an overgrown M_2 rim (backscattered electron image; Md83-12-03). (b) X-ray maps for thorium and yttrium. M_2 rims are thorium-rich but poor in yttrium (lighter colours correspond to higher concentrations; Md90-1-03). (c) Monazite with a magmatic core (M_0), a metamorphic core (M_1), and an overgrown M_2 rim (backscattered electron image; Md83-13-03). (d) Irregularly shaped monazite inclusion (M_1) in garnet, showing no younger rim (backscattered electron image; Md82-2-03).

place during two phases. The first phase was prior to and during garnet growth, and the second may be related to the peak-metamorphic stage and the retrograde path. Unfortunately, no textures have been found that allow to assign the different zones to specific monazite-forming reactions. However, in the sample used for garnet–monazite thermometry (Md90-1-03), apatite is just found as inclusions in garnet, but is lacking in the matrix of the rock, pointing to growth of monazite at the expense of apatite. Narrow monazite rims have also been observed elsewhere (Braun *et al.*, 1998; de Wit *et al.*, 2001; Santosh *et al.*, 2005), where they are interpreted as either due to diffusive Pb loss or late-stage hydrothermal interaction or recrystallization during a later metamorphic event. It has been demonstrated by Cherniak *et al.* (2004) that diffusive Pb loss plays no significant role, but an origin of the rims from recrystallization or hydrothermal interaction cannot

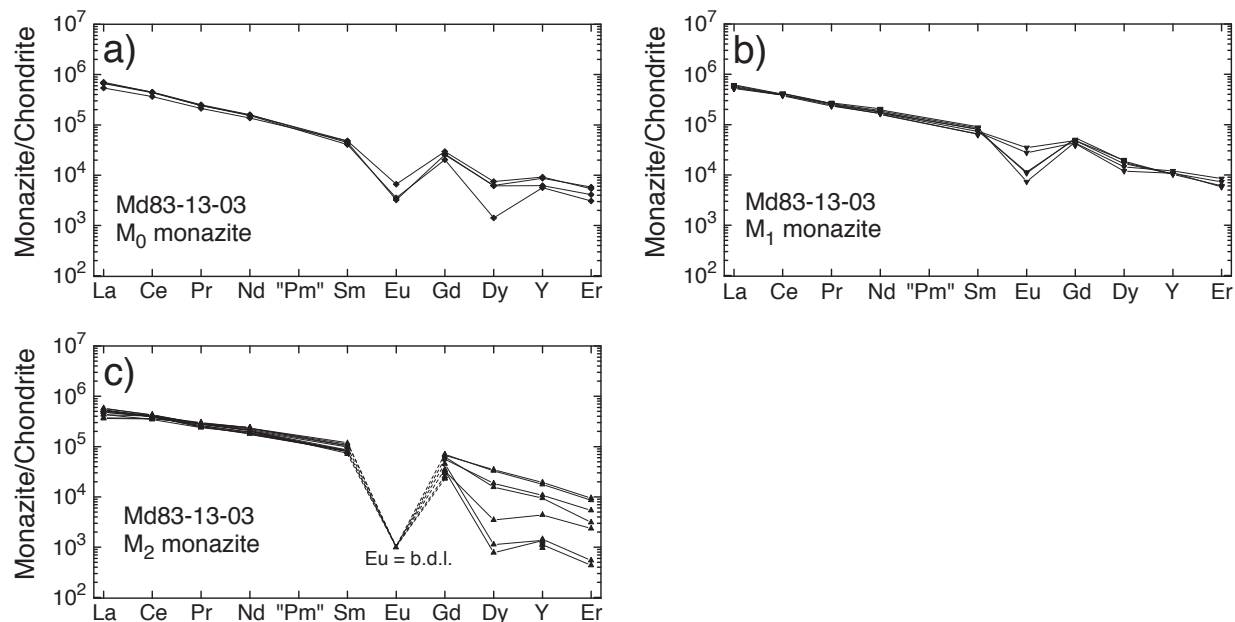


Figure 2.10: Chondrite-normalised REE + Y distribution patterns of monazite analyses from a meta-pelitic sample (Md83-13-03; 6 monazite grains). There are no clear differences in chemistry between magmatically-zoned cores (a) and metamorphic cores (b). Metamorphically-overgrown rims (c) have Eu values below the limit of detection (arbitrarily fixed in the diagram). Normalisation values taken from McDonough & Sun (1995).

be excluded. However, such a recrystallization would be expected to take place during the peak or the retrograde stage of metamorphism, leaving our interpretation uninfluenced.

2.8.2 Geochronological results

Six samples from 6 localities were analysed, covering the whole southern part of the Bemarivo Belt: sample Md48-1-03 from the Sambirano river; samples Md82-2-03, Md83-12-03, Md83-13-03, Md84-1-03, and Md90-1-03 from the Andapa region. Results are given in Table 2.9 and Figure 2.11.

Magmatic (M_0) ages are rarely preserved by a few apparent ages in the range from 640 to 850 Ma. The best estimate for M_0 can be made from the sample Md83-13-03, where 4 analyses vary in their ThO_2^* from ca. 3–15 wt.%, giving 737 ± 19 Ma (Fig. 11d). Because of our observation, that metamorphic monazite mostly shows two-stage growth textures (M_1 and M_2), measurements from both the cores and the rims were evaluated separately. Isochron ages for the M_1 stage of metamorphism are in the range from 563 ± 28 Ma to 532 ± 23 Ma, whereas the M_2 stage gives slightly lower results from 521 ± 25 Ma to 513 ± 14 Ma (Tab. 2.9). These results are overlapping within their 2σ errors, nonetheless due to textural and chemical differences, it is considered to be likely that both represent true metamorphic ages. Although precision is poor, they indicate a timeframe of ca. 18–44 Ma from prograde garnet formation to peak-metamorphism and cooling.

Table 2.9: Results of monazite dating for 6 metapelitic samples. Given are the number of measurement points used for age calculation (n), the age (errors are 2σ), and the MSWD of the isochron line. Ages for magmatic (M_0), as well as two metamorphic stages (M_1 and M_2) have been calculated separately.

Sample	Md48-1-03	Md82-2-03	Md83-12-03	Md83-13-03	Md84-1-03	Md90-1-03
No. of monazites	5	5	7	6	8	5
n (M_0)	—	—	—	4	—	4
age (M_0)	—	—	—	737 ± 19 Ma	—	770 ± 219 Ma
MSWD (M_0)	—	—	—	0.9479	—	1.9753
n (M_1)	21	47	21	33	73	17
age (M_1)	547 ± 40 Ma	532 ± 23 Ma	543 ± 21 Ma	550 ± 38 Ma	563 ± 28 Ma	538 ± 17 Ma
MSWD (M_1)	0.7311	0.7705	0.6296	0.7602	1.0093	0.4498
n (M_2)	12	15	18	17	9	23
age (M_2)	521 ± 25 Ma	513 ± 14 Ma	518 ± 25 Ma	512 ± 18 Ma	519 ± 29 Ma	520 ± 13 Ma
MSWD (M_2)	0.8231	0.5588	0.4996	0.3810	0.1481	0.4989

2.9 Discussion and conclusions

2.9.1 P - T path and geodynamic interpretation

Magmatic ages of ca. 715 Ma (Tucker *et al.*, 1999a) in the Série de Daraina-Milanoa and 753.8 ± 1.7 Ma (Tucker *et al.* in Ashwal, 1997) from the granites of the central Bemarivo Belt are known, but have never been reported from the Série de Sahantaha. U-Pb dating of zircon from the Antananarivo Block (Tucker *et al.*, 1999b; Kröner *et al.*, 2000) also revealed a period of granitoid magmatism in the middle Neoproterozoic (825–640 Ma). Although we have not dated zircon, which is a common detrital mineral, the magmatic zonation patterns found in monazite of a metapelite let us conclude that within the cores of some grains relics of detrital monazite were preserved, and therefore point to 737 ± 19 Ma as a maximum age for sedimentation. Their host rock may originate from the Neoproterozoic continental arc, the relics of which are assumed to be found in the northern Bemarivo Belt and in the Seychelles (Buchwaldt & Tucker, 2001; Tucker *et al.*, 1999a). An origin in the Antananarivo Block is less likely, but cannot be excluded. After erosion and transport, the Série de Sahantaha was deposited. During the amalgamation of Gondwana, the continental arc may have collided with the already consolidated continental fragments of Gondwana, i. e. the Antongil Block, the Indian Dharwar craton, and the Antananarivo Block. The collision and overthrusting led to burial of the Série de Sahantaha to a depth of > 25 km and its syntectonic metamorphism. It is possible that the Série de Daraina-Milanoa in the northern Bemarivo Belt was also affected by this tectonism, but buried to lower depth and therefore overprinted to lower-metamorphic grades of just 500–600 °C. The burial of the Série de Sahantaha was followed by heating to temperatures of ca. 900–950 °C, locally even reaching higher temperatures of nearly 1000 °C. Such ultrahigh temperatures are likely to be caused by magma intrusions into the thickened lower crust. The large charnockite complexes in the southern Bemarivo Belt may represent such intrusive bodies deliver-

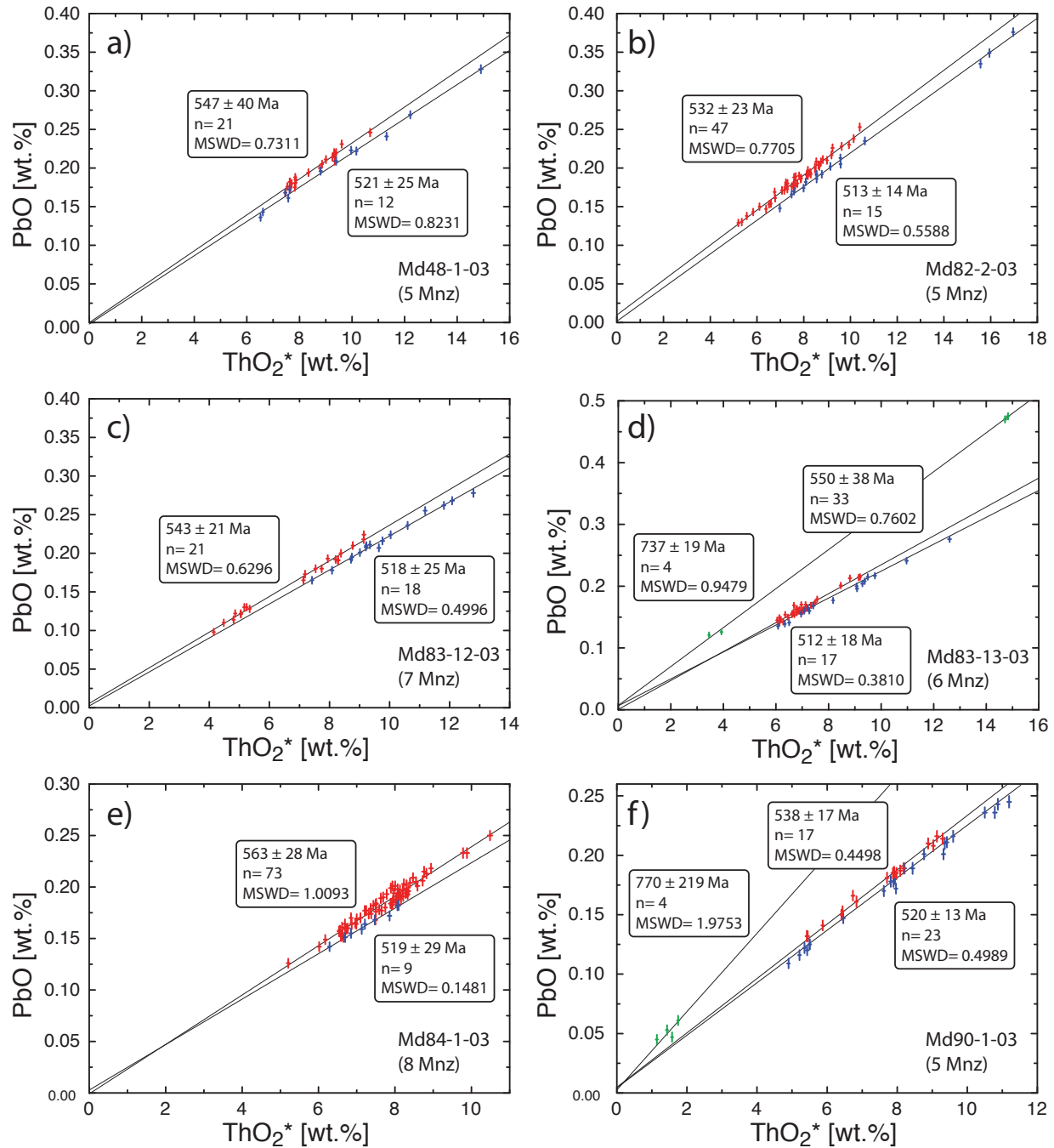


Figure 2.11: ThO_2^* vs. PbO diagrams showing isochrons plotted for distinct parts of monazite grains, i.e. cores and rims have been evaluated separately. Rims generally display a larger variation in ThO_2^* values. Just in rare cases (Md83-13-03, Md90-1-03) older magmatic cores are preserved (symbol sizes correspond to analytical uncertainty).

ing the heat for high-temperature metamorphism. Decompression took also place under high-temperature conditions, as deduced from the extensive late-stage formation of broad cordierite rims around garnet. There are two main tectonothermal models for isothermal decompression following crustal thickening: extensional tectonics leading to tectonic denudation (e. g., Ridley, 1989) or prolonged transpression causing extrusion of the lower crust (e. g., Thompson *et al.*, 1997; Schulmann *et al.*, 2002). Up to now, structural data are lacking for the studied area. Therefore none of these models can be excluded. Although cordierite-bearing assemblages in the Sambirano area of the Série de Sahantaha have not been found, the occurrence of charnockites, mesoperthitic feldspars in metasediments, and the chemistry of biotite is consistent with the metamorphic conditions deduced from the metapelites of the Andapa region more to the east. However, peak-pressure estimates in the Sambirano area are lacking due to missing suitable assemblages. It has to be mentioned that the variation in mineral chemistry seen in samples of the Andapa area must not stringently be due to a general increase in metamorphic conditions in the whole southern Bemarivo Belt from east to west (as proposed by Hottin, 1976). Possibly, the observed regional systematic change in mineral chemistry reflects the local influence of the Massif de Marojezy, delivering heat and causing higher metamorphic temperatures.

2.9.2 Interpretation of the geochronological results

Both monazite ages and peak-temperature conditions are similar in the whole southern Bemarivo Belt, but M_0 ages have not been found in the Sambirano area. An age of 737 ± 19 Ma is consistent with known magmatic ages from the northern Bemarivo Belt and therefore considered as the age of the detritus delivering source rocks. Interpreting the geochronological results of M_1 cores and M_2 rims of monazite, which differ 18–44 Ma in age, one has to consider the results of Buchwaldt *et al.* (2003). These authors performed conventional U/Pb geochronology, and dated the metamorphism with single pelitic monazite grains at 519.2 ± 0.7 Ma and 520 ± 1 Ma. Titanite from metapelitic granulites gave 511 ± 5 Ma and zircon from the Massif de Marojezy is 520.9 ± 4.2 Ma in age, interpreted as the timing of charnockite emplacement. These geochronological results can be correlated with our M_2 results, whereas the M_1 ages have not been determined by Buchwaldt *et al.* (2003). The most likely scenario is that the emplacement of the Marojezy charnockite took place at ca. 521 Ma, causing the high-temperature metamorphism and growth of M_2 monazite. The M_1 ages (563–532 Ma) date the prograde metamorphic stage, representing the time of crustal thickening.

2.9.3 The Bemarivo Belt and its relation to the formation of Gondwana

The ages obtained in the Bemarivo Belt are among the youngest for high-grade metamorphism in Madagascar. Just metamorphism in southern Madagascar, especially shear zone activity, is of similar age or even younger (Kröner *et al.*, 1996; Montel *et al.*, 1996; Martelat *et al.*, 1999, 2000). Rocks of the famous UHT-metamorphic Andriamena unit

(Tsaratanana sheet, north-central Madagascar) show late Neoproterozoic or even Cambrian growth of monazite, interpreted as either due to fluid-assisted resetting or cooling (Goncalves *et al.*, 2003, 2004; Paquette *et al.*, 2004). Similar monazite ages from the Itremo region of central Madagascar are also ascribed to late-stage fluid circulation (Fernandez *et al.*, 2003). Granulite-facies metamorphism in the central Antananarivo Block is believed to date back to ca. 550 Ma, deduced from U-Pb analyses of metamorphically overgrown zircon rims (Kröner *et al.*, 2000) or to 580–520 Ma from lower discordia intercepts (Tucker *et al.*, 1999b). However, estimates for metamorphic conditions in rocks of the Antananarivo Block are not well constrained due to the scarcity of metapelitic rocks. Stratoid granites, which occur frequently and widely distributed in the Antananarivo Block, are interpreted to have formed in a post-collisional extensional setting (Nédélec *et al.*, 1995), and were used to constrain the time of collision with East Africa to ca. 650 Ma (Paquette & Nédélec, 1998), which would be much older than the collisional event in the Bemarivo Belt. In contrast, the high-grade metamorphism in Tanzania is of similar age (650–620 Ma), but is interpreted to result from magmatic underplating (Appel *et al.*, 1998; Möller *et al.*, 2000) preceding the collisional event, which occurred at ca. 540 Ma (A. Möller pers. comm.; see discussion in Jöns & Schenk, 2004). Other interpretations consider the collisional event at ca. 650 Ma, followed by ca. 550 Ma postcollisional extension and shearing (Stern, 1994; Meert *et al.*, 1995; Meert, 2003). However, these interpretations are not based on correlations of metamorphic P - T paths with radiometric ages. In this context the timing of the collision in Madagascar remains also debateable. A partial overthrusting of the Bemarivo Belt onto the already consolidated Antananarivo Block and Antongil Block has been assumed by Collins *et al.* (2000a), and therefore collision and syntectonic metamorphism is a conclusive scenario. This collision represents a stage of the final assembly of the Gondwana supercontinent, when the proposed Betsimisaraka suture zone (Kröner *et al.*, 2000) of eastern Madagascar may already have been closed. The collision in western Madagascar may also fall into this time period, but detailed work on the metamorphic history of the Antananarivo Block is needed to get a more conclusive picture for both Madagascar and East Africa.

2.10 Acknowledgements

We thank B. Mader for her help with the microprobe analyses and A. Fehler for producing the thin sections. Thorough reviews of J.-E. Martelat and R. Buchwaldt helped to improve the manuscript and are kindly acknowledged. D. Robinson is thanked for his careful editorial work. N. Jöns is grateful to the German Academic Exchange Service (DAAD) and the Studienstiftung des deutschen Volkes (German National Academic Foundation) for financial support. The Deutsche Forschungsgemeinschaft (DFG) supported the project through grants Sche 256/16-1 and Sche 256/17-1.

References

- Appel, P., Möller, A. & Schenk, V., 1998. High-pressure granulite facies metamorphism in the Pan-African belt of eastern Tanzania: P-T-t evidence against granulite formation by continent collision. *Journal of metamorphic Geology*, **16**, 491–509.
- Armstrong, J. T., 1995. CITZAF: A package of correction programs for the quantitative electron microbeam X-ray analysis of thick polished materials, thin films, and particles. *Microbeam Analysis*, **4**, 177–200.
- Ashwal, L. D., 1997. Proterozoic geology of Madagascar: guidebook to field excursions. Technical report, Gondwana Research Group, Misc. Publications. Tucker et al. (Alter der Granitoide des Bemarivo Belt).
- Berman, R. G., 1991. Thermobarometry using multiequilibrium calculations: a new technique with petrologic applications. *Canadian Mineralogist*, **29**, 833–855.
- Berman, R. G. & Aranovich, L. Y., 1996. Optimized standard state and solution properties of minerals I. Model calibration for Olivine, orthopyroxene, cordierite, garnet, and ilmenite in the system MgO-FeO-MgO-CaO-Al₂O₃-TiO₂-SiO₂. *Contributions to Mineralogy and Petrology*, **126**, 1–24.
- Besairie, H., 1970. Description géologique du massif ancien de Madagascar: Centre Nord et Nord-Est. Documentation du Bureau géologique Numéro 177a, République Malagasy, Service géologique.
- Braun, I., Montel, J. M. & Nicollet, C., 1998. Electron microprobe dating of monazites from high-grade gneisses and pegmatites of the Kerala Khondalite Belt, southern India. *Chemical Geology*, **146**, 65–85.
- Buchwaldt, R. & Tucker, R. D., 2001. P-T-time constraints on the metamorphic rocks of North Madagascar and their relevance on the assembly of Gondwanaland. *Geological Society of America Abstracts with Programs*, **33**, 436.
- Buchwaldt, R., Tucker, R. D. & Dymek, R. F., 2003. Geothermobarometry and U-Pb geochronology of metapelitic granulites and pelitic migmatites from the Lokoho region, Northern Madagascar. *American Mineralogist*, **88**, 1753–1768.
- Cherniak, D. J., Watson, E. B., Grove, M. & Harrison, T. M., 2004. Pb diffusion in monazite: a combined RBS/SIMS study. *Geochimica et Cosmochimica Acta*, **68**, 829–840.
- Cocherie, A., Legendre, O., Peucat, J. J. & Kouamelan, A. N., 1998. Geochronology of polygenetic monazites constrained by in situ electron microprobe Th-U-total lead determination: implications for lead behaviour in monazite. *Geochimica et Cosmochimica Acta*, **62**, 2475–2497.

- Collins, A. S., Kröner, A., Razakamanana, T. & Windley, B. F., 2000a. The tectonic architecture and the East African Orogen in central Madagascar: a structural and geochronological perspective. *Journal of African Earth Sciences*, **30**, 21.
- Collins, A. S., Razakamanana, T. & Windley, B. F., 2000b. Neoproterozoic extensional detachment in central Madagascar: implications for the collapse of the East African Orogen. *Geological Magazine*, **137**, 39–51.
- Collins, A. S. & Windley, B. F., 2002. The tectonic evolution of Central and Northern Madagascar and its place in the final assembly of Gondwana. *The Journal of Geology*, **110**, 325–339.
- de Wit, M. J., Bowring, S. A., Ashwal, L. D., Randrianasolo, L. G., Morel, V. P. I. & Rambeloson, R. A., 2001. Age and tectonic evolution of Neoproterozoic ductile shear zones in southwestern Madagascar, with implications for Gondwana studies. *Tectonics*, **20**, 1–45.
- Fernandez, A., Schreurs, G., Villa, I. M., Huber, S. & Rakotondrazafy, M. A. F., 2003. Age constraints on the tectonic evolution of the Itremo region in Central Madagascar. *Precambrian Research*, **123**, 87–110.
- Fitzsimons, I. C. W. & Harley, S. L., 1994. The influence of retrograde exchange on granulite P-T estimates and a convergence technique for the recovery of peak metamorphic conditions. *Journal of Petrology*, **35**, 543–576.
- Fuhrmann, M. L. & Lindsley, D. H., 1988. Ternary-feldspar modelling and thermometry. *American Mineralogist*, **73**, 201–215.
- Goncalves, P., Nicollet, C. & Lardeaux, J.-M., 2003. Finite strain pattern in Andriamena unit (north-central Madagascar): evidence for late Neoproterozoic-Cambrian thrusting during continental convergence. *Precambrian Research*, **123**, 135–157.
- Goncalves, P., Nicollet, C. & Montel, J.-M., 2004. Petrology and in situ U-Th-Pb monazite geochronology of ultrahigh-temperature metamorphism from the Andriamena mafic unit, North-Central Madagascar. Significance of a petrographical P-T path in a poly-metamorphic context. *Journal of Petrology*, **45**, 1923–1957.
- Harley, S. L. & Green, D. H., 1982. Garnet-orthopyroxene barometry for granulites and peridotites. *Nature*, **300**, 697–701.
- Harley, S. L. & Motoyoshi, Y., 2000. Al zoning in orthopyroxene in a sapphirine quartzite: evidence for >1120°C UHT metamorphism in the Napier Complex, Antarctica, and implications for the entropy of sapphirine. *Contributions to Mineralogy and Petrology*, **138**, 293–307.
- Higgins, J. B., Ribbe, P. H. & Herd, R. K., 1979. Sapphirine I: crystal chemical contributions. *Contributions to Mineralogy and Petrology*, **68**, 349–356.

- Hottin, G., 1976. Présentation et essai d'interprétation du Précambrien de Madagascar. *Bulletin du Bureau de Recherches géologiques et minière*, **2**, 117–153.
- Jarosewich, E. & Boatner, L. A., 1991. Rare-earth element reference samples for electron microprobe analysis. *Geostandards Newsletter*, **15**, 397–399.
- Jöns, N. & Schenk, V., 2004. Petrology of whiteschists and associated rocks at Mautia Hill (Tanzania): Fluid infiltration during high-grade metamorphism? *Journal of Petrology*, **45**, 1959–1981.
- Käse, H. & Metz, P., 1980. Experimental investigation of the metamorphism of siliceous dolomites. *Contributions to Mineralogy and Petrology*, **73**, 151–159.
- Kato, T., Suzuki, K. & Adachi, M., 1999. Computer program for the CHIME age calculation. *Journal of Earth and Planetary Sciences, Nagoya University*, **46**, 49–56.
- Kelsey, D. E., White, R. W. & Powell, R., 2005. Calculated phase equilibria in K_2O – FeO – MgO – Al_2O_3 – SiO_2 – H_2O for silica-undersaturated sapphirine-bearing mineral assemblages. *Journal of metamorphic Geology*, **23**, 217–239.
- Koziol, A. M., 1989. Recalibration of the garnet-plagioclase- Al_2SiO_5 -quartz (GASP) geobarometer and application to natural parageneses. *EOS Transactions*, **70**, 493.
- Kretz, R., 1983. Symbols for rock-forming minerals. *American Mineralogist*, **68**, 277–279.
- Kröner, A., Braun, I. & Jaeckel, P., 1996. Zircon geochronology of anatexitic melts and residues from a high-grade pelitic assemblage at Ihosy, southern Madagascar: evidence for Pan-African granulite metamorphism. *Geological Magazine*, **133**, 311–323.
- Kröner, A., Hegner, E., Collins, A. S., Windley, B. F., Brewer, T. S., Razakamanana, T. & Pidgeon, R. T., 2000. Age and magmatic history of the Antananarivo Block, Central Madagascar, as derived from zircon geochronology and Nd isotopic systematics. *American Journal of Science*, **300**, 251–288.
- Kusky, T. M., Abdelsalam, M., Tucker, R. D. & Stern, R. J., 2003. Evolution of the East African and related orogens, and the assembly of Gondwana. *Precambrian Research*, **123**, 81–85.
- Lacroix, A., 1922. *Minéralogie de Madagascar*, volume 1-3. Société d'éditions géographiques, maritimes et coloniales, Paris.
- Martelat, J.-E., Lardeaux, J.-M., Nicollet, C. & Rakotondrazafy, M. A. F., 2000. Strain pattern and late Precambrian deformation history in southern Madagascar. *Precambrian Research*, **102**, 1–20.
- Martelat, J. E., Lardeaux, J. M., Nicollet, C. & Rakotondrazafy, R., 1999. Exhumation of granulites within a transpressive regime; an example from southern Madagascar. *Gondwana Research*, **2**, 363–367.

- McDonough, W. F. & Sun, S. S., 1995. The composition of the Earth. *Chemical Geology*, **120**, 223–253.
- McWilliams, M. O., 1981. Palaeomagnetism and Precambrian tectonic evolution of Gondwana. In: *Precambrian Plate Tectonics* (ed. Kröner, A.), Elsevier, Amsterdam, Developments in Precambrian Geology. 649–687.
- Meert, J. G., 2003. A synopsis of events related to the assembly of eastern Gondwana. *Tectonophysics*, **362**, 1–40.
- Meert, J. G., van der Voo, R. & Ayub, S., 1995. Paleomagnetic investigation of the Neoproterozoic Gagwe lavas and Mbozi Complex, Tanzania and the assembly of Gondwana. *Precambrian Research*, **74**, 225–244.
- Möller, A., Mezger, K. & Schenk, V., 2000. U-Pb dating of metamorphic minerals: Pan-African metamorphism and prolonged slow cooling of high pressure granulites in Tanzania, East Africa. *Precambrian Research*, **104**, 123–146.
- Montel, J.-M., Foret, S., Veschambre, M., Nicollet, C. & Provost, A., 1996. Electron microprobe dating of monazite. *Chemical Geology*, **131**, 37–53.
- Montel, J.-M., Veschambre, M. & Nicollet, C., 1994. Datation de la monazite à la microsonde électronique. *Comptes rendus de l'Académie des sciences, Série II*, **318**, 1489–1495.
- Nédélec, A., Stephens, W. E. & Fallick, A. E., 1995. The Panafrikan stratoid granites of Madagascar: alkaline magmatism in a post-collisional extensional setting. *Journal of Petrology*, **36**, 1367–1391.
- Paquette, J. L., Goncalves, P., Devouard, B. & Nicollet, C., 2004. Micro-drilling ID-TIMS U-Pb dating of single monazites: A new method to unravel complex poly-metamorphic evolutions. Application to the UHT granulites of Andriamena (North-Central Madagascar). *Contributions to Mineralogy and Petrology*, **147**, 110–122.
- Paquette, J. L. & Nédélec, A., 1998. A new insight into Pan-African tectonics in the East-West Gondwana collision zone by U-Pb zircon dating of granites from central Madagascar. *Earth and Planetary Science Letters*, **155**, 45–56.
- Paquette, J. L., Nédélec, A., Moine, B. & Rakotondrazafy, M., 1994. U-Pb, single zircon Pb-evaporation, and Sm-Nd isotopic study of a granulite domain in SE Madagascar. *The Journal of Geology*, **102**, 523–538.
- Parrish, R. R., 1990. U-Pb dating of monazite and its application to geological problems. *Canadian Journal of Earth Sciences (Revue Canadienne des Sciences de la Terre)*, **35**, 1431–1450.

- Pyle, J. M., Spear, F. S., Rudnick, R. L. & McDonough, W. F., 2001. Monazite-xenotime-garnet equilibrium in metapelites and a new monazite-garnet thermometer. *Journal of Petrology*, **42**, 2083–2107.
- Raase, P. & Schenk, V., 1994. Petrology of granulite-facies metapelites of the Highland Complex, Sri Lanka; implications for the metamorphic zonation and the P-T path. In: *Tectonic, metamorphic and isotopic evolution of deep crustal rocks, with special emphasis on Sri Lanka* (eds. Raith, M. & Hoernes, S.), Elsevier, Amsterdam. 265–294.
- Ridley, J., 1989. Vertical movement in orogenic belts and the timing of metamorphism relative to deformation. In: *Evolution of metamorphic belts* (eds. Daly, J. S., Cliff, R. A. & Yardley, B. W. D.), Geological Society of London, London. 103–115.
- Robinson, P., Hollocher, K. T., Tracy, R. J. & Dietsch, C. W., 1982. High grade Acadian regional metamorphism in South-central Massachusetts. In: *Guidebook for fieldtrips in Connecticut and South central Massachusetts*, State Geological and Natural History Survey of Connecticut, Storrs. 289–339.
- Santosh, M., Tanaka, K., Yokoyama, K. & Collins, A. S., 2005. Late Neoproterozoic-Cambrian felsic magmatism along transcrustal shear zones in Southern India: U-Pb electron microprobe ages and implications for the amalgamation of the Gondwana supercontinent. *Gondwana Research*, **8**, 31–42.
- Schenk, V., 1984. Petrology of felsic granulites, metapelites, metabasics, ultramafics, and metacarbonates from Southern Calabria (Italy): Prograde metamorphism, uplift and cooling of a former lower crust. *Journal of Petrology*, **25**, 255–298.
- Schulmann, K., Schaltegger, U., Thompson, A. B. & Edel, J.-B., 2002. Rapid burial and exhumation during orogeny: thickening and synconvergent exhumation of thermally weakened and thinned crust (Variscan Orogen in Western Europe). *American Journal of Science*, **302**, 856–879.
- Steiger, R. H. & Jäger, E., 1977. Subcommittee on geochronology: convention on the use of decay constants in geo- and cosmochronology. *Earth and Planetary Science Letters*, **36**, 359–362.
- Stern, R. J., 1994. Arc assembly and continental collision in the Neoproterozoic East African Orogen: Implications for the consolidation of Gondwanaland. *Annual Reviews of Earth and Planetary Sciences*, **22**, 319–351.
- Suzuki, K. & Adachi, M., 1991. Precambrian provenance and Silurian metamorphism of the Tsubonosawa paragneiss in the South Kitakami terrane, Northeast Japan, revealed by the chemical Th-U-total Pb isochron ages of monazite, zircon and xenotime. *Geochemical Journal*, **25**, 357–376.

- Suzuki, K. & Adachi, M., 1994. Middle Precambrian detrital monazite and zircon from the Hida gneiss in the Oki-Dogo Island, Japan: their origin and implication for the correlation of the basement of Southwest Japan and Korea. *Tectonophysics*, **235**, 277–292.
- Thompson, A. B., Schulmann, K. & Ježek, J., 1997. Extrusion tectonics and elevation of lower crustal metamorphic rocks in convergent orogens. *Geology*, **25**, 491–494.
- Torsvik, T. H., Carter, L. M., Ashwal, L. D., Bhushan, S. K., Pandit, M. K. & Jamtveit, B., 2001. Rodinia refined or obscured: palaeomagnetism of the Malani Igneous Suite (NW India). *Precambrian Research*, **108**, 319–333.
- Tucker, R. D., Ashwal, L. D., Hamilton, M. A., Torsvik, T. H. & Carter, L. M., 1999a. Neoproterozoic silicic magmatism of northern Madagascar, Seychelles, and NW India; clues to Rodinia's assembly and dispersal. *Geological Society of America Abstracts with Programs*, **31**, A–317.
- Tucker, R. D., Ashwal, L. D., Handke, M. J., Hamilton, M. A., Le Grange, M. & Rambe-
loson, R. A., 1999b. U-Pb geochronology and isotope geochemistry of the Archean and Proterozoic rocks of North-Central Madagascar. *The Journal of Geology*, **107**, 135–153.
- York, D., 1966. Least-squares fitting of a straight line. *Canadian Journal of Physics*, **44**, 1079–1086.
- Zhu, X. K. & O'Nions, R. K., 1999. Monazite chemical compositions: some implications for monazite geochronology. *Contributions to Mineralogy and Petrology*, **137**, 351–363.

Chapter 3

Relics of the Mozambique Ocean in the central East African Orogen: evidence from the Vohibory Block of southern Madagascar

3.1 Abstract

The Vohibory Block of southwestern Madagascar is part of the East African Orogen, the formation of which is related to the assembly of the Gondwana supercontinent. It is dominated by metabasic rocks with chemical compositions similar to those of recent basalts from a mid-ocean ridge, back-arc and island-arc setting. Their age of formation has been dated at 850 to 700 Ma by U–Pb SHRIMP dating of zircon, pointing to their origin as an island arc terrane and associated back-arc basin, marking the position of the Neoproterozoic Mozambique Ocean. In the early stage of the Pan-African orogeny (612.3 ± 4.8 Ma) these rocks experienced high-pressure amphibolite- to granulite-facies metamorphism ($P= 9\text{--}11$ kbar, $T= 750\text{--}820$ °C), most likely related to collision of the arc terrane and closure of the back-arc basin.

3.2 Introduction

Gondwana is one of the best known supercontinents in Earth's history. The still most accepted theory is that its final assembly occurred when East (India, Antarctica, Australia) and West Gondwana (Africa, America) collided and formed the Neoproterozoic (ca. 650–500 Ma) East African Orogen (e. g., McWilliams, 1981; Meert *et al.*, 1995; Collins & Pisarevsky, 2005). It is one of the largest orogens known on Earth, extending from Arabia through eastern Africa into Antarctica. Although a pacific-sized Mozambique Ocean is postulated to have separated East and West Gondwana (Stern, 1994), relics of this huge oceanic basin have not been found in the central East African Orogen. In Northeast Africa and Arabia there are several occurrences of ophiolite complexes, providing evidence for the positions of suture zones (e. g., Shackleton, 1996; Woldehaimanot, 2000; Abd El-Naby & Frisch, 2006). The southernmost indicators of the former Mozambique Ocean occur in the

Shackleton Range, Antarctica, from where ophiolitic rocks and eclogite-facies ultrabasites have been reported (Talarico *et al.*, 1999; Schmädicke & Will, 2006). However, in the central high-grade metamorphic part of the East African Orogen, which stretches for more than 5000 km, neither ophiolites nor eclogites of Pan-African age have been discovered so far, leading only to speculative hypotheses of palaeo-suture locations (e.g., Meert *et al.*, 1995; Collins & Pisarevsky, 2005; Fitzsimons & Hulscher, 2005). Due to its central position in reconstructions of Gondwana, Madagascar holds a key position for locating former suture zones. Recent structural geological investigations and detrital zircon geochronology imply that in Neoproterozoic times, Madagascar in part formed the stable continental Block “Azania” between East and West Gondwana, implying that at least two oceanic basins existed (Collins & Pisarevsky, 2005; Fitzsimons & Hulscher, 2005). However, there is only indirect evidence for the existence of suture zones, and the sequence and timing of their formation and closure is still a matter of debate. In this paper, we present geochemical and geochronological data, as well as pressure-temperature estimates of metabasic rocks from the Vohibory Block in southern Madagascar. These rocks have ocean-crust and continental-arc affinities suggesting their formation in a back-arc/island arc setting, which is consequently thought to be associated with an ocean. These findings have important implications for locating a suture zone of the Mozambique Ocean. Furthermore, results on the metamorphic history provide clues for the timing of closure of the ocean basin in the context of the Gondwana formation.

3.3 Geological setting

In the eastern two thirds of the island of Madagascar, Archaean and Proterozoic rocks crop out, most of which have been affected by the Pan-African orogeny. Two lithological units are found, that are rich in metabasic rocks and therefore may represent ancient suture zones: the Betsimisaraka suture (Collins *et al.*, 2000; Kröner *et al.*, 2000) in eastern Madagascar and the Vohibory Block in southwestern Madagascar (Fig. 3.1). The Betsimisaraka suture rims the Archaean cratonic Antongil Block. No geochemical analyses have been published directly from the basic rocks of this assumed suture, but in the westerly adjacent Antananarivo Block granitoid rocks of Middle Neoproterozoic age are assigned to a continental arc setting (Tucker *et al.*, 1999; Kröner *et al.*, 2000), leading to the interpretation of a west dipping subduction zone below the Antananarivo Block. The NNE–SSW striking Vohibory Block is dominated by metabasites and biotite-hornblende gneisses. Furthermore, there are intercalated bands of marbles, amphibolites, serpentinites, granitic gneisses, and rare metapelites (Fig. 3.1). Based on its lithology and field observations, this tectonic unit has been proposed to represent a shelf sequence interthrust with orthogneisses and slices of ophiolitic complexes (Windley *et al.*, 1994). To the East, the Vohibory Block borders the Pan-African Ampanihy shear-zone, which has completely different lithologies. To all other directions, it is covered by younger (Palaeozoic–Mesozoic) sedimentary rocks.

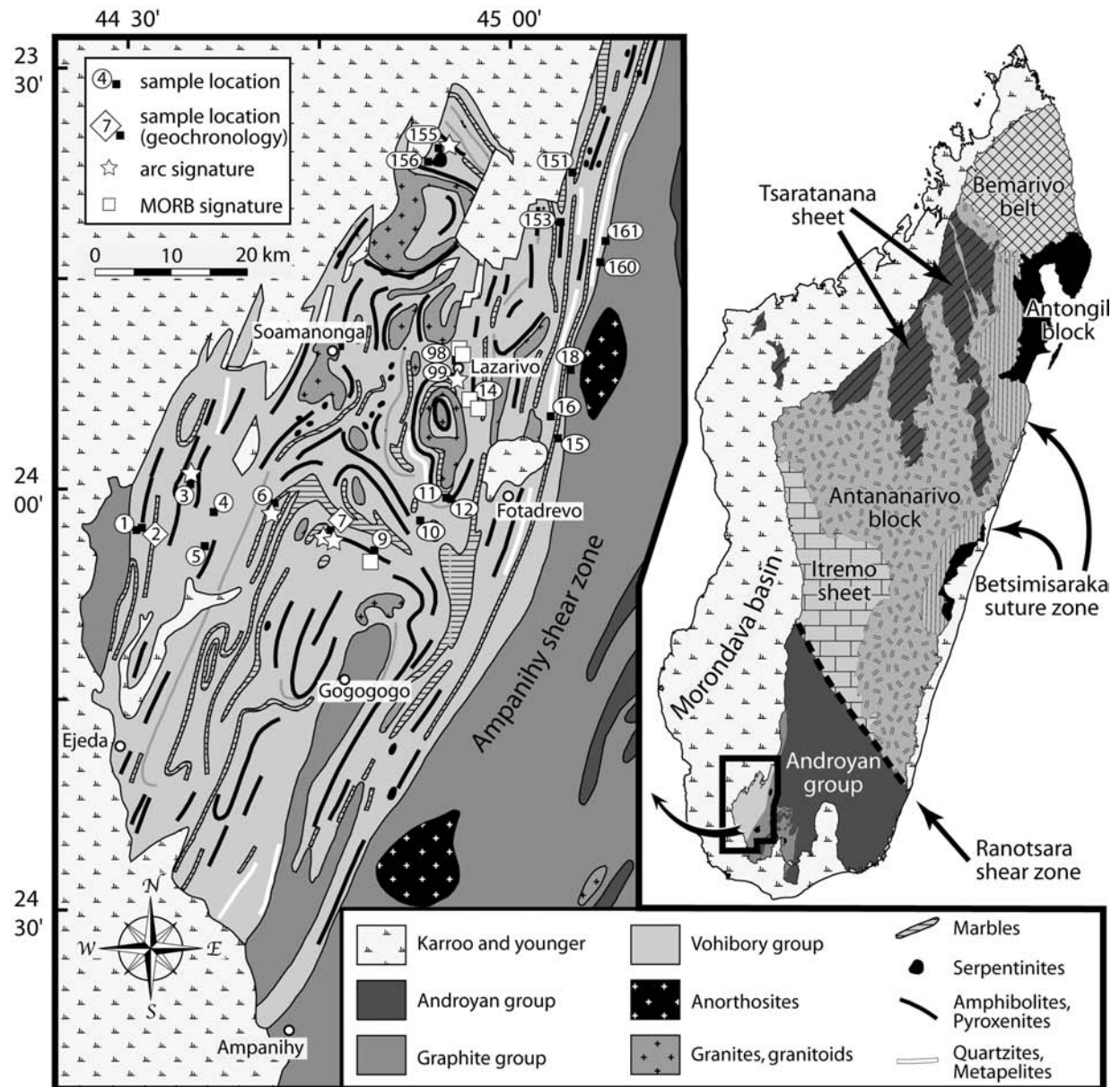


Figure 3.1: Tectonic units of Madagascar (modified after Collins & Windley, 2002), and geological map of the Vohibory Block (Besairie, 1970), showing sample locations. White squares indicate localities of metabasites with MORB-type chemistry, white stars metabasic samples with arc-type chemistry.

3.4 Petrography and mineral chemistry

The most common rock type in the Vohibory Block is a biotite-hornblende gneiss containing the assemblage garnet + biotite + ferropargasitic hornblende + plagioclase + quartz. Apart from a narrow (ca. 0.2 mm) re-equilibrated rim, garnet is unzoned with a composition of almandine (Alm)_{52–54}, pyrope (Prp)_{11–14}, spessartine (Sps)_{6–9}, and grossular (Grs)_{27–28}. Plagioclase preserves a weak growth zoning with core compositions of anorthite (An)_{62–65} and rim compositions of (An)_{70–78}. Massive metabasites contain the assemblage garnet + clinopyroxene + plagioclase ± quartz ± orthopyroxene ± scapolite ± rutile ± titanite. Garnet forms rims around clinopyroxene, and locally late-stage epidote and magnesiohornblende have formed. In some of these rocks all pyroxene has been replaced by hornblende. A few occurrences of magnesium-rich (> 20 wt.% MgO) metatroctolites are known, which feature complex symplectitic reaction textures formed during cooling. These rocks contain relics of olivine and late-stage formations of spinel, sapphirine, and staurolite (Nicollet, 1985, 1986). Peraluminous (> 30 wt.% Al₂O₃) corundum-bearing amphibolites and ultrabasic amphibolites are locally found, but occur just as small lenses included in other metabasic rocks.

Metasedimentary rocks occur in small volumes as intercalated bands within the metabasites. They are mainly marbles, which are either pure metacarbonates or contain minerals like spinel, olivine, phlogopite, graphite, diopside, or amphibole. Metapelites are rare, and we just collected two samples: a garnet-biotite-graphite schist and a garnet-biotite-sillimanite gneiss. Garnet in the latter rock sample is slightly zoned with (Alm)_{53–55}, (Prp)_{39–41}, (Sps)₁, (Grs)_{4–6} in the core and (Alm)_{58–61}, (Prp)_{35–38}, (Sps)₁, (Grs)_{1–3} towards the rim. Matrix plagioclase is unzoned with (An)_{19–22}, whereas inclusions in garnet are zoned with (An)₁₄ in the core and (An)₂₂ at the rim.

Finally, granitic and dioritic gneisses occur, but they are subordinate in volume.

3.5 Geothermobarometry and pressure-temperature evolution

Estimates of peak-metamorphic temperatures and pressures are obtained from metabasic and metapelitic samples (Table 3.1). Pressure estimates in metabasites and biotite-hornblende gneisses are based on the assemblages garnet-clinopyroxene-plagioclase±quartz (GADS; Moecher *et al.*, 1988), and garnet-plagioclase-hornblende-quartz (Kohn & Spear, 1990), yielding 8.5 to 9.5 kbar (for 750 to 800 °C). Temperature estimates are obtained from Fe-Mg exchange thermometers using core compositions of coexisting garnet + clinopyroxene (ca. 790 °C for 8 kbar; Ellis & Green, 1979), garnet + hornblende (ca. 720 to 820 °C for 8 to 10 kbar; Graham & Powell, 1984), and garnet + biotite (ca. 790 °C for 10 kbar; Ferry & Spear, 1978). These estimates are in general accordance with results for a metapelitic sample, based on garnet-sillimanite-plagioclase-quartz barometry (GASP; ca. 11 kbar for 850 °C; Newton & Haselton, 1981) and garnet-biotite thermometry (ca. 820 °C for 11 kbar). The obtained pressures are in general accordance to those derived from phase relations of

Table 3.1: Geothermobarometry for metabasic & metapelitic rocks of the Vohibory Block. Mineral analyses are given in the appendix (Table B.1)

Sample	Thermometry (°C)				Barometry (kbar)			
	P(ref)*	Grt-Cpx ⁽¹⁾	Grt-Hbl ⁽²⁾	Grt-Bt ⁽³⁾	T(ref)*	GADS ⁽⁴⁾	Grt-Pl-Hbl-Qtz ⁽⁵⁾	GASP ⁽⁶⁾
Md6-1-04	8 kbar	791	724	—	750 °C	8.5	—	—
Md7-1-04	10 kbar	—	818	792	800 °C	—	9.5	-
Md11-4-04	9 kbar	751	—	—	750 °C	8.9	—	—
Md16-1-04	11 kbar	—	—	822	850 °C	—	—	10.9

⁽¹⁾ Ellis & Green (1979); ⁽²⁾ Graham & Powell (1984); ⁽³⁾ Ferry & Spear (1978); ⁽⁴⁾ Moecher *et al.* (1988); ⁽⁵⁾ Kohn & Spear (1990); ⁽⁶⁾ Newton & Haselton (1981); * assumed values for calculation

the sapphirine- and staurolite-bearing metatroctolites (9–11.5 kbar, 750–800 °C; Nicollet, 1985, 1986).

Information on the retrograde P - T evolution was deduced from metatroctolites that show the breakdown of orthopyroxene + plagioclase and formation of garnet-clinopyroxene coronas. This texture is attributed to cooling subsequent to peak-metamorphic temperatures. P - T estimates yield ca. 750 °C (garnet-clinopyroxene) and ca. 9 kbar.

Even if nearly no reaction textures are preserved that could provide qualitative constraints on the relative pressure-temperature evolution, the high-pressure amphibolite-facies metamorphism points to a lower crustal depth of ca. 30 km, indicating a period of crustal thickening due to a collisional event.

3.6 Geochemistry

A set of 22 samples was geochemically analysed according to the method described by John *et al.* (accepted) to define the tectonic setting in which the Vohibory lithologies formed (Table 3.2). These samples are mainly metabasic rocks, but few of them are meta-ultrabasites ($\text{SiO}_2 = 41\text{--}57$ wt.%). From their trace element patterns they are subdivided into three main groups: MORB-type rocks, arc-related rocks, and cumulate-type rocks. In chondrite-normalised rare earth element (REE) patterns, rocks of the MORB group show a slight depletion of the light REEs, which is characteristic for mid-ocean-ridge and back-arc basalts (Fig. 3.2a). This is furthermore reflected by relatively low $(\text{La}/\text{Sm})_N$ ratios of 0.58–1.11 (Fig. 3.2b). The precursor melts did not undergo significant crustal contamination, as evidenced by low Ce/Zr (0.11–0.29) and Nb/La ratios (0.38–1.08). The Nb/Zr ratios range from 0.02–0.06, pointing to a depleted mantle source. Therefore, these rocks are interpreted to have formed in a mid-ocean ridge or back-arc spreading environment. In contrast, samples of the arc group show an enrichment of the light REEs over the heavy REEs ($[\text{La}/\text{Sm}]_N = 2.19\text{--}3.31$; Fig. 3.2b). Normalised against MORB, they feature prominent negative Nb, Ta, and Ti anomalies (Fig. 3.2c), which point to residual mineral phases like rutile, titanite or ilmenite in their source. Low Nb/La of 0.20–0.54 (Fig. 3.2b) exclude involvement of crustal contamination. Altogether, these samples seem

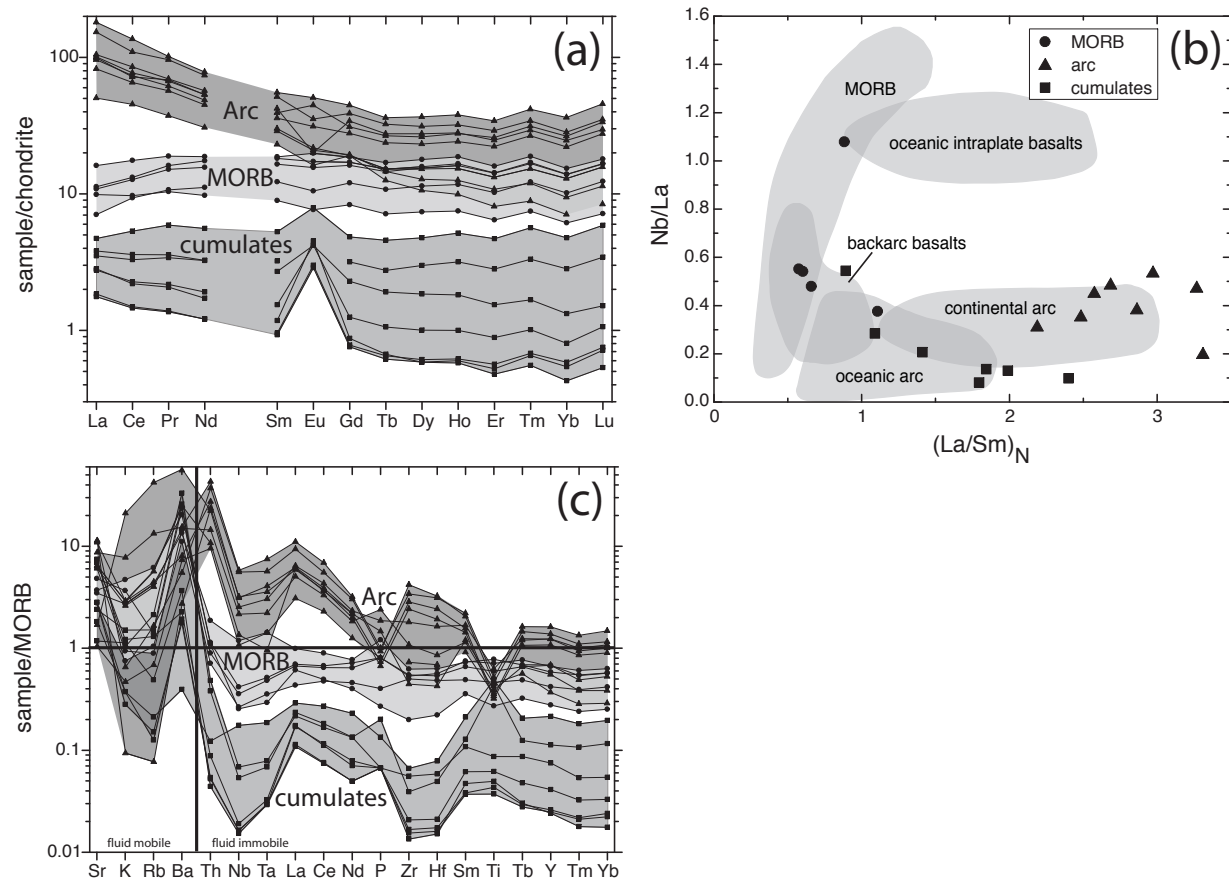


Figure 3.2: (a) Chondrite-normalised (McDonough & Sun, 1995) rare earth element variation plot of 22 metabasic samples. (b) Metabasic samples in a plot $(La/Sm)_N$ vs. Nb/La . Shaded fields indicate chemistry of basaltic rocks from different geotectonic settings (modified after John *et al.*, 2003). (c) Plot of trace element variation, normalised to MORB (Hofmann, 1988).

to have formed in a continental- or island-arc related setting. The third group of samples is characterised by flat REE patterns that are lower than 5 times chondritic with a positive Eu anomaly (Fig. 3.2a). Compared to MORB, they have pronounced negative Nb-Ta and Zr-Hf anomalies (Fig. 3.2c). With low Nb/La (0.05–0.54) at variable $[La/Sm]_N$ of 0.89–2.40 they resemble a back-arc/oceanic arc/island arc succession (Fig. 3.2b), and most likely represent cumulates of the lower mafic crust.

Our findings imply that the Vohibory Block contains a suite of rocks, which may represent a succession of an evolved back-arc basin with formation of oceanic crust, the associated island arc and some mafic rocks of the lower oceanic and arc crust. This mélange is now intercalated with marbles and quartzites, interpreted as former shelf sediments.

Table 3.2: Geochemical analyses of metabasites from the Vohibory Block.

Sample	3-2	6-1	7-1	7-2	9-1	14-1	14-2	3-1	3-3	3-4	11-2	11-3	11-4	11-5	12-1	12-2	12-4	155-1	156-1	98 X	98 XII	99 III	
Type*	Arc	Cumu	Arc	Arc	MORB	MORB	MORB	Arc	Arc	Arc	Cumu	Cumu	Cumu	Cumu	Cumu	Cumu	Cumu	Arc	Cumu	MORB	MORB	Arc	
[wt.%]																							
SiO ₂	39.49	43.69	61.10	53.46	51.86	45.62	50.28	40.53	40.57	39.63	44.75	44.52	43.39	43.36	44.68	45.26	45.22	59.65	45.03	45.76	46.32	48.76	
Al ₂ O ₃	25.96	16.53	15.45	11.14	18.17	12.19	14.84	25.93	26.50	25.95	16.59	21.90	14.86	15.02	26.26	32.98	33.00	15.79	18.41	17.08	17.21	13.70	
TiO ₂	0.84	0.70	1.02	0.58	0.44	0.75	0.96	0.75	0.52	0.55	0.10	0.14	0.06	0.07	0.08	0.04	0.04	0.63	0.79	1.26	1.15	0.73	
Fe ₂ O ₃	8.16	16.20	7.69	7.84	5.42	9.50	9.19	7.91	7.79	8.84	10.05	7.68	11.59	11.20	4.92	0.85	1.13	7.20	14.68	10.30	10.78	9.22	
MgO	1.03	8.28	2.87	4.63	7.51	5.35	3.18	1.14	0.58	1.41	16.60	11.02	20.81	20.67	7.51	1.27	1.10	3.09	6.82	3.96	5.72	8.83	
MnO	0.15	0.20	0.17	0.38	0.10	0.23	0.15	0.16	0.14	0.16	0.14	0.11	0.16	0.15	0.06	0.01	0.01	0.26	0.24	0.19	0.16	0.20	
CaO	21.69	13.48	6.37	18.37	12.32	21.07	16.72	22.58	22.70	22.17	9.29	11.96	7.80	7.92	13.34	17.04	16.92	10.64	13.70	16.66	12.59	13.66	
Na ₂ O	0.18	0.77	1.10	0.99	3.36	1.58	2.62	0.21	0.23	0.18	1.27	0.94	1.09	1.02	1.58	1.34	1.36	0.62	0.91	2.35	3.24	2.93	
K ₂ O	0.83	0.16	2.26	0.05	0.39	0.08	0.10	0.07	0.01	0.31	0.12	0.11	0.03	0.04	0.13	0.04	0.03	0.28	0.04	0.29	0.50	0.31	
P ₂ O ₅	0.15	0.03	0.28	0.12	0.04	0.06	0.12	0.14	0.10	0.11	0.01	0.01	0.01	0.01	0.01	0.01	0.01	0.36	0.02	0.18	0.12	0.22	
LOI	1.54	0.00	1.02	0.99	0.81	2.90	1.55	0.50	0.70	1.07	1.50	1.61	0.39	0.71	1.48	0.67	0.90	1.15	0.00	1.14	1.04	1.04	
Total	100.02	100.04	99.33	98.55	100.42	99.33	99.71	99.92	99.84	100.38	100.42	100.00	100.19	100.17	100.05	99.51	99.72	99.67	100.64	99.17	98.83	99.60	
[ppm]																							
Li	30.5	5.49	20.2	16.5	2.01	8.49	6.59	5.00	0.318	11.2	3.93	10.9	0.654	0.749	5.75	0.068	0.015	7.06	4.23	8.94	8.84	17.5	
K	6890	1328	18762	415	3237	664	830	581	83.0	2573	996	913	249	332	1079	332	249	2325	332	2408	4151	2574	
Rb	17.0	1.91	53.9	0.870	1.76	1.320	1.12	2.12	0.098	5.66	0.619	2.69	0.191	0.159	1.64	0.796	0.783	5.09	0.266	5.35	7.78	7.20	
Sr	990	271	118	118	545	313	699	1290	1295	1244	134	845	318	318	787	1408	1335	690	206	392	419	735	
Cs	0.369	0.035	0.949	0.104	0.008	0.464	0.375	0.054	0.006	0.114	0.012	0.177	0.028	0.019	0.079	0.020	0.054	0.423	0.009	0.108	0.052	0.119	
Ba	215	359	867	102	327	154	198	76.9	38.1	112	50.8	460	24.6	26.7	31.4	68.7	62.4	209	5.46	187	282	350	
P	654	130	1221	523	174	261	523	610	436	480	43.6	43.6	43.6	43.6	43.6	43.6	43.6	1571	87.3	786	524	960	
Ti	5035	4196	6114	3477	2637	4496	5755	4496	3117	3297	600	839	360	420	480	240	240	3777	4736	7554	6894	4376	
Y	58.5	4.07	44.3	24.6	9.96	15.0	24.4	49.8	38.8	44.4	1.47	2.68	0.885	0.934	0.864	0.366	0.411	19.9	7.70	20.9	23.8	13.3	
Zr	358	4.07	188	76.5	20.7	52.0	57.2	441	254	298	2.16	5.80	1.61	1.74	1.40	0.367	0.309	11.3	6.91	65.2	55.6	46.8	
Nb	20.6	0.239	8.97	3.79	0.894	0.932	1.25	19.8	11.3	11.0	0.053	0.188	0.057	0.057	0.067	0.059	0.033	7.64	0.616	4.17	1.47	4.77	
Hf	9.33	0.147	4.91	2.07	0.657	1.44	1.59	9.73	5.75	7.28	0.063	0.174	0.048	0.052	0.045	0.016	0.012	2.56	0.234	1.88	1.68	1.28	
Ta	1.45	0.015	0.588	0.273	0.056	0.068	0.093	1.10	0.690	0.789	0.006	0.013	0.006	0.006	0.006	0.007	0.004	0.429	0.036	0.274	0.099	0.185	
Pb	15.9	0.989	6.36	5.95	3.10	3.19	3.07	12.7	14.2	16.0	0.418	1.01	0.360	0.287	1.47	2.07	2.03	4.86	0.414	3.93	3.24	4.18	
U	3.72	0.039	1.39	0.870	0.132	0.035	0.035	3.14	2.57	3.64	0.006	0.019	0.006	0.006	0.011	0.005	0.006	0.881	0.015	0.065	0.058	0.525	
La	43.5	0.843	25.2	12.1	2.38	1.69	2.61	36.8	23.1	24.3	0.664	0.916	0.443	0.423	0.679	0.690	0.640	19.8	1.13	3.867	2.71	23.9	
Ce	83.5	2.01	52.2	27.7	5.93	5.71	7.77	67.0	45.0	47.0	1.39	2.20	0.910	0.889	1.34	1.03	0.995	40.0	3.25	10.8	8.08	44.0	
Pr	9.17	0.307	6.29	3.37	0.933	0.962	1.36	8.69	5.56	6.04	0.195	0.322	0.125	0.123	0.187	0.098	0.092	5.15	0.531	1.70	1.45	6.18	
Nd	36.1	1.50	26.2	14.1	4.48	5.14	7.20	34.1	22.4	24.6	0.880	1.50	0.555	0.557	0.790	0.364	0.342	20.7	2.57	8.63	8.04	24.6	
Sm	8.31	0.483	6.35	3.46	1.34	1.84	2.48	7.74	5.39	5.90	0.231	0.406	0.139	0.143	0.177	0.078	0.068	4.33	0.792	2.73	2.81	4.52	
Eu	3.05	< 0.050	1.20	0.976	0.460	0.630	0.935	2.12	1.88	2.68	0.253	0.251	0.173	0.180	0.271	0.203	0.208	1.26	0.476	1.04	1.19	1.31	
Gd	8.95	0.636	6.85	3.81	1.66	2.41	3.24	7.78	5.57	6.21	0.250	0.458	0.152	0.156	0.175	0.083	0.077	3.88	0.969	3.41	3.72	3.82	
Tb	1.45	0.110	1.11	0.610	0.290	0.432	0.582	1.30	0.949	1.07	0.042	0.077	0.025	0.026	0.027	0.012	0.012	0.585	0.183	0.608	0.677	0.50	
Dy	9.21	0.747	6.91	3.81	1.85	2.85	3.87	7.82	5.81	6.56	0.251	0.461	0.146	0.153	0.146	0.064	0.067	3.21	1.19	3.96	4.46	2.66	
Ho	1.90	0.159	1.40	0.768	0.375	0.586	0.806	1.61	1.21	1.39	0.050	0.091	0.030	0.031	0.029	0.013	0.014	0.629	0.258	0.831	0.934	0.497	
Er	5.49	0.449	3.96	2.12	1.03	1.64	2.27	4.66	3.57	4.14	0.142	0.246	0.084	0.090	0.077	0.032	0.037	1.73	0.753	2.28	2.55	1.30	
Tm	0.837	0.066	0.587	0.306	0.149	0.244	0.334	0.69	0.535	0.628	0.020	0.033	0.013	0.014	0.011	0.005	0.006	0.240	0.113	0.340	0.377	0.178	
Yb	5.82	0.453	3.95	2.08	0.982	1.62	2.23	4.53	3.54	4.24	0.129	0.212	0.087	0.094	0.068	0.029	0.035	1.51	0.764	2.23	2.46	1.13	
Lu	0.916	0.069	0.594	0.316	0.143	0.247	0.331	0.704	0.553	0.671	0.021	0.030	0.014	0.015	0.011	0.004	0.005	0.229	0.118	0.334	0.360	0.169	

* Arc = arc-type; Cumu = cumulate-type; MORB = MORB-type

3.7 Geochronology

Zircon from an arc-type metabasic sample (Md7-1-04) was dated to constrain the timing of formation of the island arc. U–Pb isotopic data were collected on the sensitive high-mass resolution ion microprobe (SHRIMP II). Magmatically-zoned zircon cores yield $^{206}\text{Pb}/^{238}\text{U}$ ages ranging from 850.1 ± 5.3 to 709.9 ± 7.0 Ma (1σ errors; Fig. 3.3a, Table 3.3). The wide range of ages points to a volcanoclastic sediment as a precursor rock or to partial Pb loss during metamorphic overprinting. Overgrown rims on zircons were used to constrain the timing of metamorphism at 612.3 ± 4.8 Ma (2σ error). However, some older ages are present, most likely as a result of partial Pb loss of magmatic zircons during this Pan-African metamorphic event. Younger ages of ca. 570 Ma give evidence for a second metamorphism, which has frequently been determined in eastern Africa (e.g., Paquette *et al.*, 1994; de Wit *et al.*, 2001; Meert, 2003; John *et al.*, 2004a).

The results obtained for the timing of metamorphism are furthermore confirmed by U–Th–total Pb dating of monazite from a metapelitic sample (Fig. 3.3b; analytical method described by Jöns *et al.*, 2006). Sample Md2-3-04 from the easternmost part of the Vohibory Block is dated at 638 ± 25 Ma, which is in agreement with the zircon data (Fig. 3.3a). Although we did not date MORB-type samples (zircon contains just ca. 0.3 ppm U), the formation age of the arc-type samples suggests that the island arc and oceanic crust formation is indeed related to the Mozambique Ocean, which is assumed to have existed from ca. 850–700 Ma (Stern, 1994). The metamorphic and tectonic overprinting of these rocks in the early stage of the Pan-African orogeny marks a collisional event, most likely indicating closure of a back-arc basin.

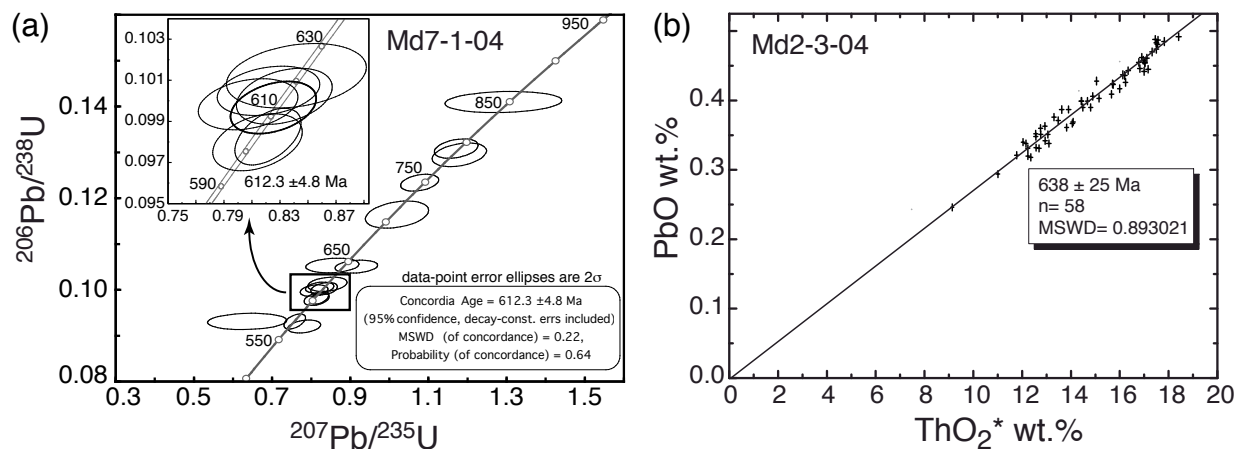


Figure 3.3: Geochronological results from samples of the Vohibory block. (a) Results of SHRIMP zircon dating of metabasic sample Md7-1-04. Magmatic cores give ages ranging from ca. 850–700 Ma. The main metamorphic event is dated at 612.3 ± 4.8 Ma (see inset). (b) U–Th–total Pb dating of monazite from metapelitic sample Md2-3-04. The main metamorphism is dated at 638 ± 25 Ma, which is in agreement with zircon data. Symbol sizes correspond to analytical errors.

Table 3.3: Results of SHRIMP analyses of the metabasic sample Md7-1-04. Age errors are given as 1σ .

No.	U (ppm)	Th (ppm)	$\frac{^{232}\text{Th}}{^{238}\text{U}}$	comm. $\frac{^{206}\text{Pb}}{^{206}\text{Pb}}$ (%)	$\frac{^{207}\text{Pb}}{^{206}\text{Pb}}$ * error (%)	$\frac{^{206}\text{Pb}}{^{238}\text{U}}$ * error (%)	$\frac{^{207}\text{Pb}}{^{235}\text{U}}$ * error (%)	$\frac{^{208}\text{Pb}}{^{232}\text{Th}}$ * error (%)	% disc.	Age (Ma)* $\frac{^{207}\text{Pb}}{^{206}\text{Pb}}$	±	Age (Ma)* $\frac{^{206}\text{Pb}}{^{238}\text{U}}$	±				
Md7.1.1	513	129	0.261	0.306	0.0633	1.01	0.1234	0.61	1.0774	1.08	0.0392	2.67	-4.1	719.4	36.8	750.0	4.3
Md7.1.2	547	2	0.004	0.257	0.0603	1.12	0.1012	0.63	0.8417	0.84	—	10.94	-1.1	614.6	50.5	621.6	3.7
Md7.2.1	681	3	0.005	0.000	0.0606	1.01	0.0983	0.57	0.8214	0.82	0.0625	6.66	3.6	626.2	22.1	604.2	3.3
Md7.2.2	709	3	0.004	0.241	0.0602	0.98	0.0980	0.58	0.8139	0.81	-0.0507	6.03	1.6	612.4	32.3	602.6	3.3
Md7.3.1	360	150	0.431	0.258	0.0649	1.15	0.1308	0.66	1.1712	1.17	0.0417	1.35	-2.6	772.2	38.7	792.5	4.9
Md7.3.2	281	86	0.316	0.280	0.0661	1.34	0.1294	0.81	1.1789	1.18	0.0403	1.77	3.0	808.1	47.5	784.7	6.0
Md7.4.1	618	273	0.457	4.339	0.0665	1.64	0.1410	0.67	1.2917	1.29	0.0584	3.57	-3.4	820.9	97.6	850.1	5.3
Md7.1.3	106	0	0.003	0.086	0.0635	2.87	0.1164	1.04	1.0196	1.02	0.1935	11.91	2.2	725.8	65.3	709.9	7.0
Md7.5.1	636	6	0.009	0.330	0.0612	1.06	0.0998	0.51	0.8072	1.80	-0.0226	97.50	-9.7	553.9	37.7	613.4	3.0
Md7.5.2	704	4	0.007	0.245	0.0612	0.99	0.1005	0.49	0.8218	1.82	—	—	-6.2	578.7	38.1	617.2	2.9
Md7.6.1	486	3	0.006	0.000	0.0620	1.46	0.1051	0.55	0.9158	2.43	0.1130	50.12	11.1	715.7	50.2	644.0	3.4
Md7.6.2	374	2	0.005	0.336	0.0615	1.33	0.1053	0.62	0.8545	3.26	—	—	-13.0	561.4	69.7	645.5	3.8
Md7.7.1	447	3	0.006	0.105	0.0611	1.24	0.1002	0.56	0.8331	1.68	0.0255	99.55	-0.3	613.9	34.2	615.7	3.3
Md7.7.2	358	1	0.002	0.000	0.0604	1.50	0.0920	0.63	0.7821	2.19	0.3662	42.25	16.8	662.5	45.0	567.3	3.4
Md7.2.3	299	1	0.002	1.370	0.0603	1.66	0.0931	0.78	0.6362	6.50	-1.1851	34.10	-69.6	174.4	150.6	573.9	4.3
Md7.7.3	349	1	0.002	0.000	0.0586	1.23	0.0931	0.72	0.7578	1.49	0.1839	25.08	-0.9	568.5	28.4	573.8	3.9

* common Pb corrected using measured ^{204}Pb .

3.8 Discussion and conclusions

The geochemical and geochronological characteristics of the metabasic rocks studied here provide evidence that the Vohibory Block contains the first well-documented relics of the Neoproterozoic Mozambique Ocean in the central East African Orogen. They originate in a back-arc/volcanic arc/continental arc succession, which is intercalated with shelf sediments. The arc formation in the period of 850–700 Ma was followed by a Pan-African high-pressure amphibolite- to granulite-facies metamorphism at 612.3 ± 4.8 Ma. The high-pressure metamorphism points to a period of crustal thickening, most likely related to collision and closure of an oceanic basin. However, our findings do not stringently imply that this event marks the final closure of the whole Mozambique Ocean. It may rather be related to collision of a microcontinental plate or arc terrane and closure of a back-arc basin. These findings point against a simple single pacific-sized Mozambique Ocean. We assume that a more likely scenario is accretion of intra-oceanic arc terranes separated from each other by small basins, a situation comparable to the Arabian-Nubian Shield during the Neoproterozoic or the recent western Pacific region. However, the intense and prolonged thermal and tectonic overprinting of the central East African Orogen led to a more complicated situation for locating the position of palaeo-sutures.

The Vohibory Block is situated south of the prominent Ranotsara shear zone (Fig. 3.1), the shear sense of which is assumed to be sinistral (Nicollet, 1990). Therefore, the examined area has more likely to be correlated with the western part of the East African Orogen, but not with any of the other proposed sutures in Madagascar, the existence of which is deduced on the basis of detrital zircon geochronology and structural geology only (e.g., Collins *et al.*, 2000; Kröner *et al.*, 2000; Collins *et al.*, 2003a,b; Cox *et al.*, 2004; Fitzsimons & Hulscher, 2005; Collins & Pisarevsky, 2005). Consequently, the Vohibory rocks formed as an arc terrane and its back-arc basin at the margin of the “Neomozambique Ocean” (Fitzsimons & Hulscher, 2005), west of the microcontinent “Azania” (Collins & Pisarevsky, 2005). After its accretion to the western margin of Azania at ca. 610 Ma, it took another 75 Ma until the Mozambique Ocean completely closed, as evidenced by the age of whiteschist metamorphism in Tanzania (536 ± 2 Ma, A. Möller pers. comm.; see discussion in Jöns & Schenk, 2004). In this context it is interesting to note that a comparable situation has been found in the Lufilian Arc/Zambezi Belt of Zambia, where ocean crust is assumed to have formed at ca. 720 Ma, followed by a period of convergence and eclogitization at 650–600 Ma and continental collision at ca. 530 Ma (John *et al.*, 2003, 2004a,b).

3.9 Acknowledgements

We thank B. Mader for help with the microprobe analyses, A. Weinkauff for XRF analyses, A. Fehler for thin sections, D. Garbe-Schönberg for ICP-MS analyses, and T. Razakamanana for support during field work. We gratefully acknowledge the help of T. John during laboratory work. A. Larionov, I. Paderin, S. Presniakov and N. Rodionov (Centre of Isotopic

Research, VSEGEI, St. Petersburg) is thanked for efficient support during SHRIMP measurements. N. Jöns was funded by the Studienstiftung des deutschen Volkes (German National Academic Foundation). The Deutsche Forschungsgemeinschaft supported the project through grants Sche 256/16-1 and Sche 256/17-1.

References

- Abd El-Naby, H. & Frisch, W., 2006. Geochemical constraints from the Hafatit Metamorphic Complex (HMC): evidence of Neoproterozoic back-arc basin development in the central Eastern Desert of Egypt. *Journal of African Earth Sciences*, **45**, 173–186.
- Besairie, H., 1970. Description géologique du Massif ancien de Madagascar: Le Sud. Documentation du Bureau géologique Numéro 177e, République Malagasy, Service géologique.
- Collins, A. S., Fitzsimons, I. C. W., Hulscher, B. & Razakamanana, T., 2003a. Structure of the eastern margin of the East African Orogen in central Madagascar. *Precambrian Research*, **123**, 111–133.
- Collins, A. S., Kröner, A., Fitzsimons, I. C. W. & Razakamanana, T., 2003b. Detrital footprint of the Mozambique ocean: U-Pb SHRIMP and Pb evaporation zircon geochronology of metasedimentary gneisses in eastern Madagascar. *Tectonophysics*, **375**, 77–99.
- Collins, A. S. & Pisarevsky, S. A., 2005. Amalgamating eastern Gondwana: The evolution of the Circum-Indian Orogens. *Earth-Science Reviews*, **71**, 229–270.
- Collins, A. S., Razakamanana, T. & Windley, B. F., 2000. Neoproterozoic extensional detachment in central Madagascar: implications for the collapse of the East African Orogen. *Geological Magazine*, **137**, 39–51.
- Collins, A. S. & Windley, B. F., 2002. The tectonic evolution of Central and Northern Madagascar and its place in the final assembly of Gondwana. *The Journal of Geology*, **110**, 325–339.
- Cox, R., Coleman, D. S., Chokel, C. B., DeOreo, S. B., Wooden, J. L., Collins, A. S., De Waele, B. & Kröner, A., 2004. Proterozoic tectonostratigraphy and Paleogeography of Central Madagascar derived from detrital zircon U-Pb age populations. *The Journal of Geology*, **112**, 379–399.
- de Wit, M. J., Bowring, S. A., Ashwal, L. D., Randrianasolo, L. G., Morel, V. P. I. & Rabeloson, R. A., 2001. Age and tectonic evolution of Neoproterozoic ductile shear zones in southwestern Madagascar, with implications for Gondwana studies. *Tectonics*, **20**, 1–45.
- Ellis, D. J. & Green, D. H., 1979. An experimental study of the effect of Ca upon garnet-clinopyroxene Fe-Mg exchange equilibria. *Contributions to Mineralogy and Petrology*, **71**, 13–22.

- Ferry, J. & Spear, F., 1978. Experimental calibration of the partitioning of Fe and Mg between biotite and garnet. *Contributions to Mineralogy and Petrology*, **66**, 113–117.
- Fitzsimons, I. C. W. & Hulscher, B., 2005. Out of Africa: detrital zircon provenance of central Madagascar and Neoproterozoic terrane transfer across the Mozambique Ocean. *Terra Nova*, **17**, 224–235.
- Graham, C. & Powell, R., 1984. A garnet-hornblende geothermometer: calibration, testing, and application to the Pelona schist, southern California. *Journal of metamorphic Geology*, **2**, 13–31.
- Hofmann, A. W., 1988. Chemical differentiation of the Earth: the relationship between mantle, continental crust, and oceanic crust. *Earth and Planetary Science Letters*, **90**, 297–314.
- John, T., Klemd, R., Gao, J. & Garbe-Schönberg, D., accepted. Trace element mobilization in slabs due to non steady-state fluid-rock interaction: constraints from an eclogite-facies transport vein in blueschist (Tianshan, China). *Lithos*.
- John, T., Schenk, V., Haase, K., Scherer, E. & Tembo, F., 2003. Evidence for a Neoproterozoic ocean in south-central Africa from mid-oceanic-ridge-type geochemical signatures and pressure-temperature estimates of Zambian eclogites. *Geology*, **31**, 243–246.
- John, T., Schenk, V., Mezger, K. & Tembo, F., 2004a. Timing and P-T evolution of whiteschist metamorphism in the Lufilian Arc - Zambesi Belt orogen (Zambia): implications for the assembly of Gondwana. *Journal of Geology*, **112**, 71–90.
- John, T., Scherer, E. E., Haase, K. & Schenk, V., 2004b. Trace element fractionation during fluid-induced eclogitization in a subducting slab: trace element and Lu–Hf–Sm–Nd isotope systematics. *Earth and Planetary Science Letters*, **227**, 441–456.
- Jöns, N. & Schenk, V., 2004. Petrology of whiteschists and associated rocks at Mautia Hill (Tanzania): Fluid infiltration during high-grade metamorphism? *Journal of Petrology*, **45**, 1959–1981.
- Jöns, N., Schenk, V., Appel, P. & Razakamanana, T., 2006. Two-stage metamorphic evolution of the Bemarivo Belt of Northern Madagascar: constraints from reaction textures and in-situ monazite dating. *Journal of metamorphic Geology*, **24**, 329–347.
- Kohn, M. J. & Spear, F. S., 1990. Two new barometers for garnet amphibolites with applications to eastern Vermont. *American Mineralogist*, **75**, 89–96.
- Kröner, A., Hegner, E., Collins, A. S., Windley, B. F., Brewer, T. S., Razakamanana, T. & Pidgeon, R. T., 2000. Age and magmatic history of the Antananarivo Block, Central Madagascar, as derived from zircon geochronology and Nd isotopic systematics. *American Journal of Science*, **300**, 251–288.

- McDonough, W. F. & Sun, S. S., 1995. The composition of the Earth. *Chemical Geology*, **120**, 223–253.
- McWilliams, M. O., 1981. Palaeomagnetism and Precambrian tectonic evolution of Gondwana. In: *Precambrian Plate Tectonics* (ed. Kröner, A.), Elsevier, Amsterdam, Developments in Precambrian Geology. 649–687.
- Meert, J. G., 2003. A synopsis of events related to the assembly of eastern Gondwana. *Tectonophysics*, **362**, 1–40.
- Meert, J. G., van der Voo, R. & Ayub, S., 1995. Paleomagnetic investigation of the Neoproterozoic Gagwe lavas and Mbozi Complex, Tanzania and the assembly of Gondwana. *Precambrian Research*, **74**, 225–244.
- Moecher, D. P., Essene, E. J. & Anovitz, L. M., 1988. Calculation and application of clinopyroxene-garnet-plagioclase-quartz geobarometers. *Contributions to Mineralogy and Petrology*, **100**, 92–106.
- Newton, R. C. & Haselton, H. T., 1981. Thermodynamics of the garnet-plagioclase- Al_2SiO_5 -quartz geobarometer. In: *Thermodynamics of minerals and melts* (ed. Newton, R. C.), Springer Verlag, New York. 131–147.
- Nicollet, C., 1985. Origine des amphibolites à saphirine, corindon et grenat de la formation précambrienne du Vohibory (SW de Madagascar). *Comptes Rendus de l'Académie des Sciences, Série II*, **301**, 167–170.
- Nicollet, C., 1986. Saphirine et staurotide riche en magnésium et chrome dans les amphibolites et anorthosites à corindon du Vohibory Sud, Madagascar. *Bulletin de Minéralogie*, **109**, 599–612.
- Nicollet, C., 1990. Crustal evolution of the granulites of Madagascar. In: *Granulites and Crustal Evolution* (eds. Vielzeuf, D. & Vidal, P.), Kluwer Academic Publishers. 291–310.
- Paquette, J. L., Nédélec, A., Moine, B. & Rakotondrazafy, M., 1994. U-Pb, single zircon Pb-evaporation, and Sm-Nd isotopic study of a granulite domain in SE Madagascar. *The Journal of Geology*, **102**, 523–538.
- Schmädicke, E. & Will, T. M., 2006. First evidence of eclogite facies metamorphism in the Shackleton Range, Antarctica: trace of a suture between East and West Gondwana? *Geology*, **34**, 133–136.
- Shackleton, R. M., 1996. The final collision zone between East and West Gondwana: where is it? *Journal of African Earth Sciences*, **23**, 271–287.
- Stern, R. J., 1994. Arc assembly and continental collision in the Neoproterozoic East African Orogen: Implications for the consolidation of Gondwanaland. *Annual Reviews of Earth and Planetary Sciences*, **22**, 319–351.

- Talarico, F., Kleinschmidt, G. & Henjes-Kunst, F., 1999. An ophiolitic complex in the northern Shackleton Range, Antarctica. *Terra Antartica*, **6**, 293–315.
- Tucker, R. D., Ashwal, L. D., Handke, M. J., Hamilton, M. A., Le Grange, M. & Rambe-
loson, R. A., 1999. U-Pb geochronology and isotope geochemistry of the Archean and
Proterozoic rocks of North-Central Madagascar. *The Journal of Geology*, **107**, 135–153.
- Windley, B. F., Razafiniparany, A., Razakamanana, T. & Ackermann, D., 1994. Tectonic
framework of the Precambrian of Madagascar and its Gondwana connections: a review
and reappraisal. *Geologische Rundschau*, **83**, 642–659.
- Woldehaimanot, B., 2000. Tectonic setting and geochemical characterisation of Neopro-
terozoic volcanics and granitoids from the Adobha Belt, northern Eritrea. *Journal of
African Earth Sciences*, **30**, 817–831.

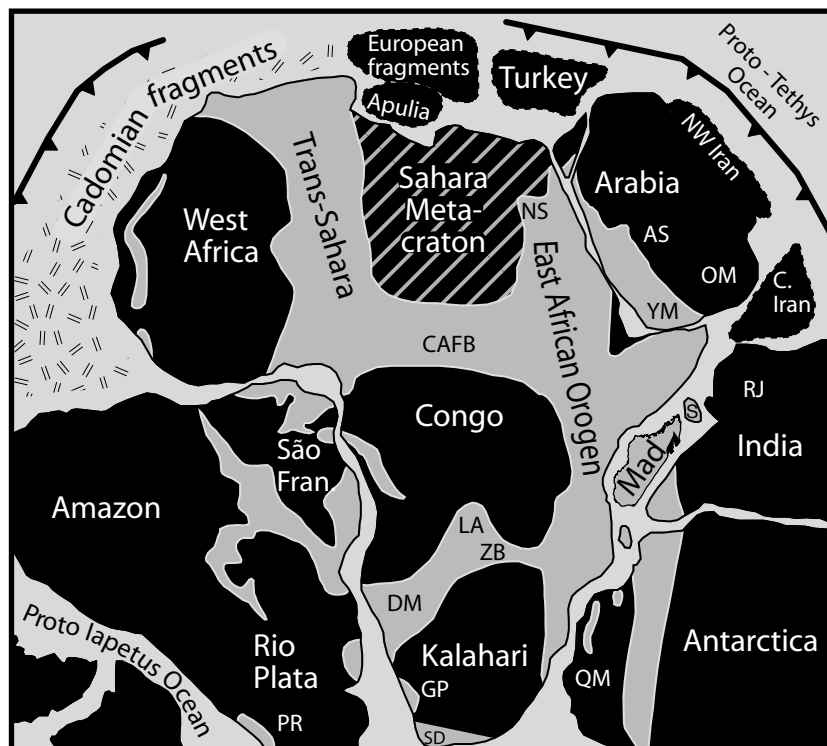
Chapter 4

The ultra-high temperature granulites of southern Madagascar in a polymetamorphic context: implications for the amalgamation of the Gondwana supercontinent

4.1 Abstract

The high-grade metamorphic character of rocks from southern Madagascar has been well known for a long time, however, specific UHT mineral assemblages like sapphirine-quartz, orthopyroxene-sillimanite-quartz, or osumilite-garnet and their regional distribution have not yet been described in detail. We examined the petrology of metapelitic samples from the Androyan group, south of the prominent Ranotsara shear zone, and performed U-Pb SHRIMP dating on zircon and U-Th-totalPb dating on monazite. High-temperature metamorphism is evidenced by Spl-Qtz assemblages found over ca. 75000 km² in the whole Androyan group. The occurrence of symplectites consisting of Crd + Kfs + Qtz + Opx or Crd + Kfs + Qtz + Bt seems to be restricted to a smaller area of just ca. 250 km². These symplectites are interpreted as pseudomorphs pointing to the former existence of metamorphic osumilite. Furthermore, in some pelites Spr + Qtz + Sil or Opx + Sil + Qtz formed the peak-metamorphic assemblage, which broke down to Crd ± Spl. Peak-metamorphic Opx is aluminous with Al₂O₃ = 9–10 wt.%. Peak-metamorphic conditions of T = 950–1000 °C and P = 8–11 kbar are followed by decompression at high temperatures, as evidenced by the formation of Crd + Opx₂ (Opx with 6–8 wt.% Al₂O₃) symplectites from Grt-Qtz-Opx₁ (8–9 wt.% Al₂O₃). The pressure drop is furthermore constrained by Spr-Crd symplectites in SiO₂-undersaturated metapelites, and extensive formation of late-stage cordierite in the whole Androyan group. During subsequent cooling, locally, cordierite broke down to form And + Carb + Chl + Qtz. In the whole Androyan group we have dated monazite at 560–530 Ma (M₂). Except for samples containing ultrahigh-temperature assemblages, an earlier metamorphic event at 600–650 Ma (M₁) is preserved in monazite cores. Zircon generally shows both metamorphic ages. Therefore, the deduced *P-T* evolution and UHT metamorphism obviously correspond to the M₂ event, which affected the whole Androyan group.

Figure 4.1: Reconstruction of a part of the Gondwana supercontinent, approximately 544 Ma ago (modified after Kusky *et al.*, 2003, and references therein), showing the relationship between Madagascar and the surrounding areas. Pan-African orogens are marked in grey, cratons in black. AS, Arabian Shield; CAFB, Central African Fold Belt; GP, Gariiep; DM, Damara; LA, Lufilian Arc; Mad, Madagascar; OM, Oman; PR, Pampean Ranges; PS, Paterson; QM, Queen Maud Land; RJ, Rajasthan; São Fran., São Francisco; SD, Saldania; S, Seychelles; YM, Yemen; NS, Nubian Shield; ZB, Zambezi Belt.



As a result of the intense M_2 overprint, P - T conditions of the older M_1 metamorphism are generally irreconizable. In the area showing temperatures of nearly 1000°C , even older monazite is completely recrystallised. The near-isothermal decompression points to rapid uplift of a formerly overthickened crust during the M_2 metamorphism at 530–560 Ma. Therefore, we interpret this event to reflect the assembly of the Gondwana supercontinent, most likely related to the collision of the Tanzania Craton with the Azania microcontinent and the closure of the Mozambique Ocean.

4.2 Introduction

The southern part of the island of Madagascar has long been known to consist of high-grade metamorphic granulite-facies rocks, the mineralogy of which is diverse and locally exceptional (e.g., Lacroix, 1922; de la Roche, 1963; Besairie, 1970; Hottin, 1976; Nicollet, 1985a; Ackermann *et al.*, 1989; Nicollet, 1990a,b; Ackermann *et al.*, 1991; Windley *et al.*, 1994; Rakotondrazafy *et al.*, 1996; Martelat *et al.*, 1999b; Markl *et al.*, 2000; Razakamanana *et al.*, 2000). Due to the central position of Madagascar in the Neoproterozoic East African Orogen (Fig. 4.1), which has been formed during the final assembly of the Gondwana supercontinent, these rocks can provide insights into the geodynamic evolution of the lower continental crust during this important tectonothermal episode.

However, the timing and geodynamic interpretation of metamorphic events within the East African Orogen is not yet well understood. The main controversy emanates from

the bimodal distribution of geochronological data within the East African Orogen (see summary of Meert, 2003): at ca. 630 Ma and at 530 Ma. Most authors speculate that the collision between East and West Gondwana and thus the final step in the amalgamation of Gondwana occurred at ca. 630 Ma, followed by extensional collapse and escape tectonics in the period of 600–500 Ma (e.g., Stern, 1994; Meert *et al.*, 1995; de Wit *et al.*, 2001; Collins & Pisarevsky, 2005). However, this interpretation is not in agreement with the counterclockwise P - T path of 610–655 Ma granulite metamorphism (Appel *et al.*, 1998; Möller *et al.*, 2000) and younger clockwise whiteschist metamorphism in Tanzania (Jöns & Schenk, 2004), pointing to a collision at ca. 540 Ma, preceded by magmatic underplating. As for southern Madagascar, which holds a position similar to Tanzania with respect to the formation of Gondwana (Fig. 4.1), the timing, distribution and character of metamorphic events are only poorly known.

Although the UHT-metamorphic character of rocks from southern Madagascar has often been mentioned by former workers (e.g., Nicollet, 1990a; Waters, 1991), detailed descriptions of characteristic mineral assemblages and retrograde reaction textures in aluminous granulites are mostly lacking. The interpretation that this area experienced metamorphism under ultrahigh temperatures is based on the frequent occurrence of spinel–quartz assemblages in metapelitic rocks (Ackermann *et al.*, 1989; Nicollet, 1990a; Waters, 1991). However, the interpretation of such high temperatures is only valid for a system under low oxygen fugacities, where incorporation of trivalent iron is not shifting the spinel + quartz stability field towards lower temperatures. Despite this complication, we here prove the UHT metamorphic character of southern Madagascar by reporting other characteristic mineral assemblages like osunilite + garnet, orthopyroxene + sillimanite + quartz and sapphirine + quartz. Such assemblages occur frequently in other high-grade metamorphic terranes (e.g., Nixon *et al.*, 1973; Sandiford *et al.*, 1987; Harley *et al.*, 1990; Harley & Motoyoshi, 2000; Goncalves *et al.*, 2004; Baldwin *et al.*, 2005; Das *et al.*, 2006), but they had, up to now, not been reported from rocks of southern Madagascar. We examined samples of metapelites, marbles, calcsilicates, charnockites, and metabasites from whole southern Madagascar. These rocks are used to deduce the geodynamic setting of their formation. Additional *in situ* dating of monazite and U–Pb SHRIMP dating of zircon was performed to constrain the timing of metamorphic events.

4.3 Previous work and geological setting

In reconstructions of Gondwana, Madagascar holds a central position (Fig. 4.1). It is situated in the center of the Pan-African East African Orogen, the formation of which is attributed to the final formation of this supercontinent (ca. 650–500 Ma). Recent structural geological, detrital zircon (Collins & Pisarevsky, 2005; Fitzsimons & Hulscher, 2005) and geochemical work (Jöns & Schenk, in review) contributed to the insight that Madagascar in part formed a microcontinent (named Azania; Collins & Pisarevsky, 2005), which was situated between East and West Gondwana during the middle Neoproterozoic. The Pan-African orogeny led to the collision of several continental blocks of East and West

Gondwana after the closure of two oceanic basins (Palaeomozambique Ocean separating Azania and the Dharwar Craton, Neomozambique Ocean between Azania and the Tanzania Craton; Fitzsimons & Hulscher, 2005). In vast areas of Madagascar, rocks are found that have been affected by this orogeny, making the region an ideal location for studying the geodynamics of the Gondwana formation.

Several attempts have been made to subdivide the Precambrian of Madagascar into litho-tectonic units. Some of these interpretations have been summarised by, e.g., Besairie (1973), Hottin (1976), and Collins (2006). Based on their different lithological character, Besairie (1973) described three distinct units in the Precambrian of southern Madagascar (from west to east; Fig. 4.2b): (1) the Vohibory group, consisting of upper amphibolite to granulite facies metabasic rocks with intercalated marbles; (2) the Graphite group, made up mainly of granulite facies calcsilicates and metapelites, which are locally graphite-bearing. Four large anorthosite complexes are situated in the Graphite group, which have been objects of intense studies (Ashwal *et al.*, 1998). (3) The Androyan group includes calcsilicate rocks, leucocratic gneisses and metapelites that locally show evidence for ultrahigh-temperature metamorphism. Furthermore, the large Anosyan Charnockite Complex occurs within the eastern part of the Androyan group. The structural geology of southern Madagascar is dominated by the occurrence of several major shear zones (SZ). The most prominent is the Ranotsara shear zone (i.e. the Bongolava-Ranotsara lineament of Hottin, 1976), which strikes NW–SE (Fig. 4.2) and possibly correlates with the Aswa shear zone in Uganda (Almond, 1969), and Sudan, or the Palghat-Cauvery (Janardhan, 1999) or Achankovil (Windley *et al.*, 1994) shear zones of southern India. Furthermore, the area south of the Ranotsara shear zone exhibits several subvertical N–S trending major shear zones, such as the Ejeda, Ampanihy, Beraketa (i.e. the Vorokafotra SZ of de Wit *et al.*, 2001), and Tranomaro shear zones (Fig. 4.2b; Windley *et al.*, 1994; Martelat *et al.*, 1995; Pili *et al.*, 1997; Martelat *et al.*, 2000; Nicollet, 1990a). Based on the occurrence of such shear zones, Windley *et al.* (1994) proposed a subdivision into six N-S striking tectonic belts, which are termed from west to east: Vohibory belt, Ampanihy belt, Bekily belt, Betroka belt, Tranomaro belt, and Fort Dauphin-Anosyan belt (Fig. 4.2b).

Nearly the whole suite of Precambrian rocks south of the Ranotsara shear zone has experienced granulite-facies metamorphism (e.g., de la Roche, 1963; Bazot *et al.*, 1971; Nicollet, 1990a; Ackermann *et al.*, 1989; Martelat *et al.*, 1997; Markl *et al.*, 2000), however, temperature estimates for the Vohibory and Graphite group are lower (ca. 700–850 °C; Martelat *et al.*, 1997) than those for the Androyan group (ca. 900–1000 °C; Ackermann *et al.*, 1989; Markl *et al.*, 2000). A difference in peak pressure from ca. 9–11 kbar in the Vohibory group (Nicollet, 1983, 1985b, 1986; Martelat *et al.*, 1997) to ca. 5–8 kbar more to the east (Nicollet, 1990a; Ackermann *et al.*, 1991) was proposed. For the area east of the Ampanihy shear zone, most former workers report post-peak decompression and coeval cooling (Ackermann *et al.*, 1989; Martelat *et al.*, 2000), whereas Nicollet (1990a) assumes near-isobaric cooling at ca. 5 kbar followed by decompression. A similar *P-T* evolution is also reported by Pierdzig (1992), where decompression at 600–700 °C is preceded by a period of cooling at 8–9 kbar. The reason for such different results may be the restricted

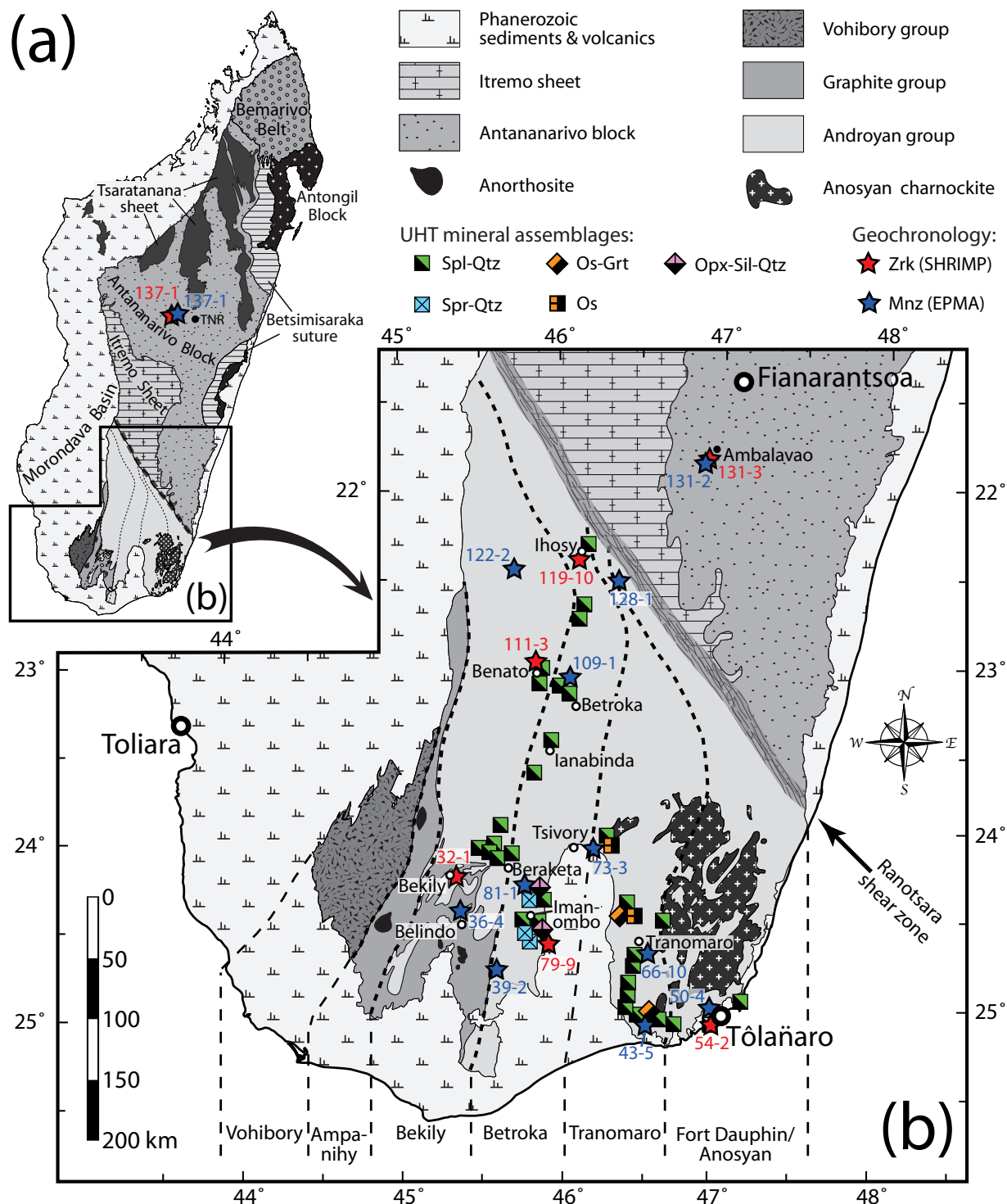


Figure 4.2: (a) Map of the main tectonic units of Madagascar, modified after Collins & Windley (2002). TNR: Antananarivo; (b) Simplified geological map of southern Madagascar, modified after Besairie (1973), showing ultrahigh-temperature mineral assemblages and locations of geochronological samples (sample names are without prefix ‘Md’ and suffix ‘-04’). Dashed lines mark the tectonic belts as proposed by Windley *et al.* (1994).

number of samples examined, because different lithologies often report different stages of the metamorphic history, which may even be a polymetamorphic one.

Pre-Pan-African ages, which range from 720 Ma to 2.2 Ga, have been reported to occur in rocks of the Androyan and Graphite group (Andriamarofahatra *et al.*, 1990; Paquette *et al.*, 1994; Kröner *et al.*, 1996; Ito *et al.*, 1997; Ashwal *et al.*, 1998; Kröner *et al.*, 1999; Martelat *et al.*, 2000; de Wit *et al.*, 2001; Collins *et al.*, 2005; Berger *et al.*, 2006). They are generally interpreted as inherited ages, pointing to a minimum age of ca. 720 Ma for the deposition of the sedimentary protoliths. Evidence for Archaean ages is just equivocal (de Wit *et al.*, 2001). Monazite ages younger than 500 Ma are found to occur mostly within shear zones (Martelat *et al.*, 2000; Berger *et al.*, 2006) and therefore might be caused by late fluid assisted resetting. Published Pan-African metamorphic ages range from 600 Ma to 490 Ma, but controversy exists over their correlation with the metamorphic pressure-temperature history. Most authors consider the main peak metamorphism in the Androyan group to date back to 600–530 Ma (Andriamarofahatra *et al.*, 1990; Paquette *et al.*, 1994; Kröner *et al.*, 1996; Montel *et al.*, 1996; Ito *et al.*, 1997; Ashwal *et al.*, 1998; Kröner *et al.*, 1999; Martelat *et al.*, 2000; de Wit *et al.*, 2001; Collins *et al.*, 2005; Berger *et al.*, 2006), however, younger monazite ages of 550–490 Ma are either explained by a low-pressure metamorphic stage (de Wit *et al.*, 2001) or metasomatism under granulite-facies conditions (Paquette *et al.*, 1994). Data for the westernmost units are more sparse, but the peak metamorphism seems to be significantly older there (Vohibory system: ca. 610–640 Ma, Graphite system: 642–648 Ma; de Wit *et al.*, 2001; Jöns & Schenk, in review).

To date specific parts of the geodynamic evolution, careful petrographic observations and pressure-temperature estimates on appropriate samples have to be combined with *in situ* geochronology of monazite and zircon. Here, we report our results on a large set of samples from the Androyan as well as the Graphite group south of the Ranotsara shear zone. These samples are mainly metapelites and calcsilicates, but in minor amounts also felsic gneisses, marbles, and metabasic rocks. For comparability reasons, we also examined a few metapelitic samples from north of the Ranotsara shear zone (Fig. 4.2a, b).

4.4 Analytical procedures

4.4.1 Sampling

The samples used in this study have been collected during our 2004 field trip. The graphite group was sampled during our journey from the Ankafotra anorthosite via Ambahita, Sakoandroa, Bekily, Ampanamperandrotsy, and Belindo to Ambovombe. Samples from the Androyan group have been collected mostly near the roadside from Tôlaïaro to Amboasary, Tranomaro, Tsivory, Imanombo, Beraketa, Ianabinda, Betroka, and Benato to Ihosy (Fig. 4.2b). Sampling of the Antananarivo block was restricted to two areas: near Ambalavao in the south (Fig. 4.2b) and around Miarinarivo (W of Antananarivo; Fig. 4.2a). A total of ca. 370 samples was taken and petrographically examined.

4.4.2 Electron microprobe analyses and U-Th-total Pb dating

We performed measurements on a JEOL Superprobe JXA-8900R electron microprobe at the University of Kiel, equipped with five wavelength-dispersive spectrometers. The accelerating voltage was generally 15 kV for a probe current of 20 nA. Synthetic and natural mineral standards were used. Sample spot sizes were 1–7 μm in diameter. We applied the CITZAF method of Armstrong (1995) for raw data correction.

For feldspar thermometry we reintegrated the composition of mesoperthitic grains from measurements of plagioclase and alkali-feldspar. The proportions of host and lamellae were determined from backscattered electron images using an image analysis software.

An accelerating voltage of 20 kV with a probe current of 80 nA was used for chemical U-Th-total Pb dating of monazite. All monazite was analysed in-situ to have textural control over the mineral inclusion relationships. For control over internal zoning, we obtained backscattered electron images, as well as X-ray maps of Y, Th, U, and Pb. The samples were polished on Pb-free polishing discs. A more detailed description of used X-ray lines, standards, and data evaluation can be found in Jöns *et al.* (2006).

4.4.3 Sensitive high-mass resolution ion microprobe (SHRIMP)

Selected samples were crushed, and zircons were separated using a magnetic separator and heavy liquids (methylene iodide, Clerici's solution). The grains were handpicked and mounted in epoxy resin discs that were coated with a gold film (ca. 100 Å). These mounts were examined in reflected and transmitted light photographs, as well as cathodoluminescence (CL) SEM images. Based on the CL images, measurement spots were chosen, which account for crystal growth zoning and radiation damage.

The U–Pb isotopic measurements were performed on a SHRIMP II at the Centre of Isotopic Research, All-Russian Geological Research Institute (VSEGEI) in Saint Petersburg (Russia). The primary beam of O_2^- ions had a current of 3–5 nA and the sputtered secondary ions were accelerated with a voltage of 10 kV. Each analysis consisted of five mass scans, the diameter of the measurement spot was 20–25 μm . Pb/U isotopic ratios were corrected for instrumental inter-element discrimination using repeated measurements of the Temora 1 standard. This zircon is from the Middledale gabbroic diorite of the Lachlan orogen in East Australia and has a $^{206}\text{Pb}/^{238}\text{U}$ age of 416.8 ± 1.1 Ma (Black *et al.*, 2003). The 91500 zircon with a uranium concentration of 81.2 ppm (Wiedenbeck *et al.*, 1995) acted as uranium concentration standard. Data reduction and age calculations were done using the programs SQUID (Ludwig, 2001) and Isoplot (Ludwig, 2003), with decay constants of Steiger & Jäger (1977).

4.5 Petrography and mineral chemistry

4.5.1 Felsic and intermediate gneisses

Rock types

Felsic and intermediate gneisses are found throughout southern Madagascar. They are medium- to coarse-grained quartzo-feldspathic rocks that show a massive or a foliated texture. If present, the foliation is accentuated by dark garnet- and biotite-rich layers, alternating with lighter portions consisting mainly of feldspar and quartz. In many cases, cm-thick leucosomes lie concordantly to the schistosity plane, pointing to penetrative deformation following anatexis. In the outcrop scale, mafic layers or boudins are locally included. In proximity to shear zones the rocks show a well-developed schistosity due to the presence of quartz ribbons.

Petrography and mineral assemblages

On the basis of their mineral assemblages, eight different groups can be distinguished (Table 4.1). Most assemblages contain orthopyroxene, and therefore, these rocks may be termed charnockitic or charno-enderbitic gneisses. The rocks are generally equigranular with garnet and orthopyroxene forming porphyroblasts. Orthopyroxene-bearing samples contain just a minor amount of biotite in the matrix, but it is frequently found as inclusion in garnet. In some cases orthopyroxene is situated in leucosomes, indicating its formation by dehydration of biotite. Reaction textures have not been found. An exceptional rock type (sample Md32-1-04) has been found as a concordant layer in felsic granulites of the Menarandra river in Bekily (Graphite group): intermediate gneisses with cm-sized garnet porphyroblasts contain inverted pigeonite.

Mineral chemistry

In rocks with assemblage 2 (Table 4.1) garnet is generally unzoned, but varies in composition from sample to sample: $X_{Prp} = 0.20\text{--}0.33$, $X_{Alm} = 0.62\text{--}0.73$, $X_{Sps} = 0.01\text{--}0.05$, and $X_{Grs} = 0.03\text{--}0.04$. Orthopyroxene (Fig. 4.3a) is also unzoned in Fe-Mg ($X_{En} = 0.41\text{--}0.51$, $X_{Fs} = 0.49\text{--}0.59$), but has high Al_2O_3 contents in the cores of porphyroblasts (up to 3.7 wt.%), decreasing towards the rims (0.8–2.5 wt.%). Plagioclase shows a narrow range of compositions: $X_{An} = 0.33\text{--}0.36$, $X_{Ab} = 0.61\text{--}0.65$, and $X_{Or} < 0.04$. Cores generally have slightly higher An-content. Alkali-feldspar is more variable in composition with $X_{Or} = 0.50\text{--}0.90$, $X_{An} < 0.07$, and $X_{Ab} = 0.30\text{--}0.65$. Spinel is hercynitic ($\text{Mg}/[\text{Mg}+\text{Fe}] = 0.20\text{--}0.35$) and contains 1.5–1.7 wt.% ZnO. Biotite is characterised by an X_{Mg} ($\text{Mg}/[\text{Mg}+\text{Fe}^{2+}]$) of ca. 0.6 and TiO_2 contents ranging from 5.5 to 5.8 wt.%. In samples containing inverted pigeonite (assemblage 3 in Table 4.1) garnet is more Ca-rich: $X_{Prp} = 0.02\text{--}0.05$, $X_{Alm} = 0.68\text{--}0.72$, $X_{Sps} = 0.04\text{--}0.05$, and $X_{Grs} = 0.20\text{--}0.24$. The pyroxene contains different generations of exsolution lamellae. Both host and lamellae are iron-rich (Opx: $X_{En} = 0.13\text{--}0.15$, $X_{Fs} = 0.83\text{--}0.85$, $X_{Wol} = 0.02\text{--}0.03$; Cpx: $X_{En} = 0.11\text{--}0.13$, $X_{Fs} = 0.42\text{--}0.46$, $X_{Wol} = 0.43\text{--}0.46$). Plagio-

Table 4.1: Mineral assemblages found in felsic and intermediate gneisses of southern Madagascar.

1	Pl	Kfs	Qtz	Grt	± Bt	—	—
2	Pl	Kfs	Qtz	Grt	Bt	Spl	Opx
3	Pl	Kfs	Qtz	Grt	—	—	inv. Pig.
4	Pl	Kfs	Qtz	Grt	± Bt	—	Opx
5	Pl	—	Qtz	Grt	± Bt	—	Opx
6	Pl	Kfs	Qtz	—	± Bt	—	Opx
7	Pl	—	Qtz	—	± Bt	—	Opx
8	Pl	Kfs	Qtz	Grt	Bt	Spl	—

common accessories: apatite, zircon, monazite, ilmenite

class can be described as $An_{24-27}Ab_{71-73}Or_{1-4}$ and alkali-feldspar as $Ab_{5-9}Or_{91-95}$. Assemblage 5 (Table 4.1) contains grossular-rich garnet ($Prp_{17-23}Alm_{57-64}Sp_{3-5}Grs_{16-18}$), and orthopyroxene is characterised by $Al_2O_3 = 0.8-1.1$ wt.% and $X_{En} = 0.48-0.50$ (Fig. 4.3a). Plagioclase is generally $An_{46-51}Ab_{50-52}Or_1$, but inclusions in garnet porphyroblasts may have even higher An-contents of 60–75 wt.%.

4.5.2 Metabasites

Rock types

While the Vohibory group is dominated by metabasites, minor amounts have been found in the Graphite and Androyan group. They form centimetre- to decimetre-sized concordant layers or boudins within other lithologies, locally cut by centimetre-thick leucosomes. They are generally fine- to medium-grained equigranular rocks with a massive appearance. Locally, especially if larger amounts of amphibole are present, they may show a well-developed schistosity.

Mineral assemblages and textures

Six different mineral assemblages have been found, which are listed in Table 4.2. In most cases, amphibole is a retrograde phase, formed as a result of the late-stage rehydration of pyroxene. From textural observations, locally also biotite has to be interpreted as a late-stage formation. Reaction textures are absent, except for a manganese-rich sample of assemblage 1 (Table 4.2), where secondary orthopyroxene forms rims around clinopyroxene and garnet. The following reaction is proposed:



This reaction is supposed to take place during the transition from the high-pressure to medium-pressure granulite facies (Green & Ringwood, 1967, 1972) indicating a decompressional P - T evolution.

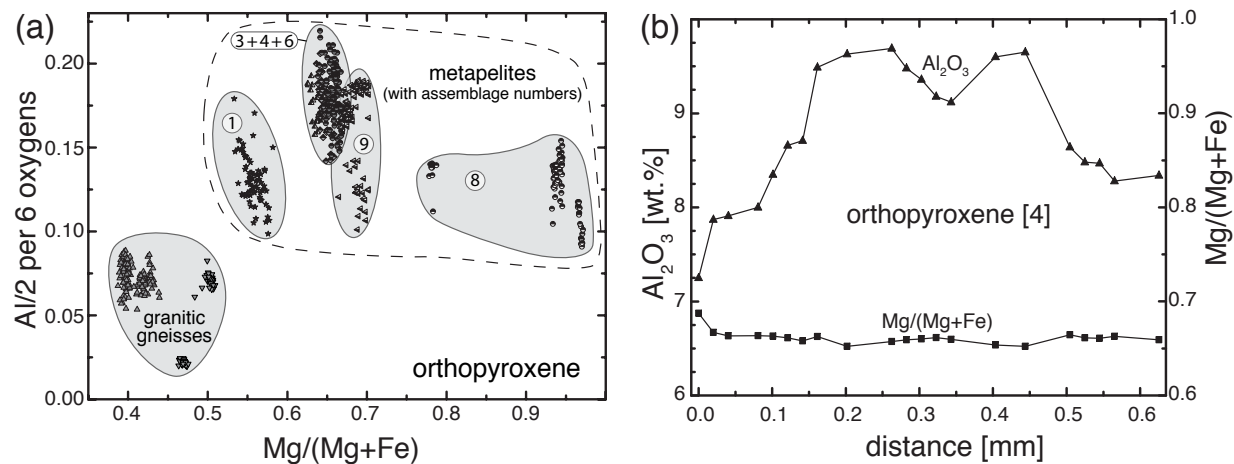


Figure 4.3: Composition of orthopyroxene from metapelitic rocks and granitic/charnockitic gneisses (assemblage numbers correspond to Table 4.3). (a) X_{Mg} vs. Al/2 (calculation based on 6 oxygens). Orthopyroxene from granitic gneisses is poorer in alumina than that from metapelites. Orthopyroxene from SiO₂-undersaturated pelites shows the most magnesium-rich compositions. (b) Typical zonation profile from a metapelitic orthopyroxene. While no zonation is observed in X_{Mg} due to re-equilibration, high Al-contents are preserved in the cores of porphyroblasts.

Mineral chemistry

Due to the scarcity of metabasic samples in southern Madagascar and the limited usability of the mostly garnet-free samples for thermobarometric estimates, only the mineral chemistry of a few samples has been determined. In rocks featuring assemblage 1 (Table 4.2) garnet has a composition of $X_{Prp} = 0.12-0.23$, $X_{Alm} = 0.55-0.64$, $X_{Sps} = 0.03-0.04$, and $X_{Grs} = 0.18-0.20$. Slightly increasing Prp-contents are generally found towards the rims of porphyroblasts. Orthopyroxene can be characterised as $En_{42-53}Fs_{46-56}Wol_{1-3}$ and clinopyroxene as $En_{30-37}Fs_{16-25}Wol_{44-47}$. Plagioclase is generally zoned with X_{An} increasing towards the rims. Amphibole is of pargasitic or ferropargasitic composition.

4.5.3 Metapelites

Rock types

Metapelites are the most widespread rocks occurring in the Androyan group, and they display a great mineralogical diversity (Table 4.3). The most common ones medium- to fine-grained aluminous paragneisses containing porphyroblasts of garnet. As a result of the presence of spinel, they are relatively dark, however, they frequently underwent migmatization resulting in a banded appearance with alternating spinel-sillimanite-rich layers and concordant leucosomes. Locally they contain mineral assemblages pointing to ultrahigh temperatures. Silica-undersaturated metapelites are also common and have been sampled at four locations (Fig. 4.2): Ankeniheny (near Tranomaro), Ampandranda (north of Beraketa), Vohidava (near Ianabinda), and Imanombo. Samples from the latter locality are massive kornepine-spinel-sillimanite rocks, whereas at the other locations coarse grained

Table 4.2: Mineral assemblages found in metabasites of southern Madagascar. Bracketed minerals are late-stage formations.

1	Pl	Grt	Opx	Cpx	± Qtz	(± Amph)	(± Bt)
2	Pl	Grt	Opx	—	—	(Amph)	(± Bt)
3	Pl	—	Opx	Cpx	± Qtz	(± Amph)	(± Bt)
4	Pl	Grt	—	Cpx	± Qtz	(± Amph)	—
5	Pl	—	—	Cpx	± Qtz	(Amph)	(± Bt)
6	Pl	Grt	—	—	± Qtz	—	(± Bt)

common accessories: apatite, zircon, ilmenite

in no. 4: titanite

rare accessories: scapolite, pyrite

phlogopite-rich and sapphirine-bearing rocks with a well-developed schistosity occur. The southern part of the Androyan group between Tôlañaro and Tranomaro is dominated by light-coloured gneisses, which are also known as leptynites. They consist mainly of quartz and feldspar, and contain just millimetre-thin layers consisting of spinel, garnet, sillimanite and late-stage cordierite.

Petrography and mineral assemblages

It is a remarkable observation that the occurrence of garnet-orthopyroxene-bearing pelitic assemblages (Fig. 4.4a) is restricted to the southern part of the Androyan group. Other typical UHT assemblages, like sapphirine-quartz, orthopyroxene-sillimanite-quartz and osumilite-garnet, have also been found to occur in the extreme south of the studied area (Fig. 4.2). On the other hand, spinel-quartz assemblages are found throughout the Androyan group. This might point to higher metamorphic temperatures in the southern part, which is also confirmed by a systematic change of mineral compositions, with the most Mg-rich minerals found in the south (Fig. 4.4b). An overall feature of most metapelites is the presence of cordierite, ranging from thin rims around spinel in the leptynites of the Tôlañaro area, to cordierite-dominated pelites, occurring in the whole area between Imanombo and Ihosy (Fig. 4.2). The formation of cordierite is a late-stage process and often accompanied by coeval migmatization, evidenced by thick cordierite-rich leucosomes. Just in Mg-rich and SiO₂-undersaturated rocks cordierite belongs to the peak assemblage. In total, sixteen mineral assemblages have been identified (Table 4.3). Representative mineral analyses are given in Tables 4.4–4.10.

Mineral reactions and chemistry

Assemblage 1. The most prominent feature of this metapelite assemblage is the large amount of symplectitic intergrowths (Fig. 4.5a) consisting of cordierite, alkali-feldspar, quartz, and orthopyroxene. Orthopyroxene is not equally distributed within the symplectites, but is concentrated on trails, which occur predominantly near spinel, garnet, and

Table 4.3: Mineral assemblages in metapelites of southern Madagascar. Bracketed minerals are late-stage formations.

1	P1	Kfs/(Kfs)	Qtz/(Qtz)	Grt/(Grt)	Sil	(Crd)	±Bt/(±Bt)	±Spl	(±Opx)	Osu-pseud	—
2	P1	Kfs/(Kfs)	Qtz/(Qtz)	—	Sil	(Crd)	Bt	Spl	—	Osu-pseud	—
3	P1	Kfs	Qtz	—	Sil	(Crd)	—	Spl	Opx	—	Spr
4	P1	Kfs	Qtz	Grt	Sil	((Crd))	—	(Spl)	(Opx)	—	Spr
5	P1	Kfs	Qtz	Grt	Sil	((Crd))	Bt	(Spl)	—	—	Spr
6	P1	Kfs	Qtz	Grt	Sil	(Crd)	Bt	Spl	Opx	—	—
7	±P1	Kfs	—	—	—	±Crd/(±Crd)	Bt	±Spl	—	—	Spr
8	—	±Kfs	—	—	—	±Crd/(±Crd)	Bt	—	Opx	—	—
9	P1	±Kfs	±Qtz	Grt	—	±Crd/(Crd)	Bt	—	Opx/(±Opx)	—	—
10	—	—	—	—	—	Crd	Bt	—	Opx	—	—
11	P1	Kfs	Qtz	Grt	Sil	±Crd/(Crd)	±Bt/(±Bt)	Spl	—	—	—
12	±P1	Kfs	±Qtz	Grt	Sil	(Crd)	Bt	—	—	—	—
13	±P1	±Kfs	Qtz	Grt	Sil	—	±Bt	—	—	—	—
14	±P1	Kfs	Qtz	Grt	—	(Crd)	±Bt	Spl	—	—	—
15	±P1	±Kfs	Qtz	—	Sil	(Crd)	±Bt	Spl	—	—	—
16	±P1	±Kfs	Qtz	—	—	(±Crd)	±Bt	Spl	—	—	—

common accessories: monazite, zircon, ilmenite; in no. 7 and 8: corundum; in no. 9: rutile
 Osu-pseud= pseudomorph replacement of osunilite; other abbreviations after Kretz (1983)

Table 4.4: Representative analyses of garnet from metapelitic and metagranitic samples of southern Madagascar.

Sample No.	38-1 Grt25	38-1 Grt75	89-1 Grt627	89-1 Grt645	89-1 Grt579	89-1 Grt584	91-2 Grt54	91-2 Grt57	109-1 Grt100	109-1 Grt104	109-1 Grt47	109-1 Grt52	119-5 Grt357	119-5 Grt358	55-1 Grt39	55-1 Grt54
Asbl.*	[5] ^{gr}	[5] ^{gr}	[9] ^{mp}	[9] ^{mp}	[9] ^{mp}	[9] ^{mp}	[11] ^{mp}	[11] ^{mp}	[11] ^{mp}	[11] ^{mp}	[11] ^{mp}	[11] ^{mp}	[11] ^{mp}	[11] ^{mp}	[4] ^{gr}	[4] ^{gr}
SiO ₂	38.47	38.31	40.01	39.72	39.49	39.83	38.86	38.74	39.68	39.88	39.42	39.16	38.09	38.06	37.61	37.57
TiO ₂	0.05	0.06	0.03	0.03	0.02	0.06	0.00	0.05	0.04	0.07	0.05	0.01	0.02	0.06	0.05	0.02
Al ₂ O ₃	21.32	21.44	22.46	22.36	22.19	22.22	21.56	21.52	21.86	21.58	21.76	21.42	21.37	21.48	21.25	21.31
Cr ₂ O ₃	0.00	0.00	0.05	0.02	0.08	0.04	0.02	0.02	0.01	0.02	0.02	0.04	0.06	0.00	0.06	0.07
FeO	26.66	27.49	22.75	22.68	23.65	23.64	26.89	26.40	29.18	29.05	29.46	30.19	32.58	32.62	33.62	33.86
MgO	6.03	4.93	13.40	13.36	12.60	12.86	8.67	8.76	8.35	8.37	8.02	7.55	5.31	5.31	5.00	5.02
MnO	1.26	1.59	0.16	0.14	0.14	0.19	2.81	2.97	0.91	0.91	0.99	0.89	1.79	1.95	1.08	1.02
CaO	6.01	6.38	1.10	1.11	1.67	1.29	1.07	1.06	0.79	0.77	0.83	0.83	1.27	1.27	1.17	1.13
Total	99.80	100.20	99.96	99.41	99.84	100.13	99.88	99.51	100.82	100.65	100.55	100.09	100.49	100.75	99.84	100.00
Si	3.008	3.002	2.998	2.994	2.984	2.995	3.012	3.011	3.042	3.060	3.038	3.044	3.005	2.997	2.996	2.990
Ti	0.003	0.004	0.002	0.001	0.001	0.004	0.000	0.003	0.002	0.004	0.003	0.001	0.001	0.004	0.003	0.001
Al	1.964	1.980	1.984	1.986	1.977	1.970	1.970	1.971	1.975	1.951	1.976	1.962	1.987	1.994	1.995	1.998
Cr	0.000	0.000	0.003	0.001	0.005	0.003	0.001	0.001	0.000	0.001	0.001	0.002	0.004	0.000	0.004	0.004
Fe ²⁺	1.743	1.801	1.425	1.430	1.494	1.487	1.743	1.716	1.871	1.864	1.899	1.963	2.150	2.148	2.239	2.253
Mg	0.702	0.576	1.497	1.501	1.419	1.441	1.002	1.015	0.954	0.957	0.921	0.874	0.625	0.623	0.593	0.595
Mn	0.083	0.105	0.010	0.009	0.009	0.012	0.185	0.195	0.059	0.059	0.065	0.059	0.120	0.130	0.073	0.069
Ca	0.504	0.536	0.088	0.089	0.135	0.104	0.089	0.088	0.065	0.063	0.069	0.069	0.107	0.107	0.100	0.097
Total	8.007	8.004	8.007	8.012	8.024	8.015	8.002	8.000	7.968	7.960	7.971	7.974	7.999	8.003	8.003	8.007
X _{Mg}	0.29	0.24	0.51	0.51	0.49	0.49	0.37	0.37	0.34	0.34	0.33	0.31	0.23	0.22	0.21	0.21
X _{Prp}	0.23	0.19	0.50	0.50	0.46	0.47	0.33	0.34	0.32	0.33	0.31	0.29	0.21	0.21	0.20	0.20
X _{Alm}	0.57	0.60	0.47	0.47	0.49	0.49	0.58	0.57	0.63	0.63	0.64	0.66	0.72	0.71	0.75	0.75
X _{Sps}	0.03	0.03	0.00	0.00	0.00	0.00	0.06	0.06	0.02	0.02	0.02	0.02	0.04	0.04	0.02	0.02
X _{Grs}	0.17	0.18	0.03	0.03	0.04	0.03	0.03	0.03	0.02	0.02	0.02	0.02	0.03	0.04	0.03	0.03
X _{Uv}	0.00	0.00	0.00	0.00	0.00	0.00	0.00	0.00	0.00	0.00	0.00	0.00	0.00	0.00	0.00	0.00

* Assemblage number corresponds to Table 4.1 for metagranitic (*gr*) and to Table 4.3 for metapelitic (*mp*) samples
Cations calculated on the basis of 12 oxygens

Table 4.4: (continued) Representative analyses of garnet from metapelitic and metagranitic samples of southern Madagascar.

Sample No.	55-1	69-1	69-1	79-9	79-9	81-1	81-1	78-1	78-1	101-4	101-4	56-1	56-1	89-1	89-1
Gr+86	Gr+139	Gr+173	Gr+234	Gr+316	Gr+295	Gr+349	Gr+244	Gr+252	Gr+93	Gr+98	Gr+276	Gr+278	Gr+670	Gr+686	
Asbl.*	[4] ^{gr}	[1] ^{mp}	[1] ^{mp}	[6] ^{mp}	[6] ^{mp}	[4] ^{mp}	[4] ^{mp}	[12] ^{mp}	[12] ^{mp}	[11] ^{mp}	[11] ^{mp}	[2] ^{gr}	[2] ^{gr}	[9] ^{mp}	[9] ^{mp}
SiO ₂	37.59	38.06	37.90	38.94	39.22	39.18	39.51	39.03	39.35	39.02	39.01	38.38	38.26	40.02	39.87
TiO ₂	0.08	0.03	0.03	0.04	0.04	0.00	0.12	0.01	0.02	0.02	0.00	0.02	0.07	0.04	0.06
Al ₂ O ₃	21.35	21.65	21.35	21.99	22.46	22.05	22.15	22.10	22.15	21.43	21.13	21.83	21.69	22.58	22.50
Cr ₂ O ₃	0.02	0.01	0.01	0.04	0.00	0.00	0.01	0.03	0.01	0.00	0.02	0.02	0.08	0.04	0.01
FeO	33.54	31.03	30.21	24.47	22.99	20.80	20.83	24.16	23.70	29.86	29.71	30.91	30.72	22.63	22.66
MgO	5.15	6.35	6.89	9.07	10.32	10.86	11.67	9.82	9.87	7.60	7.43	7.08	7.22	13.44	12.91
MnO	0.96	2.30	2.14	5.58	5.03	5.96	5.03	4.46	4.46	1.71	1.94	1.00	0.91	0.15	0.13
CaO	1.23	1.17	0.87	0.73	0.73	0.85	0.77	0.60	0.64	1.16	1.12	1.30	1.38	1.18	1.47
Total	99.92	100.59	99.40	100.86	100.79	99.70	100.08	100.21	100.20	100.81	100.35	100.54	100.32	100.08	99.61
Si	2.989	2.984	2.994	2.989	2.981	2.996	2.996	2.994	3.010	3.022	3.036	2.990	2.986	2.994	2.999
Ti	0.005	0.002	0.002	0.003	0.003	0.000	0.007	0.000	0.001	0.001	0.000	0.001	0.004	0.002	0.004
Al	2.001	2.000	1.988	1.989	2.012	1.988	1.980	1.998	1.997	1.956	1.939	2.004	1.995	1.991	1.996
Cr	0.001	0.001	0.001	0.002	0.000	0.000	0.001	0.002	0.001	0.000	0.001	0.001	0.005	0.002	0.000
Fe ²⁺	2.230	2.035	1.996	1.571	1.462	1.331	1.321	1.550	1.516	1.934	1.934	2.014	2.005	1.416	1.426
Mg	0.610	0.742	0.812	1.037	1.169	1.239	1.319	1.123	1.125	0.878	0.862	0.822	0.840	1.499	1.448
Mn	0.064	0.153	0.143	0.363	0.324	0.386	0.323	0.290	0.289	0.112	0.128	0.066	0.060	0.009	0.008
Ca	0.105	0.098	0.073	0.060	0.059	0.070	0.062	0.049	0.052	0.097	0.093	0.108	0.115	0.095	0.119
Total	8.005	8.014	8.009	8.014	8.010	8.010	8.008	8.006	7.991	8.000	7.993	8.007	8.010	8.009	8.000
X _{Mg}	0.21	0.27	0.29	0.40	0.44	0.48	0.50	0.42	0.43	0.31	0.31	0.29	0.30	0.51	0.50
X _{Prrp}	0.20	0.25	0.27	0.34	0.39	0.41	0.44	0.37	0.38	0.29	0.29	0.27	0.28	0.50	0.48
X _{Alm}	0.74	0.67	0.66	0.52	0.49	0.44	0.44	0.51	0.51	0.64	0.64	0.67	0.66	0.47	0.48
X _{SpS}	0.02	0.05	0.05	0.12	0.11	0.13	0.11	0.10	0.10	0.04	0.04	0.02	0.02	0.00	0.00
X _{GrS}	0.03	0.03	0.02	0.02	0.02	0.02	0.02	0.02	0.02	0.03	0.03	0.04	0.04	0.03	0.04
X _{Uv}	0.00	0.00	0.00	0.00	0.00	0.00	0.00	0.00	0.00	0.00	0.00	0.00	0.00	0.00	0.00

* Assemblage number corresponds to Table 4.1 for metagranitic (*gr*) and to Table 4.3 for metapelitic (*mp*) samples
Cations calculated on the basis of 12 oxygens

Table 4.5: Representative analyses of orthopyroxene from metapelitic and metagranitic samples of southern Madagascar.

Sample No.	38-1 [5] _{gr}	38-1 Opx138 [5] _{gr}	89-1 Opx554 [9] _{mp}	89-1 Opx566 [9] _{mp}	89-1 Opx777 [9] _{mp}	89-1 Opx783 [9] _{mp}	55-1 Opx135 [4] _{gr}	55-1 Opx151 [4] _{gr}	55-1 Opx177 [4] _{gr}	69-1 Opx274 [1] _{mp}	69-1 Opx276 [1] _{mp}	79-9 Opx253 [6] _{mp}	79-9 Opx291 [6] _{mp}
SiO ₂	50.60	50.28	49.17	49.75	50.41	51.42	48.22	47.98	47.60	48.81	47.56	46.58	48.13
TiO ₂	0.08	0.11	0.23	0.23	0.17	0.11	0.22	0.21	0.25	0.11	0.12	0.15	0.15
Al ₂ O ₃	1.11	1.19	8.67	8.81	6.58	5.26	3.38	3.41	3.66	6.03	7.34	8.13	8.56
Cr ₂ O ₃	0.03	0.02	0.00	0.00	0.00	0.00	0.06	0.03	0.03	0.00	0.00	0.04	0.02
FeO	29.82	30.17	18.60	18.09	19.25	19.05	34.59	34.96	34.40	25.96	26.83	21.23	21.35
MgO	16.55	16.23	23.09	23.24	23.30	24.00	12.79	12.73	12.61	18.04	17.61	21.70	20.02
MnO	0.76	0.76	0.07	0.08	0.03	0.07	0.43	0.38	0.45	0.71	0.78	1.43	1.75
CaO	0.58	0.55	0.09	0.10	0.08	0.09	0.14	0.12	0.14	0.12	0.06	0.04	0.03
Total	99.53	99.30	99.92	100.29	99.82	100.00	99.83	99.82	99.15	99.78	100.30	99.30	100.01
Si	1.969	1.965	1.797	1.805	1.848	1.879	1.912	1.906	1.902	1.856	1.810	1.756	1.795
Ti	0.003	0.003	0.006	0.006	0.005	0.003	0.007	0.006	0.008	0.003	0.003	0.004	0.004
Al	0.051	0.055	0.373	0.377	0.284	0.227	0.158	0.160	0.172	0.270	0.329	0.361	0.376
Cr	0.001	0.001	0.000	0.000	0.000	0.000	0.002	0.001	0.001	0.000	0.000	0.001	0.001
Fe ²⁺	0.970	0.986	0.569	0.549	0.590	0.582	1.147	1.162	1.150	0.826	0.854	0.669	0.666
Mg	0.960	0.946	1.258	1.257	1.273	1.308	0.756	0.754	0.751	1.023	0.999	1.220	1.113
Mn	0.025	0.025	0.002	0.002	0.001	0.002	0.014	0.013	0.015	0.023	0.025	0.046	0.055
Ca	0.024	0.023	0.003	0.004	0.003	0.004	0.006	0.005	0.006	0.005	0.003	0.002	0.001
Total	4.003	4.004	4.009	4.000	4.004	4.005	4.002	4.007	4.005	4.006	4.023	4.059	4.011
X _{En}	0.49	0.48	0.69	0.69	0.68	0.69	0.40	0.39	0.39	0.55	0.53	0.65	0.63
X _{Fs}	0.50	0.50	0.31	0.30	0.32	0.31	0.60	0.60	0.60	0.45	0.47	0.35	0.37
X _{Wol}	0.01	0.01	0.00	0.00	0.00	0.00	0.00	0.00	0.00	0.00	0.00	0.00	0.00

* Assemblage number corresponds to Table 4.1 for metagranitic (*gr*) and to Table 4.3 for metapelitic (*mp*) samples
Cations calculated on the basis of 6 oxygens

Table 4.5: (continued) Representative analyses of orthopyroxene from metapelitic and metagranitic samples.

Sample No.	81-1 Opx258 [4] ^{mp}	81-1 Opx266 [4] ^{mp}	56-1 Opx345 [2] ^{gr}	56-1 Opx348 [2] ^{gr}	77-2 Opx380 [3] ^{mp}	77-2 Opx388 [3] ^{mp}	103-1 Opx41 [8] ^{mp}	103-1 Opx42 [8] ^{mp}	89-8 Opx122 [8] ^{mp}	89-8 Opx126 [8] ^{mp}	66-8 Opx74 [8] ^{mp}	66-8 Opx77 [8] ^{mp}
SiO ₂	47.61	48.49	49.34	49.23	47.42	47.80	55.55	55.39	51.45	51.80	54.30	54.76
TiO ₂	0.19	0.19	0.19	0.16	0.20	0.18	0.02	0.05	0.14	0.11	0.10	0.11
Al ₂ O ₃	8.88	9.35	3.16	3.08	9.40	9.08	5.89	5.77	6.28	6.32	6.79	6.38
Cr ₂ O ₃	0.00	0.00	0.06	0.09	0.03	0.03	0.01	0.00	0.01	0.01	0.00	0.00
FeO	19.85	19.71	29.18	29.70	20.74	20.81	2.33	2.29	13.90	13.55	4.13	4.03
MgO	20.93	20.55	16.77	16.84	20.79	20.79	35.87	36.03	27.34	27.28	34.23	34.30
MnO	2.04	1.90	0.32	0.35	1.34	1.19	0.03	0.03	0.06	0.05	0.01	0.05
CaO	0.05	0.05	0.19	0.19	0.04	0.03	0.05	0.06	0.16	0.14	0.04	0.05
Total	99.55	100.25	99.20	99.64	99.96	99.90	99.75	99.61	99.33	99.25	99.61	99.67
Si	1.777	1.789	1.916	1.910	1.764	1.777	1.882	1.880	1.851	1.860	1.859	1.872
Ti	0.005	0.005	0.006	0.005	0.006	0.005	0.000	0.001	0.004	0.003	0.003	0.003
Al	0.391	0.407	0.144	0.141	0.412	0.398	0.235	0.231	0.266	0.267	0.274	0.257
Cr	0.000	0.000	0.002	0.003	0.001	0.001	0.000	0.000	0.000	0.000	0.000	0.000
Fe ²⁺	0.619	0.608	0.948	0.963	0.645	0.647	0.066	0.065	0.418	0.407	0.118	0.115
Mg	1.164	1.131	0.971	0.974	1.153	1.152	1.812	1.823	1.466	1.460	1.747	1.748
Mn	0.065	0.060	0.011	0.012	0.042	0.037	0.001	0.001	0.002	0.002	0.000	0.001
Ca	0.002	0.002	0.008	0.008	0.002	0.001	0.002	0.002	0.006	0.005	0.002	0.002
Total	4.023	4.002	4.005	4.015	4.024	4.018	3.999	4.003	4.013	4.004	4.003	3.998
X _{En}	0.63	0.63	0.50	0.50	0.64	0.64	0.96	0.96	0.78	0.78	0.94	0.94
X _{Fs}	0.37	0.37	0.49	0.50	0.36	0.36	0.04	0.03	0.22	0.22	0.06	0.06
X _{Wd}	0.00	0.00	0.00	0.00	0.00	0.00	0.00	0.00	0.00	0.00	0.00	0.00

* Assemblage number corresponds to Table 4.1 for metagranitic (*gr*) and to Table 4.3 for metapelitic (*mp*) samples
Cations calculated on the basis of 6 oxygens

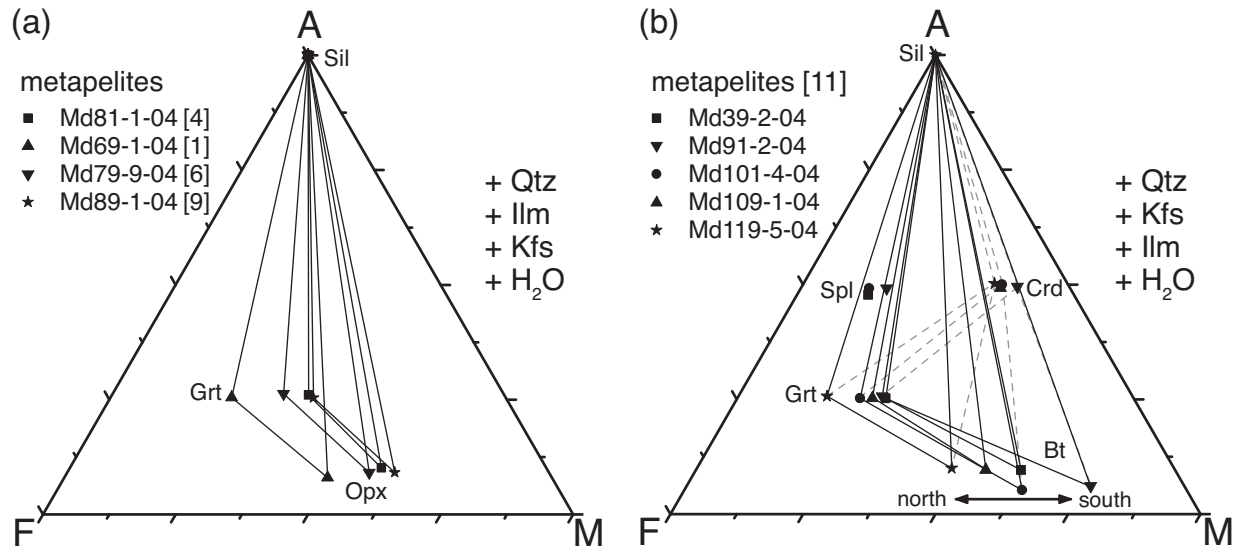
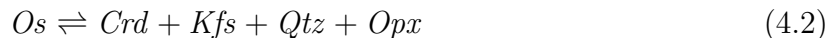
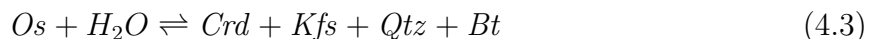


Figure 4.4: (a) AFM diagram showing coexisting garnet and orthopyroxene from different metapelitic assemblages (assemblage numbers refer to Table 4.3; further minerals are not shown). The occurrence of orthopyroxene + garnet in metapelites is restricted to the southernmost Androyan group. (b) Composition of coexisting garnet and biotite from metapelites of assemblage 11 (cp. Table 4.3). A regional trend can be observed: Mg-rich assemblages are found in the southernmost Androyan group (sample Md39-2-04) and minerals become more Fe-rich towards the North (sample Md119-5-04 is from Ihosy, close to the Ranotsara SZ). Shown spinel compositions are likely to be modified due to magnetite exsolution. Cordierite is a late-stage formation.

biotite (Fig. 4.5b, c). This texture has frequently been described in the literature, and it is generally assumed that these intergrowths are breakdown products of the high-temperature mineral osumilite (e. g., Berg, 1977; Ellis *et al.*, 1980; Grew, 1982), formed as a result of the reaction



The orthopyroxene is not present in all rocks, however, biotite seems to have formed instead, leading to the reaction



This reaction represents the breakdown of osumilite under hydrous conditions (Hensen, 1977; Olesch & Seifert, 1981) and points to variable water fugacity and/or bulk rock compositions. The observed symplectites let us conclude that osumilite was stable during the metamorphic evolution, coexisting with garnet and spinel.

The replacement of osumilite by the described symplectites was followed by breakdown of the low-pressure granulite-facies assemblage spinel + quartz. Spinel is separated from matrix quartz by cordierite, garnet, and sillimanite. These breakdown products are distributed heterogeneously, e. g., locally spinel is just rimmed by cordierite, whereas elsewhere double rims of garnet and cordierite are formed (Fig. 4.5d, e). Sillimanite is not equally distributed and does not form perfect corona textures. The newly grown garnet is

Table 4.6: Representative analyses of cordierite from metapelitic samples.

Sample No.	91-2 66	91-2 76	109-1 174	109-1 197	78-1 295	78-1 296	101-4 105	101-4 110	69-2 Crd107	43-2 Crd296
Asbl.*	[11] ^{mp}	[11] ^{mp}	[11] ^{mp}	[11] ^{mp}	[12] ^{mp}	[12] ^{mp}	[11] ^{mp}	[11] ^{mp}	[1] ^{mp}	[1] ^{mp}
SiO ₂	49.34	49.58	49.82	49.68	49.51	49.53	49.62	49.45	50.69	49.84
TiO ₂	0.00	0.00	0.00	0.00	0.00	0.00	0.00	0.00	0.04	0.03
Al ₂ O ₃	32.86	32.94	33.09	32.97	33.41	33.35	33.30	33.16	33.04	33.34
Cr ₂ O ₃	0.00	0.00	0.00	0.00	0.00	0.00	0.00	0.00	0.00	0.00
FeO	4.72	4.87	5.77	5.74	4.03	4.21	5.37	5.72	4.21	6.16
MgO	10.52	10.66	10.12	10.05	10.84	10.72	10.34	9.89	11.08	9.93
MnO	0.14	0.16	0.05	0.08	0.24	0.26	0.09	0.09	0.25	0.07
CaO	0.01	0.01	0.02	0.01	0.00	0.02	0.00	0.02	0.18	0.01
Na ₂ O	0.04	0.03	0.04	0.05	0.06	0.06	0.07	0.07	0.05	0.01
K ₂ O	0.00	0.00	0.00	0.00	0.01	0.01	0.01	0.02	0.06	0.03
Total	97.64	98.25	98.90	98.58	98.11	98.15	98.80	98.42	99.59	99.43
Si	5.029	5.026	5.034	5.037	5.010	5.013	5.013	5.023	5.058	5.019
Ti	0.000	0.000	0.000	0.000	0.000	0.000	0.000	0.000	0.003	0.002
Al	3.948	3.937	3.941	3.940	3.985	3.979	3.965	3.969	3.886	3.958
Cr	0.000	0.000	0.000	0.000	0.000	0.000	0.000	0.000	0.000	0.000
Fe ²⁺	0.402	0.413	0.488	0.487	0.341	0.356	0.454	0.486	0.352	0.519
Mg	1.599	1.611	1.524	1.518	1.635	1.618	1.557	1.497	1.649	1.491
Mn	0.013	0.014	0.004	0.007	0.021	0.022	0.008	0.008	0.021	0.006
Ca	0.001	0.001	0.002	0.001	0.000	0.002	0.000	0.002	0.020	0.001
Na	0.009	0.007	0.007	0.010	0.012	0.011	0.013	0.013	0.010	0.002
K	0.000	0.000	0.000	0.000	0.002	0.001	0.001	0.003	0.007	0.004
Total	11.000	11.009	11.000	10.999	11.006	11.002	11.011	11.001	11.005	11.003
X _{Mg}	0.80	0.80	0.76	0.76	0.83	0.82	0.77	0.75	0.82	0.74

* Assemblage number corresponds to Table 4.3 for metapelitic (*mp*) samples

Cations calculated on the basis of 18 oxygens

locally found to overgrow the symplectites formed after osumilite (Fig. 4.5e), but also forms narrow rims around pre-existing sillimanite (Fig. 4.5f). Therefore a combination of the reactions



seems to account for the observed textures.

Garnet porphyroblasts have a composition of X_{Prp} = 0.25–0.35, X_{Alm} = 0.53–0.70, X_{Sps} = 0.05–0.10, and X_{Grs} = 0.02–0.03. Late-stage garnet rims around spinel and sillimanite have generally low magnesium contents (X_{Prp} = 0.25–0.30). Cordierite within the symplectites is

Table 4.6: (continued) Representative analyses of cordierite from metapelitic samples.

Sample No.	68-1 Crd98 [2] ^{mp}	77-2 Crd410 [3] ^{mp}	81-1 Crd488 [4] ^{mp}	79-9 Crd336 [6] ^{mp}	66-7 Crd31 [7] ^{mp}	66-8 Crd62 [8] ^{mp}	89-8 Crd120 [8] ^{mp}	103-1 Crd13 [8] ^{mp}	89-1 Crd771 [9] ^{mp}
Asbl.*	[2] ^{mp}	[3] ^{mp}	[4] ^{mp}	[6] ^{mp}	[7] ^{mp}	[8] ^{mp}	[8] ^{mp}	[8] ^{mp}	[9] ^{mp}
SiO ₂	49.45	50.01	50.00	49.71	51.03	51.28	50.20	51.08	50.12
TiO ₂	0.00	n.d.	0.00	n.d.	0.00	0.01	0.00	0.00	0.00
Al ₂ O ₃	33.28	33.61	33.93	34.17	33.89	33.76	33.43	33.95	34.36
Cr ₂ O ₃	0.00	n.d.	0.00	n.d.	0.02	0.02	0.04	0.00	0.00
FeO	6.11	3.39	3.24	3.67	0.66	0.59	2.41	0.31	3.35
MgO	9.74	11.32	10.96	11.10	13.21	13.37	12.41	13.46	11.49
MnO	0.19	0.24	0.41	0.28	0.00	0.00	0.00	0.05	0.00
CaO	0.03	0.01	0.00	0.00	0.02	0.00	0.03	0.00	0.02
Na ₂ O	0.04	0.07	0.08	0.04	0.09	0.08	0.06	0.07	0.00
K ₂ O	0.00	0.01	0.16	0.00	0.02	0.06	0.00	0.04	0.02
Total	98.84	98.65	98.78	98.97	98.93	99.17	98.58	98.96	99.36
Si	5.012	5.017	5.012	4.978	5.037	5.049	5.016	5.034	4.985
Ti	0.000	n.d.	0.000	n.d.	0.000	0.001	0.000	0.000	0.000
Al	3.975	3.974	4.009	4.034	3.943	3.917	3.937	3.944	4.029
Cr	0.000	n.d.	0.000	n.d.	0.001	0.001	0.003	0.000	0.000
Fe ²⁺	0.518	0.284	0.272	0.307	0.055	0.049	0.201	0.026	0.278
Mg	1.471	1.693	1.638	1.658	1.944	1.962	1.848	1.977	1.704
Mn	0.017	0.020	0.035	0.024	0.000	0.000	0.000	0.004	0.000
Ca	0.003	0.001	0.000	0.000	0.002	0.000	0.004	0.000	0.002
Na	0.008	0.013	0.015	0.008	0.017	0.016	0.012	0.014	0.001
K	0.000	0.001	0.020	0.000	0.002	0.008	0.000	0.005	0.002
Total	11.003	11.003	11.001	11.008	11.000	11.002	11.020	11.003	11.001
X _{Mg}	0.74	0.86	0.86	0.84	0.97	0.98	0.90	0.99	0.86

* Assemblage number corresponds to Table 4.3 for metapelitic (*mp*) samples

Cations calculated on the basis of 18 oxygens

Mg-rich with $X_{Mg} = 0.67-0.82$ (Table 4.6). The late-stage orthopyroxene, which is another product of the osumilite breakdown, has an X_{En} of 0.53–0.57 (Fig. 4.3a; Table 4.5). Some larger grains show a slight zonation in alumina, ranging from ca. 8.0 wt.% in the core to ca. 5.7 wt.% at the rim. Biotite is characterised by high TiO₂ contents (4.0–5.5 wt.%) and an X_{Mg} of 0.66–0.82 (Fig. 4.6a; Table 4.7). The spinel, which is found to be surrounded by late-stage garnet rims, is hercynitic in composition ($X_{Mg} = 0.25-0.35$) and poor in zinc (ZnO < 0.5 wt.%; Table 4.8). However, a common feature are exsolution lamellae of magnetite, indicating that the original spinel composition is not preserved. Large grains of mesoperthitic feldspar, which have reintegrated compositions of An_{15–19}Ab_{56–60}Or_{20–28}, occur. Some grains of plagioclase are obviously derived from exsolution and recrystallisation of former mesoperthites. Alkalifeldspar within the symplectites is An_{1–3}Ab_{10–20}Or_{80–90}.

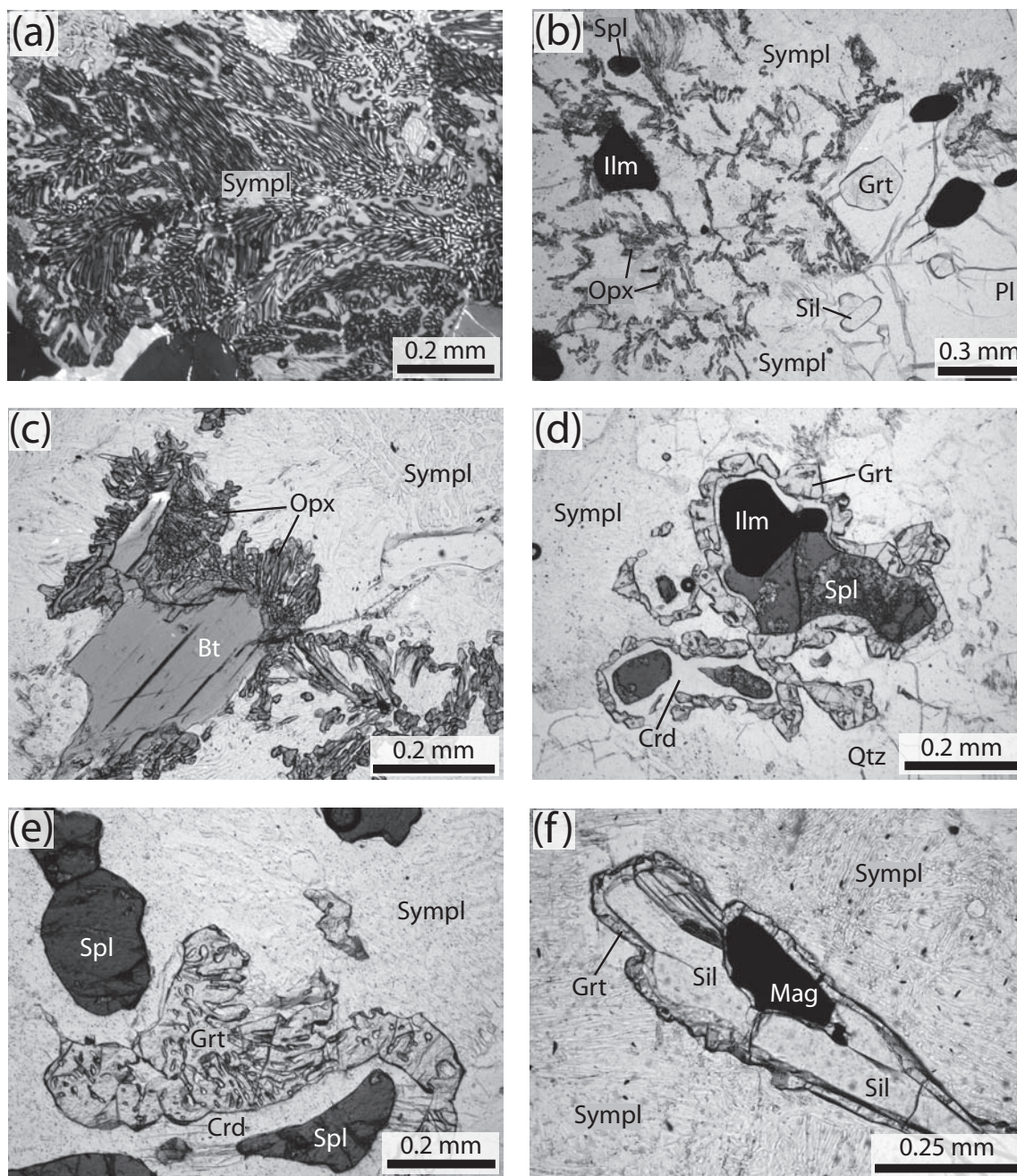


Figure 4.5: Thin section photographs showing microtextures in metapelitic rocks of assemblage 1 (cp. Table 4.3). (a) “Fingerprint-like” symplectitic intergrowth of quartz, cordierite, and K-feldspar, replacing former osumilite (cross polarised light; Md43-2-04). (b) Symplectitic intergrowth of quartz, cordierite, K-feldspar, and orthopyroxene. The latter forms trails within the symplectite (plane polarised light; Md69-1-04). (c) Orthopyroxene in symplectites after osumilite is found to grow near biotite (plane polarised light; Md69-1-04). (d) Partly retrogressed spinel, surrounded by coronas consisting of garnet ± cordierite (plane polarised light; Md43-2-04). (e) Cordierite and garnet forming coronas around hercynitic spinel. The retrograde garnet overgrows the cordierite + quartz + K-feldspar symplectite, which formed after osumilite (plane polarised light; Md43-2-04). (f) Sillimanite surrounded by a narrow rim of garnet. The matrix is made up of symplectitic intergrowths formed after osumilite (plane polarised light; Md69-2-04).

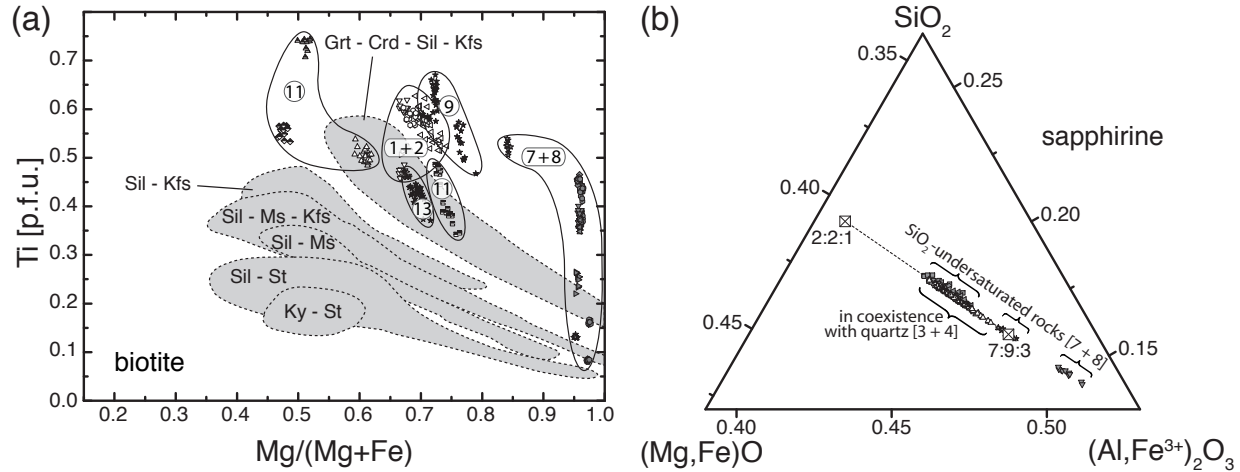


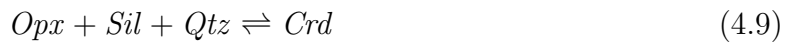
Figure 4.6: (a) Biotite compositions in the diagram X_{Mg} vs. Ti (coexisting with ilmenite or rutile; calculation based on 22 oxygens). Assemblage numbers correspond to Table 4.3. Shaded fields: compositional ranges of biotite from metamorphic zones in New England (Robinson *et al.*, 1982). (b) Sapphirine analyses in the diagram $(Mg,Fe)O-(Al,Fe^{3+})_2O_3-SiO_2$.

Assemblage 2. Besides the lack of garnet, rocks of assemblage no. 2 are similar to those of no. 1. Furthermore, the symplectites formed after osumilite do always contain biotite ($X_{Mg}=0.67-0.71$, $TiO_2=3.8-5.4$ wt.%; Table 4.7), but orthopyroxene is lacking (cf. reaction 4.3). The late-stage breakdown of spinel + quartz to cordierite ($X_{Mg}=0.73-0.80$; Tab 4.6) is ascribed to reaction 4.4.

Assemblage 3. These garnet-free metapelites contain the critical peak-metamorphic assemblages sapphirine + quartz and orthopyroxene + sillimanite + quartz. Tiny inclusions of sapphirine and quartz are found within sillimanite. Larger grains of sapphirine are surrounded by spinel-cordierite intergrowths and sillimanite (Fig. 4.7a). These textures reflect the breakdown of the peak assemblage as a result of the reaction



In some rock domains, orthopyroxene + sillimanite + quartz formed the peak assemblage, now separated by rims of cordierite (Fig. 4.7b):



After breakdown of these high-temperature high-pressure parageneses, the rocks were partially re-equilibrated with the assemblage spinel + quartz + cordierite + sillimanite. Subsequently spinel + quartz reacted to form cordierite (cf. reaction 4.4).

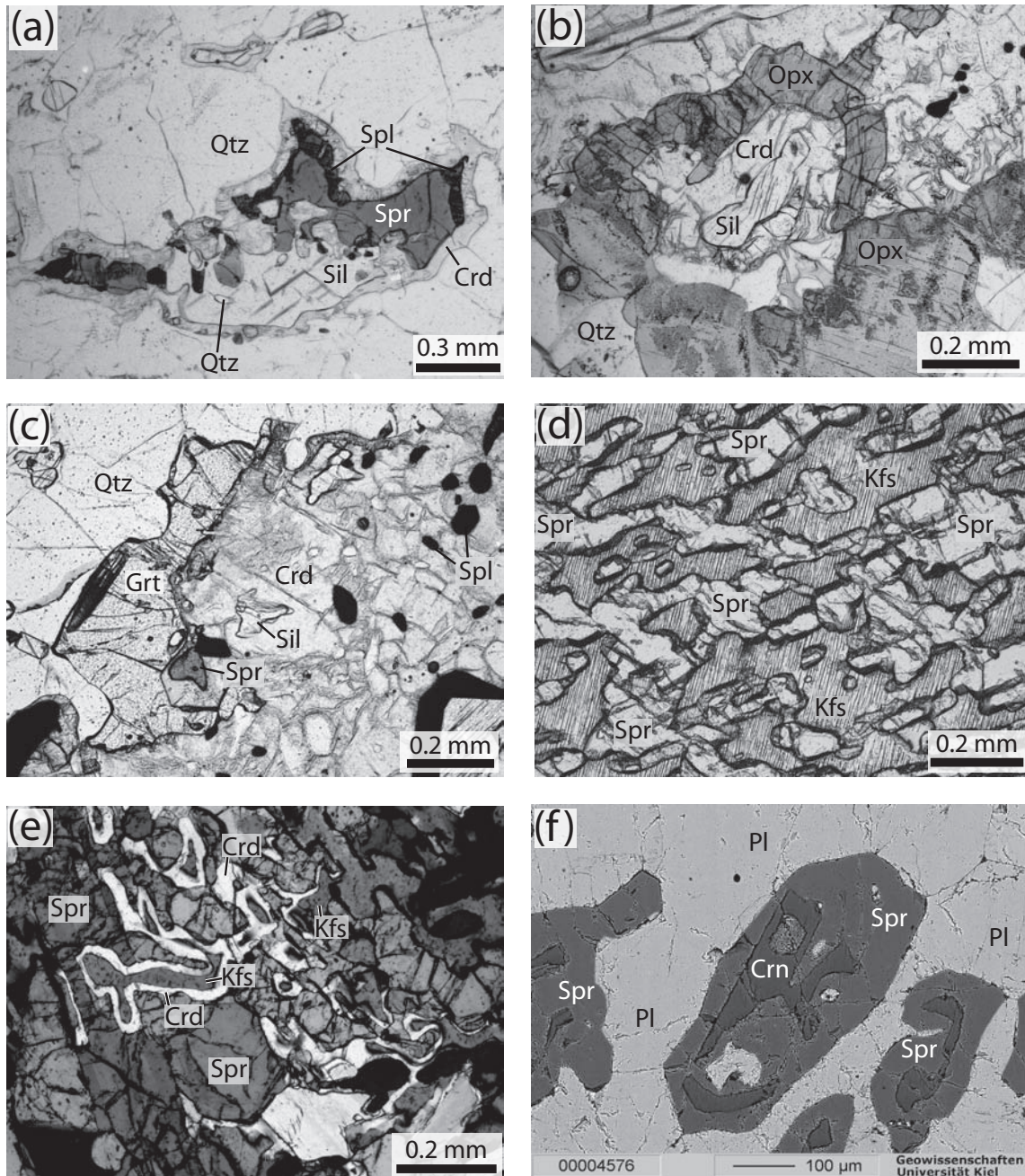


Figure 4.7: Thin section photographs showing microtextures in metapelitic rocks. (a) Breakdown of formerly coexisting sapphirine + quartz to form hercynitic spinel, sillimanite and cordierite (plane polarised light; assemblage 3, Md81-1-04). (b) Peak-metamorphic orthopyroxene and sillimanite are separated by late-stage cordierite (plane polarised light; assemblage 3, Md81-1-04). (c) Garnet, sapphirine and sillimanite break down to form cordierite (pinitised) and spinel (plane polarised light; assemblage 4, Md81-1-04). (d) Symplectite consisting of perthitic alkali-feldspar and sapphirine (plane polarised light; assemblage 7, Md66-4-04). (e) Intergrowth of sapphirine and alkali-feldspar, separated by narrow rims of cordierite (cross polarised light; assemblage 7, Md66-8-04). (f) Sapphirine in a plagioclase matrix surrounds tiny relics of corundum (backscattered electron image; assemblage 8, Md103-2-04).

Table 4.7: Representative electron microprobe analyses of biotite from metapelitic samples.

Sample No.	43-2	73-3	66-7	103-2	89-8	103-1	89-1	39-2	91-2	109-1	119-5
Asbl.*	[1] ^{mp}	[2] ^{mp}	[7] ^{mp}	[7] ^{mp}	[8] ^{mp}	[8] ^{mp}	[9] ^{mp}	[11] ^{mp}	[11] ^{mp}	[11] ^{mp}	[11] ^{mp}
SiO ₂	38.12	38.55	40.07	39.92	40.13	39.87	39.41	36.30	38.63	35.91	35.00
TiO ₂	5.34	5.21	3.50	1.21	4.91	0.79	4.54	4.47	3.44	6.51	4.80
Al ₂ O ₃	13.21	13.79	14.26	16.66	13.11	17.28	13.43	16.03	14.76	15.48	15.95
Cr ₂ O ₃	n.d.	0.00	0.00	0.00	0.00	0.00	0.00	0.00	0.00	0.00	0.00
FeO	13.31	12.68	1.73	2.07	6.80	1.23	9.79	15.42	10.27	18.01	19.69
MgO	15.28	14.88	23.85	23.88	20.10	24.73	18.40	13.50	17.34	10.46	9.89
MnO	0.10	0.08	0.00	0.00	0.00	0.06	0.08	0.04	0.11	0.06	0.05
Na ₂ O	0.11	0.12	0.34	0.18	0.23	0.21	0.06	0.13	0.13	0.09	0.09
K ₂ O	10.07	10.30	10.87	10.79	10.41	10.73	10.28	9.85	10.41	9.89	9.91
Total	95.54	95.61	94.62	94.71	95.69	94.91	95.99	95.74	95.09	96.41	95.38
Si	5.661	5.698	5.693	5.648	5.758	5.605	5.715	5.428	5.672	5.407	5.382
Ti	0.596	0.579	0.374	0.129	0.530	0.084	0.495	0.503	0.380	0.738	0.555
Al	2.312	2.402	2.387	2.778	2.217	2.864	2.297	2.826	2.555	2.748	2.890
Cr	n.d.	0.000	0.000	0.000	0.000	0.000	0.000	0.000	0.000	0.000	0.000
Fe ²⁺	1.654	1.567	0.206	0.244	0.816	0.145	1.187	1.928	1.261	2.268	2.532
Mg	3.382	3.278	5.049	5.037	4.298	5.182	3.978	3.008	3.796	2.349	2.267
Mn	0.012	0.010	0.000	0.000	0.000	0.007	0.009	0.005	0.013	0.007	0.006
Na	0.033	0.034	0.093	0.049	0.064	0.058	0.017	0.038	0.038	0.027	0.028
K	1.908	1.943	1.970	1.947	1.906	1.924	1.903	1.879	1.949	1.901	1.944
Total	15.558	15.511	15.772	15.831	15.589	15.869	15.602	15.615	15.664	15.445	15.604
X _{Mg}	0.67	0.68	0.96	0.95	0.84	0.97	0.77	0.61	0.75	0.51	0.47

* Assemblage number corresponds to Table 4.3 for metapelitic (*mp*) samples

Cations calculated on the basis of 22 oxygens

Sapphirine is rich in magnesium ($X_{Mg} = 0.72\text{--}0.74$; Table 4.9) and ca. 25–30 % of the iron contained is trivalent (calculated assuming stoichiometry). Its composition is near the 7:9:3 ([Mg,Fe]O:[Al,Fe]₂O₃:SiO₂) end-member, but slightly poorer in alumina (Fig. 4.6b). Peak-metamorphic orthopyroxene is characterised as En_{64–66}Fs_{34–36} and contains up to 9.4 wt.% Al₂O₃ (Fig. 4.3a; Table 4.5). Grains of mesoperthitic feldspar have reintegrated compositions of An_{8–11}Ab_{45–49}Or_{42–45}. Late-stage cordierite has an X_{Mg} of 0.85–0.87 (Table 4.6) and spinel of 0.3–0.4 (Table 4.8).

Assemblage 4. These rocks are similar to assemblage 3 metapelites, but contain additional garnet, leading to the peak assemblages sapphirine + garnet + quartz and orthopyroxene + sillimanite + quartz. Reactions are the same as in assemblage 3 (cf. reactions 4.7, 4.8, 4.9, and 4.4). In addition, relics of garnet, sapphirine, and sillimanite are found

Table 4.8: Representative analyses of spinel from metapelitic samples of southern Madagascar.

Sample	43-2	69-2	68-1	73-3	77-2	81-1	79-9	66-3	66-13	91-2	101-4
No.	Spl269	Spl65	Spl17	Spl27	Spl425	Spl427	Spl389	Spl77	Spl48	Spl30	Spl162
Asbl.*	[1] ^{mp}	[1] ^{mp}	[2] ^{mp}	[2] ^{mp}	[3] ^{mp}	[4] ^{mp}	[6] ^{mp}	[7] ^{mp}	[7] ^{mp}	[11] ^{mp}	[11] ^{mp}
SiO ₂	0.04	0.05	0.00	0.01	n.d.	n.d.	0.39	0.04	0.04	0.05	0.01
TiO ₂	0.04	0.00	0.04	0.01	0.00	0.00	0.00	0.01	0.04	0.01	0.03
Al ₂ O ₃	58.60	58.96	56.50	58.19	59.66	61.20	60.37	69.67	69.03	57.79	56.93
Cr ₂ O ₃	0.47	0.21	0.17	0.50	0.16	0.23	0.30	0.00	0.01	0.26	0.05
FeO	31.87	27.59	30.93	27.28	30.12	24.55	25.62	4.88	4.62	28.87	31.48
Fe ₂ O ₃	2.57	4.07	5.79	4.36	2.20	2.37	1.50	0.30	0.79	4.71	5.09
MgO	5.86	8.52	6.19	8.28	6.78	10.46	8.86	24.86	24.90	7.59	5.84
MnO	0.12	0.63	0.59	0.83	0.89	1.09	0.81	0.00	0.04	0.51	0.26
CaO	0.00	0.02	n.d.	0.01	n.d.	n.d.	0.00	0.01	0.00	0.00	0.00
ZnO	0.44	0.18	n.d.	0.41	n.d.	n.d.	2.34	0.15	0.14	0.21	0.40
Total	100.01	100.21	100.20	99.89	99.81	99.91	100.19	99.92	99.62	100.00	100.08
Si	0.001	0.001	0.000	0.000	n.d.	n.d.	0.011	0.001	0.001	0.001	0.000
Ti	0.001	0.000	0.001	0.000	0.000	0.000	0.000	0.000	0.001	0.000	0.001
Al	1.932	1.909	1.872	1.897	1.951	1.947	1.941	1.992	1.982	1.893	1.889
Cr	0.010	0.005	0.004	0.011	0.004	0.005	0.006	0.000	0.000	0.006	0.001
Fe ²⁺	0.745	0.634	0.727	0.631	0.699	0.554	0.585	0.099	0.094	0.671	0.741
Fe ³⁺	0.054	0.084	0.122	0.091	0.046	0.048	0.031	0.005	0.014	0.098	0.108
Mg	0.244	0.349	0.259	0.341	0.280	0.421	0.360	0.899	0.904	0.314	0.245
Mn	0.003	0.015	0.014	0.019	0.021	0.025	0.019	0.000	0.001	0.012	0.006
Ca	0.000	0.000	n.d.	0.000	n.d.	n.d.	0.000	0.000	0.000	0.000	0.000
Zn	0.009	0.004	n.d.	0.008	n.d.	n.d.	0.047	0.003	0.003	0.004	0.008
Total	3.000	3.000	3.000	3.000	3.000	3.000	3.000	3.000	3.000	3.000	3.000
X _{Mg}	0.25	0.36	0.26	0.35	0.29	0.43	0.38	0.90	0.91	0.32	0.25

* Assemblage number corresponds to Table 4.3 for metapelitic (*mp*) samples

Cations calculated on the basis of 4 oxygens; Fe³⁺ calculated assuming stoichiometry

to be surrounded by cordierite and spinel (Fig. 4.7c), indicating the breakdown reaction



The composition of sapphirine is similar to that of the previously described assemblage ($X_{Mg} = 0.75\text{--}0.80$; Fig. 4.6b; Table 4.9). Garnet is rich in magnesium with a maximum X_{Mg} of 0.52 (Fig. 4.4a; Table 4.4) and can be described as $\text{Prp}_{40\text{--}46}\text{Alm}_{42\text{--}46}\text{Sps}_{10\text{--}14}\text{Grs}_{2\text{--}3}$. Orthopyroxene is unzoned in Fe-Mg with $\text{En}_{63\text{--}65}\text{Fs}_{35\text{--}37}$, but shows a strong zonation in alumina, ranging from a maximum of 9.9 wt.% Al_2O_3 in the core to just ca. 7.0 wt.% at the rim (Fig. 4.3a, b; Table 4.5). Cordierite is Mg-rich with $X_{Mg} = 0.85\text{--}0.88$ (Table 4.6); spinel has an X_{Mg} of 0.42–0.48 (Table 4.8).

Table 4.9: Representative analyses of sapphirine from pelitic samples of southern Madagascar.

Sample No.	77-2 Spr319	77-2 Spr314	81-1 Spr138	81-1 Spr119	66-7 Spr25	66-7 Spr26	103-2 Spr61	103-2 Spr65	66-8 Spr52	89-8 Spr109	103-1 Spr9
Asbl.*	[3] ^{mp}	[3] ^{mp}	[4] ^{mp}	[4] ^{mp}	[7] ^{mp}	[7] ^{mp}	[7] ^{mp}	[7] ^{mp}	[8] ^{mp}	[8] ^{mp}	[8] ^{mp}
SiO ₂	13.46	13.84	13.71	12.82	14.53	14.10	11.63	11.52	14.78	12.86	14.26
TiO ₂	0.06	0.02	0.05	0.03	0.01	0.07	0.03	0.01	0.09	0.07	0.00
Al ₂ O ₃	58.09	56.88	57.56	59.04	62.95	63.47	67.53	67.59	62.44	63.67	63.78
Cr ₂ O ₃	0.09	0.06	0.00	0.00	0.01	0.00	0.08	0.05	0.03	0.21	0.00
FeO	9.22	9.93	8.55	7.39	1.98	1.28	1.31	1.15	1.41	5.17	0.84
Fe ₂ O ₃	3.90	4.48	4.39	4.65	0.06	0.66	0.54	0.83	0.47	1.00	0.08
MgO	14.65	14.37	14.98	15.04	20.13	20.26	18.58	18.52	20.59	17.05	20.67
MnO	0.43	0.55	0.80	0.82	0.01	0.00	0.05	0.11	0.02	0.03	0.03
CaO	0.00	0.02	0.03	0.01	0.01	0.01	0.02	0.02	0.10	0.00	0.02
Na ₂ O	n.d.	n.d.	n.d.	n.d.	0.01	0.03	0.00	0.02	0.02	0.03	0.00
K ₂ O	n.d.	n.d.	n.d.	n.d.	0.01	0.00	0.01	0.00	0.02	0.00	0.00
Total	99.90	100.16	100.06	99.81	99.70	99.88	99.78	99.82	99.98	100.08	99.67
Si	1.640	1.692	1.668	1.557	1.688	1.634	1.350	1.338	1.712	1.517	1.649
Ti	0.006	0.002	0.004	0.003	0.001	0.006	0.003	0.001	0.008	0.006	0.000
Al	8.343	8.194	8.253	8.453	8.620	8.670	9.241	9.249	8.523	8.852	8.694
Cr	0.008	0.006	0.000	0.000	0.001	0.000	0.007	0.005	0.003	0.020	0.000
Fe ²⁺	0.940	1.015	0.869	0.751	0.192	0.124	0.127	0.112	0.136	0.510	0.081
Fe ³⁺	0.357	0.412	0.402	0.426	0.005	0.057	0.047	0.073	0.041	0.088	0.007
Mg	2.661	2.619	2.717	2.724	3.487	3.501	3.216	3.206	3.555	2.998	3.564
Mn	0.045	0.057	0.082	0.084	0.001	0.000	0.004	0.010	0.002	0.003	0.003
Ca	0.000	0.003	0.003	0.002	0.001	0.001	0.002	0.003	0.012	0.000	0.002
Na	n.d.	n.d.	n.d.	n.d.	0.003	0.007	0.000	0.004	0.005	0.006	0.000
K	n.d.	n.d.	n.d.	n.d.	0.001	0.000	0.001	0.000	0.002	0.000	0.000
Total	14.000	14.000	14.000	14.000	14.000	14.000	14.000	14.000	14.000	14.000	14.000
X _{Mg}	0.74	0.72	0.76	0.78	0.95	0.97	0.96	0.97	0.96	0.85	0.98

* Assemblage number corresponds to Table 4.3 for metapelitic (*mp*) samples

Cations calculated on the basis of 20 oxygens; Fe³⁺ calculated assuming stoichiometry

Assemblage 5. In rocks of assemblage 5 the occurrence of sapphirine is restricted to small inclusions in sillimanite. Quartz inclusions occur as well, pointing to sapphirine + quartz as a formerly stable assemblage, which broke down to form sillimanite (cf. reaction 4.7). Orthopyroxene is not present.

Assemblage 6. These rocks are sapphirine-free and contain the peak assemblage orthopyroxene + sillimanite + garnet + quartz. Like in assemblage 3 pelites, breakdown of

Table 4.10: Representative electron microprobe analyses of plagioclase from metapelitic and metagranitic samples of southern Madagascar.

Sample No.	38-1 P1106	38-1 P1109	89-1 P1707	89-1 P1709	91-2 P1112	91-2 P1114	109-1 P1180	109-1 P1185	119-5 P1459	119-5 P1469
Asbl.*	[5] ^{gr}	[5] ^{gr}	[9] ^{gr}	[9] ^{gr}	[11] ^{mp}	[11] ^{mp}	[11] ^{mp}	[11] ^{mp}	[11] ^{mp}	[11] ^{mp}
SiO ₂	52.74	51.07	59.21	59.39	60.41	60.66	61.20	60.85	58.40	58.34
Al ₂ O ₃	29.81	31.03	25.96	25.81	25.17	25.18	24.73	24.67	26.51	26.36
Fe ₂ O ₃	0.20	0.29	0.05	0.00	0.08	0.01	0.09	0.10	0.04	0.23
CaO	12.13	13.28	7.85	7.60	6.75	6.90	5.46	5.59	7.69	7.60
Na ₂ O	4.48	3.73	6.75	6.85	7.71	7.54	8.29	8.25	7.06	7.07
K ₂ O	0.09	0.04	0.57	0.58	0.16	0.17	0.16	0.19	0.16	0.17
BaO	0.05	0.03	0.00	0.00	0.00	0.00	0.00	0.00	0.11	0.06
Total	99.50	99.47	100.39	100.23	100.28	100.47	99.92	99.65	99.97	99.84
Si	2.400	2.332	2.636	2.646	2.682	2.686	2.716	2.711	2.611	2.612
Al	1.598	1.670	1.362	1.356	1.317	1.314	1.294	1.295	1.397	1.391
Fe ³⁺	0.007	0.010	0.002	0.000	0.003	0.000	0.003	0.003	0.001	0.008
Ca	0.591	0.650	0.374	0.363	0.321	0.328	0.260	0.267	0.368	0.365
Na	0.395	0.330	0.583	0.592	0.664	0.647	0.713	0.713	0.612	0.614
K	0.005	0.003	0.032	0.033	0.009	0.010	0.009	0.011	0.009	0.010
Ba	0.001	0.001	0.000	0.000	0.000	0.000	0.000	0.000	0.002	0.001
Total	4.997	4.995	4.989	4.990	4.996	4.985	4.997	5.002	5.000	5.001
X _{An}	0.60	0.66	0.38	0.37	0.32	0.33	0.26	0.27	0.37	0.37
X _{Ab}	0.40	0.34	0.59	0.60	0.67	0.66	0.73	0.72	0.62	0.62
X _{Or}	0.01	0.00	0.03	0.03	0.01	0.01	0.01	0.01	0.01	0.01

* Assemblage number corresponds to Table 4.1 for metagranitic (*gr*) and to Table 4.3 for metapelitic (*mp*) samples

Cations calculated on the basis of 8 oxygens; all iron calculated as Fe³⁺

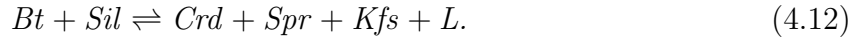
orthopyroxene + sillimanite + quartz led to a late-stage assemblage of spinel + quartz + cordierite (reactions 4.8 and 4.9). Also garnet broke down to form cordierite via the reaction



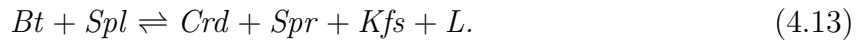
Garnet is chemically characterised as Prp_{33–39}Alm_{48–53}Sps_{10–14}Grs_{2–3} (Table 4.4). The coexisting orthopyroxene has an En-content of 62–64 % and contains 6.7–8.8 wt.% Al₂O₃ (Fig. 4.3a). Spinel (X_{Mg} ≈ 0.37; Table 4.8) contains exsolution lamellae of magnetite. Cordierite is Mg-rich (X_{Mg} = 0.83–0.87; Table 4.6).

Assemblage 7. The SiO₂-undersaturated pelites contain different types of symplectites, consisting either of cordierite + sapphirine or alkali-feldspar + sapphirine (Fig. 4.7d). Additionally, a combination of both has been found, where sapphirine is separated from alkali-feldspar by a narrow rim of cordierite (Fig. 4.7e). Similar symplectites have often been

described from silica-undersaturated pelites (Kelsey *et al.*, 2005, and references therein) and are also found in the Bemarivo Belt of northern Madagascar (Jöns *et al.*, 2006). They can be ascribed to the reaction



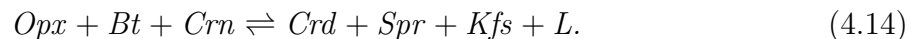
Although we did not find sillimanite in our samples, it has been reported to occur occasionally as a relic (Razakamanana, 1990; Razakamanana *et al.*, 2006). In a few cases, pale-green spinel porphyroblasts are surrounded by pale-purple sapphirine. We interpret this texture as a result of the reaction



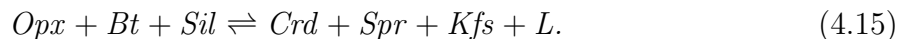
Magnesium-rich purple sapphirine is also occasionally reported from other SiO₂-undersaturated metapelites (e. g., Harley, 1993; Langer *et al.*, 1994). In plagioclase-rich samples, sapphirine grains contain tiny inclusions of corundum, indicating that corundum is another possible reactant for the sapphirine formation. All textures described are interpreted to develop during a down-pressure evolution (Kelsey *et al.*, 2005, and references therein).

The SiO₂-undersaturated rocks are rich in magnesium. The X_{Mg} of sapphirine (Fig. 4.6b; Table 4.9) is in the range of 0.95–0.97. Also biotite is nearly a pure Mg end-member (X_{Mg} = 0.95–0.97; Table 4.7) with TiO₂ contents ranging from 0.4–4.2 wt.% (Fig. 4.6a). Cordierite (X_{Mg} ≈ 0.97; Table 4.6) is often strongly pinitised. Spinel has an X_{Mg} of ca. 0.9 with low contents of ZnO (0.1–0.2 wt.%; Table 4.8). Alkalifeldspar is An_{1–11}Ab_{25–55}Or_{40–70}; plagioclase in the corundum-bearing sample is anorthite-rich (An₉₀Ab₁₀).

Assemblage 8. Pelites of assemblage 8 are also SiO₂-undersaturated, but contain orthopyroxene and are spinel-free. As in assemblage 7, sapphirine-cordierite symplectites are present. Corundum is occasionally found within these symplectites, where it is rimmed by sapphirine (Fig. 4.7f). From textural observations we interpret that orthopyroxene + biotite break down:



Our orthopyroxene-bearing samples do not contain any sillimanite, however, like in assemblage 7 it has to be considered that orthopyroxene + sillimanite was once stable, but that sillimanite is now completely replaced by the reaction



The mineral chemistry of assemblage 8 is similar to the orthopyroxene-free silica-undersaturated rocks of assemblage 7. Sapphirine (X_{Mg} = 0.94–0.99; Fig. 4.6a; Table 4.9), cordierite (X_{Mg} = 0.96–0.99; Table 4.6), biotite (X_{Mg} = 0.95–0.98; Fig. 4.6b; Table 4.7), and orthopyroxene (X_{Mg} = 0.93–0.97; Fig. 4.3a; Table 4.5) are Mg-rich. Rutile is always present. There are regional differences in the maximum Al₂O₃ content of orthopyroxene

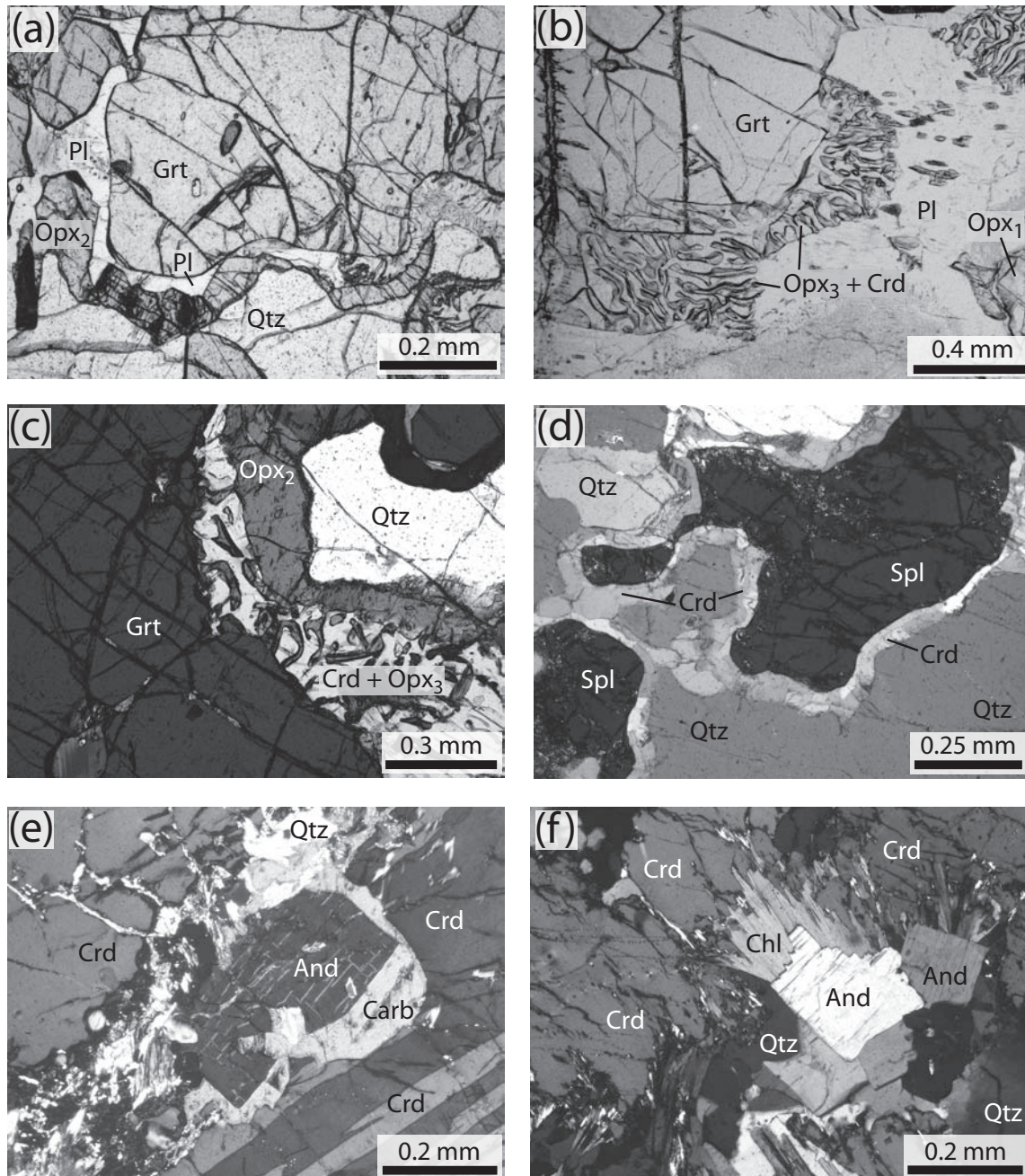


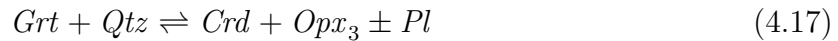
Figure 4.8: Thin section photographs showing microtextures in metapelitic rocks. (a) Garnet surrounded by a corona of plagioclase and orthopyroxene (plane polarised light; assemblage 9, Md89-3-04). (b) Garnet breakdown and formation of symplectites consisting of orthopyroxene and cordierite (plane polarised light; assemblage 9, Md89-3-04). (c) Garnet surrounded by cordierite-orthopyroxene intergrowths and a massive orthopyroxene rim (cross polarised light; assemblage 9, Md89-3-04). (d) Spinel and quartz react to form a narrow corona of cordierite (cross polarised light; assemblage 11, Md43-1-04). (e) Late-stage breakdown of cordierite and formation of andalusite, quartz, and Mg-Fe carbonate (cross polarised light; assemblage 15, Md119-9-04). (f) Formation of andalusite, chlorite and quartz, resulting from late-stage breakdown of cordierite (cross polarised light; assemblage 15, Md121-1-04).

(7.8 wt.% at Ankeniheny/ Tranomaro; 5.9 wt.% at Vohidava/ Ianabinda; Fig. 4.2) and in the maximum TiO₂ content of biotite (Ankeniheny: 4.4 wt.%; Vohidava: 1.6 wt.%). An exceptional case are rocks from the Ampandrandava mine (near Beraketa; Fig. 4.2), where SiO₂-undersaturated metapelites (sample Md89-8-04) occur as centimetre-sized layers within garnet-orthopyroxene-cordierite-bearing pelites. All mineral phases have slightly lower X_{Mg} ratios (orthopyroxene: 0.78–0.79; sapphirine: 0.85–0.86; biotite: 0.84–0.85; cordierite: ≈ 0.9; Tables 4.5–4.7 and 4.9) in this sample. Biotite contains up to 5.0 wt.% TiO₂, coexisting with rutile; orthopyroxene is aluminous with a maximum Al₂O₃ content of 6.6 wt.%.

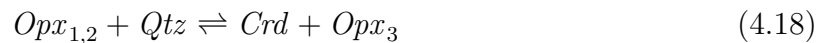
Assemblage 9. Garnet + orthopyroxene₁ + plagioclase is the peak assemblage in pelites found in the vicinity of the Ampandrandava mine (near Beraketa; Fig. 4.2). Rocks from this mine were examined and described by many previous workers (e. g., Joo', 1968; Pierdzig, 1992; Markl *et al.*, 2000), but mostly with the focus on phlogopite mineralisation. However, the 'normal' metapelites do also comprise important information about the pressure-temperature evolution. Garnet porphyroblasts are surrounded by a double corona of plagioclase at the garnet and orthopyroxene₂ towards matrix quartz (Fig. 4.8a). This may have formed due to the reaction



Locally there are symplectitic intergrowths of cordierite + orthopyroxene₃ ± plagioclase (Fig. 4.8b, c) that form between garnet and the orthopyroxene₂ moats via the reaction



These two reactions may also have taken place in a continuous process, beginning with growth of the coarse Al-rich orthopyroxene₂ rims, continuing during cooling with less aluminous orthopyroxene of the symplectites. However, locally it seems that the thick corona of orthopyroxene₂ as well as orthopyroxene₁ porphyroblasts break down to form the described symplectites (Fig. 4.8c), presumably developed through the reaction



Garnet porphyroblasts are chemically characterised as Prp_{46–50}Alm_{46–49}Grs_{3–4} (Table 4.4). The coexisting orthopyroxene has an X_{En} of 0.68–0.70 and maximum Al₂O₃ contents of 8.9 wt.% (Fig. 4.3a; Table 4.5). Late-stage pyroxene contained in the symplectites is less aluminous (Al₂O₃ = 5.0–6.6 wt.%; X_{En} = 0.68–0.70). Biotite contains high amounts of TiO₂ (up to 6 wt.%; X_{Mg} = 0.70–0.73; Fig. 4.6a; Table 4.7). Plagioclase porphyroblasts are An₃₆Ab_{56–61}Or_{2–4}, whereas plagioclase forming rims around garnet is more Ca-rich (X_{An} = 0.50–0.54). Cordierite is Mg-rich (X_{Mg} = 0.86–0.88; Table 4.6).

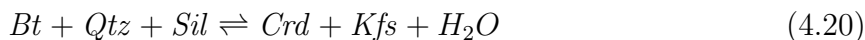
Assemblage 10. Samples with mineral assemblage 10 are very similar to assemblage 9 metapelites, but they do not contain garnet, quartz, and feldspar. They just consist of

orthopyroxene porphyroblasts ($X_{Mg} \approx 0.8$) in a cordierite matrix ($X_{Mg} \approx 0.9$). Biotite occurs, which is obviously derived from late-stage breakdown of orthopyroxene. In some respects, these rocks are comparable to SiO_2 -undersaturated samples of assemblage 8, but sapphirine is missing here.

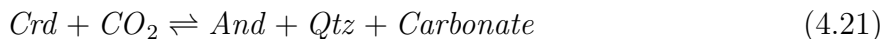
Assemblages 11 to 16. Rocks containing assemblages 11 to 16 (Table 4.3) are the most common metapelites in the area between Beraketa and Ihosy (Fig. 4.2). They typically contain spinel, quartz, garnet, sillimanite, cordierite, biotite, alkali-feldspar, and plagioclase (assemblage 11), however, some of these minerals may be missing (assemblages 12–16). A common feature is the formation of cordierite, which is found to form coronas around spinel, resulting from breakdown of spinel + quartz (cf. reaction 4.4; Fig. 4.8d). Cordierite is not found as an inclusion in garnet, but replaces garnet at the rims, most likely due to the reaction



The formation of cordierite may not be restricted to the late-stage metamorphic evolution. In many samples, it occurs as large hypidiomorphic crystals, which seem to have coexisted with peak-metamorphic garnet, sillimanite, and biotite. Cordierite is also found in leucosomes, where it may have formed by dehydration melting of biotite:



Furthermore, in some samples cordierite is partially replaced by late-stage idiomorphic andalusite, quartz, and Mg-Fe carbonate (Fig. 4.8e) or chlorite (Fig. 4.8f), a phenomenon that has also been reported from other high-grade metamorphic terranes, such as Calabria (Schenk, 1989, 1990) and Sri Lanka (Raase & Schenk, 1994; Ellis & Hiroi, 1997). This observation can be ascribed to the carbonatisation/hydration reactions



The finding that both reactions take place, points to variations in water fugacity within the examined samples. Biotite is also partially replaced by Mg-Fe carbonate and muscovite.

The frequent occurrence of metapelites featuring assemblage 11 allows for determining regional changes in mineral chemistry. We observe that garnet, biotite, and spinel are magnesium-rich in the southern part of the study area and become more iron-rich towards the Ranotsara SZ in the north (Fig. 4.4b).

4.5.4 Calcsilicates

Rock types

Calcsilicate rocks are common rocks found in the Androyan group. They occur as concordant layers of variable thickness (centimeters to several meters) within metapelites and marbles. Their appearance is diverse, ranging from extremely fine-grained to coarse-grained,

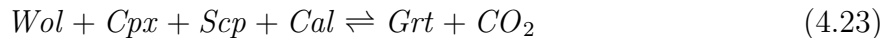
Table 4.11: Mineral assemblages found in calcsilicates of southern Madagascar. Bracketed minerals are late-stage formations.

1	Pl	Qtz	Grt/(Grt)	Cpx	Scap	Wol	—	—	—
2	—	—	Grt	Cpx	Scap	—	Carb	Amph	—
3	± Pl/(Pl)	(Qtz)	(Grt)	Cpx	Scap	Wol	± Carb/(Carb)	—	—
4	(Pl)	(± Qtz)	-	Cpx	Scap	Wol	(± Carb)	—	—
5	Pl	—	—	—	Scap	Wol	(± Carb)	(± Amph)	—
6	Pl	—	—	Cpx	Scap	—	± Carb	± Amph	± Bt
7	—	—	—	Cpx	Scap	—	± Carb	(± Amph)	—

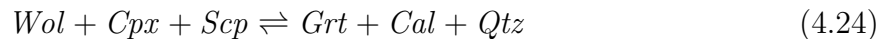
and from dark ‘metabasite-like’ to light greenish in colour. This variability is a result of the differences in proportions of the constituent mineral phases, but is mostly independent from mineral assemblages.

Mineral assemblages and reaction textures

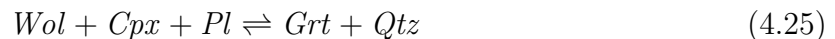
Seven different mineral assemblages have been identified in calcsilicate rocks from southern Madagascar (Table 4.11). Scapolite and clinopyroxene are the most common minerals that are contained in nearly all examined samples. A few assemblages contain garnet that forms porphyroblasts (assemblages 1 and 2 in Table 4.11) and/or narrow coronas around wollastonite, scapolite, and clinopyroxene (Fig. 4.9a; assemblages 1 and 3 in Table 4.11). These are interpreted to result from the reaction



In a few samples, calcite and quartz are formed together with the garnet coronas, related to the reaction



Locally, garnet is also found to form rims around plagioclase. This can be explained by two possible reactions:



Occasionally, scapolite is replaced by a symplectite consisting of plagioclase and calcite (Fig. 4.9b):



Both, the breakdown of scapolite and the aforementioned garnet-forming reactions are interpreted to develop in response to cooling of the rocks. Similar textures have also been reported from other high-grade terranes (e. g., Schenk, 1984; Warren *et al.*, 1987; Fitzsimons & Harley, 1994).

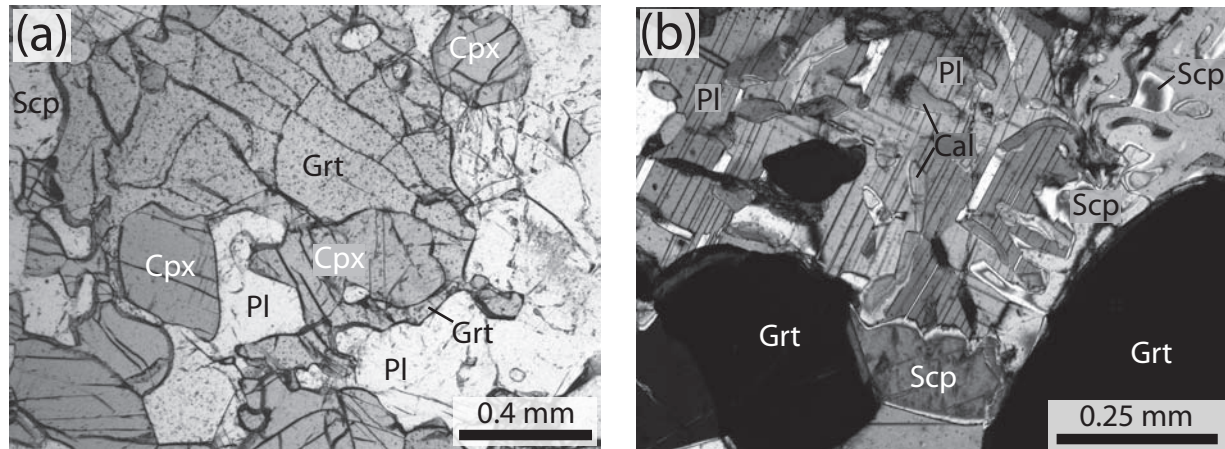


Figure 4.9: Microtextures in calcsilicates. (a) Garnet growing between clinopyroxene and plagioclase (plane polarised light; Md130-1-04). (b) Plagioclase-calcite symplectite replacing earlier scapolite (cross polarised light; Md38-4-04).

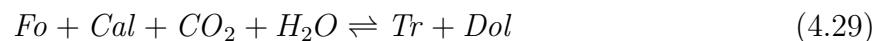
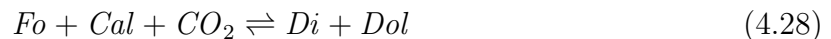
4.5.5 Marbles

Rock types

Marbles occur frequently in the Androyan group. They form decimetre- to metre-sized layers or lenses interstratified with metapelites and calcsilicate rocks. They are medium- to coarse grained and contain variable amounts of non-carbonate minerals.

Mineral assemblages and reaction textures

Five mineral assemblages have been found, which are listed in Table 4.12. Marbles containing the peak assemblage forsterite–calcite are common. Forsterite is partially serpentinised and may show reaction rims consisting of diopside and/or tremolite. This can be explained by the reactions



These reactions reflect retrograde cooling of the rocks to temperatures below 700°C. In many cases, dolomite seems to be a late-stage phase, formed as a result of the aforementioned reactions or as an exsolution from primary Mg-bearing calcite.

4.5.6 Anorthosites

Rock types and reaction textures

Anorthosites form four huge massifs (named Ankafotra, Saririaky, Manambahy and Volovolo) within the Graphite group (Fig. 4.2b). Their occurrence is bound to the N–S trending Ampanihy shear zone. The structural context, petrology, and geochemistry of these

Table 4.12: Mineral assemblages found in marbles of southern Madagascar. Bracketed minerals are late-stage formations.

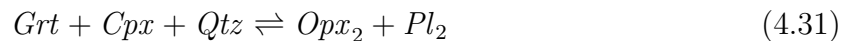
1	Spl	Carb	Fo	—	—	(± Cpx)	(± Tr)
2	—	Carb	Fo	± Phl	—	(Cpx)	(± Tr)
3	Spl	Carb	—	± Phl	± Chu	(± Cpx)	—
4	—	Carb	—	Phl	—	—	(Tr)
5	—	Carb	—	—	—	—	—

common accessories: apatite, graphite, scapolite

anorthosites has been described by e. g., Ashwal *et al.* (1998). We have sampled the northernmost massif (Ankafotra). The uniform rock matrix consists of cm-sized plagioclase crystals. Locally there is large orthopyroxene, which is surrounded by an inner corona of clinopyroxene and an outer corona of garnet (Fig. 4.10). The latter contains elongate inclusions of quartz, indicating the mineral reaction



This reaction marks the transition from the intermediate-pressure to high-pressure granulite facies and may have occurred during cooling after magmatic emplacement. We observe, however, that secondary orthopyroxene and plagioclase form between the garnet and clinopyroxene rims (Fig. 4.10), pointing to a reversal of the reaction during later decompression:



Ortho- and clinopyroxene get furthermore partially replaced by late-stage biotite.

Mineral chemistry

Plagioclase of the rock matrix has a composition of $X_{An} = 0.50\text{--}0.53$, $X_{Ab} = 0.47\text{--}0.50$, and $X_{Or} = 0.02$. Towards the rims, slightly lower An-contents are found (ca. 0.48). Secondary plagioclase, formed from breakdown of garnet-clinopyroxene coronas, is of similar composition, but close to the garnet, the An-content may increase to $X_{An} \approx 0.88$. Orthopyroxene porphyroblasts (Opx_1) are characterised as $En_{58\text{--}60}Fs_{39\text{--}41}Wo_1$ with Al_2O_3 ranging from 1.25 to 1.9 wt.%. Late-stage orthopyroxene (Opx_2) may be slightly more magnesian ($X_{En} \approx 0.60\text{--}0.62$) and less aluminous ($Al_2O_3 \approx 1.0\text{--}1.2$ wt.%). Garnet coronas have a composition of $X_{Prp} = 0.22\text{--}0.27$, $X_{Alm} = 0.53\text{--}0.57$, $X_{Sps} = 0.02\text{--}0.03$, and $X_{Grs} = 0.17\text{--}0.19$ and clinopyroxene is $En_{38\text{--}39}Fs_{14\text{--}15}Wo_{46\text{--}48}$. The late-stage biotite is characterised by an X_{Mg} of ca. 0.65 and a TiO_2 content ranging from 3.7 to 3.8 wt.%.

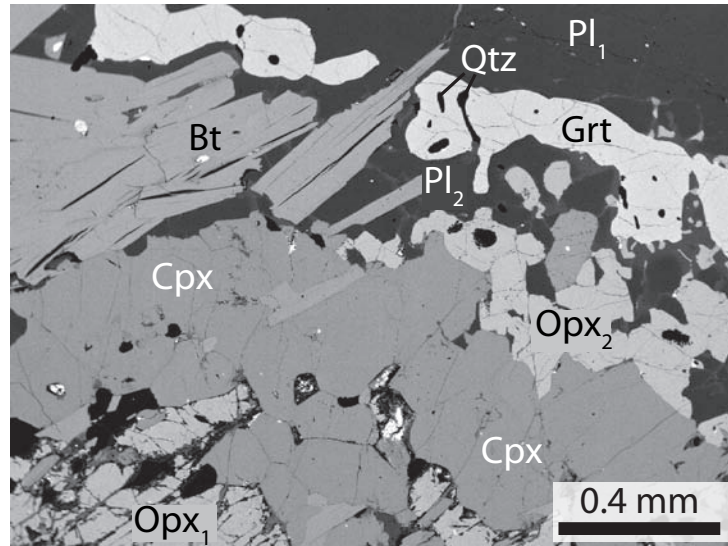


Figure 4.10: Microtexture observed in anorthosite, showing the breakdown of primary orthopyroxene₁ and plagioclase₁ to form garnet, clinopyroxene, and quartz. The subsequent back reaction produced secondary orthopyroxene₂ and plagioclase₂ (backscattered-electron image; Md21-9-04).

4.6 Thermobarometric estimates and $P-T$ evolution

4.6.1 Qualitative estimates from reaction textures

The $P-T$ evolution of rocks from southern Madagascar can be qualitatively deduced from observations of reaction textures. As a result of the high-grade character of metamorphism, generally, no relics related to the prograde $P-T$ paths are found. The assemblages sapphirine + quartz, orthopyroxene + sillimanite + quartz, and osumilite + garnet point to ultrahigh-temperature (UHT) conditions during peak-metamorphism (e.g., Harley, 1989; Carrington & Harley, 1995; Kelsey *et al.*, 2003). This is confirmed by high alumina contents of metapelitic orthopyroxene (ca. 8–10 wt.% Al_2O_3) and the frequent occurrence of mesoperthitic feldspar in metapelitic rocks. However, these UHT assemblages are restricted to the southernmost part of the Androyan group (Fig. 4.2) and the variability observed in the chemistry of coexisting garnet and biotite (assemblage 11 metapelites; Fig. 4.4b) also points to a systematic regional change in temperature, with highest temperatures in the southern Androyan group and lower temperatures towards the north. The assemblage spinel + quartz, another indicator for high-temperature metamorphic conditions, is found throughout the Androyan group, but is missing in the Graphite group and Vohibory group, indicating that these units experienced lower-grade metamorphism. Spinel + quartz assemblages are also absent in metapelites found north of the Ranotsara shear zone, indicating that this shear zone separates units of distinct metamorphic character (unlike the observations of Markl *et al.*, 2000).

The peak of metamorphism was followed by decompression of the rocks, which is evidenced by the breakdown of garnet to cordierite-orthopyroxene symplectites (Fig. 4.8b, c) and the formation of sapphirine-cordierite symplectites in SiO_2 -undersaturated rocks (Fig. 4.7e). Also the frequent occurrence of late-stage cordierite and formation of cordierite-

Table 4.13: Reintegrated feldspar compositions as well as compositions and proportions of hosts and exsolution lamellae from metapelites and a granitic gneiss.

Sample	Rock type*	Vol.%	Pl composition	Vol.%	Kfs composition	integrated composition
Md39-2-04	metapelite [11]	54.02	An _{11.0} Ab _{88.4} Or _{0.6}	45.98	An _{0.2} Ab _{10.4} Or _{89.4}	An _{6.07} Ab _{52.82} Or _{41.11}
		55.05	An _{12.8} Ab _{85.5} Or _{1.7}	44.95	An _{0.4} Ab _{15.3} Or _{84.3}	An _{7.26} Ab _{54.12} Or _{38.62}
Md43-2-04	metapelite [1]	69.47	An _{25.0} Ab _{74.2} Or _{0.9}	30.53	An _{5.4} Ab _{28.6} Or _{66.0}	An _{18.98} Ab _{60.19} Or _{20.82}
		75.51	An _{19.8} Ab _{65.4} Or _{14.8}	24.49	An _{2.8} Ab _{29.5} Or _{67.7}	An _{15.6} Ab _{56.54} Or _{27.86}
Md55-1-04	granit. gneiss [4]	52.26	An _{23.8} Ab _{75.5} Or _{0.8}	47.74	An _{1.3} Ab _{25.5} Or _{73.2}	An _{13.04} Ab _{51.58} Or _{35.38}
		55.50	An _{23.7} Ab _{75.6} Or _{0.7}	44.50	An _{2.0} Ab _{24.0} Or _{74.0}	An _{14.04} Ab _{52.62} Or _{33.34}
Md68-1-04	metapelite [2]	29.61	An _{23.1} Ab _{75.9} Or _{1.1}	70.39	An _{1.7} Ab _{28.5} Or _{69.8}	An _{8.02} Ab _{42.49} Or _{49.49}
		31.24	An _{24.6} Ab _{74.5} Or _{0.9}	68.76	An _{1.4} Ab _{24.0} Or _{74.7}	An _{8.63} Ab _{39.73} Or _{51.64}
		74.44	An _{24.5} Ab _{74.7} Or _{0.8}	25.56	An _{0.3} Ab _{9.6} Or _{90.2}	An _{18.34} Ab _{58.13} Or _{23.53}
Md73-3-04	metapelite [2]	62.24	An _{23.8} Ab _{75.5} Or _{0.7}	37.76	An _{0.4} Ab _{11.9} Or _{87.7}	An _{15.00} Ab _{51.57} Or _{33.43}
		59.71	An _{23.0} Ab _{76.3} Or _{0.7}	40.29	An _{0.1} Ab _{6.6} Or _{93.3}	An _{13.83} Ab _{48.83} Or _{37.80}
Md77-2-04	metapelite [3]	37.66	An _{21.7} Ab _{76.9} Or _{1.4}	62.34	An _{1.0} Ab _{31.9} Or _{67.1}	An _{8.77} Ab _{48.80} Or _{42.43}
		51.03	An _{18.7} Ab _{80.3} Or _{1.1}	48.97	An _{0.3} Ab _{12.2} Or _{87.6}	An _{9.72} Ab _{47.05} Or _{43.23}
		50.06	An _{20.7} Ab _{78.6} Or _{0.8}	49.94	An _{0.3} Ab _{11.5} Or _{88.2}	An _{10.55} Ab _{45.20} Or _{44.25}
Md78-1-04	metapelite [12]	55.41	An _{15.2} Ab _{81.7} Or _{3.1}	44.59	An _{1.5} Ab _{18.3} Or _{80.2}	An _{9.11} Ab _{53.52} Or _{37.37}
Md79-9-04	metapelite [6]	51.80	An _{19.8} Ab _{74.7} Or _{5.4}	48.20	An _{0.3} Ab _{8.9} Or _{90.9}	An _{10.44} Ab _{43.11} Or _{46.46}

* bracketed number corresponds to assemblage number in Tables 4.1 and 4.3

bearing leucosomes is in accordance with a decompression. This decompression may be described as near-isothermal, but slight cooling is evidenced by lower alumina contents in late-stage orthopyroxene. The breakdown of cordierite to form andalusite-bearing assemblages (Fig. 4.8e, f) evidences cooling of the rocks at pressures below that of the aluminosilicate triple point. This pressure-temperature evolution is interpreted as part of a clockwise P – T path.

4.6.2 Conventional geothermobarometry

Thermobarometric calculations were undertaken to quantify the different stages of the P – T evolution. The estimate of temperatures for UHT rocks is not straightforward, because most thermometers are based on Fe–Mg exchange between minerals, which is easily affected by re-equilibration during cooling. The omnipresent spinel has also not been included in P – T calculations, because in most cases, it contains irregular exsolution lamellae of magnetite, which cannot easily be reintegrated. Therefore, temperatures of the peak-metamorphic stage have been estimated using feldspar thermometry and alumina solubility in orthopyroxene (Al-in-Opx; Harley & Green, 1982). Mesoperthitic feldspars occur frequently in metapelitic rocks of the southern Androyan group. Their reintegrated compositions are shown in Fig. 4.11 and Table 4.13. For a pressure of 10 kbar (Fuhrmann & Lindsley, 1988), minimum temperatures of 920–1020 °C are deduced. Peak pressures have been estimated from Al-in-Opx (Harley & Green, 1982) and garnet-plagioclase-orthopyroxene-quartz equilibria. Results for the southern Androyan group are in the range of ca. 8–11 kbar (calculated at 1000 °C; Table 4.14). We also performed average P – T (Powell & Holland, 1994) calcu-

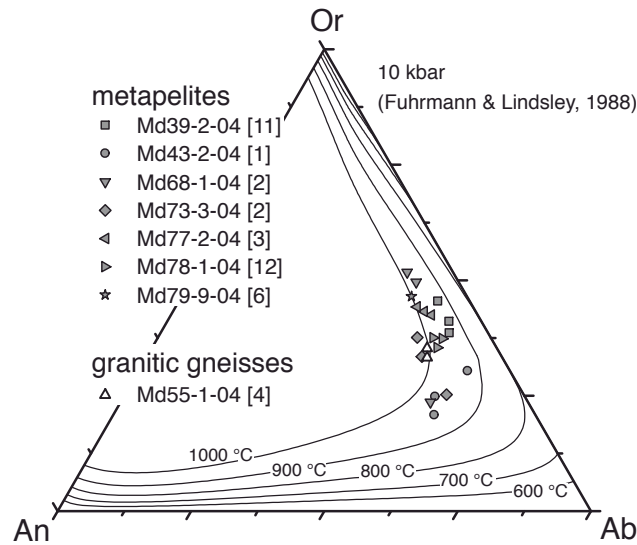


Figure 4.11: Reintegrated compositions of mesoperthitic feldspars used for thermometric estimates. Most analyses are from metapelites of the southern Androyan group (assemblage numbers correspond to Table 4.1 and 4.3). Isotherms are for 10 kbar after Fuhrmann & Lindsley (1988).

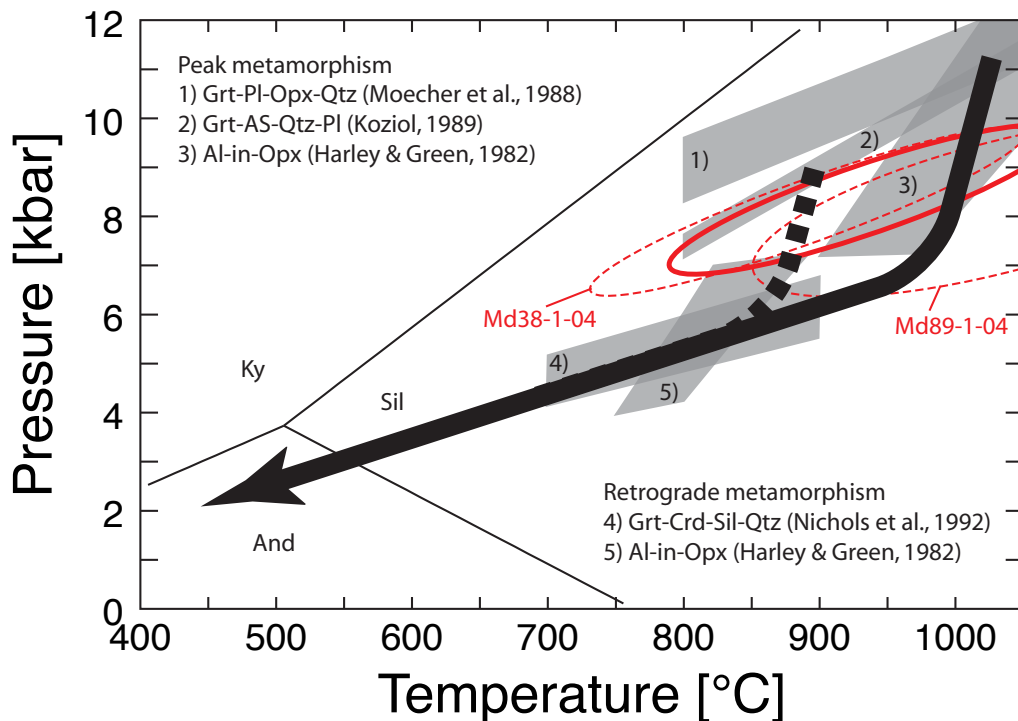


Figure 4.12: Pressure-temperature evolution of rocks from southern Madagascar. The solid P - T path is for the southern part of the Androyan group. The dashed path accounts for lower P - T conditions of the northern part. Numbers within the shaded fields correspond to different geothermobarometers (references given in the figure). Dashed ellipses are THERMOCALC average P - T estimates (1σ errors) for two samples from the southern Androyan group, the solid ellipse gives an average of both samples.

Table 4.14: Geothermobarometric results for samples from southern Madagascar.

Sample	Asbl.*	Analyses	T [†] [°C]	Grt-Pl- Opx-Qtz ¹	GASP ²	Al-in-Opx ³	Grt-Crd- Sil-Qtz ⁴
Md38-1-04	[5] ^{gr}	Grt25, Pl109, Opx114	1000	10.6	—	—	—
		Grt75, Pl106, Opx138	1000	11.0	—	—	—
Md55-1-04	[4] ^{gr}	Grt39, Opx135	1000	—	—	11.2	—
		Grt54, Opx151	1000	—	—	11.1	—
		Grt86, Opx177	1000	—	—	10.4	—
Md69-1-04	[1] ^{mp}	Grt139, Opx276	1000	—	—	8.0	—
		Grt173, Opx274	1000	—	—	9.7	—
Md79-9-04	[6] ^{mp}	Grt234, Opx253	1000	—	—	8.9	—
		Grt316, Opx291	1000	—	—	8.4	—
Md81-1-04	[4] ^{mp}	Grt295, Opx266	1000	—	—	8.1	—
		Grt349, Opx258	1000	—	—	8.4	—
Md89-1-04	[9] ^{mp}	Grt627, Opx566	1000	—	—	9.0	—
		Grt645, Opx554	1000	—	—	9.0	—
Md91-2-04	[11] ^{mp}	Grt54, Pl112	1000	—	10.8	—	—
		Grt57, Pl114	1000	—	10.6	—	—
Md109-1-04	[11] ^{mp}	Grt100, Pl180	1000	—	10.6	—	—
		Grt104, Pl185	1000	—	10.3	—	—
Md119-5-04	[11] ^{mp}	Grt357, Pl459	1000	—	10.5	—	—
		Grt358, Pl469	1000	—	10.5	—	—
Md56-1-04	[2] ^{gr}	Grt276, Opx345	800	—	—	6.0	—
		Grt278, Opx348	800	—	—	6.0	—
Md78-1-04	[12] ^{mp}	Grt252, Crd296	800	—	—	—	6.6
		Grt244, Crd295	800	—	—	—	6.8
Md89-1-04	[9] ^{mp}	Grt584, Opx777	800	—	—	4.2	—
		Grt579, Opx783	800	—	—	5.8	—
Md101-4-04	[11] ^{mp}	Grt93, Crd110	800	—	—	—	6.3
		Grt98, Crd105	800	—	—	—	6.6
Md109-1-04	[11] ^{mp}	Grt52, Crd174	800	—	—	—	6.5
		Grt47, Crd197	800	—	—	—	6.3

* Number corresponds to Table 4.1 for metagranitic/charnockitic (*gr*) and to Table 4.3 for metapelitic (*mp*) samples

† Assumed values for calculation

¹ Moecher *et al.* (1988); ² Koziol (1989); ³ Harley & Green (1982); ⁴ Nichols *et al.* (1992);

lations for two samples using the software THERMOCALC 3.25 (Holland & Powell, 1998; Powell *et al.*, 1998, dataset 5.5). The average of 936 ± 190 °C and 8.3 ± 2.0 kbar (errors are given as 2σ) is in agreement with the conventional geothermobarometry. For the northern Androyan group, peak pressure estimates are based on garnet-sillimanite-quartz-plagioclase equilibria (GASP; Koziol, 1989). Calculations for 1000 °C also yield pressures of 10–11 kbar, however, temperatures in this area are thought to be somewhat lower, which, in turn, would also lead to lower pressure estimates. Independent peak temperature estimates for this area have not been undertaken due to the lack of orthopyroxene-bearing assemblages and suitable ternary feldspars. However, the omnipresence of spinel + quartz assemblages indicates that temperatures have reached at least ca. 900 °C. P - T estimates for the cordierite-dominated retrograde stage of metamorphism are based on Al-in-Opx for Al-poor late-stage orthopyroxene (ca. 4–6 kbar for 800 °C; Table 4.14) and on garnet-cordierite-sillimanite-quartz barometry (ca. 6 kbar for 800 °C; Table 4.14; Nichols *et al.*, 1992). The P - T evolution of rocks from southern Madagascar is summarised in Fig. 4.12.

4.7 Geochronology

Geochronological techniques have been applied to constrain the timing of metamorphism. We used two different approaches: U-Th-total Pb dating of monazite and U-Pb isotopic dating of zircons. Both, monazite and zircon analyses were undertaken using high-spatial resolution techniques: EPMA for monazites and SHRIMP for zircons. Results of monazite dating are summarised in Fig. 4.13 and Table 4.15. SHRIMP zircon data are given in Fig. 4.14 and Table 4.16.

4.7.1 U-Th-total Pb dating of monazite

Md36-4-04 (S24°23'26.87"; E045°22'57.21"). This light-coloured metapelite consists of garnet, sillimanite, plagioclase, quartz, and graphite, with accessory rutile and monazite. It has been sampled between Bekily and Belindo in a strongly weathered outcrop located where the main road crosses the small river Ampanamperandrotsy. The dated monazite is ca. 30–150 μm in diameter and in backscattered electron (BSE) images it features a homogeneous core with a narrow light rim. Core analyses give an age of 650 ± 26 Ma, whereas rim analyses give 543 ± 28 Ma (Fig. 4.13a).

Md39-2-04 (S24°44'57.87"; E045°35'34.07"). The outcrop of this metapelitic sample is located at the main road (RN13), ca. 65 km south of Beraketa. It contains spinel, quartz, garnet, sillimanite, biotite, plagioclase, mesoperthitic alkali-feldspar, and late-stage coronas of cordierite around spinel. The accessory monazite crystals are xenomorphic, 50–200 μm in size, and mostly of homogeneous appearance, giving an age of 650 ± 46 Ma. A few crystals have been found that show a narrow overgrown rim. These rims exhibit a broad scatter of ThO_2^* values (11–33 wt.%), resulting in 564 ± 11 Ma (Fig. 4.13b).

Md43-5-04 (S24°59'49.99"; E046°31'53.70"). At the road RN13 between the towns of Ambovombe and Tôlaïaro, we sampled this light leptynitic gneiss. It is banded and consists of layers rich in plagioclase and K-feldspar, alternating with more garnet- and biotite-rich bands. The xenomorphic monazite is of variable size (ca. 15–200 μm), but of homogeneous appearance in BSE images. We obtained an age of 563 ± 44 Ma (Fig. 4.13c).

Md50-4-04 (S25°01'02.76"; E046°58'23.54"). The quarry 'Bezavona Sud' is located just a few kilometres north of Tôlaïaro. It consist of metapelitic leptynites of a banded appearance. The sample Md50-4-04 is a metapelitic gneiss, rich in feldspar and quartz, with minor amounts of spinel, cordierite, sillimanite, garnet, and biotite. The accessory monazite is irregularly shaped and varies in size from 20 to 600 μm . Some are homogeneous, others have overgrown rims. In rare cases, also patchy zonation patterns have been observed. Analyses give a broad scatter of apparent ages from ca. 2 Ga to 500 Ma. From the youngest rims an age of 534 ± 44 Ma was calculated (Fig. 4.13d). The older apparent ages may point to a detrital origin of monazite cores, but also an older metamorphic event cannot be completely ruled out.

Md66-10-04 (S24°36'42.04"; E046°31'19.71"). This SiO₂-undersaturated metapelite was sampled at Ankeniheny, west of Tranomaro. The sample contains biotite, orthopyroxene, K-feldspar, as well as late-stage symplectites consisting of sapphirine and cordierite. Monazite is either tiny (ca. 10–20 μm) and euhedral or larger (20–150 μm) and xenomorphic. Both types are homogeneous in BSE images. We calculated an age of 522 ± 15 Ma (Fig. 4.13e), however, a few older apparent ages were determined as well.

Md73-3-04 (S24°03'35.90"; E046°15'55.68"). The sample location is ca. 3.5 km ESE of Elonty (east of Tsivory). The outcrop consists of banded metapelites. The sample Md73-3-04 contains spinel, quartz, sillimanite, and biotite. Furthermore, cordierite–K-feldspar–quartz symplectites are present, which are interpreted as pseudomorphs after osumilite. The accessory monazite grains are relatively small (20–60 μm) and unzoned in the BSE image. They give an age of 535 ± 22 Ma (Fig. 4.13f).

Md81-1-04 (S24°19'50.18"; E045°49'59.22"). This sample is a migmatitic metapelite from an outcrop ca. 3.8 km WNW of Antevamena (north of Imanombo). It contains garnet, orthopyroxene, sillimanite, spinel, sapphirine, quartz, cordierite, and K-feldspar. The accessory monazite appears unzoned in BSE image and the age is 542 ± 13 Ma (Fig. 4.13g).

Md109-1-04 (S23°08'03.28"; E046°00'05.37"). Approximately 20 km NW of Betroka, directly at the road to Benato, banded migmatitic metapelites crop out. Sample Md109-1-04 contains spinel, garnet, sillimanite, biotite, quartz, plagioclase, K-feldspar, and cordierite. Monazite is up to 600 μm in diameter and in BSE images it shows a clear zonation with a homogeneous core and an irregularly overgrown rim. Core analyses have a relatively low

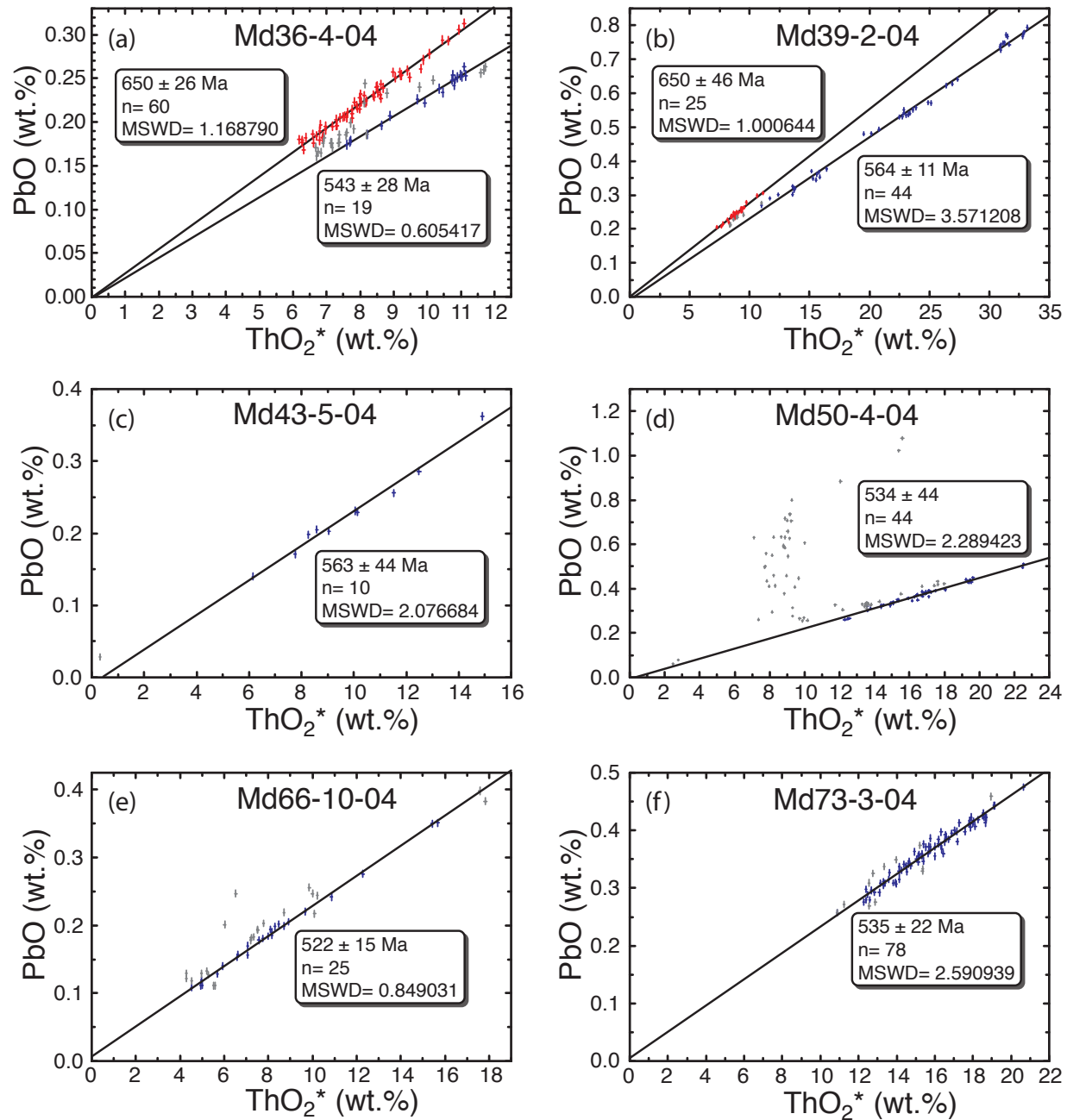


Figure 4.13: Results of the U-Th-totalPb dating of monazite from metapelites. Analyses belonging to different age populations are shown in different colours. Grey symbols represent analyses not used for age calculation. Symbol sizes correspond to analytical uncertainty.

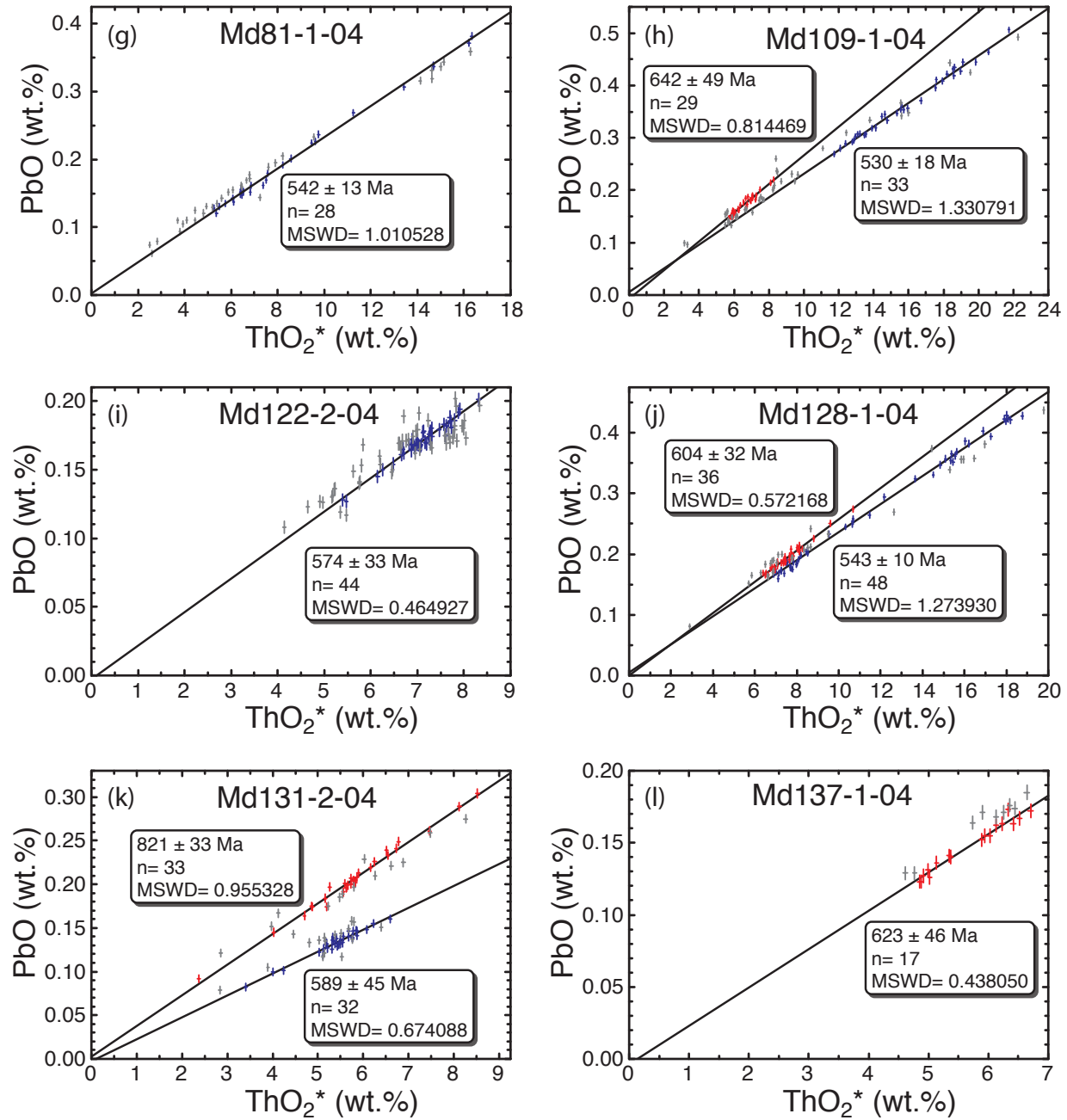


Figure 4.13: (continued) Results of the U-Th-total Pb dating of monazite from metapelites.

Table 4.15: Results of U-Th-total Pb dating of monazites from metapelitic samples.

Sample	Rock type*	Geologic unit ¹	Tectonic unit ²	Age
Md36-4-04	metapelite [13]	Graphite group	Bekily belt	650 ± 26 Ma (n=60; MSWD=1.168790) 543 ± 28 Ma (n=19; MSWD=0.605417)
Md39-2-04	metapelite [11]	Androyan group	Betroka belt	650 ± 46 Ma (n=25; MSWD=1.000644) 564 ± 11 Ma (n=44; MSWD=3.571208)
Md43-5-04	metapelite [13]	Androyan group	Tranomaro belt	563 ± 44 Ma (n=10; MSWD=2.076684)
Md50-4-04	metapelite [11]	Androyan group	Fort Dauphin belt	app. ages ranging from 625 to 1993 Ma 534 ± 25 Ma (n=44; MSWD=2.289423)
Md66-10-04	metapelite [8]	Androyan group	Tranomaro belt	522 ± 15 Ma (n=25; MSWD=0.849031)
Md73-3-04	metapelite [2]	Androyan group	Tranomaro belt	535 ± 22 Ma (n=78; MSWD=2.590939)
Md81-1-04	metapelite [4]	Androyan group	Betroka belt	542 ± 13 Ma (n=28; MSWD=1.010528)
Md109-1-04	metapelite [11]	Androyan group	Betroka belt	642 ± 49 Ma (n=29; MSWD=0.814469) 530 ± 18 Ma (n=33; MSWD=1.330791)
Md122-2-04	metapelite [14]	Androyan group	Bekily belt	574 ± 33 Ma (n=44; MSWD=0.464927)
Md128-1-04	metapelite [13]	Androyan group	Ranoatsara SZ	604 ± 32 Ma (n=36; MSWD=0.572168) 543 ± 10 Ma (n=48; MSWD=1.273930)
Md131-2-04	metapelite [12]	—	Antananarivo block	821 ± 33 Ma (n=29; MSWD=0.955328) 589 ± 45 Ma (n=32; MSWD=0.674088)
Md137-1-04	metapelite	—	Antananarivo block	623 ± 46 Ma (n=17; MSWD=0.438050)

* bracketed number corresponds to assemblage number in Table 4.3; ¹ after Besairie (1973); ² after Windley *et al.* (1994)

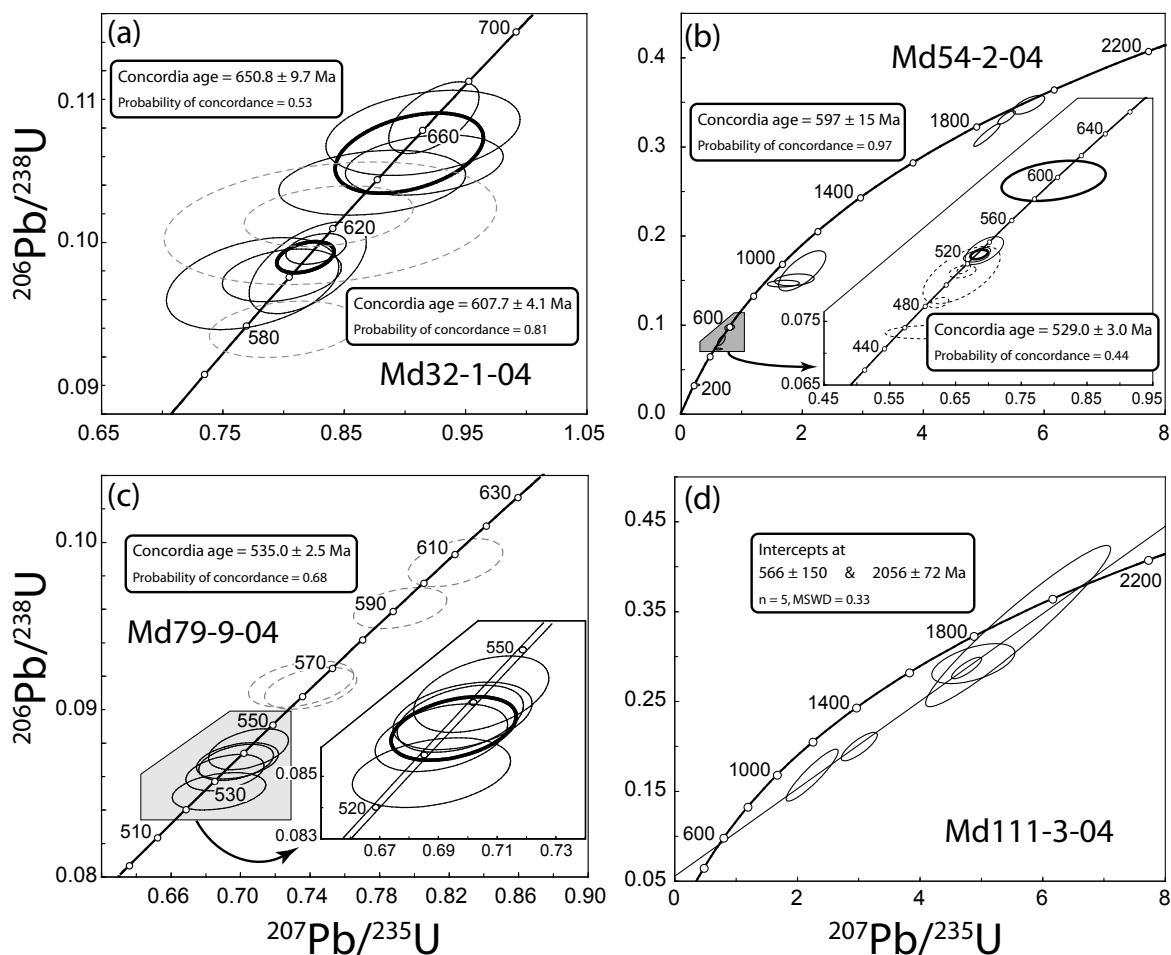


Figure 4.14: SHRIMP U–Pb concordia diagrams for zircons from Madagascar. Sample locations are marked in Fig. 4.2. All errors and error ellipses are 2σ , decay constant errors are included.

$\text{ThO}_2^* < 9$ wt.% and an age of 642 ± 49 Ma (Fig. 4.13h). Rims have mostly higher ThO_2^* (up to 22 wt.%) and are significantly younger (530 ± 18 Ma; Fig. 4.13h).

Md122-2-04 (S22°29'55.11"; E045°42'16.03"). Sample Md122-2-04 is a garnet-spinel-cordierite-bearing metapelite from the poorly exposed Horombe plateau west of Ihosy. Monazite is a frequent accessory phase and mostly unzoned in BSE image. We calculated an age of 574 ± 33 Ma, however, this result is not unambiguous as the apparent ages scatter from 675–500 Ma (Fig. 4.13i). This may reflect the existence of two metamorphic ages, which cannot be distinguished from the obtained data.

Md128-1-04 (S22°33'50.51"; E046°20'53.06"). This sample was taken at the roadside from Ihosy to Sahambano. The outcrop is located in the prominent Ranotsara shear zone, where strongly foliated granitic gneisses are intercalated with garnet-sillimanite-bearing mylonites. The latter contain monazite, which is 50–150 μm in diameter and strongly

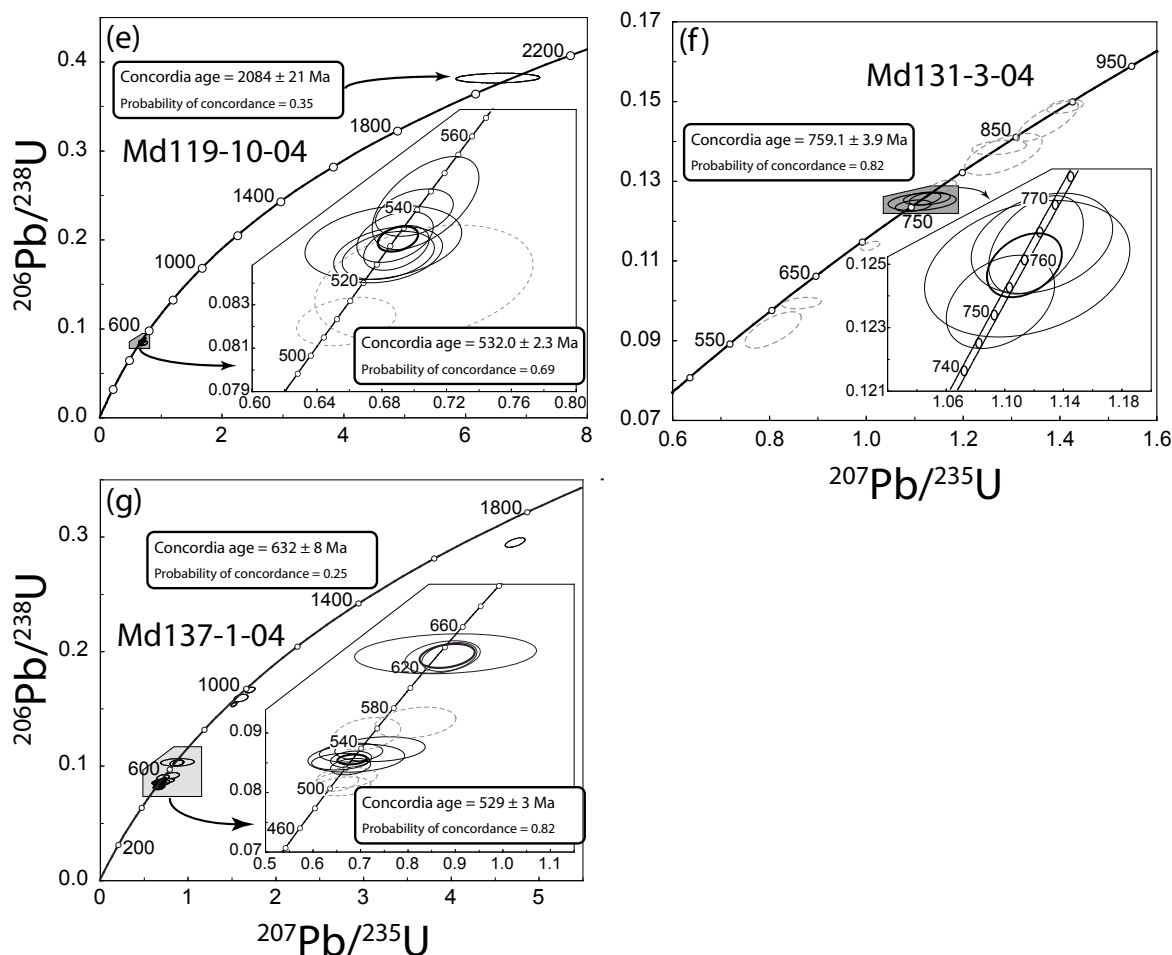


Figure 4.14: (continued) SHRIMP U–Pb concordia diagrams for zircons from Madagascar. Sample locations are marked in Fig. 4.2. All errors and error ellipses are 2σ , decay constant errors are included.

zoned in the BSE image. Cores and rims were evaluated separately and give 604 ± 32 Ma and 543 ± 10 Ma, respectively (Fig. 4.13j).

Md131-2-04 ($S21^{\circ}52'21.17''$; $E046^{\circ}54'39.35''$). The outcrop of this sample is located in the Antananarivo Block (as defined by Collins & Windley, 2002), at the main road between Ihosy and Fianarantsoa (RN7), close to the village Ianabohita. The sample is a migmatitic metapelite with large garnet porphyroblasts as well as biotite, quartz, K-feldspar, and late-stage cordierite. Monazite is relatively small ($20\text{--}80\ \mu\text{m}$) and seems to be unzoned in the BSE image. Nonetheless two distinct age populations are present: at 821 ± 33 Ma and at 589 ± 45 Ma (Fig. 4.13k).

Md137-1-04 ($S18^{\circ}49'48.13''$; $E047^{\circ}03'50.37''$). This sample is from an outcrop ca. 50 km west of Antananarivo, at the road between Zoma-Bealoka and Bejafo. It is situated in the central Antananarivo Block. Close to a stratoid granite, banded migmatitic gneisses occur,

Table 4.16: Results of SHRIMP zircon analyses (Md32-1-04, Md54-2-04). Age errors are given as 1σ .

No.	U (ppm)	Th (ppm)	$\frac{^{232}\text{Th}}{^{238}\text{U}}$	comm. ^{206}Pb (%)	$\frac{^{207}\text{Pb}}{^{206}\text{Pb}}$	error (%)	$\frac{^{206}\text{Pb}}{^{238}\text{U}}$	error (%)	$\frac{^{207}\text{Pb}}{^{235}\text{U}}$	error (%)	$\frac{^{208}\text{Pb}}{^{232}\text{Th}}$	error (%)	% disc.	Age (Ma)* $\frac{^{207}\text{Pb}}{^{206}\text{Pb}}$	\pm	Age (Ma)* $\frac{^{206}\text{Pb}}{^{238}\text{U}}$	\pm
Md32.1.1	185	29	0.164	0.207	0.0609	1.91	0.0977	0.77	0.7986	2.51	0.0335	4.71	-3.9	577.6	52.0	600.9	4.4
Md32.1.2	132	66	0.512	0.170	0.0621	2.91	0.1042	0.89	0.8731	3.60	0.0344	2.75	-1.2	631.5	75.2	638.8	5.4
Md32.2.1	200	46	0.238	0.055	0.0634	2.69	0.1054	0.82	0.9160	2.90	0.0350	2.94	9.7	709.0	59.2	646.1	5.0
Md32.2.2	188	25	0.137	0.000	0.0598	1.93	0.0982	1.33	0.8200	2.41	0.0364	4.03	3.2	623.2	43.3	604.0	7.7
Md32.3.1	101	35	0.359	0.344	0.0643	2.52	0.1077	1.13	0.9149	3.57	0.0350	4.10	0.3	661.4	72.6	659.1	7.1
Md32.3.2	203	27	0.138	0.463	0.0614	2.03	0.0971	1.35	0.7745	3.75	0.0283	11.08	-12.4	523.5	76.6	597.5	7.7
Md32.4.1	1162	212	0.189	0.103	0.0610	0.79	0.0995	0.44	0.8268	1.23	0.0322	2.44	0.1	612.2	24.7	611.7	2.6
Md32.4.2	162	21	0.135	0.333	0.0644	2.07	0.0940	0.86	0.8007	3.13	0.0328	8.02	15.3	667.6	64.4	578.9	4.7
Md32.5.1	89	26	0.297	0.579	0.0645	2.75	0.1013	1.72	0.8383	6.68	0.0288	11.41	-3.1	603.2	139.8	622.3	10.2
Md32.6.1	399	144	0.373	0.032	0.0619	1.29	0.1087	0.94	0.9239	1.65	0.0370	2.58	-0.6	661.3	29.0	665.3	6.0
Md32.6.2	219	88	0.416	0.211	0.0613	1.81	0.1018	0.85	0.8369	3.41	0.0333	3.71	-5.5	590.4	71.6	624.8	5.1
Md54.1.1	1930	275	0.147	4.925	0.0602	4.38	0.0733	0.59	0.6090	4.42	0.0293	13.83	34.3	612.5	94.7	456.1	2.6
Md54.1.2	1074	190	0.182	0.356	0.0581	2.86	0.0822	2.24	0.6592	3.63	0.0292	6.91	5.0	534.8	62.6	509.5	11.0
Md54.1.3	1073	302	0.291	0.453	0.1169	0.69	0.3132	1.62	5.0491	1.76	0.1018	2.27	8.7	1909.9	12.3	1756.3	25.0
Md54.2.1	2080	8	0.004	0.110	0.0582	0.88	0.0779	0.43	0.6248	0.98	—	—	10.8	535.9	19.2	483.6	2.0
Md54.2.2	1195	163	0.141	0.121	0.0900	6.88	0.1507	1.81	1.8700	7.12	0.0463	5.22	57.4	1425.0	131.4	905.1	15.3
Md54.3.1	2225	19	0.009	0.394	0.0834	6.22	0.1465	1.04	1.6850	6.31	—	—	45.2	1279.3	121.3	881.2	8.5
Md54.3.2	686	329	0.495	0.000	0.1171	0.68	0.3331	0.91	5.3766	1.13	0.1040	1.12	3.2	1911.8	12.2	1853.4	14.6
Md54.4.1	2095	47	0.023	0.241	0.0579	1.17	0.0828	0.49	0.6606	1.27	0.0223	22.58	2.5	525.3	25.7	512.7	2.4
Md54.4.2	2844	21	0.008	0.374	0.0580	1.08	0.0852	0.43	0.6814	1.16	0.0381	39.85	0.5	529.7	23.6	527.1	2.2
Md54.1.4	2012	259	0.133	0.019	0.0583	0.75	0.0857	0.43	0.6888	0.87	0.0294	1.40	2.0	540.8	16.5	530.1	2.2
Md54.1.5	1259	249	0.204	0.200	0.0597	3.84	0.0970	1.33	0.7992	4.06	0.0312	5.50	-0.5	593.9	83.1	597.0	7.6
Md54.5.1	2748	12	0.004	0.104	0.0584	1.38	0.0861	1.03	0.6938	1.72	—	—	2.6	546.5	30.2	532.4	5.3
Md54.5.3	2603	13	0.005	0.630	0.0901	5.64	0.1609	5.75	1.9988	8.05	0.0561	90.75	48.4	1427.4	107.7	961.9	51.4
Md54.5.2	331	89	0.277	0.000	0.1200	1.38	0.3473	1.26	5.7463	1.87	0.1113	2.20	1.8	1956.1	24.7	1921.8	20.9
Md54.6.1	9940	61	0.006	12.041	0.0589	5.17	0.0325	0.60	0.2642	5.21	-0.0820	99.49	172.8	563.2	112.7	206.4	1.2
Md54.6.2	6157	27	0.005	0.025	0.0577	0.51	0.0833	0.40	0.6627	0.65	0.0207	28.15	0.7	519.2	11.2	515.6	2.0

* common Pb corrected using measured ^{204}Pb .

Table 4.16: (continued) Results of SHRIMP zircon analyses (Md79-9-04, Md111-3-04, Md119-10-04). Age errors are given as 1σ .

No.	U (ppm)	Th (ppm)	^{232}Th / ^{238}U	comm. ^{206}Pb (%)	^{207}Pb * ^{206}Pb (%)	error (%)	^{206}Pb * ^{238}U (%)	error (%)	^{207}Pb * ^{235}U (%)	error (%)	^{206}Pb * ^{232}Th (%)	error (%)	% disc.	Age (Ma) * ^{207}Pb / ^{206}Pb	\pm	Age (Ma) * ^{206}Pb / ^{238}U	\pm
Md79.1.1	711	94	0.137	0.066	0.0583	1.21	0.0876	0.57	0.7046	1.33	0.0283	2.67	0.0	541.4	26.4	541.5	3.0
Md79.1.2	630	15	0.024	0.093	0.1112	1.19	0.3309	0.50	5.0737	1.29	0.0855	11.50	-1.3	1819.3	21.5	1842.7	8.0
Md79.2.1	727	93	0.133	0.000	0.0581	1.23	0.0862	0.51	0.6910	1.33	0.0313	2.49	0.1	534.0	26.9	533.3	2.6
Md79.3.1	498	83	0.172	0.000	0.0582	1.56	0.0915	0.63	0.7346	1.68	0.0321	2.99	-4.7	537.8	34.1	564.6	3.4
Md79.1.3	751	101	0.139	0.000	0.0582	1.15	0.0869	0.51	0.6975	1.26	0.0306	2.09	0.4	538.8	25.2	536.9	2.6
Md79.2.2	695	92	0.137	0.000	0.0586	1.51	0.0851	0.54	0.6877	1.60	0.0309	3.66	4.8	551.9	32.9	526.7	2.7
Md79.1.4	567	17	0.032	0.053	0.0604	1.21	0.0988	0.60	0.8333	1.35	0.0367	6.13	2.0	619.5	26.2	607.3	3.5
Md79.2.3	653	22	0.035	0.000	0.0598	1.27	0.0960	0.52	0.7919	1.37	0.0380	7.88	0.8	596.2	27.5	591.2	3.0
Md79.2.4	396	193	0.503	0.000	0.1356	0.51	0.3893	0.48	7.2782	0.70	0.1212	0.97	2.4	2171.5	8.9	2119.7	8.8
Md79.2.5	417	14	0.036	0.000	0.1183	0.71	0.2908	3.03	4.7450	3.11	0.0929	5.07	17.4	1931.4	12.8	1645.5	44.0
Md79.1.5	765	105	0.142	0.000	0.0582	1.29	0.0869	0.51	0.6982	1.38	0.0290	2.82	0.3	539.0	28.2	537.5	2.6
Md79.1.6	538	34	0.065	0.065	0.0588	1.36	0.0913	0.54	0.7404	1.47	0.0296	5.05	-0.5	560.6	29.7	563.1	2.9
Md111.1.1	1289	11	0.009	0.019	0.1208	4.82	0.2923	3.11	4.8689	5.74	0.0880	11.35	19.1	1968.3	86.0	1652.9	45.4
Md111.1.2	1017	11	0.012	0.001	0.1202	1.20	0.2873	1.74	4.7625	2.11	0.0957	3.45	20.4	1959.7	21.4	1627.9	25.0
Md111.1.3	1475	15	0.010	0.076	0.1093	2.30	0.1998	3.22	3.0095	3.96	0.0419	25.88	52.2	1787.2	41.9	1174.0	34.5
Md111.2.1	1339	11	0.009	0.012	0.1218	3.34	0.3337	10.85	5.6030	11.35	0.1048	15.23	6.8	1982.5	59.4	1856.2	175.0
Md111.2.2	1391	15	0.011	0.130	0.0966	3.15	0.1682	6.97	2.2399	7.65	0.0295	56.11	55.6	1559.3	59.1	1002.1	64.7
Md119.1.1	911	23	0.026	0.000	0.0582	1.58	0.0853	0.53	0.6839	1.66	0.0383	15.44	1.6	535.8	34.5	527.6	2.7
Md119.2.1	952	34	0.037	0.080	0.0584	1.12	0.0856	0.49	0.6890	1.22	0.0265	6.67	2.6	543.5	24.5	529.6	2.5
Md119.2.2	973	32	0.034	0.136	0.0582	1.35	0.0873	0.51	0.7005	1.44	0.0232	14.09	-0.2	538.3	29.5	539.3	2.6
Md119.3.1	894	191	0.221	0.122	0.0580	1.31	0.0861	0.56	0.6882	1.42	0.0290	2.08	-0.9	527.9	28.7	532.6	2.8
Md119.4.1	316	109	0.356	0.056	0.1241	4.23	0.3819	0.58	6.5347	4.27	0.1151	1.39	-3.3	2015.8	75.0	2085.3	10.4
Md119.4.2	658	243	0.381	0.083	0.0581	1.84	0.0822	0.55	0.6584	1.92	0.0278	1.49	4.6	532.9	40.4	509.3	2.7
Md119.5.1	441	103	0.241	0.110	0.0582	1.92	0.0853	0.61	0.6840	2.01	0.0280	2.95	1.5	535.7	41.9	527.7	3.1
Md119.5.2	212	60	0.291	0.171	0.0576	2.75	0.0859	0.81	0.6814	2.86	0.0282	3.62	-3.4	513.1	60.4	531.0	4.1
Md119.3.2	395	65	0.170	0.000	0.0584	1.56	0.0877	1.02	0.7066	1.86	0.0314	2.34	0.8	546.2	34.1	541.9	5.3
Md119.1.3	275	17	0.065	0.597	0.0610	3.69	0.0840	1.26	0.7064	3.90	0.0326	21.18	22.7	638.3	79.3	520.1	6.3

* common Pb corrected using measured ^{204}Pb .

Table 4.16: (continued) Results of SHRIMP zircon analyses (Md131-3-04, Md137-1-04). Age errors are given as 1σ .

No.	U (ppm)	Th (ppm)	$\frac{^{232}\text{Th}}{^{238}\text{U}}$	comm. $\frac{^{207}\text{Pb}}{^{206}\text{Pb}}$ (%)	$\frac{^{207}\text{Pb}}{^{206}\text{Pb}}$ error (%)	$\frac{^{206}\text{Pb}}{^{238}\text{U}}$ error (%)	$\frac{^{207}\text{Pb}}{^{235}\text{U}}$ error (%)	$\frac{^{208}\text{Pb}}{^{232}\text{Th}}$ error (%)	% disc.	Age (Ma)* $\frac{^{207}\text{Pb}}{^{206}\text{Pb}}$	\pm	Age (Ma)* $\frac{^{206}\text{Pb}}{^{238}\text{U}}$	\pm				
Md131.1.1	723	13	0.019	0.000	0.0647	1.07	0.1256	0.50	1.1213	1.18	0.0551	11.25	0.4	766.1	22.5	762.8	3.6
Md131.1.2	686	3	0.005	0.220	0.0687	1.25	0.1451	1.42	1.3744	1.89	-0.0656	78.39	1.9	889.9	25.8	873.4	11.6
Md131.2.1	799	15	0.020	0.120	0.0643	1.29	0.1238	0.48	1.0971	1.38	0.0349	28.21	-0.3	750.3	27.3	752.5	3.4
Md131.2.2	6095	40	0.007	0.035	0.0643	0.68	0.1137	0.41	1.0081	0.79	0.0264	14.26	8.1	750.9	14.3	694.4	2.7
Md131.3.1	676	11	0.017	0.227	0.0650	1.68	0.1257	0.51	1.1254	1.76	—	—	1.3	772.8	35.4	763.1	3.7
Md131.3.2	1072	11	0.011	0.000	0.0653	0.82	0.1287	0.50	1.1587	0.96	0.0611	10.04	0.5	784.1	17.2	780.4	3.7
Md131.4.1	537	10	0.019	0.088	0.0632	2.15	0.0927	2.01	0.8073	2.94	0.0414	22.51	24.8	713.3	45.6	571.5	11.0
Md131.1.3	605	12	0.021	0.167	0.0632	1.82	0.0994	0.60	0.8667	1.91	0.0300	34.26	17.2	716.0	38.6	611.0	3.5
Md131.5.1	448	9	0.021	0.349	0.0648	2.48	0.1249	0.70	1.1153	2.57	0.0223	72.97	1.2	767.4	52.2	758.5	5.0
Md131.6.1	519	2	0.003	0.329	0.0667	1.73	0.1385	0.54	1.2744	1.81	-0.2038	53.45	-0.7	829.9	36.0	836.1	4.2
Md131.7.1	785	3	0.004	0.047	0.0680	2.03	0.1368	1.56	1.2833	2.56	0.0320	53.47	5.3	870.0	42.0	826.4	12.1
Md131.8.1	744	2	0.003	0.126	0.0688	0.98	0.1488	0.48	1.4105	1.09	-0.0522	96.98	-0.3	891.3	20.3	894.2	4.0
Md137.1.1	132	36	0.279	0.022	0.0729	1.90	0.1595	0.82	1.6019	2.08	0.0520	2.98	5.9	1010.0	38.6	953.8	7.3
Md137.1.2	129	1	0.010	0.895	0.0617	8.82	0.1033	1.32	0.8791	8.92	—	—	4.7	663.9	189.0	633.9	7.9
Md137.2.1	799	278	0.359	0.017	0.0718	0.69	0.1538	0.48	1.5223	0.84	0.0498	0.93	6.3	979.9	14.1	922.2	4.1
Md137.2.2	540	9	0.017	0.539	0.0590	3.78	0.0825	0.84	0.6712	3.88	0.0401	70.24	10.8	566.7	82.4	511.2	4.1
Md137.3.1	272	4	0.014	0.522	0.0560	3.72	0.0852	0.66	0.6579	3.78	—	—	-14.1	452.5	82.7	527.1	3.3
Md137.3.2	279	188	0.697	0.000	0.0744	1.19	0.1665	0.59	1.7068	1.33	0.0570	1.12	5.9	1051.1	24.0	992.7	5.4
Md137.3.3	355	6	0.017	0.268	0.0576	2.53	0.0856	0.65	0.6802	2.61	0.0199	78.34	-2.6	515.8	55.6	529.4	3.3
Md137.3.4	99	14	0.144	0.000	0.0628	2.65	0.1028	0.98	0.8909	2.82	0.0491	7.04	11.4	702.7	56.4	631.0	5.9
Md137.4.1	176	104	0.613	0.000	0.1161	0.79	0.2953	0.58	4.7275	0.98	0.0934	1.03	13.8	1897.3	14.2	1667.8	8.5
Md137.4.2	133	2	0.013	0.873	0.0584	5.92	0.0858	1.12	0.6910	6.02	—	—	3.0	546.3	129.3	530.4	5.7
Md137.5.1	284	4	0.016	0.332	0.0576	2.85	0.0817	0.78	0.6490	2.95	0.0454	40.07	1.5	514.0	62.5	506.5	3.8
Md137.6.1	104	2	0.022	0.790	0.0616	5.15	0.0873	0.98	0.7413	5.24	—	—	22.4	660.2	110.3	539.4	5.1
Md137.7.1	203	5	0.024	0.500	0.0569	3.93	0.0867	0.75	0.6801	4.00	—	—	-9.0	487.5	86.7	536.0	3.8
Md137.8.1	180	3	0.015	0.273	0.0594	3.48	0.0810	0.80	0.6638	3.57	0.0295	82.80	15.9	582.2	75.6	502.3	3.8
Md137.9.1	237	4	0.019	0.174	0.0584	2.47	0.0844	0.68	0.6788	2.56	0.0255	50.12	4.0	543.1	54.0	522.1	3.4
Md137.9.2	102	1	0.011	0.356	0.0614	3.41	0.1027	1.07	0.8694	3.57	—	—	3.5	652.4	73.1	630.5	6.5
Md137.10.1	148	8	0.058	0.585	0.0576	3.87	0.0899	1.26	0.7135	4.07	0.0267	29.29	-7.4	513.7	85.0	554.8	6.7
Md137.4.3	60	2	0.031	0.231	0.0645	4.11	0.0918	1.16	0.8154	4.27	0.0480	29.97	33.7	756.6	86.8	565.9	6.3

* common Pb corrected using measured ^{204}Pb .

which contain thick layers rich in cordierite and sillimanite. Monazite is generally unzoned in the BSE image, resulting in a single age of 623 ± 46 Ma (Fig. 4.13l), however, a few older apparent ages are present.

4.7.2 U-Pb dating of zircon

Md32-1-04 (S24°13'06.01"; E045°18'50.25"). This sample was collected at the Menarandra River close to the town of Bekily. The outcrop consists of a layered series of garnet-free metabasites, garnet-biotite gneisses, and granitic gneisses. Discordant leucosomes and late-stage discordant pegmatoids are frequently present. The sample Md32-1-04 is an intermediate granulite containing large garnet porphyroblasts, together with Fe-rich inverted pigeonite, plagioclase, alkali-feldspar and small amounts of quartz. Tiny amphibole crystals are obviously derived from late-stage rehydration of pyroxene. Accessory mineral phases are apatite and zircon. Most zircon is euhedral, 150–300 μm in size, and in cathodoluminescence (CL) images the cores show oscillatory zoning, which is interpreted as a magmatic growth pattern. Furthermore, narrow rims without a visible zonation are observed, which are irregularly shaped and crosscut the zoning pattern of the core. These areas may represent recrystallised parts, which formed during a late metamorphic stage. Zircon cores have an age of 650.8 ± 9.7 Ma (Fig. 4.14a), interpreted as the time of magmatic emplacement. Younger ages are present as well (607.7 ± 4.1 Ma; Fig. 4.14a), showing that metamorphism followed the emplacement just ca. 40 Ma later.

Md54-2-04 (S25°00'29.37"; E046°58'37.80"). Following the road RN12 from Tôlaïaro just ca. 1 km to the north, large outcrops of metapelitic leptynites are found. Our sample contains the same mineral assemblage as Md50-4-04, but features a more pronounced foliation. Most zircon contains oscillatory or sector-zoned cores, which are bright in the CL image. Recrystallised rims are unzoned and much darker. Zircon cores are of detrital origin (0.9–1.9 Ga), but rims are grown during the Pan-African period. Concordant ages are at 597 ± 15 Ma and 529.0 ± 3.0 Ma, but even younger $^{206}\text{Pb}/^{238}\text{U}$ ages are present (Fig. 4.14b).

Md79-9-04 (S24°27'41.11"; E045°49'07.51"). The outcrop is located in a riverbed ca. 3 km south of Imanombo. The sample is a metapelite, containing spinel, quartz, sillimanite, orthopyroxene, garnet, plagioclase, K-feldspar, and late-stage cordierite. Zircon is irregularly shaped, ca. 100–200 μm in diameter, and shows a sector-zoned core surrounded by several rims in CL image. The outermost rims give an age of 535.0 ± 2.5 Ma, but rims further inside have $^{206}\text{Pb}/^{238}\text{U}$ ages as old as 607 Ma (Fig. 4.14c). Cores of the zircon are much older (1.6–2.1 Ga) and therefore, interpreted to be of detrital origin.

Md111-3-04 (S23°04'23.20"; E045°52'09.71"). At the phlogopite mine north of Benato we took this metapelitic sample, containing garnet, sillimanite, cordierite, quartz, K-feldspar, and small amounts of biotite. Zircon is up to 200 μm in diameter. It shows

oscillatory zoning in the core, but also irregularly recrystallised and newly grown rims. Measurements resulted in a discordia that intercepts at 2056 ± 72 Ma and 566 ± 150 Ma (Fig. 4.14d), pointing to a detrital origin of zircon cores, overprinted during the Pan-African orogeny.

Md119-10-04 (S22°24'18.70"; E046°08'47.60"). This sample is a metapelite from the Lalanandro quarry in Ihosy. It contains the assemblage sillimanite, spinel, garnet, biotite, plagioclase, K-feldspar, and quartz. Zircon cores show a well-developed oscillatory zoning, which is locally crosscut by unzoned overgrown rims. These rims are dated at 532.0 ± 2.3 Ma (Fig. 4.14e); a core analysis is at ca. 2 Ga.

Md131-3-04 (S21°52'21.17"; E046°54'39.35"). This metapelite is from the same outcrop as Md131-2-04. Compared to the previously described sample, Md131-3-04 has smaller garnet porphyroblasts. The accessory zircons are ca. 50–150 μm in size, show oscillatory-zoned cores and CL-dark rims. A concordant age at 759.1 ± 3.9 Ma can be calculated, however, younger and older ages seem to be present as well (Fig. 4.14f).

Md137-1-04 (S18°49'48.13"; E047°03'50.37"). Sampled west of Antananarivo, this rock was also used for monazite dating. Zircon cores show oscillatory zoning and are overgrown by irregularly shaped rims, which give two distinguishable ages: 632 ± 8 and 529 ± 3 Ma (Fig. 4.14g).

4.8 Discussion and conclusions

4.8.1 Pressure-temperature evolution

The clockwise P – T evolution deduced from the UHT metapelites of southern Madagascar points to a period of crustal thickening, when the rocks were buried to a depth of at least 25 km (northern Androyan group), but locally even deeper (ca. 35 km, southern Androyan group). The thickening of the crust was followed by exhumation of the lower crustal rocks to mid-crustal levels (10–20 km depth), evidenced by near-isothermal decompression from peak pressures of 8–11 kbar to 4–6 kbar. In the middle crust they cooled near-isobarically, indicating that the crust had nearly reached its normal thickness. Martelat *et al.* (1999a) proposed an exhumation along the N–S trending shear zones and a pressure gradient from the west to the east, but the authors assumed much lower peak pressures for the Androyan group than our results imply. Furthermore, their interpretation does not account for the existence of two distinct metamorphic events. We have no structural geological data to make a definite statement about the exhumation mechanism: extension leading to tectonic denudation (e. g., Ridley, 1989) or extrusion of the lower crust resulting from transpressional tectonics (e. g., Thompson *et al.*, 1997; Schulmann *et al.*, 2002) are possible mechanisms.

Although the omnipresence of spinel + quartz assemblages in the Androyan group points to a huge area where high-temperature metamorphism took place (ca. 75000 km²), the occurrence of more specific UHT assemblages (sapphirine + quartz, orthopyroxene + sillimanite + quartz, osumilite + garnet) is restricted to a smaller area (ca. 40000 km²) in the southern Androyan group, in the region around the Anosyan charnockite massif. The lack of UHT assemblages in the Graphite group and north of the Ranotsara shear zone points to lower P - T conditions. This contrasts with the results of Markl *et al.* (2000), who deduced uniform metamorphic conditions for whole southern Madagascar. However, their estimates for this huge area are just based on five samples, and they consequently missed the regional distribution of UHT assemblages, as well as the systematic Fe-Mg shift in garnet-biotite-bearing assemblages.

4.8.2 Timing of metamorphic events

The general observation that two main metamorphic events are found in the East African Orogen (e.g., Meert, 2003) proves to be true also for southern Madagascar. The distribution of metamorphic ages determined in this study is summarised in Fig. 4.15. In the southern Androyan group, zircon preserves information about two metamorphic events ($M_1 \approx 600$ Ma; $M_2 \approx 535$ Ma), whereas the monazite of this area gives only the younger age of ca. 535 Ma, interpreted to correspond to the UHT metamorphism and the deduced clockwise P - T evolution. The older M_1 event is extensively overprinted during the second metamorphism and, thus, its P - T history is not known and just imprecisely datable. Zircon dating often results in several ages clustering along the concordia (Fig. 4.14c). These most likely discordant ages result from lead loss during the M_2 UHT-metamorphic overprinting. The two metamorphic ages are also found in the central Antananarivo Block (sample Md137-1-04; Fig. 4.14g), but due to the lower metamorphic grade of the M_2 event, both ages are more easily distinguishable. In the Graphite group, the main metamorphic event was at ca. 610 Ma and the M_2 event was not determined from zircon ages. Just monazite data from one sample (Md36-4-04; Fig. 4.13a) indicate that the Graphite group also experienced the younger M_2 metamorphism, but the intensity of this metamorphic overprinting was obviously lower, possibly just a result of post-metamorphic fluid circulation. Even further to the west, in the Vohibory group, the M_1 event was the main metamorphic episode, which is here ascribed to a collisional event (Jöns & Schenk, in review). These findings disprove the postulated pressure gradient of Martelat *et al.* (1999a), who seems to have compared M_1 peak pressures in the Vohibory group with M_2 -related P - T conditions further east.

For the southern part of the Antananarivo Block (samples Md131-2-04 and Md131-3-04; Figs. 4.13k & 4.14f) the interpretation is less clear. Both, zircon and monazite show ages ranging from 750–900 Ma, which may correspond to magmatic ages of the eastern Antananarivo Block (e.g., Kröner *et al.*, 2000). The age of Pan-African metamorphism is just weakly constrained by a monazite age of 589 ± 45 Ma. In any case, our results indicate that the Ranotsara shear zone separates two areas that are distinct in the grade of metamorphism and in the distribution of metamorphic ages.

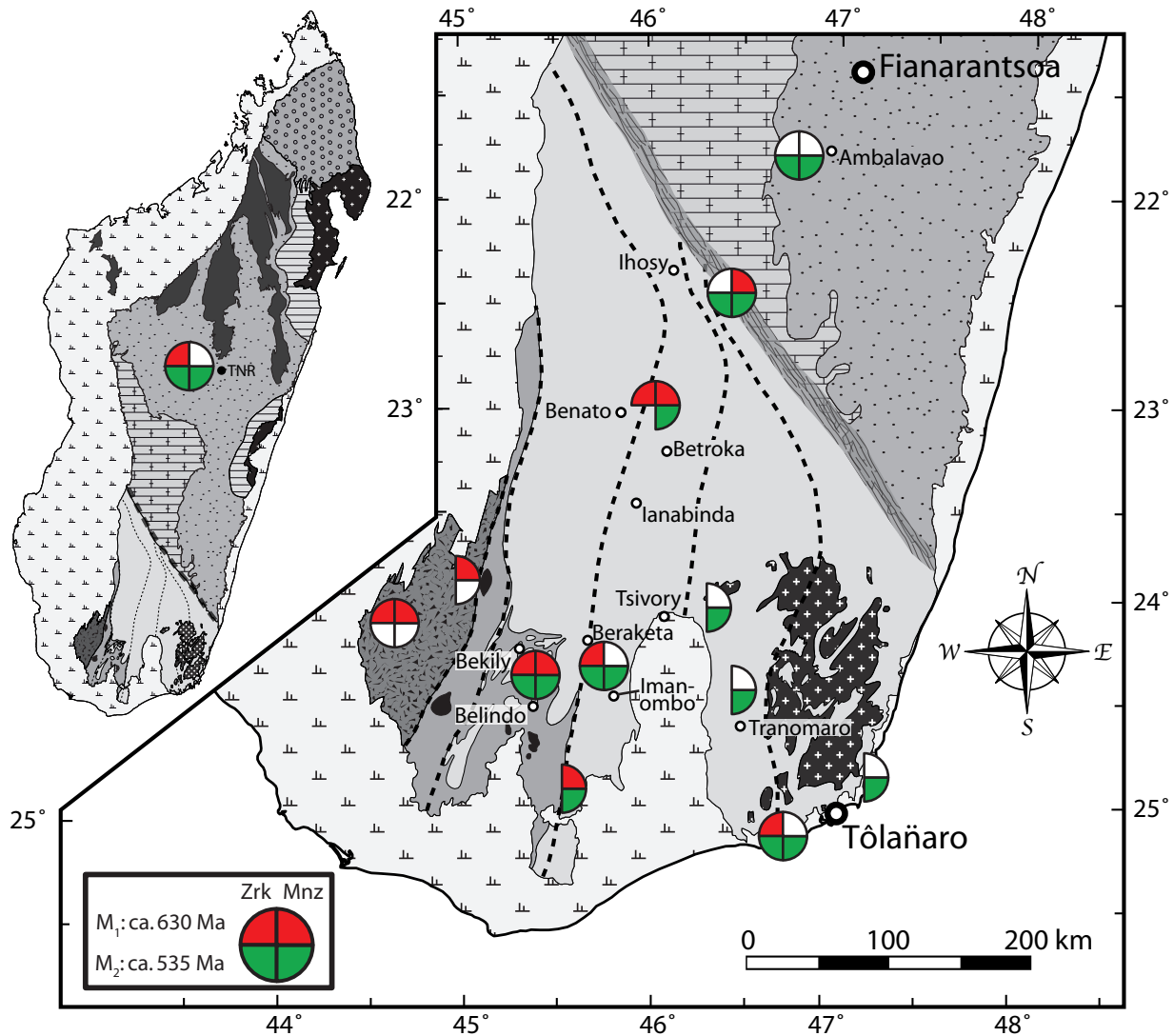


Figure 4.15: Distribution of metamorphic ages in Madagascar. The main metamorphic event in the Vohibory group was at 610 Ma and no M₂ overprinting was determined. The Graphite and Androyan group experienced both metamorphic events. Close to the Anosyan charnockite rocks contain homogeneous M₂ monazite, most likely as a result of complete recrystallisation during UHT metamorphism.

Circular symbols: red filling indicates that the M₁ event (ca. 630 Ma) has been determined, either by zircon (left side) or monazite ages (right side of the symbol). The depiction is equivalent for the M₂ age (ca. 535 Ma): green filling on the left side marks the existence of M₂ zircon ages, whereas green filling on the right side points to M₂ monazite ages. Unfilled parts indicate that an age has not been determined, missing sectors mark a lack of data. See legend of Fig. 4.2 for further explanation of the geology.

4.8.3 Implications for the Gondwana formation

Our results have to be seen in the context of the discussion about the timing of collisional events in other parts of the East African Orogen, e. g., in Tanzania and Zambia, which are adjacent to Madagascar in reconstructions of the Gondwana supercontinent. An anti-clockwise P – T evolution between ca. 655–610 Ma, interpreted as the timing of magmatic underplating processes, is deduced from widespread high-grade metamorphic rocks of Tanzania (Appel *et al.*, 1998; Möller *et al.*, 2000). This event was followed by a collision at ca. 536 Ma (see discussion in Jöns & Schenk, 2004), evidenced by whiteschist metamorphism at Mautia Hill (Tanzania). A comparable distribution of ages is also found in the Lufilian Arc–Zambezi Belt of Zambia: a period of convergence and eclogitization at 650–600 Ma was followed by continental collision at ca. 530 Ma (John *et al.*, 2003, 2004a,b). This is surprisingly similar to the age distribution found in rocks of southern Madagascar, however, the main metamorphic event in the Androyan group is the widespread ultra-high temperature metamorphism at ca. 535 Ma (M_2). This metamorphism is characterised by a clockwise P – T evolution and interpreted to be related to the main collisional event. The earlier M_1 event in southern Madagascar, which is best preserved in rocks of the Vohibory group, is interpreted to be related to accretion of an arc terrane (Jöns & Schenk, in review). We interpret that the Vohibory arc terrane collided at ca. 610 Ma (Jöns & Schenk, in review) with the western margin of the Azania microcontinent (Collins, 2006) and experienced a clockwise pressure-temperature evolution. This event is preserved in zircon and monazite ages in rocks of whole southern Madagascar. In the late stages of the Pan-African orogeny, Azania collided with the Tanzania Craton of Western Gondwana, leading to closure of the Mozambique Ocean. The collision was characterised by extensive crustal thickening and coeval magmatic underplating and inflation. The enormous dimensions of the Anosyan charnockite and the highest metamorphic temperatures found in pelites directly adjacent to the charnockite, point to such intrusions as the major heat source for the UHT metamorphism. While the Androyan group was buried to deep crustal levels, the rocks of the Graphite and Vohibory group may have been part of the upper crust, where they did not experience the ultrahigh-temperature metamorphism. The several subvertical shear zones found in southern Madagascar may be related to the late exhumation process that brought the rocks of the Androyan group back to the same crustal level, where the Graphite and Vohibory group resided.

4.9 Acknowledgements

We thank B. Mader and P. Appel for their help with the microprobe analyses, A. Fehler for the thin sections, and T. Razakamanana for support during the field work. A. Larionov, I. Paderin, S. Presniakov and N. Rodionov is thanked for help with the SHRIMP analyses. N. Jöns is grateful to the Studienstiftung des deutschen Volkes (German National Academic Foundation) for financial support. The Deutsche Forschungsgemeinschaft supported the project through grants Sche 256/16-1 and Sche 256/17-1.

References

- Ackermann, D., Windley, B. F. & Razafiniparany, A., 1989. The Precambrian mobile belt of southern Madagascar. In: *Evolution of metamorphic belts; proceedings of the 1987 joint meeting of the Metamorphic Studies Group and IGCP project 235*, Geological Society of London, London, United Kingdom. 293–296.
- Ackermann, D., Windley, B. F. & Razafiniparany, A. H., 1991. Kornerupine breakdown reactions in paragneisses from southern Madagascar. *Mineralogical Magazine*, **55**, 71–80.
- Almond, D. C., 1969. Structure and metamorphism of the basement complex of North-East Uganda. *Overseas Geology and Mineral Resources*, **10**, 146–163.
- Andriamarofahatra, J., de la Boisse, H. & Nicollet, C., 1990. Datation U-Pb sur monazites et zircons du dernier épisode tectono-métamorphique granulitique majeur dans le Sud-Est de Madagascar. *Comptes Rendus de l'Académie des Sciences, Série II*, **310**, 1643–1648.
- Appel, P., Möller, A. & Schenk, V., 1998. High-pressure granulite facies metamorphism in the Pan-African belt of eastern Tanzania: P-T-t evidence against granulite formation by continent collision. *Journal of metamorphic Geology*, **16**, 491–509.
- Armstrong, J. T., 1995. CITZAF: A package of correction programs for the quantitative electron microbeam X-ray analysis of thick polished materials, thin films, and particles. *Microbeam Analysis*, **4**, 177–200.
- Ashwal, L. D., Hamilton, M. A., Morel, V. P. I. & Rambeloson, R. A., 1998. Geology, petrology and isotope geochemistry of massif-type anorthosites from Southwest Madagascar. *Contributions to Mineralogy and Petrology*, **133**, 389–401.
- Baldwin, J. A., Powell, R., Brown, M., Moraes, R. & Fuck, R. A., 2005. Modelling of mineral equilibria in ultrahigh-temperature metamorphic rocks from the Anápolis-Itaucu Complex, central Brazil. *Journal of metamorphic Geology*, **23**, 511–531.
- Bazot, G., Bousteyak, L., Hottin, G. & Razafiniparany, A., 1971. Carte du métamorphisme de Madagascar. *Documentation du Bureau Géologique (Service Géologique, Tananarive)*, **183**, 1–24.
- Berg, J. H., 1977. Dry granulite mineral assemblages in the contact aureoles of the Nain Complex, Labrador. *Contributions to Mineralogy and Petrology*, **64**, 33–52.
- Berger, A., Gnos, E., Schreurs, G., Fernandez, A. & Rakotondrazafy, M., 2006. Late Neoproterozoic, Ordovician and Carboniferous events recorded in monazites from southern-central Madagascar. *Precambrian Research*, **144**, 278–296.
- Besairie, H., 1970. Description géologique du Massif ancien de Madagascar: Le Sud. Documentation du Bureau géologique Numéro 177e, République Malagasy, Service géologique.

- Besairie, H., 1973. Les diverses interpretations du socle Malgache. Technical report, Republique Malagasy, Service géologique.
- Black, L. P., Kamo, S. L., Allen, C. M., Aleinikoff, J. N., Davis, D. W., Korsch, R. J. & Foudoulis, C., 2003. TEMORA 1: a new zircon standard for Phanerozoic U-Pb geochronology. *Chemical Geology*, **200**, 155–170.
- Carrington, D. P. & Harley, S. L., 1995. The stability of osumilite in metapelitic granulites. *Journal of Metamorphic Geology*, **13**, 613–625.
- Collins, A. S., 2006. Madagascar and the amalgamation of central Gondwana. *Gondwana Research*, **9**, 3–16.
- Collins, A. S., Kinny, P. D., Santosh, M. & Razakamanana, T., 2005. Depositional age and provenance record of ultra-high temperature metasediment protoliths of southern Madagascar and India. In: *Supercontinents and Earth Evolution Symposium* (eds. Wingate, M. T. D. & Pisarevsky, S. A.). Geological Society of Australia Inc., Fremantle, volume 81, 121.
- Collins, A. S. & Pisarevsky, S. A., 2005. Amalgamating eastern Gondwana: The evolution of the Circum-Indian Orogens. *Earth-Science Reviews*, **71**, 229–270.
- Collins, A. S. & Windley, B. F., 2002. The tectonic evolution of Central and Northern Madagascar and its place in the final assembly of Gondwana. *The Journal of Geology*, **110**, 325–339.
- Das, S., Bhattacharya, A., Raith, M. M., Bhadra, S. & Banerjee, M., 2006. Aluminous sapphirine granulites from the Eastern Ghats Belt (India): Phase relations and relevance to counterclockwise P-T history. *European Journal of Mineralogy*, **18**, 35–48.
- de la Roche, H., 1963. Etude géologique de l'extrême Sud-Est de Madagascar (zone d'intensité métamorphique élevée). *Annales géologiques de Madagascar*, **28**, 1–101.
- de Wit, M. J., Bowring, S. A., Ashwal, L. D., Randrianasolo, L. G., Morel, V. P. I. & Rambeloson, R. A., 2001. Age and tectonic evolution of Neoproterozoic ductile shear zones in southwestern Madagascar, with implications for Gondwana studies. *Tectonics*, **20**, 1–45.
- Ellis, D. J. & Hiroi, Y., 1997. Secondary siderite-oxide-sulphide and carbonate-andalusite assemblages in cordierite granulites from Sri Lanka: post-granulite facies fluid evolution during uplift. *Contributions to Mineralogy and Petrology*, **127**, 315–335.
- Ellis, D. J., Sheraton, J. W., England, R. N. & Dallwitz, W. B., 1980. Osumilite-sapphirine-quartz granulites from Enderby Land Antarctica - Mineral assemblages and reactions. *Contributions to Mineralogy and Petrology*, **72**, 123–143.

- Fitzsimons, I. C. W. & Harley, S. L., 1994. Garnet coronas in scapolite-wollastonite calc-silicates from East Antarctica; the application and limitations of activity-corrected grids. *Journal of Metamorphic Geology*, **12**, 761–777.
- Fitzsimons, I. C. W. & Hulscher, B., 2005. Out of Africa: detrital zircon provenance of central Madagascar and Neoproterozoic terrane transfer across the Mozambique Ocean. *Terra Nova*, **17**, 224–235.
- Fuhrmann, M. L. & Lindsley, D. H., 1988. Ternary-feldspar modelling and thermometry. *American Mineralogist*, **73**, 201–215.
- Goncalves, P., Nicollet, C. & Montel, J.-M., 2004. Petrology and in situ U-Th-Pb monazite geochronology of ultrahigh-temperature metamorphism from the Andriamena mafic unit, North-Central Madagascar. Significance of a petrographical P-T path in a poly-metamorphic context. *Journal of Petrology*, **45**, 1923–1957.
- Green, D. H. & Ringwood, A. E., 1967. An experimental investigation of the gabbro to eclogite transformation and its petrological applications. *Geochimica et Cosmochimica Acta*, **31**, 767–833.
- Green, D. H. & Ringwood, A. E., 1972. A comparison of experimental data on the gabbro-garnet granulite-eclogite transition. *Journal of Geology*, **80**, 277–288.
- Grew, E. S., 1982. Osumilite in the sapphirine-quartz terrane of Enderby Land, Antarctica: implications for osumilite petrogenesis in the granulite facies. *American Mineralogist*, **67**, 762–787.
- Harley, S. L., 1989. The origins of granulites: a metamorphic perspective. *Geological Magazine*, **126** (3), 215–247.
- Harley, S. L., 1993. Sapphirine granulites from the Vestfold Hills, East Antarctica: geochemical and metamorphic evolution. *Antarctic Science*, **5**, 389–402.
- Harley, S. L. & Green, D. H., 1982. Garnet-orthopyroxene barometry for granulites and peridotites. *Nature*, **300**, 697–701.
- Harley, S. L., Hensen, B. J. & Sheraton, J. W., 1990. Two-stage decompression in orthopyroxene-sillimanite granulites from Forefinger Point, Enderby Land, Antarctica: implications for the evolution of the Archaean Napier Complex. *Journal of metamorphic Geology*, **8**, 591–613.
- Harley, S. L. & Motoyoshi, Y., 2000. Al zoning in orthopyroxene in a sapphirine quartzite: evidence for >1120 °C UHT metamorphism in the Napier Complex, Antarctica, and implications for the entropy of sapphirine. *Contributions to Mineralogy and Petrology*, **138**, 293–307.

- Hensen, B. J., 1977. The stability of osumilite in high grade metamorphic rocks. *Contributions to Mineralogy and Petrology*, **64**, 197–204.
- Holland, T. J. B. & Powell, R., 1998. An internally consistent thermodynamic dataset for phases of petrological interest. *Journal of metamorphic Geology*, **16**, 309–343.
- Hottin, G., 1976. Présentation et essai d'interprétation du Précambrien de Madagascar. *Bulletin du Bureau de Recherches géologiques et minière*, **2**, 117–153.
- Ito, M., Suzuki, K. & Yogo, S., 1997. Cambrian granulite to upper amphibolite facies metamorphism of post-797 Ma sediments in Madagascar. *Journal of Earth and Planetary Sciences, Nagoya University*, **44**, 89–102.
- Janardhan, A. S., 1999. Southern granulite terrain, south of the Palghat-Cauvery shear zone; implications for India-Madagascar connection. In: *Madagascar within Gondwanaland*, International Association for Gondwana Research, Osaka, Japan. 463–469.
- John, T., Schenk, V., Haase, K., Scherer, E. & Tembo, F., 2003. Evidence for a Neoproterozoic ocean in south-central Africa from mid-oceanic-ridge-type geochemical signatures and pressure-temperature estimates of Zambian eclogites. *Geology*, **31**, 243–246.
- John, T., Schenk, V., Mezger, K. & Tembo, F., 2004a. Timing and P-T evolution of whiteschist metamorphism in the Lufilian Arc - Zambesi Belt orogen (Zambia): implications for the assembly of Gondwana. *Journal of Geology*, **112**, 71–90.
- John, T., Scherer, E. E., Haase, K. & Schenk, V., 2004b. Trace element fractionation during fluid-induced eclogitization in a subducting slab: trace element and Lu–Hf–Sm–Nd isotope systematics. *Earth and Planetary Science Letters*, **227**, 441–456.
- Jöns, N. & Schenk, V., 2004. Petrology of whiteschists and associated rocks at Mautia Hill (Tanzania): Fluid infiltration during high-grade metamorphism? *Journal of Petrology*, **45**, 1959–1981.
- Jöns, N. & Schenk, V., in review. Relics of the Mozambique Ocean in the central East African Orogen: evidence from the Vohibory Block of southern Madagascar. *Geology*.
- Jöns, N., Schenk, V., Appel, P. & Razakamanana, T., 2006. Two-stage metamorphic evolution of the Bemarivo Belt of Northern Madagascar: constraints from reaction textures and in-situ monazite dating. *Journal of metamorphic Geology*, **24**, 329–347.
- Joo', J., 1968. Structure et minéralisation du gisement de phlogopite d'Ampandrandava Sud de Madagascar. *Comptes Rendus de la semaine géologique*, 71–75.
- Kelsey, D. E., White, R. W. & Powell, R., 2003. Orthopyroxene-sillimanite-quartz assemblages: distribution, petrology, quantitative P-T-X constraints and P-T paths. *Journal of metamorphic Geology*, **21**, 439–453.

- Kelsey, D. E., White, R. W. & Powell, R., 2005. Calculated phase equilibria in K_2O – FeO – MgO – Al_2O_3 – SiO_2 – H_2O for silica-undersaturated sapphirine-bearing mineral assemblages. *Journal of metamorphic Geology*, **23**, 217–239.
- Koziol, A. M., 1989. Recalibration of the garnet-plagioclase- Al_2SiO_5 -quartz (GASP) geobarometer and application to natural parageneses. *EOS Transactions*, **70**, 493.
- Kretz, R., 1983. Symbols for rock-forming minerals. *American Mineralogist*, **68**, 277–279.
- Kröner, A., Braun, I. & Jaeckel, P., 1996. Zircon geochronology of anatexitic melts and residues from a high-grade pelitic assemblage at Ihosy, southern Madagascar: evidence for Pan-African granulite metamorphism. *Geological Magazine*, **133**, 311–323.
- Kröner, A., Hegner, E., Collins, A. S., Windley, B. F., Brewer, T. S., Razakamanana, T. & Pidgeon, R. T., 2000. Age and magmatic history of the Antananarivo Block, Central Madagascar, as derived from zircon geochronology and Nd isotopic systematics. *American Journal of Science*, **300**, 251–288.
- Kröner, A., Windley, B. F., Jaeckel, P., Brewer, T. S. & Razakamanana, T., 1999. New zircon ages and regional significance for the evolution of the Pan-African Orogen in Madagascar. *Journal of the Geological Society of London*, **156**, 1125–1135.
- Kusky, T. M., Abdelsalam, M., Tucker, R. D. & Stern, R. J., 2003. Evolution of the East African and related orogens, and the assembly of Gondwana. *Precambrian Research*, **123**, 81–85.
- Lacroix, A., 1922. *Minéralogie de Madagascar*, volume 1-3. Société d'éditions géographiques, maritimes et coloniales, Paris.
- Langer, K., Platonov, A. N., Matsuk, S. S. & Andrut, M., 1994. Electronic absorption spectra of chromium-bearing sapphirine. *Physics and Chemistry of Minerals*, **21**, 29–35.
- Ludwig, K. R., 2001. *SQUID 1.02: a user's manual*, Berkeley Geochronology Center Special Publication, volume 2.
- Ludwig, K. R., 2003. *User's manual for Isoplot 3.00: a geochronological toolkit for Microsoft Excel*, Berkeley Geochronology Center Special Publication, volume 4.
- Markl, G., Bäuerle, J. & Grujic, D., 2000. Metamorphic evolution of Pan-African granulite-facies metapelites from southern Madagascar. *Precambrian Research*, **102**, 47–68.
- Martelat, J.-E., Lardeaux, J.-M., Nicollet, C. & Rakotondrazafy, M. A. F., 2000. Strain pattern and late Precambrian deformation history in southern Madagascar. *Precambrian Research*, **102**, 1–20.
- Martelat, J. E., Lardeaux, J. M., Nicollet, C. & Rakotondrazafy, R., 1999a. Exhumation of granulites within a transpressive regime; an example from southern Madagascar. *Gondwana Research*, **2**, 363–367.

- Martelat, J. E., Nicollet, C., Lardeaux, J.-M., Vidal, G. & Rakotondrazafy, R., 1997. Lithospheric tectonic structures developed under high-grade metamorphism in the Southern part of Madagascar. *Geodinamica Acta (Paris)*, **10** (3), 94–114.
- Martelat, J.-E., Schulmann, K., Lardeaux, J.-M., Nicollet, C. & Cardon, H., 1999b. Granulite microfabrics and deformation mechanisms in southern Madagascar. *Journal of structural geology*, **21**, 671–687.
- Martelat, J.-E., Vidal, G., Lardeaux, J.-M., Nicollet, C. & Rakotondrazafy, R., 1995. Images spatiales et tectonique profonde des continents: l'exemple du Sud-Ouest de Madagascar. *Comptes Rendus de l'Académie des Sciences, Série II*, **321**, 325–332.
- Meert, J. G., 2003. A synopsis of events related to the assembly of eastern Gondwana. *Tectonophysics*, **362**, 1–40.
- Meert, J. G., van der Voo, R. & Ayub, S., 1995. Paleomagnetic investigation of the Neoproterozoic Gagwe lavas and Mbozi Complex, Tanzania and the assembly of Gondwana. *Precambrian Research*, **74**, 225–244.
- Moecher, D. P., Essene, E. J. & Anovitz, L. M., 1988. Calculation and application of clinopyroxene-garnet-plagioclase-quartz geobarometers. *Contributions to Mineralogy and Petrology*, **100**, 92–106.
- Möller, A., Mezger, K. & Schenk, V., 2000. U-Pb dating of metamorphic minerals: Pan-African metamorphism and prolonged slow cooling of high pressure granulites in Tanzania, East Africa. *Precambrian Research*, **104**, 123–146.
- Montel, J.-M., Foret, S., Veschambre, M., Nicollet, C. & Provost, A., 1996. Electron microprobe dating of monazite. *Chemical Geology*, **131**, 37–53.
- Nichols, G. T., Berry, R. F. & Green, D. H., 1992. Internally consistent gahnitic spinel-cordierite-garnet equilibria in the FMASHZn system: geothermobarometry and applications. *Contributions to Mineralogy and Petrology*, **111**, 362–377.
- Nicollet, C., 1983. Existence de granulites de haute pression à clinopyroxène-grenat dans les formations précambriennes du Vohibory (SW de Madagascar). *Comptes Rendus de l'Académie des Sciences, Série II*, **297**, 145–148.
- Nicollet, C., 1985a. Les gneiss rubanés à cordiérite et grenat d'Ihoshy: un marqueur thermo-barométrique dans le Sud de Madagascar. *Precambrian Research*, **28**, 175–185.
- Nicollet, C., 1985b. Origine des amphibolites à saphirine, corindon et grenat de la formation précambrienne du Vohibory (SW de Madagascar). *Comptes Rendus de l'Académie des Sciences, Série II*, **301**, 167–170.

- Nicollet, C., 1986. Saphirine et staurotite riche en magnésium et chrome dans les amphibolites et anorthosites à corindon du Vohibory Sud, Madagascar. *Bulletin de Minéralogie*, **109**, 599–612.
- Nicollet, C., 1990a. Crustal evolution of the granulites of Madagascar. In: *Granulites and Crustal Evolution* (eds. Vielzeuf, D. & Vidal, P.), Kluwer Academic Publishers. 291–310.
- Nicollet, C., 1990b. Occurrences of grandidierite, serendibite and tourmaline near Ihoshy, southern Madagascar. *Mineralogical Magazine*, **54**, 131–133.
- Nixon, P. H., Reedman, A. J. & Burns, L. K., 1973. Sapphirine-bearing granulites from Labwor, Uganda. *Mineralogical Magazine*, **39**, 420–428.
- Olesch, M. & Seifert, F., 1981. The restricted stability of osumilite under hydrous conditions in the system K_2O – MgO – Al_2O_3 – SiO_2 – H_2O . *Contributions to Mineralogy and Petrology*, **76**, 362–367.
- Paquette, J. L., Nédélec, A., Moine, B. & Rakotondrazafy, M., 1994. U-Pb, single zircon Pb-evaporation, and Sm-Nd isotopic study of a granulite domain in SE Madagascar. *The Journal of Geology*, **102**, 523–538.
- Pierdzig, S., 1992. *Granulitfazielle Gesteinsserien der Ampandrandava-Formation Südmadagaskars und die Entstehung ihrer Phlogopit-Mineralisationen*, Bonner Geowissenschaftliche Schriften, volume 4. Holos-Verlag, Bonn.
- Pili, E., Ricard, Y., Lardeaux, J.-M. & Sheppard, S. M. F., 1997. Lithospheric shear zones and mantle-crust connections. *Tectonophysics*, **280**, 15–29.
- Powell, R. & Holland, T. J. B., 1994. Optimal geothermometry and geobarometry. *American Mineralogist*, **79**, 120–133.
- Powell, R., Holland, T. J. B. & Worley, B., 1998. Calculating phase diagrams involving solid solutions via non-linear equations, with examples using THERMOCALC. *Journal of metamorphic Geology*, **16**, 577–588.
- Raase, P. & Schenk, V., 1994. Petrology of granulite-facies metapelites of the Highland Complex, Sri Lanka; implications for the metamorphic zonation and the P-T path. In: *Tectonic, metamorphic and isotopic evolution of deep crustal rocks, with special emphasis on Sri Lanka* (eds. Raith, M. & Hoernes, S.), Elsevier, Amsterdam. 265–294.
- Rakotondrazafy, M. A. F., Moine, B. & Cuney, M., 1996. Mode of formation of hibonite ($CaAl_{12}O_{19}$) within the U-Th skarns from the granulites of S-E Madagascar. *Contributions to Mineralogy and Petrology*, **123**, 190–201.
- Razakamanana, T., 1990. *Les formations proterozoïques de Vohidava: Un témoin de l'évolution polytectono-métamorphique du Centre Sud Madagascar*. Diplôme de doctorat de troisième cycle, Université d'Antananarivo.

- Razakamanana, T., Ackermann, D. & Windley, B. F., 2000. Högbomite in migmatitic paragneiss in the Betroka shear belt, Vohidava area, Precambrian of southern Madagascar. *Mineralogy and Petrology*, **68**, 257–269.
- Razakamanana, T., Ackermann, D. & Windley, B. F., 2006. Metamorphic evolution of sapphirine-bearing rocks from Vohidava area, Southern Madagascar: structural and tectonic implications. In: *Proceedings of the German-Malagasy Research Cooperation in Life and Earth Sciences* (eds. Schwitzer, C., Brandt, S., Ramilijaona, O., Rakotomalala Razanahoera, M., Ackermann, D., Razakamanana, T. & Ganzhorn, J. U.), Concept Verlag, Berlin. 41–60.
- Ridley, J., 1989. Vertical movement in orogenic belts and the timing of metamorphism relative to deformation. In: *Evolution of metamorphic belts* (eds. Daly, J. S., Cliff, R. A. & Yardley, B. W. D.), Geological Society of London, London. 103–115.
- Robinson, P., Hollocher, K. T., Tracy, R. J. & Dietsch, C. W., 1982. High grade Acadian regional metamorphism in South-central Massachusetts. In: *Guidebook for fieldtrips in Connecticut and South central Massachusetts*, State Geological and Natural History Survey of Connecticut, Storrs. 289–339.
- Sandiford, M., Neall, F. B. & Powell, R., 1987. Metamorphic evolution of aluminous granulites from Labwor Hills, Uganda. *Contributions to Mineralogy and Petrology*, **95**, 217–225.
- Schenk, V., 1984. Petrology of felsic granulites, metapelites, metabasics, ultramafics, and metacarbonates from Southern Calabria (Italy): Prograde metamorphism, uplift and cooling of a former lower crust. *Journal of Petrology*, **25**, 255–298.
- Schenk, V., 1989. P-T-t path of the lower crust in the Hercynian fold belt of southern Calabria. In: *Evolution of Metamorphic Belts* (eds. Daly, J., Cliff, R. & Yardley, B.), Blackwell Scientific Publications, Cambridge. 337–342.
- Schenk, V., 1990. The exposed crustal cross-section of southern Calabria, Italy: Structure and evolution of a segment of Hercynian crust. In: *Exposed cross-sections in the continental crust* (eds. Salisbury, M. H. & Fountain, D. M.), Kluwer Academic Publishers. 21–42.
- Schulmann, K., Schaltegger, U., Thompson, A. B. & Edel, J.-B., 2002. Rapid burial and exhumation during orogeny: thickening and synconvergent exhumation of thermally weakened and thinned crust (Variscan Orogen in Western Europe). *American Journal of Science*, **302**, 856–879.
- Steiger, R. H. & Jäger, E., 1977. Subcommittee on geochronology: convention on the use of decay constants in geo- and cosmochronology. *Earth and Planetary Science Letters*, **36**, 359–362.

- Stern, R. J., 1994. Arc assembly and continental collision in the Neoproterozoic East African Orogen: Implications for the consolidation of Gondwanaland. *Annual Reviews of Earth and Planetary Sciences*, **22**, 319–351.
- Thompson, A. B., Schulmann, K. & Ježek, J., 1997. Extrusion tectonics and elevation of lower crustal metamorphic rocks in convergent orogens. *Geology*, **25**, 491–494.
- Warren, R. G., Hensen, B. J. & Ryburn, R. J., 1987. Wollastonite and scapolite in Precambrian calc-silicate granulites from Australia and Antarctica. *Journal of metamorphic Geology*, **5**, 213–223.
- Waters, D. J., 1991. Hercynite-quartz granulites: phase relations, and implications for crustal processes. *European Journal of Mineralogy*, **3**, 367–386.
- Wiedenbeck, M., Allé, P., Corfu, F., Griffin, W. L., Meier, M., Oberli, F., von Quadt, A., Roddick, J. C. & Spiegel, W., 1995. Three natural zircon standards for U–Th–Pb, Lu–Hf, trace element and REE analyses. *Geostandards Newsletter*, **19**, 1–23.
- Windley, B. F., Razafiniparany, A., Razakamanana, T. & Ackermann, D., 1994. Tectonic framework of the Precambrian of Madagascar and its Gondwana connections: a review and reappraisal. *Geologische Rundschau*, **83**, 642–659.

Chapter 5

Petrology of whiteschists and associated rocks at Mautia Hill (Tanzania): Fluid infiltration during high-grade metamorphism?

5.1 Abstract

Talc-kyanite schists (whiteschists), magnesiohornblende-kyanite-talc-quartz schists, and enstatite-sapphirine-chlorite schists occur at Mautia Hill in the East African Orogen of Tanzania. They are associated with metapelites and garnet-clinopyroxene-quartz metabasites. Geobarometry (GASP/GADS equilibria) applied to the latter two rock types indicates a peak pressure of $P = 10\text{--}11$ kbar. These results are confirmed by the high f_{O_2} assemblage hollandite-kyanite-quartz and late-stage mangian andalusite that contains up to 19.5 mole % Mn_2SiO_5 . Maximum temperatures of $T = 720^\circ\text{C}$ are inferred from late-stage yoderite + quartz. A clockwise P - T evolution is constrained by prograde kyanite inclusions in metapelitic garnet and late-stage reaction rims of cordierite between green yoderite and talc that reflect conditions at least 3-4 kbar below the peak pressure. Oxidising conditions are recorded throughout the metamorphic history of the whiteschists and chlorite schists as indicated by the presence of haematite coexisting with pseudobrookite and/or rutile. Increasing water activity near peak pressures is thought to have led to the breakdown of the high-pressure assemblages (Tlc-Ky-Hem and Mg-Hbl-Ky-Hem) and the subsequent formation of certain uncommon minerals e.g., yellow sapphirine, Mn-andalusite, green and purple yoderite, piemontite, and boron-free kornerupine. The proposed increase in water activity is attributed to fluid infiltration resulting from the devolatilisation of underlying sediments during metamorphism.

5.2 Introduction

It has been shown experimentally that the critical mineral assemblage of whiteschists, talc and kyanite, is only stable under relatively low geothermal gradients that are realised in the high-pressure part of the amphibolite facies and in the eclogite facies (Schreyer & Seifert, 1969; Massonne, 1989). In agreement with the experimental data, it has been found worldwide in different orogenic belts that whiteschists are formed either during crustal thickening or subduction, i.e. in geodynamic regimes that are characterised by clockwise P - T paths. Whiteschists occur in the Alps (Abraham *et al.*, 1974; Chopin *et al.*, 1991; Chopin & Monié, 1984; Pawlig & Baumgartner, 2001), the Hindukush (Kulke & Schreyer, 1973; Schreyer, 1977; Faryad, 1999), Tasmania (Råheim & Green, 1974), and the Dabie Shan (Rolfo *et al.*, 2000) in China. They occur also in Precambrian belts, such as the Zambezi Belt of Zambia and Zimbabwe (Vrána & Barr, 1972; Johnson & Oliver, 2002; John *et al.*, 2004) and the Mozambique Belt of Tanzania (McKie, 1959). Therefore it is likely, even in cases where eclogites and blueschists are lacking, that whiteschists mark the sites of palaeo-collision zones. In contrast to the geodynamic settings of whiteschist metamorphism, the formation of whiteschists as a rock type, which generally displays a simple MgO-Al₂O₃-SiO₂-H₂O (MASH)-silicate mineralogy coexisting with iron oxides or sulfides, is more diverse and controversial. In several cases it has been demonstrated that whiteschist formation resulted from metasomatic processes, the timing of which is mostly unknown. Thus, whiteschists may be used to study fluid-rock interaction processes at high-pressure amphibolite and eclogite facies conditions during crustal thickening. In many studied examples the precursor to whiteschists is granitic (Rolfo *et al.*, 2000; Pawlig & Baumgartner, 2001). However, metabasic rocks have also been proposed (Johnson & Oliver, 2002). Only a few occurrences are known where metasedimentary protoliths are likely (McKie, 1959; Schreyer & Abraham, 1976). In these cases, whiteschists occur in close association with other metasedimentary rocks (e. g., metapelites, marbles, quartzites, metaevaporites). In several whiteschist occurrences, evidence for high oxygen fugacity has been found (Vrána & Barr, 1972; Grew *et al.*, 1998; Johnson & Oliver, 2002), resulting in iron occurring predominantly in the trivalent state and being nearly restricted to haematite. It occurs only in small amounts in the coexisting silicates, which are near-Mg end-members. In other cases, iron is nearly confined to sulfides (Kulke & Schreyer, 1973; Pawlig & Baumgartner, 2001).

The MASH-Fe₂O₃ schists of Mautia Hill (Tanzania, Fig. 5.1) became famous in the 1950's because they feature an unusually large mineralogical variety compared to more simple whiteschist mineralogies that occur elsewhere. They therefore provide a good opportunity to investigate the processes and metamorphic boundary conditions leading to whiteschist formation. Up to now, Mautia Hill is the only known occurrence of purple yoderite (McKie, 1959) and yellow sapphirine (McKie, 1963a). Other minerals, e.g., enstatite, magnesiochlorite, högbomite (McKie, 1963b), pseudobrookite (McKie, 1963a), boron-bearing kornerupine (McKie, 1965), green yoderite (McKie & Bradshaw, 1966), piemontite, and manganian andalusite (Basu & Mruma, 1985) have also been found. In the course of this study, additional minerals were discovered, such as yellow spinel, cerianite,

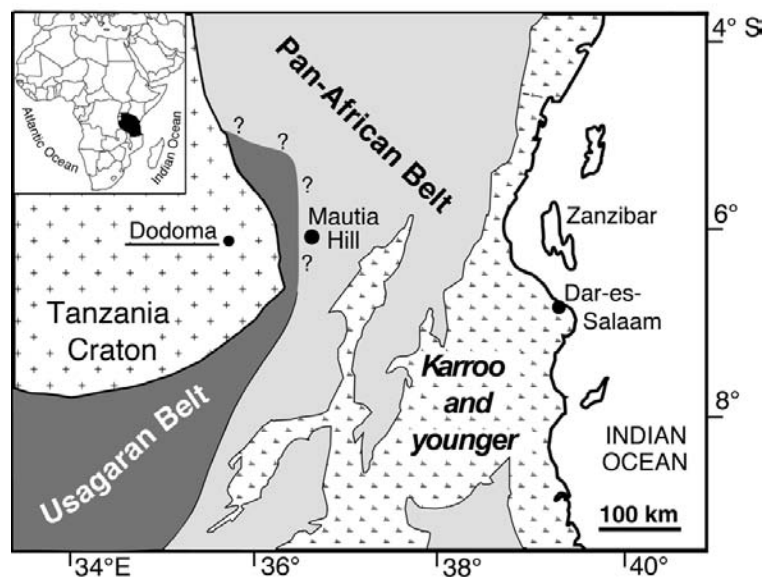


Figure 5.1: Simplified geological map of part of Tanzania. The Archean Tanzania Craton is flanked by the Paleoproterozoic Usagaran Belt and the Neoproterozoic Pan-African Belt.

cordierite, anthophyllite, boron-free kornerupine, geikielite, and hollandite. Some of these were found to occur not only in whiteschists, but also in Ca-rich amphibole-chlorite schists. Further rock types occurring at Mautia are metabasites, metapelites, marbles, quartzites, and pegmatites. The great variety of rock types allows the application of conventional geothermobarometers in addition to equilibria of the uncommon mineral assemblages to characterise the P - T -fluid conditions that prevailed during whiteschist metamorphism. Phase petrological considerations, thermobarometry and mineral-chemical data were used to estimate the f_{O_2} and a_{H_2O} conditions and to determine the time of fluid infiltration, which seems to have been essential for the formation of the uncommon whiteschist mineralogy at Mautia Hill.

5.3 Previous work and geological setting

Mautia Hill is located approximately 10 km NNE of Kongwa (Mpwapwa District, central Tanzania, Fig. 5.1). The hill is about 2.0 km long, 0.5 km wide, east trending and rising some tens of meters above the surrounding peneplain (Fig. 5.2). The geology of Mautia Hill was first mentioned in 1938, when Temperley mapped the sheet “Mpwapwa” (Temperley, 1938). He described the yoderite bearing schists as glaucophane-kyanite gneisses. Yoderite and other minerals were examined in detail in the 1950’s and 1960’s (McKie, 1959, 1963a,b, 1965; McKie & Bradshaw, 1966). Part of the P - T history of Mautia Hill has been deduced on the basis of fluid inclusion studies (Basu & Mruma, 1985; Mruma, 1986; Mruma & Basu, 1987). Phase petrological studies of Mautia Hill rocks are only preliminary and have not been published (Möller, 1995; Rickers, 1996). Mautia Hill was mapped in detail by T. Heinrichs in 1981 (Heinrichs, unpublished data; Fig. 5.2). Several rock types (metabasites, metapelites, marbles, whiteschists, chlorite schists, pegmatites, quartzites,

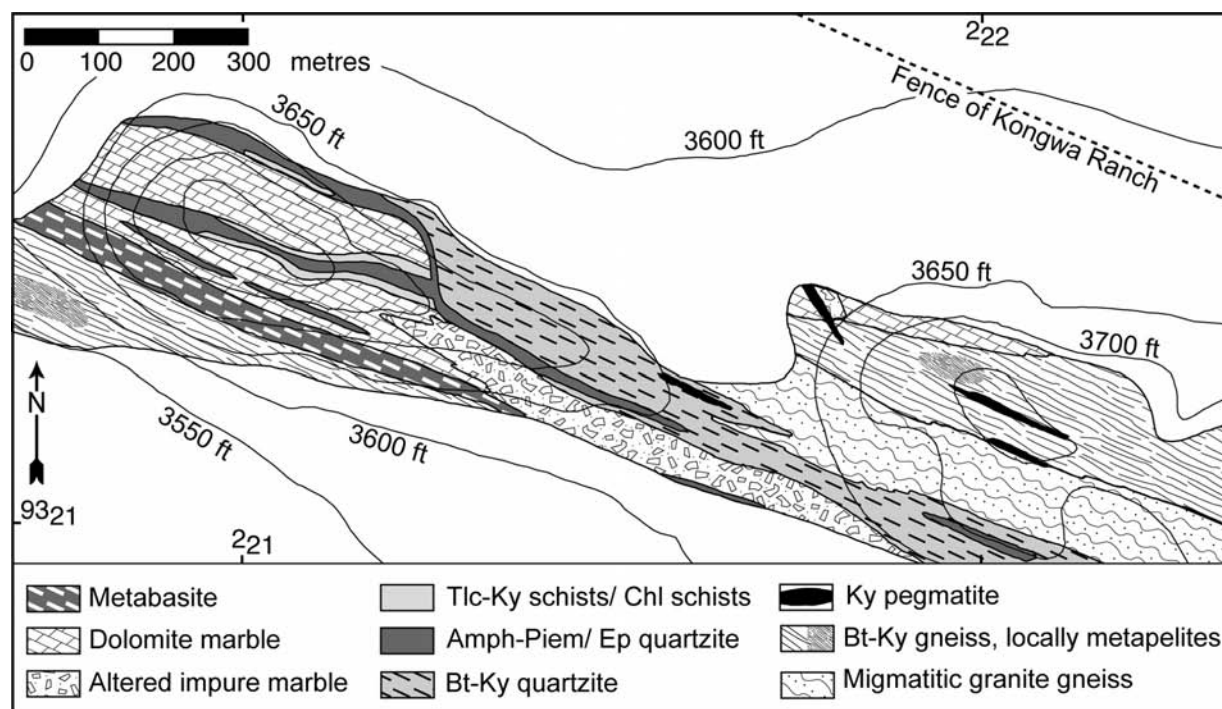


Figure 5.2: Geological map of Mautia Hill, as mapped in 1981 by T. Heinrichs (unpublished data). Contour interval: 50 ft., Mercator grid.

migmatitic gneisses) occur at Mautia Hill as thin layers parallel to the elongation of the hill, but are poorly exposed and most only occur as boulders. The best-exposed rocks are a marble and a Ky-Bt quartzite (mineral abbreviations after Kretz, 1983) that form the crest of the hill. The great lithological variety cannot be tracked into the surrounding plain, which consists of uniform migmatitic granite gneisses and is mainly covered by alluvial sediments. The earliest structure observed is a schistosity (S_1) that is isoclinally refolded by a later deformational event (D_2). The resulting S_2 -foliation trends WNW. A ubiquitous L_2 lineation is parallel to F_2 fold axes dipping in an ESE direction. It is defined by the alignment of large grains of kyanite or amphibole in different rock types. The F_2 folding is associated with the formation of the peak assemblage (En-Spr-Chl) in chlorite schists (Fig. 5.3). The close association and common deformation history of the different rock types makes it most likely that all lithological units at Mautia Hill experienced the same metamorphic evolution.

Mautia Hill is situated near the western border of the Pan-African Mozambique Belt, the formation of which is attributed to the collision of East and West Gondwana (McWilliams, 1981; Stern, 1994). To the west of Mautia Hill is the Paleoproterozoic (2.0–1.8 Ga) Usagaran Belt, which itself adjoins the Archean (2.6–2.5 Ga) Tanzania Craton (Fig. 5.1). The Mozambique Belt consists mainly of uniform granulite-facies orthogneisses (Appel *et al.*, 1998), which contrasts with the great variety of rock types occurring at Mautia Hill. In addition, the metamorphic evolution of rocks at Mautia Hill is distinct to that of the

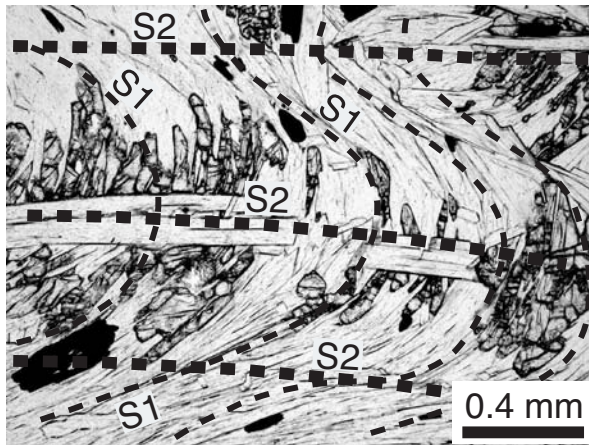


Figure 5.3: Peak-metamorphic enstatite in F_2 fold hinges and magnesiochlorite in the axial plane (S_2) (Spr-En-Chl schist, Mau27B).

granulites further east. The P - T path for the whiteschists is inferred to be clockwise and the age of metamorphism seems to be at least 50 Ma younger (A. Möller pers. com.) than that in rocks of the Pan-African Mozambique Belt further east (610–655 Ma; Möller *et al.*, 2000), where an anticlockwise P - T evolution has been proposed (Appel *et al.*, 1998).

5.4 Petrography and mineral chemistry

5.4.1 Analytical procedure

The chemical compositions of minerals were determined with a “JEOL Superprobe JXA-8900R” electron microprobe at the University of Kiel, equipped with five wavelength-dispersive spectrometers (WDS). The accelerating potential was 15 kV resp. 20 kV for a beam current of 20 nA. Sample spot sizes were 1–5 μm in diameter. Both synthetic and natural mineral standards were used. The raw data were corrected using the CITZAF method (Armstrong, 1995).

The boron content of kornrupine was also measured with the electron microprobe. The accelerating voltage was 10 kV for a beam current of 40 nA and a spot size of 5 μm . We used LDE2 (2d = 98 Å) and LDEB (2d = 145 Å) crystals. Natural danburite (Dyar *et al.*, 2002) was used as a calibration sample. Analysis was performed with 100 s counting time on peak and 50 s on each lower and upper background. For comparison we also performed measurements in peak area integration mode (15000 s total per scan, step size 50 μm).

5.4.2 Metapelites

This rock type occurs within the widespread Bt-Ky quartzites (Fig. 5.2). It is porphyroblastic, medium- to coarse-grained and composed of quartz (30–40 vol.%), biotite (25–30 vol.%), plagioclase (15–20 vol.%), and garnet (5–15 vol.%). Accessory minerals are haematite, rutile, monazite, zircon, and apatite. The rocks show a well-developed schistosity, except for samples with a lower biotite content which are more massive. Since they

do not contain alkali-feldspar, they are more precisely characterised as K-poor semipelites. Representative microprobe analyses are given in Table 5.1.

Ellipsoidal *garnet* forms porphyroblasts that contain inclusions of Pl, Qtz, and Ky. Apart from a narrow (80 μm) re-equilibrated rim, it is chemically unzoned. It has an X_{Mg} (= $\text{Mg}/(\text{Mg}+\text{Fe}^{2+})$) of 0.4, X_{Alm} = 0.55, X_{Prp} = 0.3–0.4, X_{Grs} = 0.05–0.1, and X_{Sps} < 0.05. No significant amount of Fe^{3+} was detected. The matrix *plagioclase* shows inverse zonation with an anorthite content of 0.26–0.32 mole% in the core and 0.32–0.38 mole% at the rim. Some inclusions in garnet have a slightly lower X_{An} ($\text{Ca}/(\text{Ca} + \text{Na} + \text{K})$). *Biotite* occurs as large laths within the matrix of the rock. Assuming $\text{FeO} = \text{Fe}_{tot}$ the X_{Mg} is 0.7–0.9. Locally, Bt is intergrown with haematite. *Kyanite* crystals are about 2.5 mm long and show conspicuous green colour. Microprobe analyses point to a formula $\text{Al}_{1.95}\text{Fe}_{0.05}^{3+}\text{SiO}_5$.

5.4.3 Metabasites

The metabasites crop out at the southwestern slope of the hill. They can be subdivided into two groups. The first one is a medium-grained, clearly foliated rock, which consists of plagioclase (15–25 vol.%), garnet (20–30 vol.%), clinopyroxene (20–25 vol.%), and hornblende (20–45 vol.%). The metabasites of the second group have a more massive appearance, and they contain about 15 vol.% clinozoisite. Other constituents are plagioclase (40 vol.%), clinopyroxene (15 vol.%), and garnet (15 vol.%). accessory minerals are titanite, rutile, apatite, and quartz. Some microprobe analyses are given in Table 5.1.

Garnet is homogeneous except for a thin rim (40 μm) that re-equilibrated during cooling. The X_{Mg} ratio is in the range from 0.1 to 0.2 with a small increase towards the rim. The range of garnet compositions is X_{Alm} = 0.4–0.5, X_{Prp} = 0.10–0.15, X_{Sps} < 0.05, and X_{Grs} \approx 0.35. In Czo-bearing rocks the X_{Grs} is slightly higher (0.40). *Plagioclase* mainly occurs as intergranular grains. Its anorthite content is in the range from 40 to 43% in the core and up to 50% towards the rim. In Czo-rich rocks these values are slightly higher. *Clinopyroxene* is characterised by low Na and X_{En} = 0.35, X_{Fs} = 0.17, X_{Wol} = 0.48, and an X_{Mg} ratio of ca. 0.7. It is unzoned and locally replaced by ferrotschermakitic hornblende. The X_{Mg} ratio of the *amphibole* is about 0.5. According to the nomenclature of Leake *et al.* (1997) most amphiboles are classified as magnesiohornblende and some as edenite ($\text{K} + \text{Na} = 0.47\text{--}0.53$ p.f.u., on the basis of 23 oxygens). *Clinozoisite* occurs in the matrix of the unfoliated metabasites and has a $\text{Fe}^{3+}/(\text{Fe}^{3+} + \text{Al})$ ratio of 0.18. In places it forms symplectitic Czo-Qtz intergrowths around garnet. In this case the Fe^{3+} content is slightly lower.

5.4.4 Other rock types

Biotite-kyanite quartzites

Bt-Ky quartzites locally form the crest of the hill (Fig. 5.2). They are coarse-grained, show a distinct schistosity and contain conspicuous green kyanite crystals, which are up to 15 centimetres long and form 15–25 vol.% of the rock. Further constituents are quartz (40–50

Table 5.1: Representative microprobe data for mineral phases within metapelites and metabasites.

Mineral: Analysis no:	Metapelites						Metabasites						
	Gr t core	Gr t rim	Pl core	Pl rim	Bt matrix	Hbl	Pl core	Pl rim	Gr t core	Gr t rim	Cpx core	Cpx rim	Hbl
	323	304	423	418	298	568	440	454	387	381	526	534	568
SiO ₂	39.5	39.78	61.64	61.1	38.62	57.39	56.32	38.38	38.50	51.19	51.25	44.88	44.88
TiO ₂	0.01	0.00	0.00	0.00	2.39	0.00	0.00	0.13	0.01	0.22	0.24	1.15	1.15
Al ₂ O ₃	22.41	22.43	24.30	24.79	17.34	26.58	27.17	21.61	21.32	2.93	2.96	12.60	12.60
Cr ₂ O ₃	0.00	0.00	0.00	0.00	0.03	0.00	0.00	0.06	0.10	0.02	0.02	0.10	0.10
Fe ₂ O ₃	0.06	0.00	0.05	0.07	n. c.	0.01	0.1	0.00	0.00	1.22	1.11	0.00	0.00
FeO	24.51	25.44	n. c.	n. c.	12.47	n. c.	n. c.	22.03	24.83	8.68	8.91	15.49	15.49
MgO	9.85	10.25	0.00	0.00	16.86	0.00	0.00	3.24	3.03	11.74	11.61	10.07	10.07
MnO	0.87	0.45	0.00	0.00	0.02	0.00	0.00	1.30	1.56	0.16	0.14	0.14	0.14
CaO	3.35	2.48	5.34	5.71	0.01	8.62	9.33	13.03	10.85	22.61	22.3	11.19	11.19
Na ₂ O	0.00	0.00	8.38	8.35	0.69	6.62	6.37	0.00	0.00	0.58	0.69	1.54	1.54
K ₂ O	0.00	0.00	0.08	0.07	8.39	0.03	0.05	0.00	0.00	0.00	0.00	0.23	0.23
BaO	n. d.	n. d.	0.00	0.00	0.18	0.00	0.00	n. d.	n. d.	0.00	0.00	0.03	0.03
Total	100.56	100.83	99.78	100.09	97.00	99.25	99.34	99.78	100.20	99.34	99.23	97.42	97.42
<i>Structural formulae</i>													
Si	3.00	3.01	2.74	2.71	5.55	2.59	2.55	3.00	3.02	1.93	1.94	6.63	6.63
Ti	0.00	0.00	0.00	0.00	0.26	0.00	0.00	0.01	0.00	0.01	0.01	2.19	2.19
Al	2.00	2.00	1.27	1.30	2.93	1.41	1.45	1.99	1.97	0.13	0.13	0.13	0.13
Cr	0.00	0.00	0.00	0.00	0.00	0.0	0.00	0.00	0.01	0.00	0.00	0.01	0.01
Fe ³⁺	0.06	0.0	0.05	0.07	n. c.	0.00	0.00	0.00	0.00	0.03	0.03	0.00	0.00
Fe ²⁺	1.55	1.61	n. c.	n. c.	1.50	n. c.	n. c.	1.44	1.63	0.27	0.28	1.91	1.91
Mg	1.11	1.15	0.00	0.00	3.61	0.00	0.00	0.38	0.35	0.66	0.65	2.22	2.22
Mn ²⁺	0.06	0.03	0.00	0.00	0.00	0.00	0.00	0.09	0.10	0.00	0.00	0.02	0.02
Ca	0.27	0.20	0.25	0.27	0.00	0.42	0.45	1.09	0.91	0.91	0.90	1.77	1.77
Na	0.00	0.00	0.72	0.72	0.19	0.58	0.56	0.00	0.00	0.04	0.05	0.44	0.44
K	0.00	0.00	0.00	0.00	1.54	0.00	0.00	0.00	0.00	0.00	0.00	0.04	0.04
Ba	n. d.	n. d.	0.00	0.00	0.01	0.00	0.00	n. d.	n. d.	0.00	0.00	0.00	0.00
Total	8.00	8.00	4.99	5.00	15.59	5.00	5.01	8.00	7.99	4.00	4.00	15.38	15.38
Oxygens	12	12	8	8	22	8	8	12	12	6	6	23	23

Fe³⁺ calculated assuming stoichiometry; Fe³⁺ in Hbl after (Droop, 1987); n. c. = not calculated; n. d. = not determined

vol.%), biotite (20–35 vol.%), and accessory haematite, rutile, apatite, and zircon. Local ore mineralization (chrysocolla, galena, chalcopyrite) is obvious. Biotite is Mg-rich with an X_{Mg} of 0.8–0.9. Kyanite contains 0.85–1.1 wt.% Fe_2O_3 and traces of Cr_2O_3 . Haematite and rutile may be intergrown.

Amphibole-piemontite/epidote quartzites

Both amphibole-piemontite quartzites and amphibole-epidote quartzites occur at Mautia Hill (Fig. 5.2). They consist of quartz (60–70 vol.%), amphibole (10–20 vol.%), and piemontite/epidote (15–20 vol.%). Rutile, apatite, haematite, and zircon occur as accessory phases. The amphibole is a tremolite with $X_{Mg} = 0.96–0.99$. Piemontite has a Mn_2O_3 content of 5–7 wt.%. Epidote contains just 0.3 wt.% Mn_2O_3 , but up to 9 wt.% Fe_2O_3 .

Marbles

Nearly pure dolomite marbles form the western crest of the hill (Fig. 5.2). Locally, they contain minerals like piemontite, margarite, amphibole, högbomite (general formula $(Fe,Mg)_{1.8}(Al,Ti)_{3.7}(O,OH)_8$), and late-stage sudoite $(Mg_2Al_3(Si_3Al)O_{10}(OH)_8)$. Piemontite is relatively Mn-poor (1.4–2.3 wt.% Mn_2O_3). Högbomite contains 4.5–5.0 wt.% TiO_2 .

Pegmatites

Pegmatites occur in some areas of the eastern part of the hill (Fig. 5.2). They are undeformed and consist of millimetre to centimetre crystals of quartz, plagioclase, biotite, apatite, green tourmaline (dravite), haematite, and green kyanite (up to 5 cm). The presence of kyanite points to exceptional high pressures for the formation of pegmatites.

Altered impure marbles

A thin band of impure marble occurs south of the crest of the hill. Beside dolomite also calcite, phlogopite, rutile, and tourmaline occur. Cavities are filled with spherulitic aggregates of chalcedony, pointing to late low-temperature alteration. Tourmaline is pleochroic from orange to pinkish and is classified as Al-poor member of the alkali group of Hawthorne & Henry (1999).

Migmatitic gneisses

Migmatitic gneisses have granitic compositions and consist of alkalifeldspar, plagioclase, biotite, and quartz. They are common in the eastern part of Mautia Hill (Fig. 5.2).

5.4.5 Whiteschists and chlorite schists

These unusual rock types contain rare silicate minerals, for which Mautia Hill is famous (McKie, 1959, 1963a,b, 1965; McKie & Bradshaw, 1966; Basu & Mruma, 1985; Mruma,

1986; Mruma & Basu, 1987; Fockenberg & Schreyer, 1994). The bulk chemistry of some of these rocks is well approximated by the system MgO-Al₂O₃-SiO₂-H₂O-Fe₂O₃ (MASH-Fe₂O₃). Other rocks additionally contain CaO and CO₂ (CMASH-CO₂-Fe₂O₃). Further components, such as FeO, MnO, Mn₂O₃, MnO₂, BaO, PbO, and TiO₂, are present in minor amounts, but some of them are important for the mineralogical variety. The CMASH-CO₂-Fe₂O₃ and MASH-Fe₂O₃ rocks form bands between dolomite marble and the Amph-Piem/Ep quartzite (Fig. 5.2).

Rocks of the CMASH-CO₂-Fe₂O₃ system

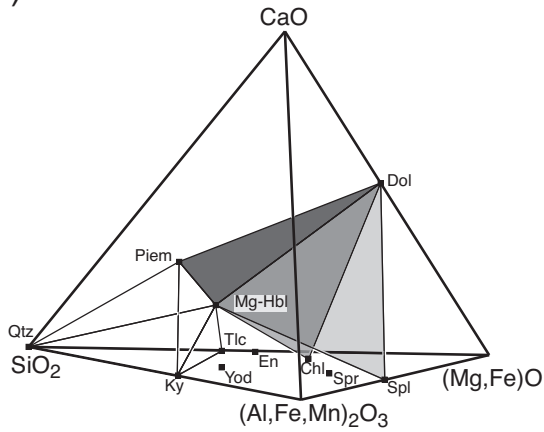
On the basis of their primary mineral assemblages, the rocks of the CMASH-CO₂-Fe₂O₃ chemical system have been subdivided into three sub-groups: amphibole-dolomite-chlorite schists, amphibole-spinel-dolomite schists, and hornblende-kyanite-talc-quartz schists. Representative microprobe analyses of selected minerals are given in Table 5.2. Phase relations and the compositional space of the different sub-groups are shown in Fig. 5.4a.

Amphibole-dolomite-chlorite schist. This Qtz-free rock type is medium- to coarse-grained, greyish-yellow in hand specimen and features a distinct foliation. It consists of magnesiochlorite (≤ 45 vol.%), amphibole (≤ 35 vol.%), and late-stage enstatite (≤ 20 vol.%). The amount of dolomite is highly variable, resulting in different carbonate/silicate ratios: the rock group includes nearly pure marbles but also nearly carbonate-free chlorite schists. Accessory minerals are haematite, rutile, talc, and zircon. Amphiboles are euhedral and lie in a finer-grained matrix of magnesiochlorite. Amphibole is partially replaced and surrounded by Chl-, Dol-, and En-bearing reaction rims. Haematite contains lamellae of rutile and/or geikielite and coexists with rutile.

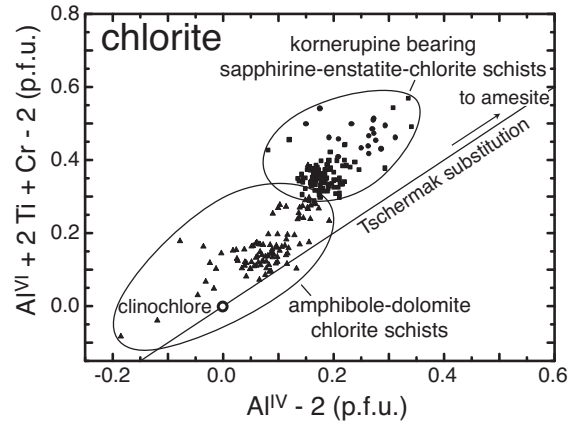
Amphibole-spinel-dolomite schist. This rock looks similar to the previously described one. Dolomite is subordinate in volume and in some patches the rock is made up just

Figure 5.4 (following page): (a) Phase relations and compositional space of CMASH-CO₂-Fe₂O₃ rocks from Mautia Hill (projected from haematite, hollandite, CO₂ and H₂O). The main rock types are situated on the three shaded plains and in the polyhedron Qtz-Ky-Tlc-Hbl-Piem. (b) Composition of magnesiochlorite from Amph-Dol-En-Chl schists (CMASH-CO₂-Fe₂O₃) and Krn-bearing Spr-En-Chl schists (MASH-Fe₂O₃). Formula units calculated on the basis of 28 oxygens. (c) Composition of yellow sapphirine from Amph-Spl-Dol schists and Yod-Crd whiteschists. For comparison analyses of sapphirine from high-temperature (open symbols) and high-pressure (filled symbols) metamorphic rocks are shown (McKie, 1963a; Schreyer & Abraham, 1975; Windley *et al.*, 1984; Sandiford *et al.*, 1987; Simon & Chopin, 2001). (d) Composition of talc from Hbl-Ky-Tlc-Qtz schists and Tlc-Ky schists (formula units calculated on the basis of 11 oxygens). (e) Compositional variability of Mn-andalusite and kyanite from Hbl-Ky-Tlc-Qtz schists. (f) Composition of kornepupine (formula units calculated on the basis of 21.5 oxygens). Assuming Al + Fe³⁺ + Cr + B = 6.9 p.f.u. (Grew *et al.*, 1990a), the maximum B₂O₃ content in Krn at Mautia Hill seems to be about 0.5 wt.%, although B could not be detected analytically. The dashed line schematically shows the shift of kornepupine compositions in assemblages with Opx. For comparison analyses of boron-bearing Krn from Mautia Hill are shown (McKie, 1965; Grew *et al.*, 1990a).

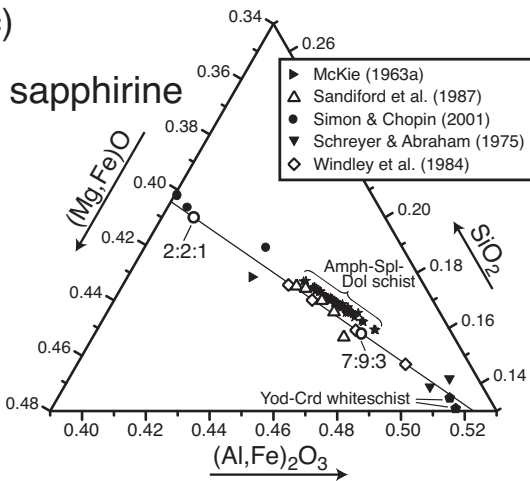
(a)



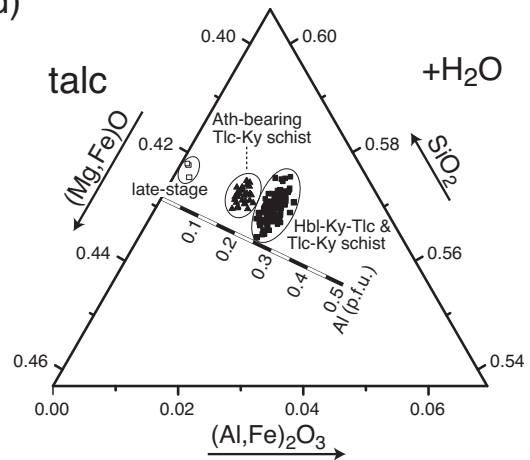
(b)



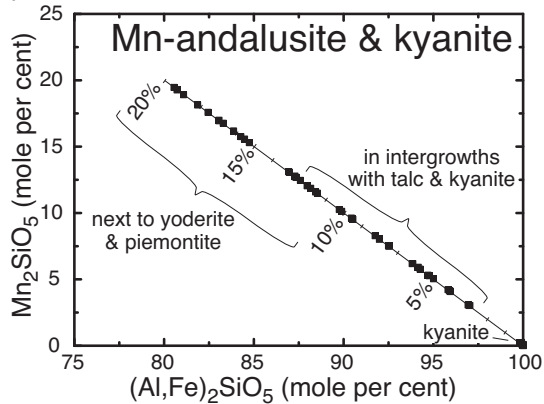
(c)



(d)



(e)



(f)

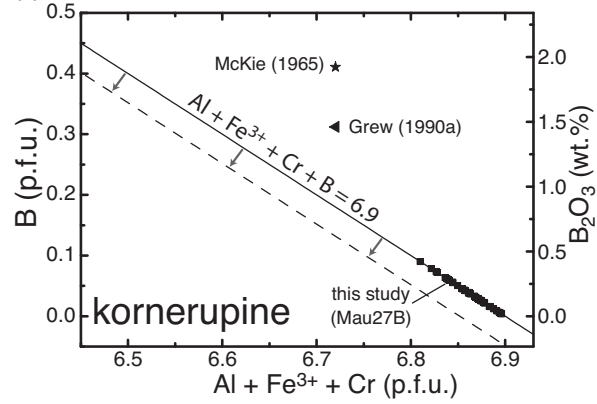


Table 5.2: Representative microprobe data for mineral phases within CMASH-CO₂-Fe₂O₃ rocks (^a Amph-Dol-Chl schist; ^b Amph-Spl-Dol schist; ^c Hbl-Ky-Tlc-Qtz schist).

Mineral: Analysis no:	Chl ^a 41	Amph ^a 138	Spr ^b 51	Spl ^b 161	Opx ^b 242	Amph ^b 379	Hög ^b 6	Bt ^c 10	Piem ^c 48	Tlc ^c 65	Ky ^c 139	Mn-And ^c 31	p.Yod ^c 37
SiO ₂	30.49	56.86	14.69	0.00	57.23	52.6	0.03	38.53	37.13	59.98	36.05	34.18	35.74
TiO ₂	0.14	0.17	0.07	0.01	0.05	0.34	1.79	1.02	0.05	0.06	0.03	0.09	0.17
Al ₂ O ₃	18.98	2.27	58.71	68.23	3.51	6.93	66.25	17.41	23.00	3.58	60.39	45.77	42.09
Cr ₂ O ₃	0.01	0.01	0.00	0.03	0.00	0.00	0.00	0.02	0.07	0.01	0.01	0.01	0.01
Fe ₂ O ₃	n.c.	0.00	5.05	3.07	0.44	1.17	n.c.	3.53	7.88	n.c.	2.31	4.42	4.55
FeO	1.70	1.10	0.55	0.07	0.67	1.11	10.74	n.c.	n.c.	0.38	n.c.	n.c.	0.77
MgO	33.39	23.60	20.95	27.18	37.92	21.30	18.68	20.51	0.13	29.17	0.05	0.00	11.66
MnO	0.05	0.00	0.03	0.03	0.05	0.00	0.02	n.c.	n.c.	0.17	n.c.	n.c.	n.c.
Mn ₂ O ₃	n.c.	n.c.	n.c.	n.c.	n.c.	n.c.	n.c.	2.18	6.62	n.c.	0.25	15.31	2.06
CaO	0.04	13.23	0.02	0.00	0.09	13.18	0.00	0.00	23.26	0.11	0.00	0.00	0.00
Na ₂ O	0.01	0.09	0.02	0.00	0.01	0.20	0.00	0.04	0.00	0.03	0.00	0.00	0.00
K ₂ O	0.03	0.06	0.00	0.00	0.00	0.18	0.00	7.12	0.00	0.00	0.00	0.00	0.00
BaO	n.d.	0.00	n.d.	n.d.	n.d.	0.01	n.d.	5.29	n.d.	0.06	0.02	n.d.	n.d.
ZnO	n.d.	n.d.	0.00	1.06	n.d.	n.d.	0.80	n.d.	n.d.	n.d.	n.d.	n.d.	n.d.
P ₂ O ₅	n.d.	n.d.	n.d.	n.d.	n.d.	n.d.	n.d.	n.d.	n.d.	n.d.	n.d.	n.d.	0.31
Total	84.84	97.40	100.09	99.69	99.98	97.04	99.91*	95.80	98.14	93.55	99.12	99.78	97.36
<i>Structural formulae</i>													
Si	5.84	7.74	1.72	0.00	1.92	7.27	0.01	5.54	2.96	3.87	0.99	0.99	3.95
Ti	0.02	0.02	0.01	0.00	0.00	0.04	0.25	0.11	0.00	0.00	0.00	0.00	0.01
Al	4.29	0.36	8.11	1.94	0.14	1.13	14.70	2.95	2.16	0.27	1.96	1.57	5.48
Cr	0.00	0.00	0.00	0.00	0.00	0.00	0.00	0.00	0.00	0.00	0.00	0.00	0.00
Fe ³⁺	n.c.	0.00	0.44	0.06	0.01	0.12	n.c.	0.38	0.47	n.c.	0.05	0.10	0.38
Fe ²⁺	0.27	0.13	0.05	0.00	0.02	0.13	1.69	n.c.	n.c.	0.02	n.c.	n.c.	0.07
Mg	9.54	4.79	3.66	0.98	1.90	4.39	5.24	4.39	0.02	2.81	0.00	0.00	1.92
Mn ²⁺	0.01	0.00	0.00	0.00	0.00	0.00	0.00	n.c.	n.c.	0.01	n.c.	n.c.	n.c.
Mn ³⁺	n.c.	n.c.	n.c.	n.c.	n.c.	n.c.	n.c.	0.24	0.40	n.c.	0.01	0.34	0.17
Ca	0.01	1.93	0.00	0.00	0.00	1.95	0.00	0.00	1.99	0.01	0.00	0.00	0.00
Na	0.01	0.02	0.00	0.00	0.00	0.05	0.00	0.01	0.00	0.00	0.00	0.00	0.00
K	0.01	0.01	0.00	0.00	0.01	0.03	0.00	1.31	0.00	0.00	0.00	0.00	0.00
Ba	n.d.	0.00	n.d.	n.d.	n.d.	0.00	n.d.	0.30	n.d.	0.00	0.00	n.d.	n.d.
Zn	n.d.	n.d.	0.00	0.02	n.d.	n.d.	0.11	n.d.	n.d.	n.d.	n.d.	n.d.	n.d.
P	n.d.	n.d.	n.d.	n.d.	n.d.	n.d.	n.d.	n.d.	n.d.	n.d.	n.d.	n.d.	0.01
Total	20.00	15.00	14.00	3.00	4.00	15.11	22.00	15.23	8.01	6.99	3.00	3.00	12.00
Oxygens	28	23	20	4	6	23	29.61	22	12.5	11	5	5	19

Fe³⁺ calculated assuming stoichiometry; Fe³⁺ in Amph after Droop (1987); n. c. = not calculated; n. d. = not determined; * Hög with 2(OH) = 1.59 H₂O (calc.)

of amphibole. Spinel is everywhere completely rimmed by yellow sapphirine, which itself is separated from the matrix amphibole by enstatite, magnesiochlorite, and dolomite (Fig. 5.5a). Zircon, haematite, talc, and baryte are accessories. A small amount of cerianite is included within sapphirine.

Hornblende-kyanite-talc-quartz schist. These eye-catching schists consist of greenish and reddish portions. The matrix consists mostly of quartz and talc, but local clusters of orange coloured biotite occur. Biotite is locally intergrown with talc. In the greenish portions of the rock kyanite is rimmed by symplectites of Mn-andalusite, piemontite, and yoderite (Fig. 5.5c). A common feature of the schists is colourless (in hand specimen reddish) magnesiohornblende, which is partially replaced and locally pseudomorphosed by intergrowths of purple yoderite, talc, and piemontite (Fig. 5.5d). Intergrowths of talc + Mn-andalusite or yoderite + Mn-andalusite + talc (Fig. 5.5f) also occur within the pseudomorphs. These intergrowths form the greenish patches seen in hand specimen. The products of breakdown are not everywhere homogeneously distributed within the pseudomorphs: for example piemontite is missing in some pseudomorphs whilst yoderite is missing in others (Fig. 5.5e and f). Large prograde grains of piemontite occur in the matrix and as inclusions in kyanite and Mg-hornblende. Late-stage piemontite formed at the expense of Mg-Hbl. Accessory minerals include apatite, hollandite ($\text{BaMn}_8\text{O}_{16}$), cerianite, manganian haematite ($\text{Fe}_{1.8}\text{Mn}_{0.2}\text{O}_3$), and rutile. The latter is typically intergrown with Mn-haematite. Locally, hollandite forms a corona between Mn-haematite and biotite/talc and seems to be a late-stage formation.

Mineral chemistry of the CMASH- CO_2 - Fe_2O_3 rocks

Magnesiochlorite from amphibole-dolomite-chlorite schists and amphibole-spinel-dolomite schists has a uniform composition near the clinocllore end-member. The small chemical variability is due to similar Tschermak ($2\text{Al} = \text{SiMg}$) and dioctahedral substitutions ($2\text{Al} = 3\text{Mg}$) in all analysed samples (Fig. 5.4b, Table 5.2). In amphibole-dolomite-chlorite schists the cores of *amphiboles* (first generation) are tremolitic, whereas the rims are classified as magnesiohornblende (second generation; Fig. 5.6a). The X_{Mg} of tremolite and Mg-hornblende is in the range from 0.96 to 1.00. Both amphibole generations show the effect of increasing Tschermak substitution with decreasing X_{Mg} values (Fig. 5.6a). Zoned amphibole crystals with tremolite cores and Mg-hornblende rims show a sharp boundary between these amphibole generations, pointing to a sudden change in metamorphic conditions (P , T or fluid; Fig. 5.6b). Hornblende-kyanite-talc-quartz schists contain only magnesiohornblende with $X_{Mg} = 0.93$ – 0.99 , but no tremolite. Magnesiohornblende is slightly enriched in alumina compared with amphiboles of the Amph-Dol-Chl schists (Fig. 5.6a). *Enstatite* has an $X_{Mg} = 0.98$ – 1.00 . In Amph-Dol-Chl schists it contains up to 2 wt.% Al_2O_3 , in spinel- and sapphirine-bearing rocks up to 4 wt.% Al_2O_3 (Table 5.2). Calculating the amount of Fe^{3+} assuming stoichiometry (20 oxygens, 14 cations) *yellow sapphirine* has an X_{Mg} of 0.98 to 1.00. It is optically positive and commonly polysynthetically twinned. The composition is near the 7:9:3 [$\text{MgO}:(\text{Al}, \text{Fe})_2\text{O}_3:\text{SiO}_2$] end-member, but subtly poorer in alumina

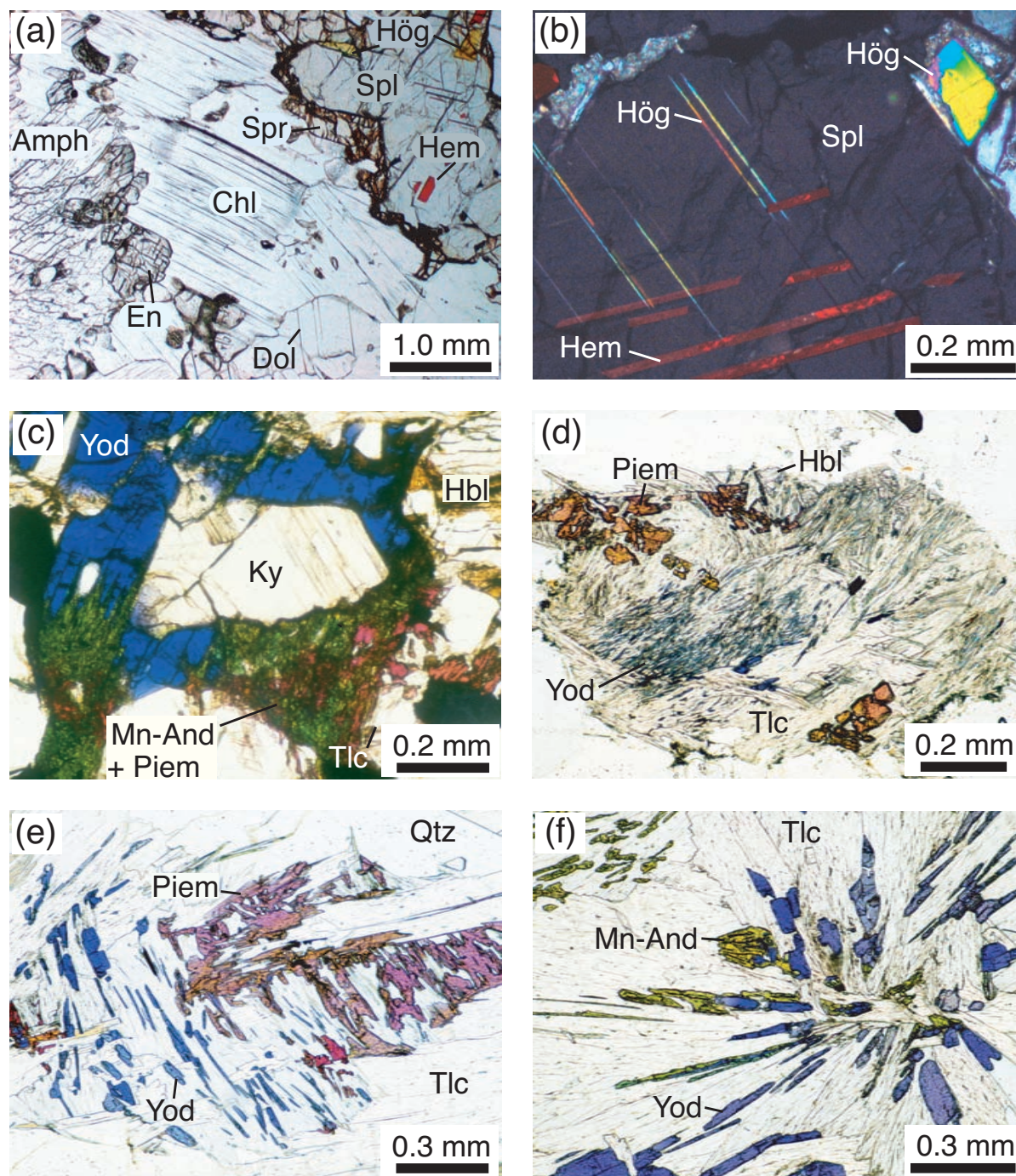


Figure 5.5: Microphotographs of CMASH-CO₂-Fe₂O₃ rocks from Mautia Hill. (a) Reaction rim of Chl, En, Spr and Dol between amphibole and spinel in an Amph-Spl-Dol schist (Mau22c). (b) Exsolution lamellae of haematite and högbomite in yellow spinel (crossed nicols; Amph-Spl-Dol schist, Mau22c). (c) Breakdown of Ky + Hbl forming Mn-And + Piem + Yod + Tlc. Opaque phases are Mn-haematite and hollandite (Hbl-Ky-Tlc-Qtz schist, Mau29-1). (d) Pseudomorphic replacement of nearly euhedral Hbl. Reaction products are Yod + Piem + Tlc (Hbl-Ky-Tlc-Qtz schist; Mau29-1). (e) Yod, Piem and Tlc as reaction products of Hbl breakdown (Hbl-Ky-Tlc-Qtz schist, T26-1-93). (f) Yod, Mn-And and Tlc as products of Hbl + Ky replacement (Hbl-Ky-Tlc-Qtz schist, T26-1-93).

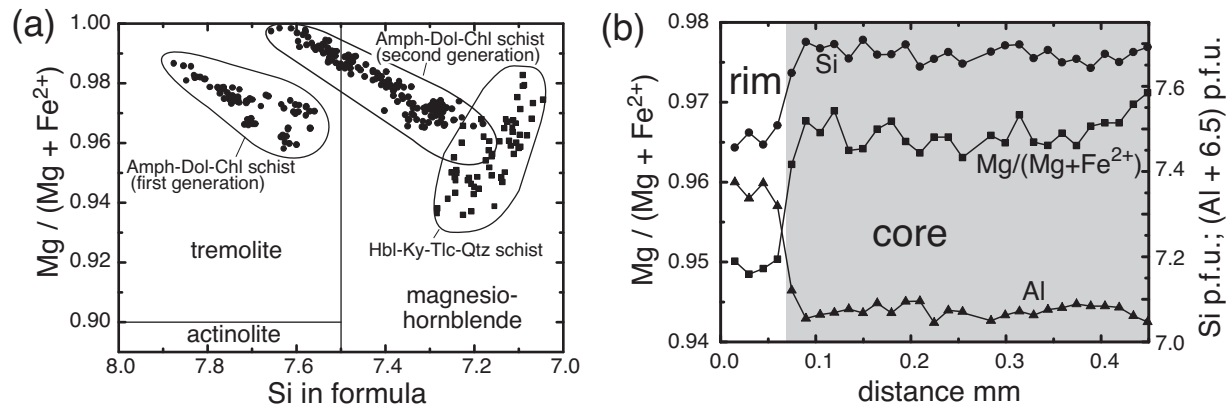


Figure 5.6: (a) Composition of amphiboles in Amph-Dol-En-Chl schists and Hbl-Ky-Tlc-Qtz schists (formula calculated on the basis of 23 oxygens). Increasing Fe-content is correlated with increasing Tschermak substitution in tremolite and hornblende. (b) Amphibole zonation (Si and Al p.f.u., calculation based on 23 oxygens) in an Amph-Dol-En-Chl schist. There is a sudden change in composition from the core (tremolite) to the rim (Mg-hornblende).

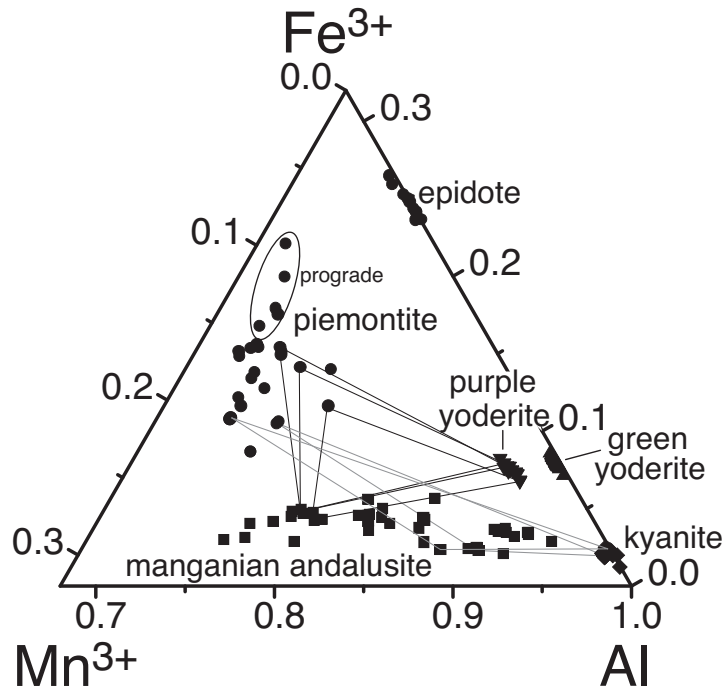


Figure 5.7: Chemical variation of kyanite, manganian andalusite, piemontite, and yoderite. Coexisting minerals are connected by tie lines. Mn³⁺/Fe³⁺ of coexisting phases decreases in the order Mn-andalusite, piemontite, yoderite.

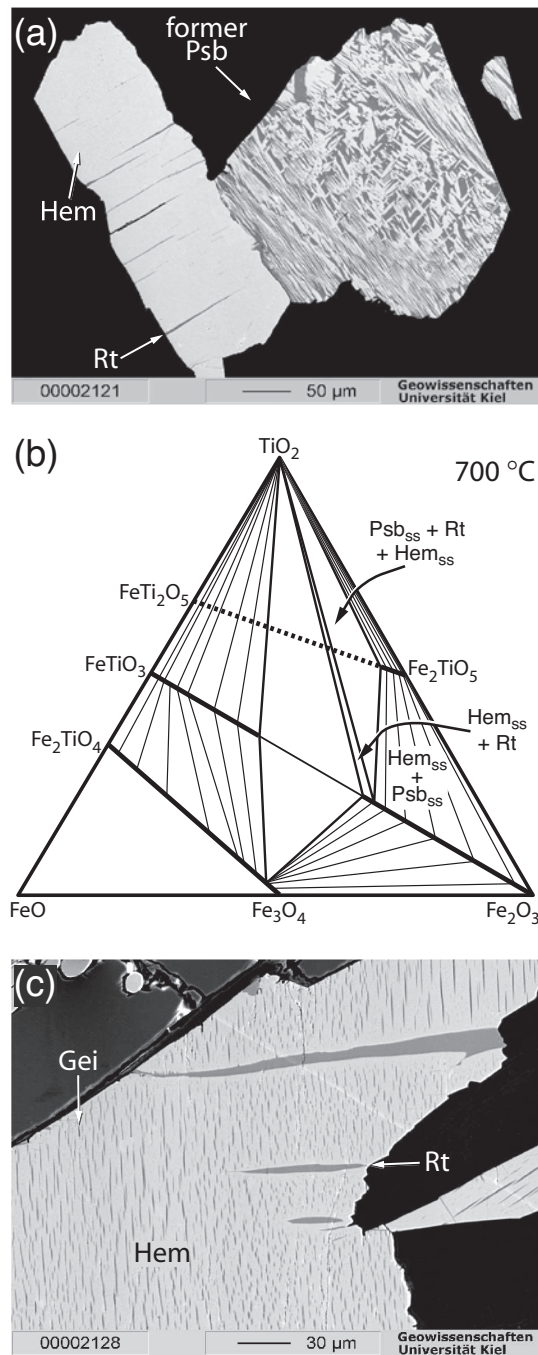


Figure 5.8: (a) Coexistence of haematite and former pseudobrookite. Pseudobrookite is completely replaced by a symplectite of rutile (dark) and haematite (light grey). Separate haematite grains contain lamellae of rutile (secondary electron image; Spr-En-Chl schist, Mau27B). (b) Schematic phase diagram for the system TiO_2 - FeO - Fe_2O_3 at ca. 700 °C (Haggerty, 1991). Prograde iron-titanium oxides of MASH- Fe_2O_3 and CMASH- CO_2 - Fe_2O_3 rocks from Mautia Hill are either Psb_{ss} - Rt - Hem_{ss} or Hem_{ss} - Rt or Hem_{ss} - Psb_{ss} . Additional components (Mg, Mn, Al) are neglected. (c) Haematite showing early lamellae of rutile, as well as late geikielite exsolution lamellae (secondary electron image; Amph-Chl-Dol schist, T25-0-93).

[$\text{Fe}^{3+}/(\text{Fe}^{3+} + \text{Al}) = 0.05$; Fig. 5.4c; Table 5.2]. The yellow colour may be related to the high oxidation ratio of iron (McKie, 1963a). *Spinel* is pale yellow and in some cases slightly birefringent. It has a composition near the Mg end-member, but contains small components of magnesioferrite (3%) and gahnite (2%; Table 5.2). Spinel contains lamellae of haematite and högbomite, possibly due to oxidation-exsolution or a former Ti content in spinel (Fig. 5.5b). *Högbomite* has a yellow colour like sapphirine and spinel, contains up to 2 wt.% TiO_2 and is Fe-poor (Table 5.2). *Piemontite* in hornblende-kyanite-talc-quartz schists shows a weak compositional variability [$\text{Mn}^{3+}/(\text{Mn}^{3+} + \text{Fe}^{3+} + \text{Al}) = 0.10\text{--}0.17$; Table 5.2]. Early piemontite, e. g., inclusions in hornblende, contain less Mn than the late-stage reaction products formed by breakdown of hornblende. In hornblende-kyanite-talc-quartz schists prograde *talc* contains 0.2–0.3 Al p.f.u. (formula calculated on the basis of 11 oxygens; Table 5.2). Other CMASH- CO_2 - Fe_2O_3 rocks contain only small amounts of late-stage talc, which is nearly Al-free (Fig. 5.4d). *Kyanite* contains < 0.4 wt.% Cr_2O_3 and up to 2.5 wt.% Fe_2O_3 (Table 5.2). Though Chinner *et al.* (1969) point to 1.6 wt.% as the maximum Fe_2O_3 content in kyanite, conditions during whiteschist metamorphism seem to have enabled higher values (e. g., $\text{Al}_{1.94}\text{Fe}_{0.05}^{3+}\text{Cr}_{0.01}\text{SiO}_5$). This is not only true for Mautia Hill, but also for yoderite-bearing whiteschists in Zimbabwe (2 wt.% Fe_2O_3 ; Johnson & Oliver, 2002). *Manganian andalusite* features a great variability in the amount of Mn_2SiO_5 component (3.0–19.5 mole%; Fig. 5.4e). So far *purple yoderite* has only been known to occur in whiteschists sensu stricto (McKie, 1959), but here it has been found as a late-stage mineral in hornblende-kyanite-talc-quartz schists (Fig. 5.5c-f). It contains up to 2.2 wt.% Mn_2O_3 , up to 5.5 wt.% Fe_2O_3 , and ca. 0.3 wt.% P_2O_5 (Table 5.2). Comparing the compositions of the three coexisting Fe-Mn-Al-bearing silicates Piem, Yod, and Mn-And, which have been formed during the late-stage metamorphic evolution, it appears that the $\text{Mn}^{3+}/\text{Fe}^{3+}$ -ratio decreases in the order Mn-And, Piem, purple Yod (Fig. 5.7). *Biotite* has a conspicuous orange-reddish colour. Microprobe analyses show 2.2 wt.% Mn_2O_3 ($\text{Mn}_{\text{tot}} = \text{Mn}^{3+}$) and up to 5.5 wt.% BaO (Table 5.2). Except for the Spl-bearing rocks *haematite* is common in all CMASH- CO_2 - Fe_2O_3 samples and coexists with rutile (Fig. 5.8b). It is Mn^{3+} -bearing and contains lamellae of rutile and/or geikielite (Fig. 5.8c). In hornblende-kyanite-talc-quartz schists haematite is locally rimmed by *hollandite* (ca. 5 wt.% PbO, nearly Sr-free). Further accessories are *apatite* (ca. 3 wt.% fluorine) and *cerianite*.

Rocks of the MASH- Fe_2O_3 system

Rocks that can be described in this chemical system are whiteschists sensu stricto and kornrupine-bearing sapphirine-enstatite-chlorite schists. Some types of these rocks have been formed due to different quartz-chlorite modal ratios in the low-grade precursor rocks (Chl-Qtz schists). Other types have been distinguished on the basis of different late-stage reaction histories. Table 5.3 shows representative microprobe data of some of the constituent minerals. Minerals of rocks of the MASH- Fe_2O_3 system found at Mautia Hill are plotted in Fig. 5.9a.

Whiteschists. In some quartz-bearing whiteschists no late-stage reaction rims between talc and kyanite have been developed. The content of talc and quartz in these schists is relatively low, resulting in locally monomineralic domains consisting just of greenish kyanite. Furthermore, they contain rutile and haematite (Fig. 5.8b).

Other talc-kyanite schists contain large amounts of late-stage Al-bearing anthophyllite, which together with quartz forms rims between talc and kyanite (Fig. 5.9e and Fig. 5.10a). Rutile and haematite are common; the latter contains lamellae of rutile and/or geikielite (Fig. 5.8c).

A third type of whiteschist has already been described by McKie (1959). These rocks are Mn-bearing and contain kyanite and talc in a quartz-rich matrix. Around kyanite there are the well-known reaction rims of purple yoderite and quartz (Fig. 5.9b and Fig. 5.10b).

The fourth type shows large kyanite porphyroblasts lying in a matrix of talc. Kyanite is surrounded by pale-purple to greenish yoderite, which itself is separated from talc by a narrow rim of pinitised cordierite (Fig. 5.10c). Quartz only occurs as small inclusions in kyanite. The mineral assemblage prior to yoderite formation in this rock type was just Tlc + Ky and the rock was poorer in SiO₂ than those described above (Fig. 5.9c,d). In addition, both yoderite-bearing types of whiteschist contain Rt-Hem symplectites formed after pseudobrookite coexisting with haematite (Fig. 5.8a).

Sapphirine-enstatite-chlorite schist. In SiO₂-poor MASH-Fe₂O₃ rocks neither talc nor kyanite are present. Instead, they consist of magnesiochlorite, enstatite, and sapphirine (Fig. 5.9f and Fig. 5.10d). Yellow sapphirine is typically surrounded by kornerupine (Fig. 5.10d), whereas kornerupine also forms large euhedral crystals lying within the matrix of the rock. The Spr-En-Chl schists contain haematite and pseudobrookite, which in most cases is replaced by Hem-Rt intergrowths (Fig. 5.8a).

Mineral chemistry of the MASH-Fe₂O₃ rocks

Talc has a similar composition to talc in the CMASH-CO₂-Fe₂O₃ rocks (Fig. 5.4d; Table 5.3). Its Al content ranges from 0.1 to 0.3 p.f.u. (formula based on 11 oxygens). The talc-kyanite schists contain Fe-rich *kyanite* (up to 2.3 wt.% Fe₂O₃). *Yoderite* occurs in two different specifications. The purple yoderite of the Mn-bearing whiteschists is similar in composition to that of the Ca-bearing rocks, but contains only 0.6 wt.% Mn₂O₃ (Table 5.3). In Qtz-free whiteschists pale-purple to green yoderite contains ca. 0.2 wt.% Mn₂O₃, but ca. 6 wt.% Fe₂O₃. Except for the small amount of manganese it is similar to the green yoderite described by McKie & Bradshaw (1966) from Mautia Hill and Johnson & Oliver (1998) from northern Zimbabwe. *Cordierite* rimming the green yoderite is strongly pinitised and analyses of the pinitised material resulted in low totals with $X_{Mg} \approx 0.86$ (Table 5.3). *Anthophyllite* has $X_{Mg} = 0.97-0.99$ and shows decreasing alumina content with increasing distance from kyanite (1.5–0.5 Al p.f.u., based on 23 oxygens). *Magnesiochlorite*, which occurs in the kornerupine-bearing schists, is nearly a pure clinocllore, but contains more Al₂O₃ than chlorite from CMASH-CO₂-Fe₂O₃ rocks (Fig. 5.4b, Table 5.3). *Enstatite* has near-end member composition, but contains up to 5.5 wt.% Al₂O₃. *Sapphirine* of

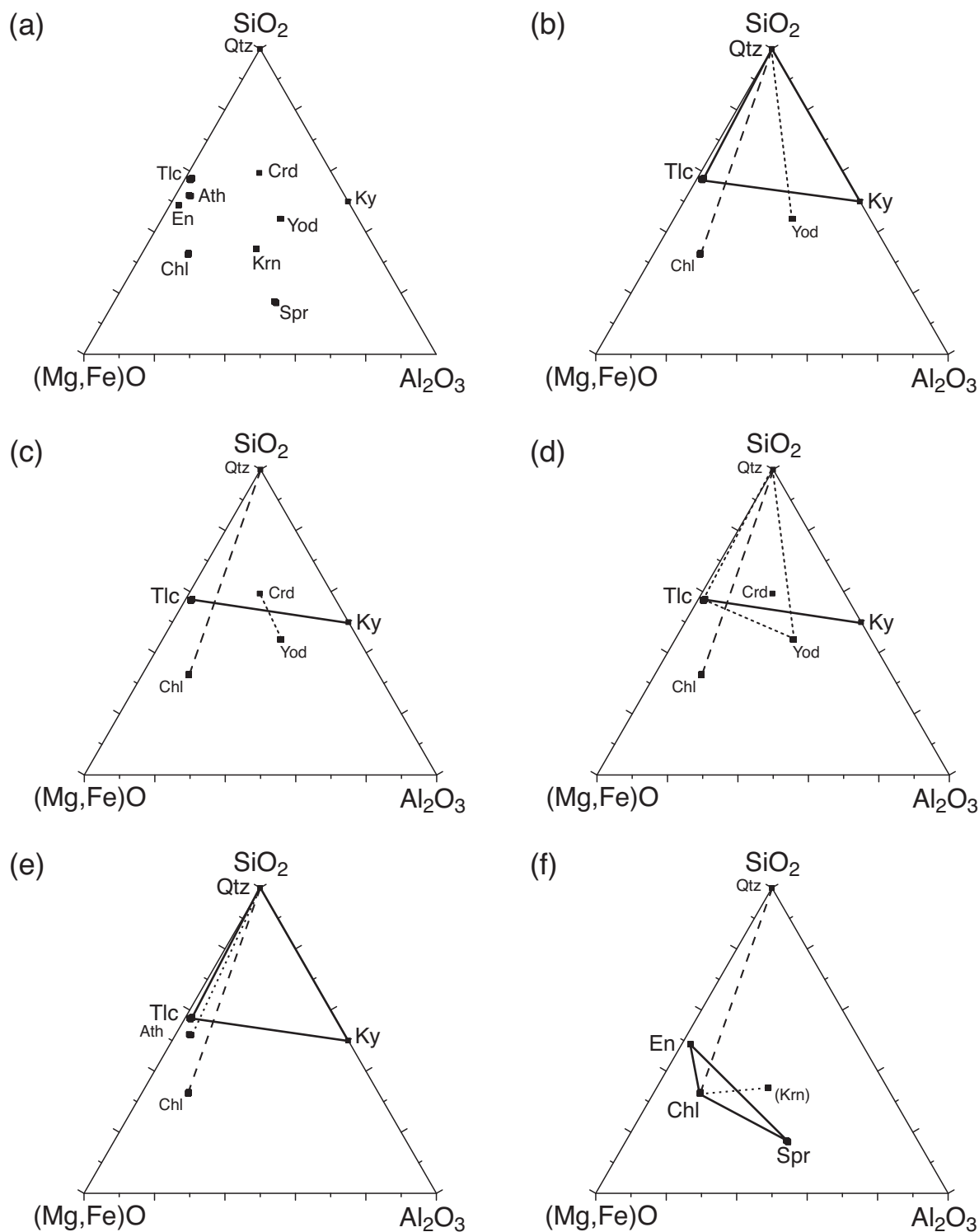


Figure 5.9: Phase relations of rocks within the system MASH-Fe₂O₃, projected from Fe₂O₃ and H₂O. (a) Mineral phases found in whiteschists or sapphirine-enstatite-chlorite schists at Mautia Hill. (b)-(f) Graphical deduction of mineral reactions found in the MASH-Fe₂O₃ rocks. Dashed tie line = prograde assemblage; solid tie line = near-peak assemblage; dotted tie line = late-stage assemblage.

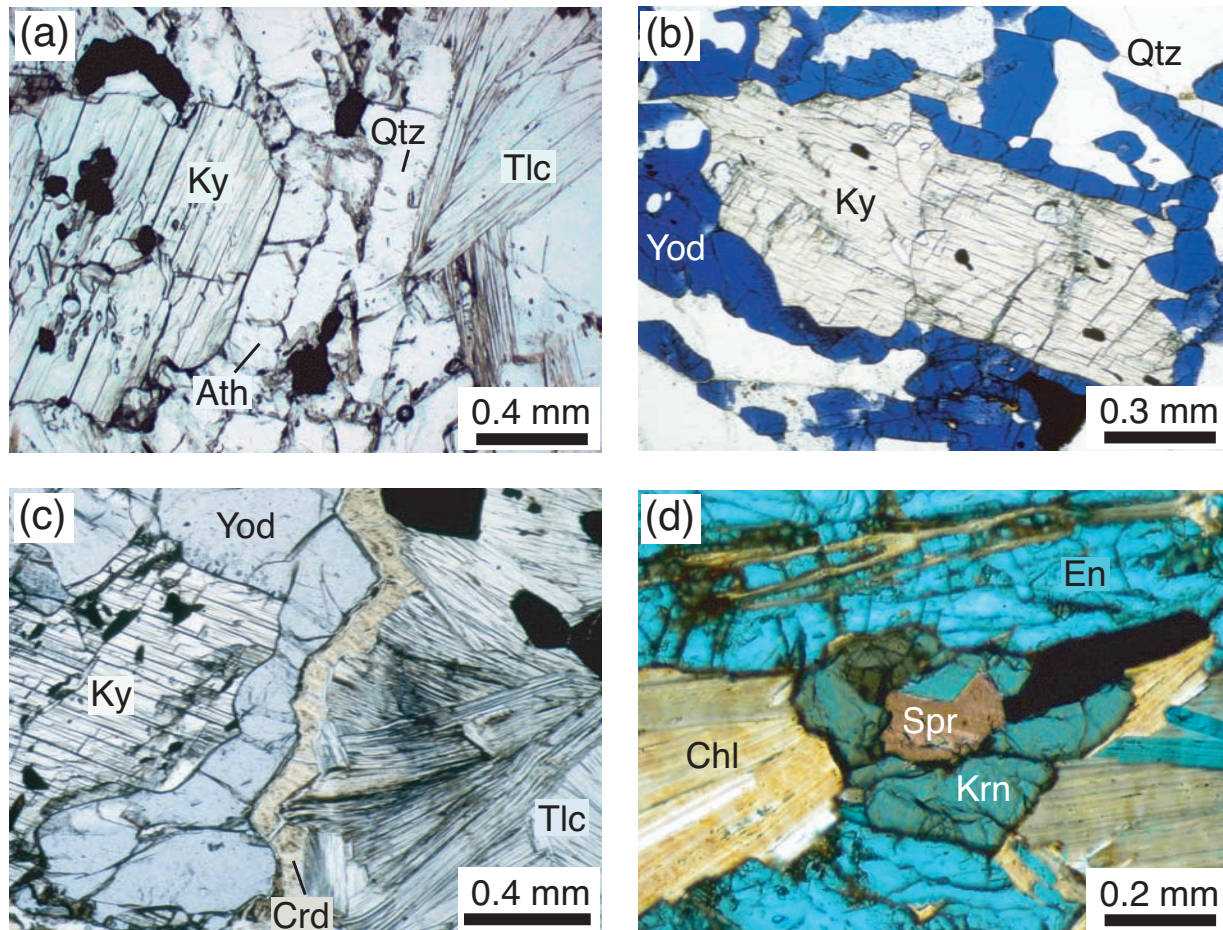


Figure 5.10: Microphotographs of MASH-Fe₂O₃ rocks from Mautia Hill. (a) A reaction rim of Ath and Qtz separates Tlc and Ky (Tlc-Ky schist, T25-9-93). (b) Ky porphyroblast rimmed by purple Yod and Qtz (Qtz-rich Tlc-Ky schist, T65-1sa). (c) Porphyroblast of Ky separated from the Tlc matrix by a reaction rim of Mn-free Yod and pinitised Crd (Qtz-free Tlc-Ky schist, T26-8-93). (d) Spr and En are separated by boron-free Krn. The matrix consists of Mg-Chl (crossed nicols; Spr-En-Chl schist, Mau27B).

the MASH-Fe₂O₃ rocks is yellow and thus similar in appearance to that of Ca-bearing rock types. In the Yod-Crd-bearing whiteschists sapphirine occurs as lamellar inclusion in Rt-Hem intergrowths and has peraluminous composition (Fig. 5.4c). *Kornerupine*, which seems to form at the expense of sapphirine, is pale violet in thin section. Electron microprobe analyses indicate that kornerupine is boron-free (Table 5.3). This is in agreement with the assumption that $Al + Fe^{3+} + Cr + B = 6.9$ p.f.u. (based on 21.5 oxygens; Grew *et al.*, 1990a, Fig. 5.4f) and the boron-poor chemistry is also approved by ion microprobe analyses (0.04 wt.% B₂O₃, H. Marschall pers. com.). Our observation contrasts that of McKie (1965) and Grew *et al.* (1990a), who found 1.92 and 1.46 wt.% B₂O₃ to occur in kornerupine from Mautia Hill (Fig. 5.4f). However, both investigated different mineral assemblages to those studied here. McKie (1965) found corundum to occur together with kornerupine. Grew *et al.* (1990a) described kyanite and tourmaline in close association

Table 5.3: Representative microprobe data for mineral phases within MASH-Fe₂O₃ rocks (^a Ath-bearing whiteschist; ^b Yod-Qtz whiteschist; ^c Yod-Crd whiteschist, ^d Spr-En-Chl schist).

Mineral	Ath ^a	Tlc ^a	Ky ^a	p.Yod ^b	Tlc ^b	Ky ^b	Tlc ^c	Spr ^c	pin.Crd ^c	g.Yod ^c	Chl ^d	Krn ^d	Opx ^d
Analysis no:	400	303	386	10	41	11	179	2	97	220	23	70	101
SiO ₂	55.06	60.69	37.38	35.80	60.47	37.17	60.81	10.60	45.96	36.16	30.22	29.32	56.56
TiO ₂	0.07	0.10	0.03	0.08	0.15	0.04	0.12	0.32	0.00	0.08	0.09	0.20	0.06
Al ₂ O ₃	9.14	2.36	60.90	41.73	3.72	61.61	3.69	67.11	27.24	42.95	20.8	43.24	4.53
Cr ₂ O ₃	0.05	0.00	0.00	0.03	0.00	0.00	0.00	0.11	0.00	0.02	0.01	0.03	0.01
Fe ₂ O ₃	1.45	n.c.	1.59	5.54	n.c.	1.06	n.c.	2.74	0.00	6.18	n.c.	4.82	0.11
FeO	0.23	0.35	n.c.	n.c.	0.47	n.c.	0.39	0.49	0.63	n.c.	1.00	n.c.	1.30
MgO	30.66	29.84	0.01	12.19	29.6	0.00	29.68	18.43	10.95	12.10	33.01	19.49	37.12
MnO	0.08	0.00	n.c.	n.c.	0.05	n.c.	0.03	0.14	0.13	n.c.	0.10	0.53	0.13
Mn ₂ O ₃	n.c.	n.c.	0.05	0.58	n.c.	0.17	n.c.	n.c.	n.c.	0.21	n.c.	n.c.	n.c.
CaO	0.30	0.05	0.00	0.01	0.11	0.00	0.11	0.00	1.17	0.00	0.01	0.06	0.03
Na ₂ O	0.06	0.06	0.00	0.01	0.07	0.01	0.05	0.00	0.14	0.00	0.00	0.02	0.01
K ₂ O	0.00	0.03	0.00	0.01	0.01	0.00	0.05	0.00	0.36	0.00	0.01	0.01	0.00
BaO	n.d.	n.d.	n.d.	n.d.	0.01	n.d.	0.04	n.d.	n.d.	0.00	n.d.	n.d.	n.d.
B ₂ O ₃	n.d.	n.d.	n.d.	n.d.	n.d.	n.d.	n.d.	n.d.	n.d.	n.d.	n.d.	0.00	n.d.
P ₂ O ₅	n.d.	n.d.	n.d.	0.46	n.d.	n.d.	n.d.	n.d.	n.d.	n.d.	n.d.	0.00	n.d.
Total	97.1	93.48	99.96	96.44	94.65	100.07	94.96	99.93	86.57	97.7	85.24	97.73	99.86
<i>Structural formulae</i>													
Si	7.26	3.91	1.01	3.96	3.86	1.01	3.86	1.24	5.22	3.96	5.74	3.7	1.91
Ti	0.01	0.00	0.00	0.01	0.01	0.00	0.01	0.03	0.00	0.01	0.01	0.02	0.00
Al	1.42	0.18	1.95	5.45	0.28	1.97	0.28	9.22	3.64	5.54	4.65	6.43	0.18
Cr	0.01	0.00	0.00	0.00	0.00	0.00	0.00	0.01	0.00	0.00	0.00	0.00	0.00
Fe ³⁺	0.14	n.c.	0.03	0.46	n.c.	0.02	n.c.	0.24	0.00	0.51	n.c.	0.46	0.00
Fe ²⁺	0.03	0.02	n.c.	n.c.	0.02	n.c.	0.02	0.05	0.06	n.c.	0.16	n.c.	0.04
Mg	6.03	2.87	0.00	2.01	2.81	0.00	2.81	3.20	1.85	1.97	9.34	3.66	1.87
Mn ²⁺	0.01	0.00	n.c.	n.c.	0.00	n.c.	0.00	0.01	0.01	n.c.	0.02	0.06	0.00
Mn ³⁺	n.c.	n.c.	0.00	0.05	n.c.	0.00	n.c.	n.c.	n.c.	0.02	n.c.	n.c.	n.c.
Ca	0.04	0.00	0.00	0.01	0.01	0.00	0.01	0.00	0.14	0.00	0.00	0.01	0.00
Na	0.02	0.01	0.00	0.00	0.01	0.00	0.01	0.00	0.03	0.00	0.00	0.00	0.00
K	0.00	0.00	0.00	0.00	0.00	0.00	0.00	0.00	0.05	0.00	0.00	0.00	0.00
Ba	n.d.	n.d.	n.d.	n.d.	0.00	n.d.	0.00	n.d.	n.d.	0	n.d.	n.d.	n.d.
B	n.d.	n.d.	n.d.	n.d.	n.d.	n.d.	n.d.	n.d.	n.d.	n.d.	n.d.	0.00	n.d.
P	n.d.	n.d.	n.d.	0.04	n.d.	n.d.	n.d.	n.d.	n.d.	n.d.	n.d.	0.00	n.d.
Total	14.96	7.00	3.00	11.99	7.00	3.00	7.00	14.00	11.01	12.00	19.92	14.34	4.00
Oxygens	23	11	5	19	11	5	11	20	18	19	28	21.5	6

Fe³⁺ calculated assuming stoichiometry; Fe³⁺ in amphiboles after Droop (1987); n.c. = not calculated; n.d. = not determined

with kornerupine. In the samples described here this is not the case. Apparently, both boron-free and boron-bearing kornerupine occur at Mautia Hill. Relics of *pseudobrookite* ($\text{Fe}_{1.46}\text{Al}_{0.10}\text{Ti}_{1.22}\text{Mg}_{0.20}\text{Mn}_{0.02}\text{O}_5$) are rarely preserved. In most cases it is replaced by symplectitic intergrowths of *rutile* and *haematite* (Fig. 5.8a). The intergrowths frequently contain small amounts of corundum; in Yod-Crd-bearing whiteschists also Spr is included. In addition, haematite containing lamellae of rutile forms separate grains, which are included in almost all other minerals, e. g., in kyanite, anthophyllite, yoderite, and kornerupine. In Ath-bearing rocks haematite contains large lamellae of rutile and small exsolution lamellae of near-Mg end-member geikielite (Fig. 5.8c).

5.5 Thermobarometry

Like all rock types metamorphosed under low geothermal gradients, whiteschists generally feature a clockwise pressure-temperature evolution (e. g., Schreyer & Abraham, 1976; Johnson & Oliver, 2002; John *et al.*, 2004). In the case of Mautia Hill, where several different rock types have experienced the same metamorphic evolution, commonly used geothermometers and geobarometers can be applied to metabasites and metapelites to obtain the P - T framework for the evolution of the highly oxidised whiteschists and chlorite schists, to which conventional geothermobarometers are not applicable.

First indications of the P - T path are obtained from kyanite inclusions in metapelitic garnet, showing that garnet growth initiated in the stability field of kyanite. Maximum temperatures during uplift are restricted to $< 720^\circ\text{C}$ by the upper thermal stability of the assemblage yoderite + quartz (Fockenberg & Schreyer, 1994). Our observation of late-stage cordierite reaction rims between yoderite and talc confirms earlier suggestions of a clockwise P - T path (Schreyer, 1977). However, this earlier interpretation was based on the evidence of yoderite reaction rims between talc and kyanite. These rims were assumed to have formed during decompression, but can also form at constant pressures due to oxidation or increase in water activity in the coexisting fluid (see later discussion).

5.5.1 Metapelites

Temperature estimates in metapelites are based on Fe-Mg partitioning between coexisting garnet and biotite. Three different calibrations have been applied (Ferry & Spear, 1978; Hodges & Spear, 1982; Kleemann & Reinhardt, 1994). The estimates were made using mineral formulae calculated without correcting for ferric iron. Even though the presence of haematite makes it most likely that some ferric iron is present in garnet and biotite, for comparability reasons it has not been taken into consideration. In any case, the maximum discrepancy between calculated temperatures from assumed Fe^{3+} -free minerals and those obtained with calculated Fe^{3+} contents amounts only to ca. 30°C . Peak temperatures were calculated using analyses of garnet cores and matrix biotite from three samples. The resulting temperatures range from 720 to 740°C at $P = 10$ kbar (Fig. 5.11 and Table 5.4) using the calibration of Kleemann & Reinhardt (1994). This lies slightly outside

Table 5.4: Representative pressure and temperature estimates from selected metapelitic samples. Temperatures were calculated on the basis of analyses given in the electronic appendix (<http://www.petrology.oupjournals.org>) and on pages 176 and 177 at a pressure of 10 kbar assuming all iron as Fe^{2+} . Pressures were calculated at a temperature of 700 °C.

Sample	Combination	Temperature: Grt-Bt [°C]			Pressure: GASP [kbar]
		H & S	F & S	K & R	Koziol (1989)
T27-1-93(1)	Grt core/ Pl core/ Bt matrix	870	838	735	9.5
T27-1-93(2)	Grt rim/ Pl rim/ Bt matrix	731	700	656	9.5
T27-2-93(3)	Grt core/ Pl core/ Bt matrix	853	817	726	10.1
T27-2-93(4)	Grt rim/ Pl rim/ Bt matrix	861	834	731	8.8
T30-2-93(5)	Grt core/ Pl core/ Bt matrix	864	837	721	9.9
T30-2-93(6)	Grt rim/ Pl rim/ Bt matrix	679	656	627	9.2

H & S: Hodges & Spear (1982); F & S: Ferry & Spear (1978); K & R: Kleemann & Reinhardt (1994)

the stability field of yoderite + quartz, whereas the calculated temperatures using Hodges & Spear (1982) or Ferry & Spear (1978) appear to be too high ($T = 835\text{--}870$ °C; Table 5.4).

The garnet-alumosilicate-quartz-plagioclase (GASP) geobarometer has been applied for pressure calculations. The calibration of Koziol (1989) gives estimates within the kyanite stability field in agreement with petrographic observations. Peak-metamorphic pressures were obtained using garnet core and plagioclase core compositions. Rim compositions of both minerals were used to determine retrograde pressures. Calculated pressures (at $T = 700$ °C) are in the range of $P = 9.5\text{--}10.1$ kbar (peak) and $P = 8.8\text{--}9.5$ kbar (retrograde; Fig. 5.11 and Table 5.4). Microprobe analyses for thermobarometry are given in the electronic appendix (<http://www.petrology.oupjournals.org>) and on pages 176 and 177.

5.5.2 Metabasites

The garnet-plagioclase-clinopyroxene-quartz (GADS) barometer (Eckert *et al.*, 1991) has been applied to metabasites. Fe-Mg partitioning between coexisting garnet and clinopyroxene (Ellis & Green, 1979; Powell, 1985), and hornblende (Graham & Powell, 1984) have been used for temperature estimates. Peak-metamorphic conditions were calculated using core compositions of minerals; for retrograde conditions the rim compositions have been used. Clinozoisite-bearing metabasites do not contain much hornblende. In these rocks temperature estimates are restricted to garnet-clinopyroxene thermometry. For the sake of comparability, all calculations were performed without consideration of ferric iron. The results are listed in Table 5.5 and shown in Fig. 5.11. Resulting temperatures are unrealistically high ($T > 850$ °C). Temperatures in clinozoisite-free metabasites are also overestimated ($T = 770\text{--}800$ °C). Even results of the garnet-hornblende thermometer lie outside the yoderite + quartz stability field ($T \approx 770$ °C; Fig. 5.11).

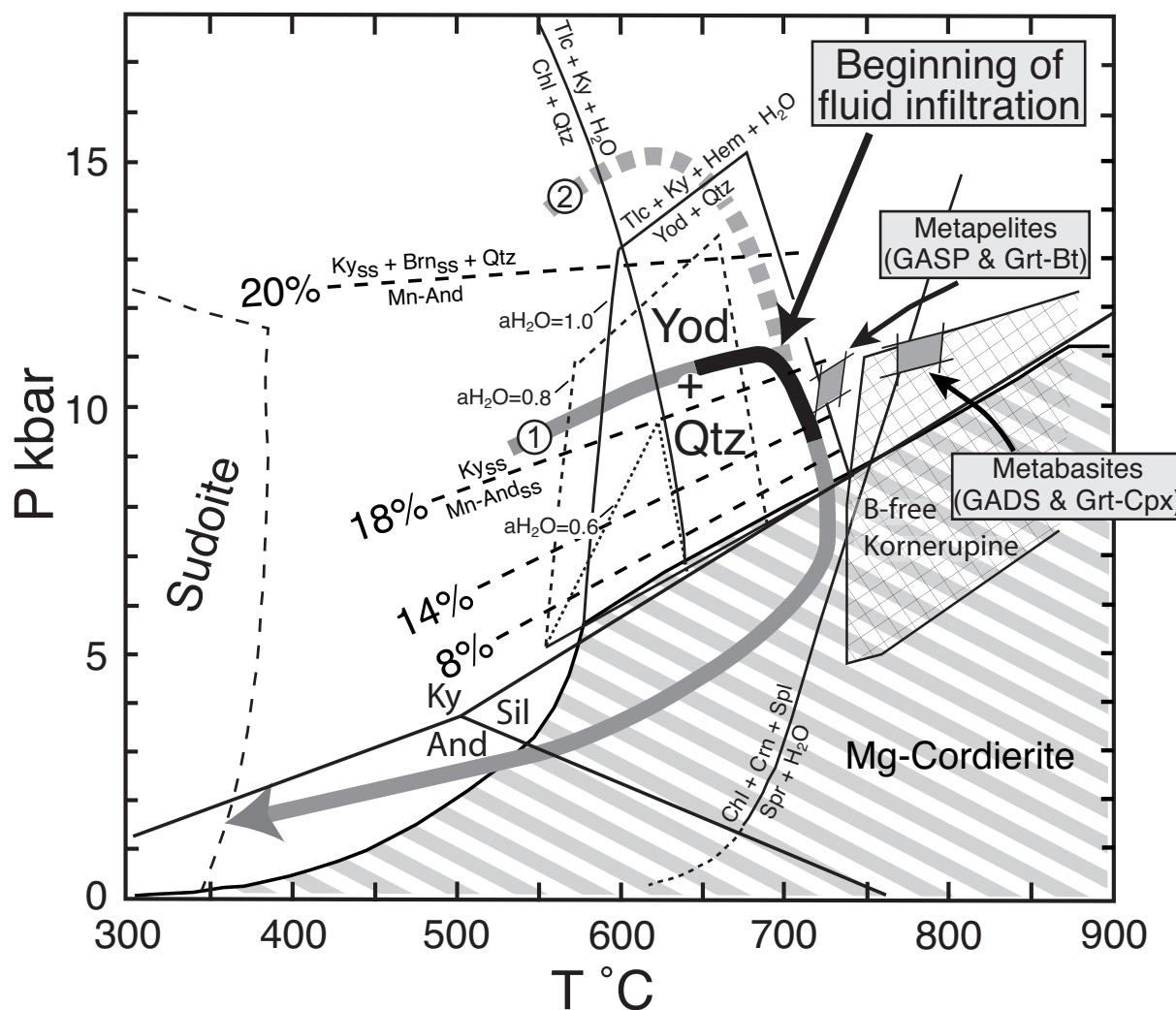


Figure 5.11: Summarised P - T evolution of rocks from Mautia Hill as deduced from geothermobarometry and reaction textures. The two possible P - T paths are shown (see text for further discussion). Aluminosilicate stability after Holdaway (1971). Yod + Qtz at different a_{H_2O} after Fockenberg & Schreyer (1994). Sudoite stability after Schreyer (1988). Chl-Qtz stability after Massonne (1989). Maximum Mn-content in And coexisting with Ky after Abs-Wurmbach *et al.* (1983). Stability of B-free kornepupine after Seifert (1975) and Wegge & Schreyer (1994). Sapphirine + H_2O stability after Ackerman *et al.* (1975). The Mg-Crd stability is after Schreyer (1986), but slightly modified to overlap with the Yod-Qtz stability field.

Table 5.5: Representative pressure and temperature estimates from selected metabasic samples. Temperatures were calculated on the basis of analyses given in the electronic appendix (<http://www.petrology.oupjournals.org>) and on pages 176 and 177 at a pressure of 10 kbar assuming all iron as Fe²⁺. Pressures were calculated at a temperature of 700 °C.

Sample	Combination	Temperature [°C]		Pressure [kbar]	
		Grt-Cpx E & G Pow.	Grt-Hbl G & P	GADS Eckert <i>et al.</i> (1991)	
T73-1-93(1)	Grt core/ Pl core/ Cpx core	888	877	—	10.7
T73-1-93(2)	Grt rim/ Pl rim/ Cpx rim	839	827	—	10
T73-8-93(3)	Grt core/ Pl core/ Cpx core/ Hbl core	793	778	768	10.1
T73-8-93(4)	Grt rim/ Pl rim/ Cpx rim/ Hbl rim	707	688	663	8.3

E & G: Ellis & Green (1979); Pow: Powell (1985); G & P: Graham & Powell (1984)

Using core compositions of garnet, plagioclase, and clinopyroxene the peak-metamorphic pressures of 10.1–10.7 kbar for both types of metabasites are in good agreement with estimates from GASP equilibria. Retrograde pressures (rim compositions of garnet, plagioclase, and clinopyroxene) range from $P = 8.3$ –10.0 kbar. Microprobe analyses for thermobarometry are given in the electronic appendix (<http://www.petrology.oupjournals.org>) and on pages 176 and 177.

5.5.3 Hornblende-kyanite-talc-quartz schists

Manganian andalusite, the formation of which is assigned to the breakdown of kyanite, quartz, and Mn-oxides, shows a variation in the amount of Mn₂SiO₅ component from 3 to 19.5%. Under high oxygen fugacities (e. g., MnO₂/Mn₂O₃ buffer), which are supported by the occurrence of oxide minerals like hollandite, the amount of Mn₂SiO₅ in manganian andalusite coexisting with hollandite, kyanite, and quartz can be used as a geobarometer (Abs-Wurmbach *et al.*, 1983). The application of this barometer yields peak pressures of $P = 10$ –12 kbar for temperatures in the stability field of yoderite + quartz. Mn-andalusites with lower Mn-contents most likely were formed during later stages of the decompression path. Alternatively, the low Mn-contents may be due to local deficiency of manganese on the thin section scale.

5.6 Reaction history

The schists of Mautia Hill exhibit a number of spectacular reaction textures. In the following paragraphs these reactions are qualitatively deduced and stoichiometrically balanced using the idealised formulae given in Table 5.6.

Intergrowths of rutile and haematite are common in all types of MASH-Fe₂O₃ rocks at Mautia Hill. These symplectitic grains mostly show a volumetric ratio of 1/3 rutile and

Mg-Hornblende	$\text{Ca}_2\text{Mg}_5\text{Si}_7\text{AlO}_{22}(\text{OH})_2$
Spinel	MgAl_2O_4
Mg-Chlorite	$\text{Mg}_5\text{Si}_3\text{Al}_2\text{O}_{10}(\text{OH})_8$
Dolomite	$\text{CaMg}(\text{CO}_3)_2$
Enstatite	$\text{Mg}_2\text{Si}_2\text{O}_6$
Sapphirine	$\text{Mg}_2\text{Al}_4\text{Fe}_{0.25}^{3+}\text{Si}_{0.75}\text{O}_{10}$
Kyanite	Al_2SiO_5
green Yoderite	$\text{Mg}_2\text{Al}_{5.6}\text{Fe}_{0.4}^{3+}\text{Si}_4\text{O}_{18}(\text{OH})_2$
purple Yoderite	$\text{Mg}_2\text{Al}_{5.6}\text{Mn}_{0.15}^{3+}\text{Fe}_{0.25}^{3+}\text{Si}_4\text{O}_{18}(\text{OH})_2$
Piemontite	$\text{Ca}_2\text{Mn}_{0.4}\text{Fe}_{0.6}\text{Al}_2\text{Si}_3\text{O}_{12}(\text{OH})$
Talc	$\text{Mg}_3\text{Si}_4\text{O}_{10}(\text{OH})_2$
Mn-Andalusite	$\text{Mn}_{0.4}\text{Al}_{1.6}\text{SiO}_5$
Anthophyllite	$\text{Mg}_7\text{Al}_{0.5}\text{Si}_{7.5}\text{O}_{22}(\text{OH})_2$
Cordierite	$\text{Mg}_2\text{Al}_4\text{Si}_5\text{O}_{18} \cdot 0.7 \text{H}_2\text{O}$
Kornerupine	$\text{Mg}_{3.7}\text{Fe}_{0.5}^{3+}\text{Al}_{6.5}\text{Si}_{3.5}\text{O}_{20}(\text{OH})_2$

Table 5.6: Idealised mineral formulae used for calculations of reaction stoichiometries.

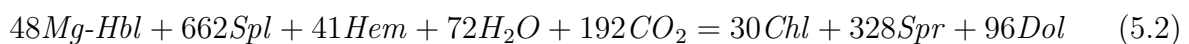
2/3 haematite (equivalent to ca. 45 mol.% TiO_2 and ca. 55 mol.% Fe_2O_3). Therefore these grains are interpreted as products of decomposition of pseudobrookite during cooling:

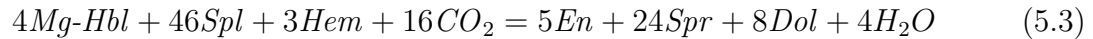


McKie (1963a) reported pseudobrookite from the sapphirine-bearing rocks of Mautia Hill, and we also observed some relics in a kornerupine-bearing schist. Pseudobrookite is a common mineral in e. g., basaltic rocks and miarolitic andesites (Frost & Lindsley, 1991), but to our knowledge its occurrence in regional-metamorphic rocks is uncommon. Haematite typically contains lamellae of rutile, which have been described by Haggerty (1991) to be the result of an “exsolution”-like process related to oxidation. The exsolution of geikielite (instead of the usual ilmenite) from haematite (Fig. 5.8c) is in agreement with the high- f_{O_2} conditions, where ilmenite is thought to be unstable. An oxygen fugacity in the range of the $\text{MnO}_2/\text{Mn}_2\text{O}_3$ buffer or higher is in agreement with the Fe-Mn oxide and silicate mineralogy of the MASH- Fe_2O_3 and CMASH- CO_2 - Fe_2O_3 rocks (Abs-Wurmbach & Peters, 1999).

5.6.1 CMASH- CO_2 - Fe_2O_3 system

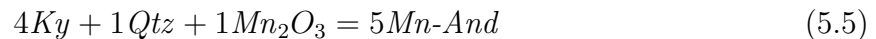
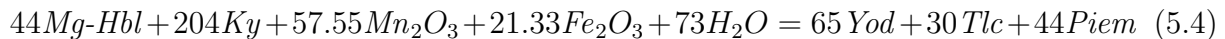
Textural evidence shows that Mg-Hbl + Spl + Dol + Hem formed the prograde metamorphic assemblage in hornblende-spinel-dolomite schists. Under oxidising conditions this assemblage broke down to form Chl, Spr, En, and additional Dol:





It seems that both reactions are typically coupled in the studied rocks, although it should be possible that they occur independently from each other. The lamellae of haematite and högbomite in spinel can be explained by oxidation exsolution (Buddington & Lindsley, 1964; Grew *et al.*, 1990b) according to the reaction $Spl_{ss} + H_2O = Hem + Hög$. Yet another indicator for extremely oxidising conditions is cerianite ($Ce^{4+}O_2$), which forms inclusions in sapphirine or talc and has to be ascribed to metamorphism, because of the textural evidence and its Pan-African U-Th-Pb age (CHIME dating; P. Appel pers. com.). Previously, this mineral has been described as forming at the Earth's surface during weathering processes (Fron del & Marvin, 1959; Braun *et al.*, 1990). Tremolite is a prograde, lower-grade metamorphic relic forming the cores of zoned amphiboles.

Hornblende-kyanite-talc-quartz schists show the decomposition of the peak-metamorphic assemblage Mg-hornblende + kyanite + haematite. Symplectitic intergrowths of Tlc, Piem, purple Yod, and Mn-And partially pseudomorph Mg-Hbl (Fig. 5.5d-f). Kyanite is rimmed by manganian andalusite-bearing symplectites (Fig. 5.5c). These textures may be related to the reactions:



Mass transport via a fluid phase must have taken place at least on the thin section scale. This is indicated by allochemical replacement of Mg-hornblende. For example, Piem is the only Ca-bearing product phase, but locally missing inside the pseudomorphs. The absence of Mn-andalusite in the prograde mineral assemblage can be explained in two ways: either the pressures were in excess of 13 kbar or the high- f_{O_2} mineral hollandite was missing, which in our case was a necessary reactant for the formation of Mn-And at lower pressures. The described reaction texture showing late-stage formation of hollandite supports the second possibility. The late-stage minerals contain trivalent and even tetravalent cations pointing to a minimum f_{O_2} near that of the MnO_2/Mn_2O_3 buffer (Abs-Wurmbach & Peters, 1999).

The occurrence of yoderite in Ca-rich rocks demands special attention: Fockenberg & Schreyer (1994) argue that the tie line amphibole + kyanite forms a chemical barrier, that restricts the formation of yoderite to a Ca-poor bulk chemistry. The coexistence of yoderite and piemontite, formed as late-stage reaction products at the expense of Mg-hornblende + kyanite, is inferred from textural relationships (Fig. 5.5d,e). This indicates that Mg-hornblende + kyanite + haematite cannot be stable in the whole yoderite stability field. This assemblage appears to be restricted to the high-pressure part of this stability field, because it becomes unstable in the low-pressure part of that stability field. The assumption can be made that Mg-Hbl + Ky + Hem is a high-pressure assemblage in analogy to the whiteschist paragenesis Tlc + Ky + Hem that also reacted to yoderite-bearing assemblages during the late-stage metamorphic evolution.

5.6.2 MASH-Fe₂O₃ system

Most rock types at Mautia Hill that can be described within the MASH-Fe₂O₃ system are whiteschists. They are characterised by the mineral assemblage Tlc + Ky, which represents at high-pressures a high-temperature equivalent of Mg-Chl + Qtz (Schreyer, 1968; Massonne, 1989). During the prograde burial and heating of the rocks of Mautia Hill, prograde Mg-Chl + Qtz broke down at ca. 600 °C forming Tlc + Ky.

McKie (1959) described the Qtz-rich whiteschists that contain purple yoderite and deduced a mineral reaction for the Yod-Qtz rims around kyanite. Later this reaction was modified by Fockenberg & Schreyer (1991), who recognised that yoderite is not a MASH mineral but contains essential Fe₂O₃ and/or Mn₂O₃. A possible Yod + Qtz-forming reaction is:

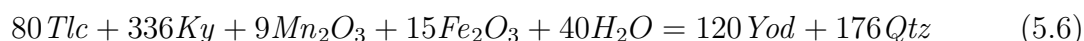


(Fig. 5.9b). In another type of whiteschist kyanite is rimmed by quartz and Al-bearing anthophyllite. This texture may be related to the reaction

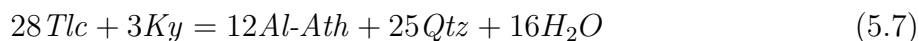
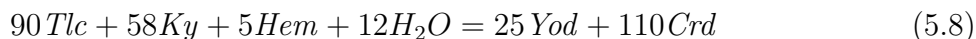
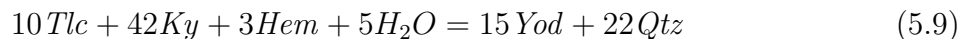


(Fig. 5.9e). Such a reaction has already been described by Schreyer & Seifert (1969) as a high-temperature low-pressure breakdown of Tlc + Ky. At Mautia Hill the late-stage decompression may be related to this reaction.

The quartz-free Tlc-Ky schists show rims of green yoderite and cordierite between talc and kyanite. The reaction



may account for this (Fig. 5.9c). This reaction would be in agreement with the SiO₂-deficient chemistry of the rock. In *P-T* space, such a reaction should lie within the small area where the stability fields of yoderite and cordierite are overlapping (at ca. 6 kbar; Fig. 5.11; Fockenberg & Schreyer, 1994). However, breakdown of Tlc + Ky + Hem + H₂O takes place at much higher pressures (at ca. 13 kbar, high H₂O activity). Thus this Crd-forming reaction may be metastable. Another possible way to form the rims involves a two-stage reaction sequence:



(compare equation 5.6).

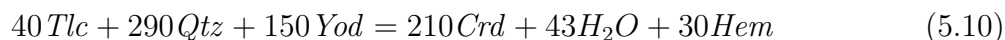
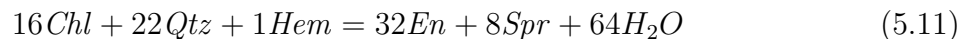


(Fig. 5.9d). The kornerupine-bearing sapphirine-enstatite-chlorite schists are not whiteschists *sensu stricto*, but their mineralogy and metamorphic evolution is similar to that of whiteschists. In rocks with SiO₂-poor bulk chemistry (below the tie line Tlc-Ky; Fig. 5.9) the prograde

assemblage containing chlorite and very little quartz also breaks down at temperatures of about 600 °C, but here no Tlc + Ky would form. Instead, the following reaction:



lead to En + Spr + Chl as the peak-metamorphic assemblage in this rock type (Fig. 5.9f). During retrograde metamorphism the reaction



may be responsible for reaction rims of boron-free kornerupine between enstatite and sapphirine (Fig. 5.9f and Fig. 5.10d). Seifert (1975) determined this mineral reaction experimentally to lie at 5–8 kbar and 750–800 °C. Because estimated peak temperatures are lower than 720 °C, this reaction must have taken place at still lower temperatures, possibly due to incorporation of Fe³⁺ in kornerupine or a reduced water activity during cooling.

5.7 Discussion and conclusions

5.7.1 *P-T* evolution

The origin of whiteschists is uncertain and two competing models have been proposed. The first suggests metamorphism of an oxidised and metasomatised precursor rock. The second proposes synmetamorphic oxidation and metasomatism. The main factors controlling the formation and subsequent breakdown of the whiteschist assemblage Tlc + Ky are pressure, temperature, oxygen fugacity, and water activity. For the rocks of Mautia Hill, maximum pressure conditions of 10–11 kbar are thought to be well constrained by conventional barometry. Retrograde decompression is documented by late-stage formation of cordierite, by mineral growth zoning (Ca-increase in plagioclase and Ca-decrease in garnet towards the rims) and the GASP and GADS barometric results obtained with mineral rim compositions (Table 5.4 & 5.5). These net-transfer reactions used for barometry are thought to be insensitive to re-equilibration. Furthermore, significant Ca-Al diffusion at temperatures near 700 °C is unlikely. In contrast, the results of geothermometers based on Fe-Mg exchange are easily influenced by late re-equilibration and the high oxidation state of the rocks. Therefore, experimentally determined mineral stabilities provide better opportunities for estimation of peak temperatures. The upper thermal stability of Yod + Qtz has been determined in the MASH-Fe₂O₃ system and estimated for different *a*H₂O (Fockenberg & Schreyer, 1994). Presumably, a change due to the incorporation of Mn₂O₃ into yoderite is relatively small compared to uncertainties in using the stability fields of sapphirine + H₂O (Ackermann *et al.*, 1975) and boron-free kornerupine (Seifert, 1975; Wegge & Schreyer, 1994). The effect of the incorporation of Fe³⁺ into these minerals is not well known. In addition, the occurrence of anthophyllite (stable below 800 °C) and talc (stable below 760 °C at 10 kbar; Greenwood, 1963) further constrains maximum peak temperatures and makes a temperature of 700–720 °C likely (Fig. 5.11).

5.7.2 Influence of water activity and oxygen fugacity

To explain the variety of unusual late-stage minerals in the MASH-Fe₂O₃ and CMASH-CO₂-Fe₂O₃ rocks, the influence of oxygen fugacity (f_{O_2}) and water activity (a_{H_2O}) has to be considered. Inclusions of haematite and piemontite in kyanite, as well as the Fe₂O₃ content of peak-metamorphic kyanite and spinel indicate an oxidised protolith or oxidation during prograde metamorphism. However, breakdown of Mn-haematite + biotite to reaction rims of hollandite around Mn-Hem and formation of rutile lamellae in haematite indicate progressive further oxidation. Assuming maximum pressures of $P = 10\text{--}11$ kbar, it is reasonable to expect that the prograde assemblage Chl + Qtz + Hem breaks down to form directly a yoderite-bearing assemblage. Because Tlc + Ky is formed from Chl + Qtz, yoderite cannot have been stable at this time. Low water activities restrict the stability field of Yod + Qtz to lower temperatures and pressures (< 9 kbar; Fig. 5.11; Fockenberg & Schreyer, 1994). Therefore our petrographic observations and geobarometric data are in agreement with the hypothesis that the metamorphic conditions involved increasing water activity leading to the formation of yoderite in the whiteschists of Mautia Hill (P - T path 1; Fig. 5.11), a possibility already discussed by Fockenberg & Schreyer (1994). Most former workers, without the benefit of conventional barometry on associated metapelites and metabasites from Mautia Hill only considered decompression as the cause for the formation of late-stage yoderite rims around kyanite (Schreyer & Yoder Jr., 1968; Schreyer, 1977; Mruma & Basu, 1987; Möller, 1995). If decompression really was the reason for yoderite formation (P - T path 2; Fig. 5.11), the results of our conventional barometry (GASP, GADS) must be influenced by re-equilibration during decompression leading to inappropriate pressure estimates: $P = 10\text{--}11$ kbar instead of 13–15 kbar. The absence of prograde Mn-andalusite in the highly oxidised whiteschists, but its late-stage formation, may support the higher-pressure interpretation. However, formation of Mn-And can also be explained by late-stage occurrence of hollandite (as discussed above). The infiltration scenario at maximum pressure conditions of 10–11 kbar, which is proposed here, is in agreement with the results of fluid inclusion studies (Basu & Mruma, 1985; Mruma, 1986; Mruma & Basu, 1987), which point to an early CO₂-rich fluid and a late H₂O-dominated fluid.

5.7.3 Metasomatism and precursor rock of whiteschists

McKie (1959) speculated on the nature of the precursor rocks and the origin of the special chemistry of whiteschists at Mautia Hill. Though he saw the possibility of their formation through Mg-metasomatism of an argillaceous sandstone, he favoured an interpretation involving isochemical metamorphism of a saponitic bentonite. Later workers demonstrated, on the basis of geochemistry and stable isotope data, that Mg-metasomatism is generally responsible for the formation of whiteschists and leucophyllites (Demény *et al.*, 1997; Pawlig & Baumgartner, 2001; Johnson & Oliver, 2002). We prefer this interpretation for Mautia Hill. The close association and common deformation history of all different rock types at Mautia Hill point to a tectonic origin for the layering, and a subsequent common metamorphic history. We consider it unlikely that the great lithologic variety (metaba-

sites, metapelites, metagranites, marbles, and different kinds of schists) reflects an original sedimentary succession. The precursor rock of the whiteschists and chlorite schists at Mautia is not obvious, because no transition from these schists into weakly metasomatised lithologies is exposed. Apart from boron-bearing kornerupine (McKie, 1965; Grew *et al.*, 1990a) in chlorite schists and tourmaline in impure marbles and pegmatites, no B_2O_3 -bearing minerals are present, which could provide indications for former evaporites (Moine *et al.*, 1981). The fact that whiteschists and chlorite schists only occur in a thin band between Mn-bearing quartzites and dolomite marbles allows for the interpretation that the protolith was of sedimentary origin, e. g., a karstbauxite (Yalçin *et al.*, 1993). The intense metasomatic overprint does not allow a more detailed interpretation from our petrographic observations.

5.7.4 Geodynamic setting

As discussed above, metamorphism was accompanied by the infiltration of an aqueous fluid (increase in aH_2O) at high pressures ($P = 10\text{--}11$ kbar), which led to the development of the oxidised mineralogy of Mn-bearing whiteschists at Mautia Hill. The most likely geodynamic scenario that could account for this observation is that water-rich rocks, buried below the Mautia Hill unit, released their water due to progressive metamorphic dehydration. Channelised fluid flow may be responsible for the localised metasomatism and oxidation seen in rocks at Mautia Hill, absent in adjoining rock units. The burial of water-rich rocks below the Mautia Hill unit, which is part of the Pan-African East African Orogen, might be related to subduction of oceanic lithosphere (“Mozambique Ocean”) in the course of the amalgamation of Gondwana. Alternatively, an intracrustal nappe stacking in the boundary region between the East African Orogen and the adjoining Palaeoproterozoic Usagaran Belt and Archean Tanzania Craton, may have initiated prograde metamorphism of buried rocks and the release of fluid phases causing the metasomatism at Mautia Hill. So far, a Pan-African suture zone between the East African Orogen and the Usagaran Belt, marked by eclogites or ophiolites, has not been documented. Mn-bearing schists similar to those described here from Mautia Hill have been reported to occur further to the southwest in the Konse Series deposited along the border of the Tanzania Craton (Meinhold & Frisch, 1970). Such sediments could have acted as a fluid source if they were buried by Pan-African crustal thickening processes like those documented at Mautia Hill. In any case, the Sm-Nd garnet age (536 ± 2 Ma; A. Möller pers. com.) suggests that the crustal thickening at Mautia Hill occurred in the late stages of the Pan-African cycle, contrasting to the age of metamorphism in the Mozambique Belt further east (610–655 Ma; Möller *et al.*, 2000). The significance of the different isotopic ages and the different P - T evolutions for Mautia Hill and the rest of the Tanzanian East African Orogen is not fully understood. The ca. 540 Ma event may have succeeded the magmatic underplating process, which is thought to have caused the peak metamorphism further to the east in the same belt (Appel *et al.*, 1998). Alternatively, the different mineral ages might reflect the different behaviour of the applied isotopic systems: At Mautia Hill, garnet has been dated with the Sm-Nd method, whereas U-Pb monazite ages have been obtained in the rest of

the belt. Only further dating with different isotopic methods will resolve the problem. John *et al.* (2004) obtained similar dating results for the Lufilian Arc-Zambezi Belt orogen of Zambia, where whiteschist metamorphism occurred at the late stages of continental collision at $531\text{--}532 \pm 2$ Ma (U-Pb monazite), following subduction and eclogite formation at about 600 Ma (Sm-Nd Grt-wr).

5.8 Acknowledgements

We thank T. Heinrichs for supplying important samples and the unpublished map of Mautia Hill. Further thanks are due to P. Appel and B. Mader for their help in conducting the microprobe analyses, to A. Möller for the geochronological information, to A. Fehler for producing the thin sections, to H. Marschall for providing ion microprobe data on the kornerupine chemistry, and to T. John for helpful discussions. We appreciate the discussion with D. Lattard concerning Fe-Ti oxide mineralogy and oxygen fugacity. We are grateful for the editorial work of G. Clarke, as well as comments and criticism expressed by W. Schreyer and an anonymous reviewer. We especially thank W. Schreyer for constructive ideas, which helped much to improve the manuscript.

References

- Abraham, K., Hörmann, P. & Raith, M., 1974. Progressive metamorphism of basic rocks from the southern Hohe Tauern area, Tyrol (Austria). *Neues Jahrbuch für Mineralogie Abhandlungen*, **122**, 1–35.
- Abs-Wurmbach, I., Langer, K. & Schreyer, W., 1983. The influence of Mn^{3+} on the stability relations of the Al_2SiO_5 polymorphs with special emphasis on manganian andalusites (viridines), $(\text{Al}_{1-x}\text{Mn}_x^{3+})_2(\text{O}/\text{SiO}_4)$: An experimental investigation. *Journal of Petrology*, **24**, 48–75.
- Abs-Wurmbach, I. & Peters, T., 1999. The Mn-Al-Si-O system: an experimental study of phase relations applied to parageneses in manganese-rich ores and rocks. *European Journal of Mineralogy*, **11**, 45–68.
- Ackermann, D., Seifert, F. & Schreyer, W., 1975. Instability of sapphirine at high pressures. *Contributions to Mineralogy and Petrology*, **50**, 79–92.
- Appel, P., Möller, A. & Schenk, V., 1998. High-pressure granulite facies metamorphism in the Pan-African belt of eastern Tanzania: P-T-t evidence against granulite formation by continent collision. *Journal of metamorphic Geology*, **16**, 491–509.
- Armstrong, J. T., 1995. CITZAF: A package of correction programs for the quantitative electron microbeam X-ray analysis of thick polished materials, thin films, and particles. *Microbeam Analysis*, **4**, 177–200.

- Basu, N. K. & Mruma, A. H., 1985. Mineral chemistry and stability relationship of talc-piemontite-viridine bearing quartzite of Mautia Hill, Mpwapwa District, Tanzania. *Indian Journal of Earth Sciences*, **12**, 223–230.
- Braun, J. J., Pagel, M., Muller, J. P., Bilong, P., Michard, A. & Guillet, B., 1990. Cerium anomalies in lateritic profiles. *Geochimica et Cosmochimica Acta*, **54**, 781–795.
- Buddington, A. F. & Lindsley, D. H., 1964. Iron-titanium oxide minerals and synthetic equivalents. *Journal of Petrology*, **5**, 310–357.
- Chinner, G. A., Smith, J. V. & Knowles, C. R., 1969. Transition-metal contents of Al: 2SiO₅ polymorphs. *American Journal of Science*, **267A**, 96–113.
- Chopin, C., Henry, C. & Michard, A., 1991. Geology and petrology of the coesite-bearing terrain, Dora Maira massif, Western Alps. *European Journal of Mineralogy*, **3**, 263–291.
- Chopin, C. & Monié, P., 1984. A unique magnesiochloritoid-bearing, high-pressure assemblage from the Monte Rosa, Western Alps: petrologic and ⁴⁰Ar-³⁹Ar radiometric study. *Contributions to Mineralogy and Petrology*, **87**, 388–398.
- Demény, A., Sharp, Z. D. & Pfeifer, H.-R., 1997. Mg-metasomatism and formation conditions of Mg-chlorite-muscovite-quartzphyllites (leucophyllites) of the Eastern Alps (W. Hungary) and their relations to Alpine whiteschists. *Contributions to Mineralogy and Petrology*, **128**, 247–260.
- Droop, G. T. R., 1987. A general equation for estimating Fe³⁺ concentrations in ferromagnesian silicates and oxides from microprobe analyses, using stoichiometric criteria. *Mineralogical Magazine*, **51**, 431–435.
- Dyar, M. D., Wiedenbeck, M., Robertson, D., Cross, L. R., Delaney, J. S., Ferguson, K., Francis, C. A., Grew, E. S., Guidotti, C. V., Hervig, R. L., Hughes, J. M., Husler, J., Leeman, W., McGuire, A. V., Rhede, D., Rothe, H., Paul, R. L., Richards, I. & Yates, M., 2002. Reference minerals for the microanalysis of light elements. *Geostandards Newsletter*, **25**, 441–463.
- Eckert, J. O., Newton, R. C. & Kleppa, O. J., 1991. The ΔH of reaction and recalibration of garnet-pyroxene-plagioclase-quartz geobarometers in the CMAS system by solution calorimetry. *American Mineralogist*, **76**, 148–160.
- Ellis, D. J. & Green, D. H., 1979. An experimental study of the effect of Ca upon garnet-clinopyroxene Fe-Mg exchange equilibria. *Contributions to Mineralogy and Petrology*, **71**, 13–22.
- Faryad, S., 1999. Metamorphic evolution of the Precambrian South Badakhshan block, based on mineral reactions in metapelites and metabasites associated with whiteschists from Sare Sang (Western Hindu Kush, Afghanistan). *Precambrian Research*, **98**, 223–241.

- Ferry, J. & Spear, F., 1978. Experimental calibration of the partitioning of Fe and Mg between biotite and garnet. *Contributions to Mineralogy and Petrology*, **66**, 113–117.
- Fockenberg, T. & Schreyer, W., 1991. Yoderite, a mineral with essential ferric iron: Its lack of occurrence in the system MgO-Al₂O₃-SiO₂-H₂O. *American Mineralogist*, **76**, 1052–1060.
- Fockenberg, T. & Schreyer, W., 1994. Stability of yoderite in the absence and in the presence of quartz: an experimental study in the system MgO-Al₂O₃-Fe₂O₃-SiO₂-H₂O. *Journal of Petrology*, **35**, 1341–1375.
- Frondel, C. & Marvin, U. B., 1959. Cerianite, CeO₂, from Pocos de Caldas, Brazil. *American Mineralogist*, **44**, 882–884.
- Frost, B. R. & Lindsley, D. H., 1991. Occurrence of iron-titanium oxides in igneous rocks. In: *Oxide minerals: Petrologic and magnetic significance* (ed. Lindsley, D. H.), Mineralogical Society of America, Blacksburg. 433–468.
- Graham, C. & Powell, R., 1984. A garnet-hornblende geothermometer: calibration, testing, and application to the Pelona schist, southern California. *Journal of metamorphic Geology*, **2**, 13–31.
- Greenwood, H. J., 1963. The synthesis and stability of anthophyllite. *Journal of Petrology*, **4**, 317–351.
- Grew, E. S., Chernosky, J. V., Werding, G., Abraham, K., Marquez, N. & Hinthorne, J. R., 1990a. Chemistry of kornerupine and associated minerals, a wet chemical, ion microprobe, and X-ray study emphasizing Li, Be, B and F contents. *Journal of Petrology*, **31**, 1025–1070.
- Grew, E. S., Hiroi, Y. & Shiraishi, K., 1990b. Högbomite from the Prince Olav Coast, East Antarctica: An example of oxidation-exsolution of a complex magnetite solid solution? *American Mineralogist*, **75**, 589–600.
- Grew, E. S., Pertsev, N. N., Vrána, S., Yates, M. G., Shearer, C. K. & Wiedenbeck, M., 1998. Kornerupine parageneses in whiteschists and other magnesian rocks: is kornerupine + talc a high-pressure assemblage equivalent to tourmaline + orthoamphibole? *Contributions to Mineralogy and Petrology*, **131**, 22–38.
- Haggerty, S. E., 1991. Oxide textures: a mini-atlas. In: *Oxide minerals: petrologic and magnetic significance* (ed. Lindsley, D. H.), Mineralogical Society of America. 129–219.
- Hawthorne, F. C. & Henry, D. J., 1999. Classification of the minerals of the tourmaline group. *European Journal of Mineralogy*, **11**, 201–215.
- Hodges, K. V. & Spear, F. S., 1982. Geothermometry, geobarometry and the Al₂SiO₅ triple point at Mt. Moosilauke, New Hampshire. *American Mineralogist*, **67**, 1118–1134.

- Holdaway, M., 1971. Stability of andalusite and the aluminium silicate phase diagram. *American Journal of Science*, **271**, 97–131.
- John, T., Schenk, V., Mezger, K. & Tembo, F., 2004. Timing and P-T evolution of whiteschist metamorphism in the Lufilian Arc - Zambesi Belt orogen (Zambia): implications for the assembly of Gondwana. *Journal of Geology*, **112**, 71–90.
- Johnson, S. P. & Oliver, G. J. H., 1998. A second natural occurrence of yoderite. *Journal of metamorphic Geology*, **16**, 809–818.
- Johnson, S. P. & Oliver, G. J. H., 2002. High fO_2 metasomatism during whiteschist metamorphism, Zambezi Belt, Northern Zimbabwe. *Journal of Petrology*, **43**, 271–290.
- Kleemann, U. & Reinhardt, J., 1994. Garnet-biotite thermometry revisited: The effect of Al^{VI} and Ti in biotite. *European Journal of Mineralogy*, **6**, 925–941.
- Koziol, A. M., 1989. Recalibration of the garnet-plagioclase- Al_2SiO_5 -quartz (GASP) geobarometer and application to natural parageneses. *EOS Transactions*, **70**, 493.
- Kretz, R., 1983. Symbols for rock-forming minerals. *American Mineralogist*, **68**, 277–279.
- Kulke, H. & Schreyer, W., 1973. Kyanite-talc Schist from Sar E Sang, Afghanistan. *Earth and Planetary Science Letters*, **18**, 324–328.
- Leake, B. E., Woolley, A. R., Arps, C. E. S., Birch, W. D., Gilbert, M. C., Grice, J. D., Hawthorne, F. C., Kato, A., Kisch, H. J., Krivovichev, V. G., Linthout, K., Laird, J., Mandarino, J., Maresch, W. V., Nickel, E. H., Rock, N. M. S., Schumacher, J. C., Smith, D. C., Stephenson, N. C. N., Ungaretti, L., Whittaker, E. J. W. & Youzhi, G., 1997. Nomenclature of amphiboles. Report of the Subcommittee on Amphiboles of the International Mineralogical Association Commission on New Minerals and Mineral Names. *European Journal of Mineralogy*, **9**, 623–651.
- Massonne, H.-J., 1989. The upper thermal stability of chlorite + quartz: an experimental study in the system $MgO-Al_2O_3-SiO_2-H_2O$. *Journal of metamorphic Geology*, **7**, 567–581.
- McKie, D., 1959. Yoderite, a new hydrous magnesium iron aluminosilicate from Mautia Hill, Tanganyika. *Mineralogical Magazine*, **32**, 282–307.
- McKie, D., 1963a. Order-disorder in sapphirine. *Mineralogical Magazine*, **33**, 635–645.
- McKie, D., 1963b. The högbomite polytypes. *Mineralogical Magazine*, **33**, 563–580.
- McKie, D., 1965. The magnesium aluminium borosilicates: kornierupine and grandidierite. *Mineralogical Magazine*, **34**, 346–357.
- McKie, D. & Bradshaw, N., 1966. A green variety of yoderite. *Nature*, **210**, 1148.

- McWilliams, M. O., 1981. Palaeomagnetism and Precambrian tectonic evolution of Gondwana. In: *Precambrian Plate Tectonics* (ed. Kröner, A.), Elsevier, Amsterdam, Developments in Precambrian Geology. 649–687.
- Meinhold, K. D. & Frisch, T., 1970. Manganese-silicate-bearing metamorphic rocks from Central Tanzania. *Schweizerische Mineralogische und Petrographische Mitteilungen*, **50**, 493–507.
- Moine, B., Sauvan, P. & Jarousse, J., 1981. Geochemistry of evaporite-bearing series: A tentative guide for the identification of metaevaporites. *Contributions to Mineralogy and Petrology*, **76**, 401–412.
- Möller, A., 1995. *Pan-African granulites and Early Proterozoic eclogites in the basement of eastern Tanzania: P-T-t history and crustal evolution of the complex Mozambique Belt*. Unpublished doctoral thesis, Christian-Albrechts-Universität, Kiel (Germany).
- Möller, A., Mezger, K. & Schenk, V., 2000. U-Pb dating of metamorphic minerals: Pan-African metamorphism and prolonged slow cooling of high pressure granulites in Tanzania, East Africa. *Precambrian Research*, **104**, 123–146.
- Mruma, A. H., 1986. P-T Regime of the white schist of Mautia Hill, Tanzania. *Tanzanian Journal of Science*, **12**, 27–34.
- Mruma, A. H. & Basu, N. K., 1987. Petrology of the talc-kyanite-yoderite-quartz schist and associated rocks of Mautia Hill, Mpwapwa District, Tanzania. *Journal of African Earth Sciences*, **6**, 301–311.
- Pawlig, S. & Baumgartner, L. P., 2001. Geochemistry of a talc-kyanite-chloritoid shear zone within the Monte Rosa granite, Val d’Ayas, Italy. *Schweizerische Mineralogische und Petrographische Mitteilungen*, **81**, 329–346.
- Powell, R., 1985. Regression diagnostics and robust regression in geothermometer / geobarometer calibration: the garnet-clinopyroxene geothermometer revisited. *Journal of metamorphic Geology*, **3**, 231–243.
- Rickers, K., 1996. *Metamorphose am Südostrand des Tansania-Kratons*. Unpublished diploma thesis, Christian-Albrechts-Universität, Kiel (Germany).
- Rolfo, F., Compagnoni, R., Xu, S. & Jiang, L., 2000. First report of felsic whiteschists in the ultrahigh-pressure metamorphic belt of Dabie Shan, China. *European Journal of Mineralogy*, **12**, 883–898.
- Råheim, A. & Green, D. H., 1974. Talc-garnet-kyanite-quartz schist from eclogite-bearing terrane, Western Tasmania. *Contributions to Mineralogy and Petrology*, **43**, 223–231.

- Sandiford, M., Neall, F. B. & Powell, R., 1987. Metamorphic evolution of aluminous granulites from Labwor Hills, Uganda. *Contributions to Mineralogy and Petrology*, **95**, 217–225.
- Schreyer, W., 1968. A reconnaissance study of the system $\text{MgO-Al}_2\text{O}_3\text{-SiO}_2\text{-H}_2\text{O}$ at pressures between 10 and 25 kb. *Carnegie Institution Washington Year Book*, **66**, 380–392.
- Schreyer, W., 1977. Whiteschists: their compositions and pressure temperature regimes based on experimental, field, and petrographic evidence. *Tectonophysics*, **43**, 127–144.
- Schreyer, W., 1986. The mineral cordierite: structure and reactions in the presence of fluid phases. *Berichte der Bunsengesellschaft für Physikalische Chemie*, **90**, 748–755.
- Schreyer, W., 1988. Experimental studies on metamorphism of crustal rocks under mantle pressures. *Mineralogical Magazine*, **52**, 1–26.
- Schreyer, W. & Abraham, K., 1975. Peraluminous sapphirine as a metastable reaction product in kyanite-gedrite-talc schists from Sar e Sang, Afghanistan. *Mineralogical Magazine*, **40**, 171–180.
- Schreyer, W. & Abraham, K., 1976. Three-stage metamorphic history of a whiteschist from Sar e Sang, Afghanistan, as part of a former evaporite deposit. *Contributions to Mineralogy and Petrology*, **59**, 111–130.
- Schreyer, W. & Seifert, F., 1969. High-pressure phases in the system $\text{MgO-Al}_2\text{O}_3\text{-SiO}_2\text{-H}_2\text{O}$. *American Journal of Science*, **267-A**, 407–443.
- Schreyer, W. & Yoder Jr., H. S., 1968. Yoderite: synthesis, stability, and interpretation of its natural occurrence. *Carnegie Institution Washington Year Book*, **66**, 376–393.
- Seifert, F., 1975. Boron-free kornerupine: a high-pressure phase. *American Journal of Science*, **275**, 57–87.
- Simon, G. & Chopin, C., 2001. Enstatite-sapphirine crack-related assemblages in ultrahigh-pressure pyrope megablasts, Dora-Maira massif, western alps. *Contributions to Mineralogy and Petrology*, **140**, 422–440.
- Stern, R. J., 1994. Arc assembly and continental collision in the Neoproterozoic East African Orogen: Implications for the consolidation of Gondwanaland. *Annual Reviews of Earth and Planetary Sciences*, **22**, 319–351.
- Temperley, B. N., 1938. The geology of the country around Mpwapwa. Technical report, Tanganyika Territory, Department of Lands and Mines, Geological Division.
- Vrána, S. & Barr, M. W. C., 1972. Talc-kyanite-quartz schist and other high-pressure assemblages from Zambia. *Mineralogical Magazine*, **38**, 837–846.

- Wegge, S. & Schreyer, W., 1994. Boron-free kornerupine: its upper pressure stability limit in the system MgO-Al₂O₃-SiO₂-H₂O (MASH). *European Journal of Mineralogy*, **6**, 67–75.
- Windley, B. F., Ackermann, D. & Herd, R. K., 1984. Sapphirine/kornerupine-bearing rocks and crustal uplift history of the Limpopo belt, Southern Africa. *Contributions to Mineralogy and Petrology*, **86**, 342–358.
- Yalçın, U., Schreyer, W. & Medenbach, O., 1993. Zn-rich högbomite formed from gahnite in the metabauxites of the Menderes Massif, SW Turkey. *Contributions to Mineralogy and Petrology*, **113**, 314–324.

List of Figures

2.1	Map of the reconstructed Gondwana supercontinent	10
2.2	Geological map of the Bemarivo Belt	11
2.3	Rock textures (Bemarivo Belt)	13
2.4	Microphotographs showing rock textures in metapelites (Bemarivo Belt)	16
2.5	Chemistry of garnet, orthopyroxene, and sapphirine (Bemarivo Belt)	18
2.6	Composition of metapelitic biotite; AFM diagram for metapelites (Bemarivo Belt)	21
2.7	Feldspar thermometry and rock texture with mesoperthitic feldspars (Bemarivo Belt)	21
2.8	Pressure-temperature path for the southern Bemarivo Belt	30
2.9	BSE images of metapelitic monazites (Bemarivo Belt)	31
2.10	REE + Y distribution patterns of metapelitic monazites	32
2.11	ThO ₂ * vs. PbO diagrams showing results of the monazite dating	34
3.1	Geological map of the Vohibory Block and tectonic units of Madagascar	45
3.2	(a) Chondrite-normalised rare earth element variation plot of metabasic samples; (b) Metabasic samples in a plot $(La/Sm)_N$ vs. Nb/La ; (c) Trace element variation of metabasic samples, normalised to MORB	48
3.3	Geochronological results of samples from the Vohibory block (SHRIMP and U-Th-total Pb)	50
4.1	Reconstruction of the Gondwana supercontinent ca. 544 Ma ago	58
4.2	Main tectonic units of Madagascar and simplified geological map of southern Madagascar	61
4.3	Composition of orthopyroxene from metapelitic rocks and granitic gneisses	66
4.4	AFM diagrams showing compositions of metapelitic minerals from southern Madagascar	73
4.5	Microtextures of metapelitic rocks (1)	76
4.6	Composition of biotite and sapphirine from metapelitic rocks	77
4.7	Microtextures of metapelitic rocks (2)	78
4.8	Microtextures of metapelitic rocks (3)	84
4.9	Microtextures of calcsilicate rocks	88
4.10	Microtextures of anorthosites	90
4.11	Reintegrated feldspar compositions used for thermometric estimates	92

4.12	Pressure-temperature evolution of rocks from southern Madagascar	92
4.13	Results of the U-Th-total Pb dating of monazite	96
4.13	Results of the U-Th-total Pb dating of monazite (continued)	97
4.14	Results of U-Pb SHRIMP dating of zircon	99
4.14	Results of U-Pb SHRIMP dating of zircon (continued)	100
4.15	Distribution of zircon and monazite ages in Madagascar	107
5.1	Simplified geological map of part of Tanzania	121
5.2	Geological map of Mautia Hill	122
5.3	Peak-metamorphic enstatite in $F2$ fold hinges and magnesiochlorite in the axial plane ($S2$).	123
5.4	Phase relations and compositional space of CMASH-CO ₂ -Fe ₂ O ₃ rocks from Mautia Hill	127
5.5	Microphotographs of CMASH-CO ₂ -Fe ₂ O ₃ rocks from Mautia Hill	131
5.6	Composition of amphiboles in Amph-Dol-En-Chl schists and Hbl-Ky-Tlc-Qtz schists from Mautia Hill	132
5.7	Chemical variation of kyanite, Mn andalusite, piemontite, and yoderite	132
5.8	Oxide mineralogy of MASH-Fe ₂ O ₃ and CMASH-CO ₂ -Fe ₂ O ₃ rocks	133
5.9	Phase relations of rocks within the system MASH-Fe ₂ O ₃	136
5.10	Microphotographs of MASH-Fe ₂ O ₃ rocks from Mautia Hill	137
5.11	Summarised P - T evolution of rocks from Mautia Hill	141
A.1	Results of SHRIMP zircon dating of samples from the Bemarivo Belt	161
A.2	CL images of zircon from the Bemarivo Belt	162
C.1	CL images of zircon from sample Md32-1-04	169
C.2	CL images of zircon from sample Md54-2-04	170
C.3	CL images of zircon from sample Md79-9-04	171
C.4	CL images of zircon from sample Md111-3-04	172
C.5	CL images of zircon from sample Md119-10-04	172
C.6	CL images of zircon from sample Md131-3-04	173
C.7	CL images of zircon from sample Md137-1-04	173

List of Tables

2.1	Measurement conditions for U-Th-total Pb dating of monazite	14
2.2	Mineral assemblages in metapelitic and semipelitic rocks (Bemarivo Belt) .	16
2.3	Representative garnet analyses (Bemarivo Belt)	19
2.4	Representative analyses of biotite, sapphirine, and cordierite	20
2.5	Representative analyses of orthopyroxene, plagioclase, and alkali feldspar . .	22
2.6	Pressure and temperature calculations for metapelites of the Andapa area .	27
2.7	Examples of reintegrated feldspar compositions (Bemarivo Belt)	28
2.8	Representative analyses of monazites (Bemarivo Belt)	29
2.9	Results of the U-Th-total Pb dating of monazite (Bemarivo Belt)	33
3.1	Geothermobarometry for metabasic & metapelitic rocks	47
3.2	Geochemical analyses of metabasites from the Vohibory Block	49
3.3	Results of SHRIMP analyses of the metabasic sample Md7-1-04	51
4.1	Mineral assemblages of felsic/intermediate gneisses of southern Madagascar	65
4.2	Mineral assemblages found in metabasites of southern Madagascar	67
4.3	Mineral assemblages in metapelites of southern Madagascar	68
4.4	Representative garnet analyses (southern Madagascar)	69
4.4	Representative garnet analyses (continued)	70
4.5	Representative orthopyroxene analyses (southern Madagascar)	71
4.5	Representative orthopyroxene analyses (continued)	72
4.6	Representative cordierite analyses (southern Madagascar)	74
4.6	Representative cordierite analyses (continued)	75
4.7	Representative biotite analyses (southern Madagascar)	79
4.8	Representative spinel analyses (southern Madagascar)	80
4.9	Representative sapphirine analyses (southern Madagascar)	81
4.10	Representative plagioclase analyses (southern Madagascar)	82
4.11	Mineral assemblages in calc-silicates of southern Madagascar	87
4.12	Mineral assemblages in marbles of southern Madagascar	89
4.13	Reintegrated feldspar compositions of rocks from southern Madagascar . .	91
4.14	Geothermobarometric results (southern Madagascar)	93
4.15	Results of U-Th-total Pb dating of monazites from metapelitic samples . .	98
4.16	Results of SHRIMP zircon analyses (Md32-1-04, Md54-2-04)	101
4.16	Results of SHRIMP zircon analyses (Md79-9-04, Md111-3-04, Md119-10-04)	102

4.16	Results of SHRIMP zircon analyses (Md131-3-04, Md137-1-04)	103
5.1	Representative microprobe data: metapelites and metabasites (Mautia Hill)	125
5.2	Representative microprobe data: CMASH-CO ₂ -Fe ₂ O ₃ rocks	129
5.3	Representative microprobe data: MASH-Fe ₂ O ₃ rocks	138
5.4	Pressure and temperature estimates for selected metapelitic samples	140
5.5	Pressure and temperature estimates for selected metabasic samples	142
5.6	Idealised mineral formulae used for calculations of reaction stoichiometries	143
A.1	Results of SHRIMP analyses of samples from the Bemarivo Belt	163
B.1	Mineral chemical analyses of samples from the Vohibory Block	166
B.2	Additional geochemical analyses of samples from the Vohibory Block and the Betsimisaraka suture zone	167
B.3	GPS positions of samples used for geochemical analyses	168
D.1	Mineral analyses for thermobarometry of metapelitic samples (Mautia Hill)	176
D.2	Mineral analyses for thermobarometry of metabasic samples (Mautia Hill)	177

Appendix A

SHRIMP zircon data of samples from the Bemarivo Belt

We have analysed zircon from two metapelite samples from the Bemarivo Belt: sample Md48-1-03 is from the Sambirano area, whereas Md83-13-03 is from the Andapa area. Results of both samples have not been included in Chapter 2. Results are graphically shown in Fig. A.1. Isotope ratios and ages are listed in Table A.1. CL images showing measurement spots are Fig. A.2.

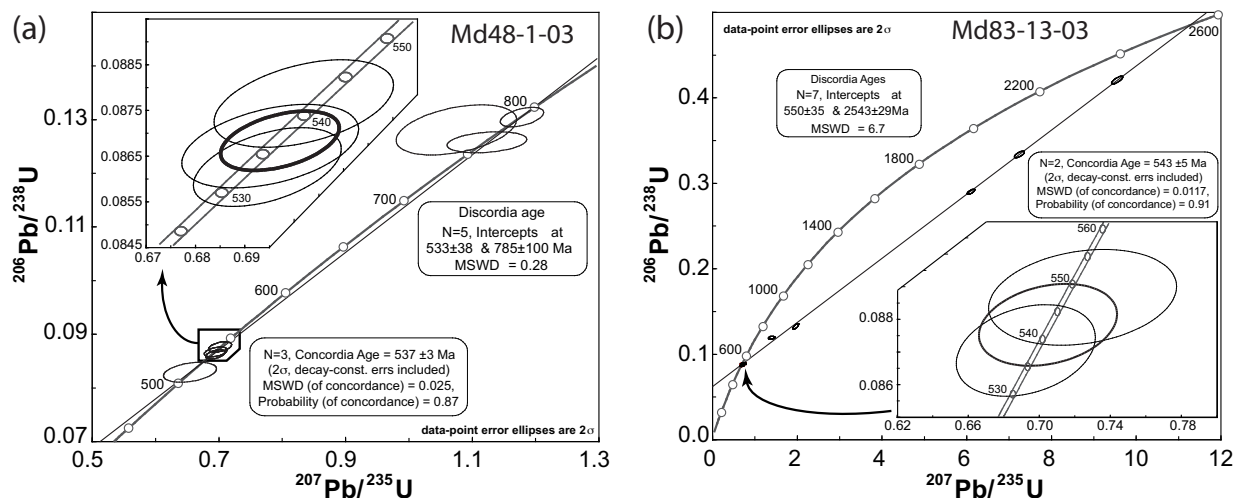


Figure A.1: Results of SHRIMP zircon dating of samples from the Bemarivo Belt. a) Sample Md48-1-03 (Sambirano area): The main metamorphic event is dated at 537 ± 3 Ma (concordant age). Magmatic cores, interpreted as detrital relics, give 785 ± 100 Ma. b) Sample Md83-13-03 (Andapa area): Metamorphically overgrown zircon rims are dated at 543 ± 5 Ma. Zircon cores are discordant and point to a formation age of 2543 ± 29 Ma, which is interpreted as the magmatic age of the source rock.

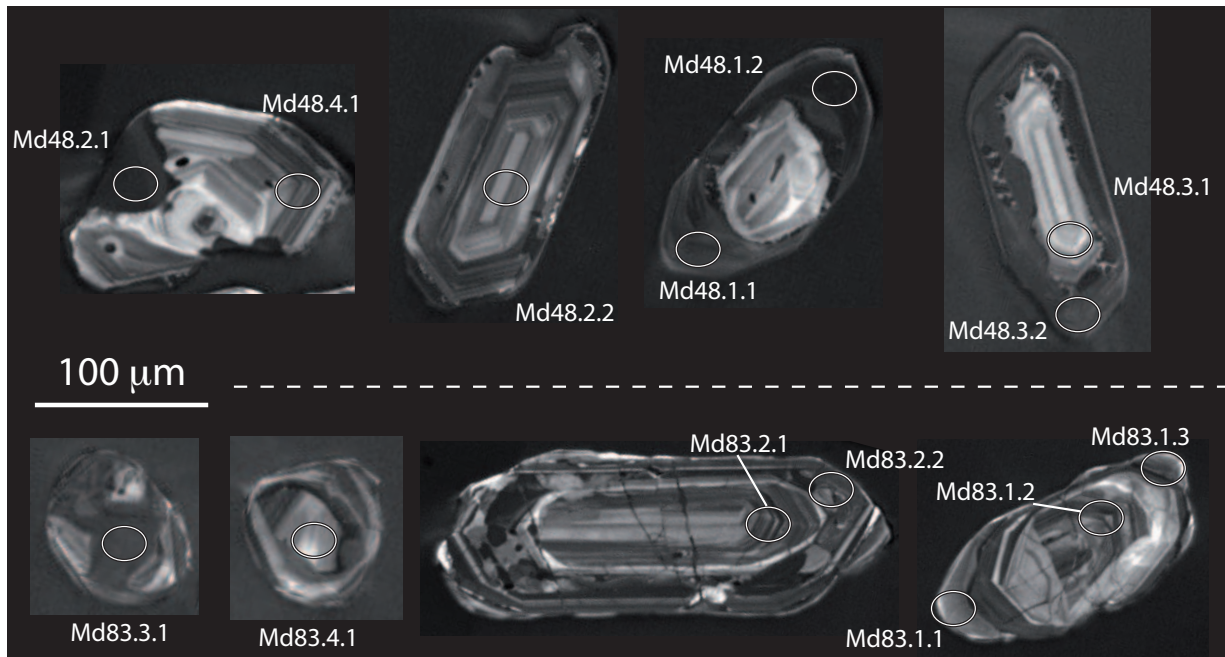


Figure A.2: CL images of zircon of two metapelitic samples (Md48-1-03, Md83-13-03) from the Bemarivo Belt. Measurement spots are indicated and correspond to Table A.1.

Table A.1: Results of SHRIMP analyses of two metapelitic samples: Md48-1-03 (Sambirano area; S13°58'55.5", E048°37'13.3") and Md83-13-03 (Andapa area; S14°30'08.7", E049°47'54.6"). Age errors are given as 1σ .

No.	U (ppm)	Th (ppm)	$\frac{^{232}\text{Th}}{^{238}\text{U}}$	comm. ^{206}Pb (%)	$\frac{^{207}\text{Pb}}{^{206}\text{Pb}}$ * error (%)	$\frac{^{206}\text{Pb}}{^{238}\text{U}}$ * error (%)	$\frac{^{207}\text{Pb}}{^{235}\text{U}}$ * error (%)	$\frac{^{208}\text{Pb}}{^{232}\text{Th}}$ * error (%)	% disc.	Age (Ma) $\frac{^{207}\text{Pb}}{^{206}\text{Pb}}$	Age (Ma) $\frac{^{206}\text{Pb}}{^{238}\text{U}}$	\pm
Md48.1.1	677	9	0.014	0.014	0.0581 0.96	0.0877 0.45	0.7020 1.06	0.0332 6.95	-1.6	532.9	541.6	2.3
Md48.1.2	999	9	0.010	0.000	0.0584 0.78	0.0863 0.41	0.6946 0.88	0.0345 6.7587	2.1	544.7	533.4	2.1
Md48.2.1	817	37	0.047	0.058	0.0581 0.96	0.0867 0.43	0.6951 1.05	0.0301 4.34	-0.2	534.9	536.1	2.2
Md48.2.2	343	267	0.804	0.000	0.0655 1.04	0.1305 0.57	1.1785 1.19	0.0411 1.04	0.0	790.5	790.6	4.2
Md48.3.1	169	108	0.657	0.580	0.0609 3.29	0.1281 1.49	1.0749 3.61	0.0391 3.0754	-18.3	634.5	777.0	10.9
Md48.3.2	652	20	0.031	0.260	0.0572 2.45	0.0829 0.91	0.6544 2.61	—	-2.5	500.6	513.5	4.5
Md48.4.1	206	206	1.033	0.289	0.0648 2.20	0.1258 0.63	1.1231 2.29	0.0383 1.48	0.3	766.4	763.8	4.6
Md83.1.1	391	5	0.013	0.275	0.0593 2.91	0.0887 0.68	0.7244 2.98	—	5.2	576.3	547.7	3.5
Md83.1.2	497	270	0.561	0.018	0.1525 0.42	0.2901 0.41	6.0992 0.59	0.0918 0.6750	44.5	2373.7	1642.2	6.0
Md83.1.3	635	21	0.034	0.201	0.0845 2.02	0.1193 0.59	1.3904 2.11	0.0751 19.63	79.5	1304.5	726.6	4.0
Md83.2.1	444	238	0.554	0.007	0.1574 0.48	0.3338 0.47	7.2418 0.67	0.1039 1.19	30.7	2427.4	1856.7	7.6
Md83.2.2	512	57	0.115	0.109	0.1074 0.97	0.1326 1.01	1.9642 1.40	0.0593 4.0401	118.8	1756.1	802.8	7.6
Md83.3.1	542	95	0.181	0.000	0.1646 0.36	0.4208 0.44	9.5489 0.56	0.1280 1.43	10.6	2503.4	2264.0	8.4
Md83.4.1	600	52	0.090	0.143	0.0577 2.21	0.0870 0.66	0.6924 2.31	0.0300 8.88	-3.7	518.0	538.1	3.4

* common Pb corrected using measured ^{204}Pb .

Appendix B

Mineral chemical and whole rock geochemical analyses of samples from the Vohibory Block and the Betsimisaraka suture zone

In Table B.1 mineral chemical analyses are shown, which have been used for geothermobarometric calculations listed in Table 3.1 (page 47). Furthermore, additional geochemical analyses are shown that have not been included in chapter 3. These are two samples from the Vohibory Block, which are not of metabasic character, as well as 10 metabasic samples from the Betsimisaraka suture zone (Table B.2). Table B.3 shows the coordinates of sample locations.

Table B.1: Mineral chemical analyses of samples from the Volihory Block, used for geothermobarometric calculations in Table 3.1.

Sample Mineral No.	6-1	7-1	7-1	11-4	11-4	16-1	16-1	16-1	6-1	7-1	7-1	7-1	7-1	16-1	6-1	7-1	11-4	16-1	6-1	7-1	11-4	16-1	11-4	
SiO ₂	38.75	38.48	38.35	40.36	40.38	39.32	39.41	44.50	40.11	40.07	35.93	37.01	45.35	51.73	48.64	62.70	50.84	53.59	53.70					
ThO ₂	0.03	0.06	0.06	0.01	0.00	0.00	0.01	1.33	1.27	1.33	3.69	4.26	1.27	3.69	4.26	0.33	0.00	0.00	0.00					
Al ₂ O ₃	20.98	21.14	21.00	22.71	22.73	22.36	22.45	11.59	13.92	13.71	16.03	17.81	34.73	30.96	33.12	23.40	3.23	2.68	2.91					
Cr ₂ O ₃	0.00	0.00	0.00	0.00	0.00	0.00	0.00	0.01	0.01	0.00	0.00	0.00	n.d.	n.d.	n.d.	n.d.	0.05	0.00	0.00					
FeO	25.21	24.50	24.45	17.39	16.74	25.34	25.39	14.91	19.52	19.33	19.24	10.86	n.c.	n.c.	n.c.	n.c.	9.77	3.79	3.88					
Fe ₂ O ₃	n.c.	n.c.	n.c.	n.c.	n.c.	n.c.	n.c.	n.c.	n.c.	n.c.	n.c.	n.c.	0.21	0.18	0.31	0.36	n.c.	n.c.	n.c.					
MgO	6.30	3.51	3.51	12.62	13.07	10.99	10.88	11.96	7.77	7.74	10.56	15.05	n.d.	n.d.	n.d.	n.d.	12.73	15.84	15.63					
MnO	0.58	2.91	2.90	0.76	0.68	0.33	0.36	0.05	0.33	0.40	0.15	0.04	n.d.	n.d.	n.d.	n.d.	0.09	0.12	0.04					
CaO	7.89	9.76	9.73	6.17	6.17	1.32	1.35	11.61	11.38	11.14	0.13	0.03	1.02	13.09	14.88	4.06	2.73	22.35	23.17					
Na ₂ O	n.d.	n.d.	n.d.	n.d.	n.d.	n.d.	n.d.	1.49	1.25	1.18	0.13	0.05	1.02	4.09	8.62	0.48	2.35	0.63	0.69					
K ₂ O	n.d.	n.d.	n.d.	n.d.	n.d.	n.d.	n.d.	0.33	1.67	1.89	9.76	10.30	0.00	0.06	0.01	n.d.	n.d.	n.d.	n.d.					
BaO	n.d.	n.d.	n.d.	n.d.	n.d.	n.d.	n.d.	n.d.	n.d.	n.d.	n.d.	n.d.	0.05	0.01	0.01	n.d.	n.d.	n.d.	n.d.					
Cl	n.d.	n.d.	n.d.	n.d.	n.d.	n.d.	n.d.	n.d.	0.00	0.01	n.d.	n.d.	n.d.	n.d.	n.d.	n.d.	n.d.	n.d.	n.d.					
Total	99.74	100.36	100.00	100.03	99.77	99.66	99.85	97.78	97.23	96.81	95.48	95.40	99.74	100.12	99.69	99.75	99.87	99.81	99.92					
Si	3.018	3.017	3.018	2.999	2.998	2.997	2.998	6.563	6.174	6.197	5.487	5.425	2.096	2.346	2.227	2.782	1.912	1.958	1.958					
Ti	0.002	0.004	0.003	0.001	0.000	0.000	0.000	0.148	0.147	0.155	0.423	0.469	n.d.	n.d.	n.d.	n.d.	0.009	0.000	0.000					
Al	1.926	1.954	1.948	1.989	1.989	2.009	2.014	2.015	2.526	2.499	2.886	3.076	1.893	1.654	1.787	1.224	0.143	0.116	0.125					
Cr	0.000	0.000	0.000	0.000	0.000	0.000	0.000	0.002	0.001	0.000	0.000	0.000	n.d.	n.d.	n.d.	n.d.	0.001	0.000	0.000					
Fe ²⁺	1.643	1.606	1.610	1.080	1.039	1.615	1.615	1.839	2.513	2.500	2.457	1.331	n.c.	n.c.	n.c.	n.c.	0.307	0.116	0.118					
Fe ³⁺	n.c.	n.c.	n.c.	n.c.	n.c.	n.c.	n.c.	n.c.	n.c.	n.c.	n.c.	n.c.	0.007	0.006	0.011	0.012	n.c.	n.c.	n.c.					
Mg	0.732	0.410	0.412	1.397	1.447	1.249	1.234	2.630	1.784	1.785	2.404	3.288	n.d.	n.d.	n.d.	n.d.	0.713	0.863	0.850					
Mn	0.038	0.193	0.193	0.048	0.043	0.021	0.024	0.006	0.043	0.053	0.019	0.005	n.d.	n.d.	n.d.	n.d.	0.003	0.004	0.001					
Ca	0.659	0.820	0.820	0.491	0.491	0.108	0.110	1.835	1.878	1.845	0.000	0.005	0.910	0.636	0.730	0.193	0.900	0.907	0.902					
Na	n.d.	n.d.	n.d.	n.d.	n.d.	n.d.	n.d.	0.426	0.372	0.354	0.037	0.013	0.091	0.360	0.242	0.742	0.035	0.044	0.049					
K	n.d.	n.d.	n.d.	n.d.	n.d.	n.d.	n.d.	0.061	0.328	0.373	1.901	1.926	0.000	0.004	0.000	0.035	n.d.	n.d.	n.d.					
Ba	n.d.	n.d.	n.d.	n.d.	n.d.	n.d.	n.d.	n.d.	n.d.	n.d.	n.d.	n.d.	0.001	0.000	0.000	n.d.	n.d.	n.d.	n.d.					
Cl	n.d.	n.d.	n.d.	n.d.	n.d.	n.d.	n.d.	n.d.	0.000	0.003	n.d.	n.d.	n.d.	n.d.	n.d.	n.d.	n.d.	n.d.	n.d.					
Total	8.018	8.004	8.004	8.005	8.007	7.999	7.994	15.524	15.767	15.764	15.614	15.537	4.999	5.006	4.997	4.988	4.024	4.008	4.003					
Mg/(Mg+Fe)	0.31	0.20	0.20	0.56	0.58	0.44	0.43	0.59	0.42	0.42	0.49	0.71					0.70	0.88	0.88					
X _{Prp}	0.24	0.14	0.14	0.46	0.48	0.42	0.41	—	—	—	—	—	—	—	—	—	—	—	—					
X _{Alm}	0.53	0.53	0.53	0.36	0.34	0.54	0.54	—	—	—	—	—	—	—	—	—	—	—	—					
X _{Sps}	0.01	0.06	0.06	0.02	0.01	0.01	0.01	—	—	—	—	—	—	—	—	—	—	—	—					
X _{Grs}	0.21	0.27	0.27	0.16	0.16	0.04	0.04	—	—	—	—	—	—	—	—	—	—	—	—					
X _{And}	0.00	0.00	0.00	0.00	0.00	0.00	0.00	—	—	—	—	—	—	—	—	—	—	—	—					
X _{Uv}	0.00	0.00	0.00	0.00	0.00	0.00	0.00	—	—	—	—	—	—	—	—	—	—	—	—					
X _{An}	—	—	—	—	—	—	—	—	—	—	—	—	0.91	0.36	0.75	0.77	—	—	—					
X _{Ab}	—	—	—	—	—	—	—	—	—	—	—	—	0.09	0.64	0.25	0.20	—	—	—					
X _{Or}	—	—	—	—	—	—	—	—	—	—	—	—	0.00	0.00	0.00	0.04	—	—	—					
X _{En}	—	—	—	—	—	—	—	—	—	—	—	—	—	—	—	—	0.37	0.46	0.45					
X _{Fs}	—	—	—	—	—	—	—	—	—	—	—	—	—	—	—	—	0.16	0.06	0.06					
X _{Wo}	—	—	—	—	—	—	—	—	—	—	—	—	—	—	—	—	0.47	0.48	0.48					

Structural formulae on the basis of: Grt= 12 oxygens; Amph = 23 oxygens; Bt= 22 oxygens; Pl= 8 oxygens; Cpx= 6 oxygens.

n.c.: not calculated; n.d.: not determined

Table B.2: Additional geochemical analyses of samples from the Vohibory Block and the Betsimisarakaka suture zone.

Sample	4-1-04 ^a	5-1-04 ^a	155-2-04 ^a	114-1-03 ^b	115-1-03 ^b	117-1-03 ^b	180-1-03 ^b	180-2-03 ^b	185-1-03 ^b	186-1-03 ^b	188-2-03 ^b	192-1-03 ^b	195-1-03 ^b
[wt.%]													
SiO ₂	55.01	72.45	75.97	52.55	51.02	53.36	46.99	39.57	48.15	46.48	52.95	47.79	46.38
Al ₂ O ₃	16.40	12.95	11.27	14.13	13.24	15.08	11.86	22.21	16.97	11.97	15.26	13.45	14.13
TiO ₂	1.62	0.40	0.22	0.39	0.37	2.43	3.80	1.65	0.59	2.78	1.00	1.70	2.48
Fe ₂ O ₃	9.60	4.61	4.54	8.28	8.70	10.12	18.27	13.00	9.55	20.93	10.47	17.08	16.1
MgO	2.47	0.49	0.11	9.72	10.66	2.79	4.66	4.89	9.05	5.21	4.56	7.34	6.27
MnO	0.19	0.06	0.06	0.14	0.14	0.14	0.23	0.18	0.14	0.24	0.24	0.22	0.21
CaO	6.33	1.58	2.57	10.11	11.51	5.88	8.07	15.71	12.51	9.25	11.23	9.39	11.27
Na ₂ O	3.98	4.75	4.20	2.76	2.20	3.61	2.76	0.91	1.66	1.76	2.80	1.63	1.53
K ₂ O	1.54	1.45	0.07	0.79	0.32	3.41	0.95	0.27	0.18	0.59	0.44	0.68	0.54
P ₂ O ₅	0.66	0.08	0.01	0.10	0.10	0.99	0.54	0.17	0.05	0.18	0.08	0.20	0.31
LOI	1.69	0.89	0.57	0.75	1.26	0.89	1.77	1.23	1.11	0.08	0.52	0.22	0.60
Total	99.49	99.71	99.59	99.72	99.52	98.7	99.9	99.79	99.96	99.47	99.61	99.79	99.84
[ppm]													
Li	14.0	7.72	2.39	11.1	12.0	8.69	9.88	2.83	7.45	9.75	16.0	3.53	4.51
K	12785	12037	581	6558	2656	28309	7886	2242	1494	4898	3653	5645	4483
Rb	13.2	3.82	0.463	17.4	2.42	69.7	20.2	2.56	5.07	9.61	4.47	4.13	4.53
Sr	780	130	94.8	734	813	1073	280	824	114	95.1	128	36.6	373
Cs	0.069	0.064	0.015	0.116	0.026	0.067	0.210	0.076	0.065	0.133	0.029	0.125	0.012
Ba	799	654	10.1	418	252	2053	303	13.3	26.4	107	39.8	36.8	110
P	2880	349	43.6	436	436	4320	2357	742	218	786	349	873	1353
Ti	9711	2398	1319	2338	2218	14568	22781	9892	3537	16666	5995	10192	14868
Y	28.8	32.1	317	13.0	11.1	60.6	59.7	72.6	13.4	41.0	75.7	29.7	30.5
Zr	116	98.3	577	125	27.9	1293	277	79.2	28.0	106	69.0	102	138
Nb	22.1	2.83	29.3	4.00	1.05	43.6	17.8	8.36	1.87	5.30	2.87	5.50	16.2
Hf	2.61	2.50	18.6	2.85	1.03	25.1	7.23	2.29	0.896	2.96	1.66	2.35	3.35
Ta	1.17	0.054	1.58	0.146	0.058	1.91	1.16	0.374	0.136	0.359	0.170	0.301	0.829
Pb	5.98	3.80	0.817	5.72	3.84	18.4	2.32	12.7	2.38	2.43	3.31	3.05	4.24
U	0.268	0.177	1.09	0.126	0.091	0.652	0.426	11.5	0.152	0.181	0.191	0.331	0.192
La	26.5	6.42	44.3	31.0	12.0	118	25.0	7.73	3.30	9.50	45.4	11.7	18.2
Ce	54.6	14.48	112	61.3	31.0	238	61.5	19.8	8.02	26.7	12.1	25.4	44.4
Pr	6.77	1.97	21.3	6.66	3.95	30.8	8.37	3.01	1.10	3.49	14.9	3.52	6.35
Nd	27.0	9.08	107	25.1	17.1	100	38.5	14.5	5.07	15.9	65.0	15.5	27.6
Sm	5.49	2.59	34.8	4.75	3.78	17.6	10.3	4.50	1.52	4.60	17.1	3.94	6.34
Eu	1.99	0.884	7.14	0.968	1.04	3.20	3.31	12.4	0.619	1.77	4.97	1.46	2.02
Gd	5.30	3.11	42.5	3.99	3.31	15.4	11.3	5.89	1.97	5.60	15.7	4.38	6.18
Tb	0.812	0.577	8.00	0.522	0.442	2.05	1.77	1.08	0.353	0.981	2.49	0.755	0.962
Dy	4.59	3.94	50.6	2.73	2.35	10.9	10.7	7.70	2.38	6.47	14.4	4.68	5.40
Ho	0.919	0.902	10.7	0.494	0.422	2.01	2.05	1.78	0.501	1.35	2.87	0.990	1.03
Er	2.56	2.82	30.8	1.31	1.10	5.34	5.45	5.79	1.43	3.87	7.89	2.86	2.80
Tm	0.360	0.435	4.47	0.180	0.148	0.721	0.760	0.973	0.216	0.580	1.13	0.417	0.374
Yb	2.25	2.89	28.1	1.16	0.956	4.64	4.87	7.45	1.46	3.91	7.69	2.72	2.31
Lu	0.337	0.442	3.99	0.167	0.136	0.682	0.701	1.24	0.217	0.587	1.18	0.410	0.337

^a Vohibory Block; ^b Betsimisarakaka suture zone

Table B.3: GPS positions of samples used for geochemical analyses (map datum: WGS84).

Sample	Longitude	Latitude
Md3-1-04	E044°34'53.67"	S23°59'39.19"
Md3-2-04	E044°34'53.67"	S23°59'39.19"
Md3-3-04	E044°34'53.67"	S23°59'39.19"
Md3-4-04	E044°34'53.67"	S23°59'39.19"
Md4-1-04	E044°36'44.25"	S24°01'27.72"
Md5-1-04	E044°36'02.63"	S24°03'38.65"
Md6-1-04	E044°41'28.14"	S24°00'52.62"
Md7-1-04	E044°45'52.60"	S24°02'38.08"
Md7-2-04	E044°45'52.60"	S24°02'38.08"
Md9-1-04	E044°49'15.47"	S24°03'53.34"
Md11-2-04	E044°54'56.90"	S24°00'33.75"
Md11-3-04	E044°54'56.90"	S24°00'33.75"
Md11-4-04	E044°54'56.90"	S24°00'33.75"
Md11-5-04	E044°54'56.90"	S24°00'33.75"
Md12-1-04	E044°55'21.63"	S24°00'34.25"
Md12-2-04	E044°55'21.63"	S24°00'34.25"
Md12-4-04	E044°55'21.63"	S24°00'34.25"
Md14-1-04	E044°57'14.27"	S23°54'13.03"
Md14-2-04	E044°57'14.27"	S23°54'13.03"
Md155-1-04	Mt. Vohibory	
Md155-2-04	Mt. Vohibory	
Md156-1-04	Mt. Vohibory	
98X	near Lazarivo	
98XII	near Lazarivo	
99III	near Lazarivo	
Md114-1-03	E048°56'14.1"	S15°54'56.2"
Md115-1-03	E048°55'38.8"	S15°53'54.6"
Md117-1-03	E048°49'03.3"	S15°49'03.3"
Md180-1-03	E049°22'46.6"	S17°27'35.9"
Md180-2-03	E049°22'46.6"	S17°27'35.9"
Md185-1-03	E049°18'12.1"	S17°58'06.5"
Md186-1-03	E049°14'01.8"	S18°19'01.0"
Md188-2-03	E049°08'10.7"	S18°23'39.4"
Md192-1-03	E049°06'03.7"	S18°19'07.8"
Md195-1-03	E049°02'57.7"	S18°18'21.4"

Appendix C

Southern Madagascar: CL images of zircon used for U-Pb dating

In the following, CL images with measurement spots of all zircons used for U-Pb SHRIMP dating are shown. Labels of measurement spots correspond to analyses given in Table 4.16 (pages 101–103).

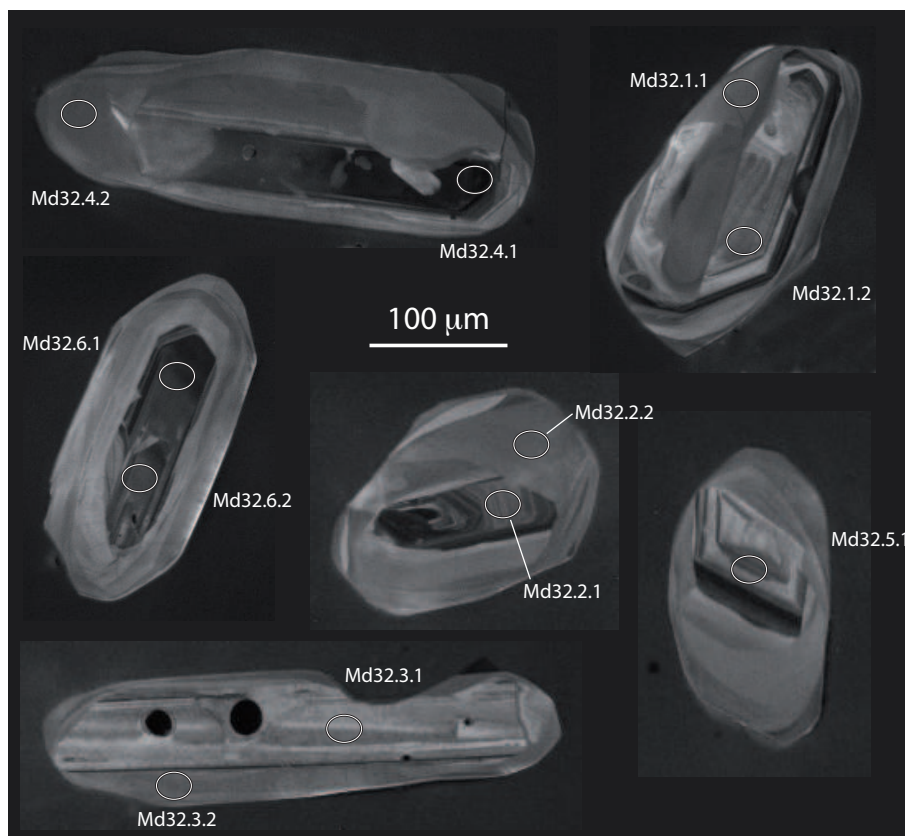


Figure C.1: CL images of zircon from sample Md32-1-04. Data for all measurement spots are given in Table 4.16 (page 101).

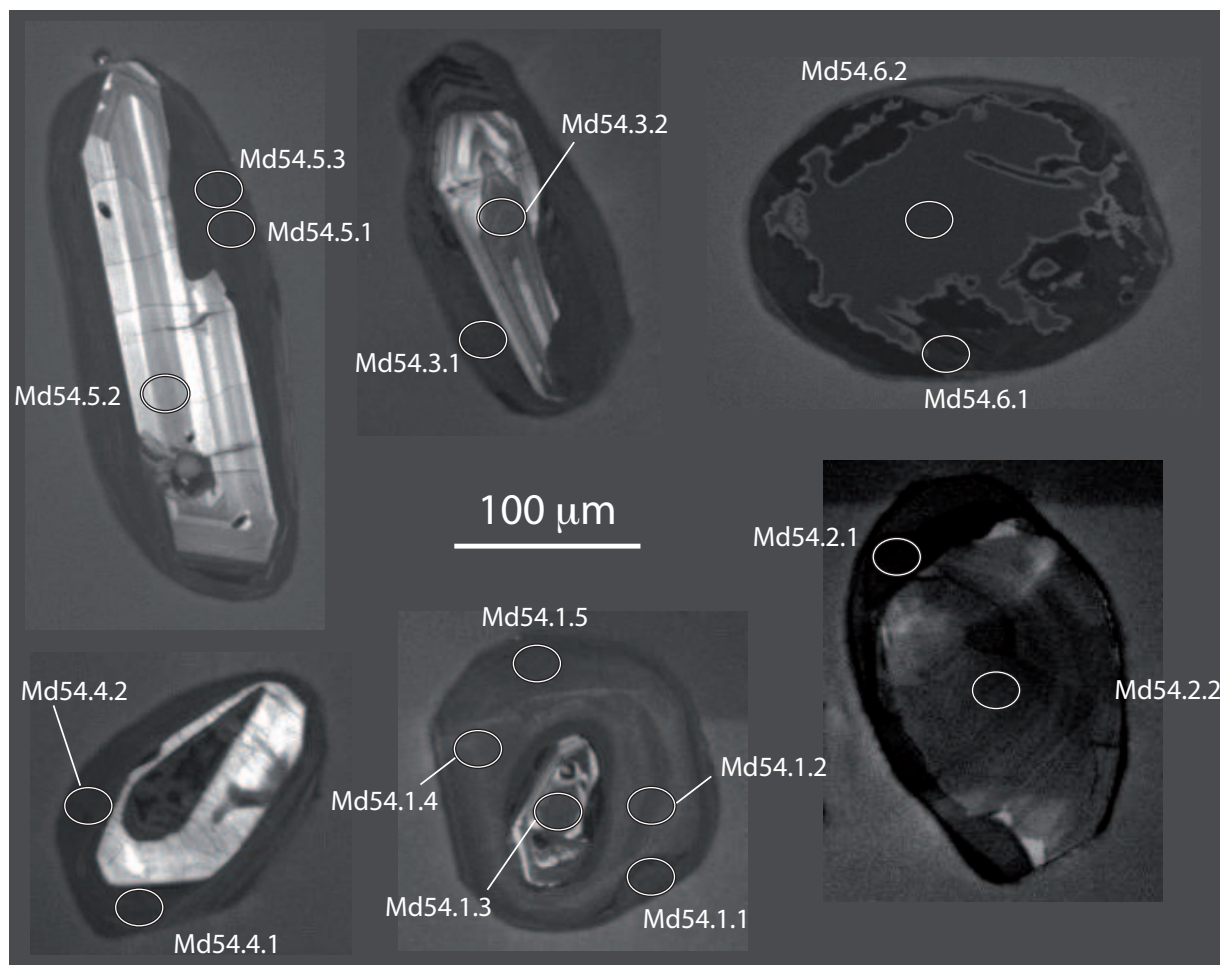


Figure C.2: CL images of zircon from sample Md54-2-04. Data for all measurement spots are given in Table 4.16 (page 101).

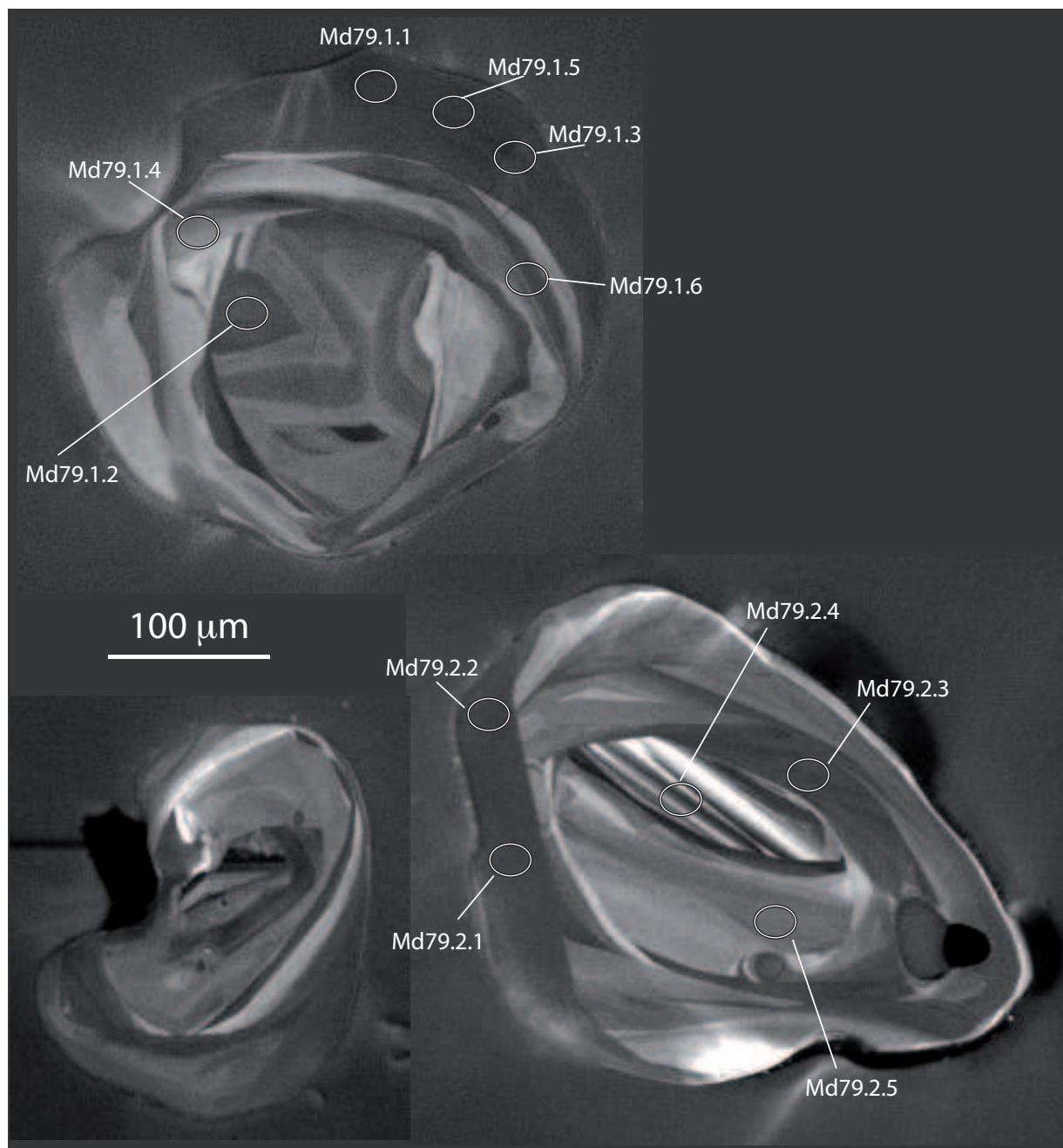


Figure C.3: CL images of zircon from sample Md79-9-04. Data for all measurement spots are given in Table 4.16 (page 102).

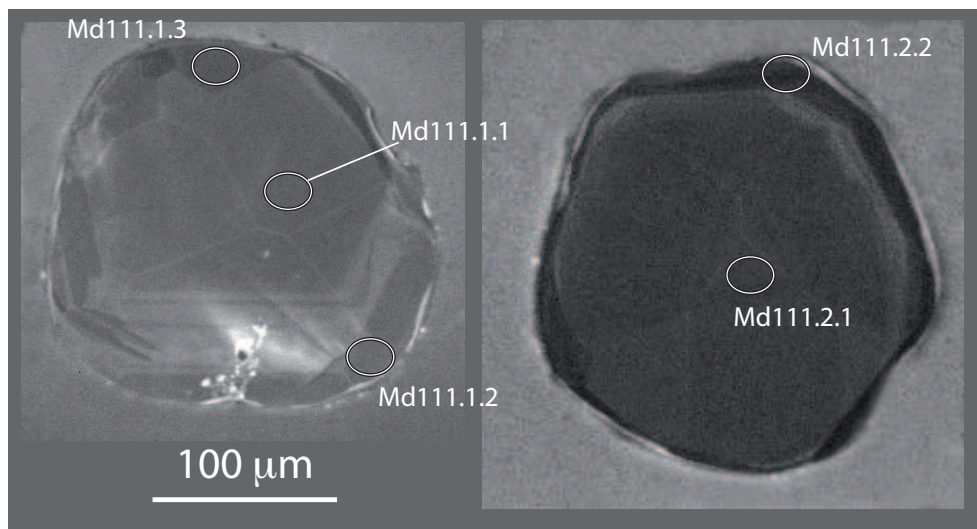


Figure C.4: CL images of zircon from sample Md111-3-04. Data for all measurement spots are given in Table 4.16 (page 102).

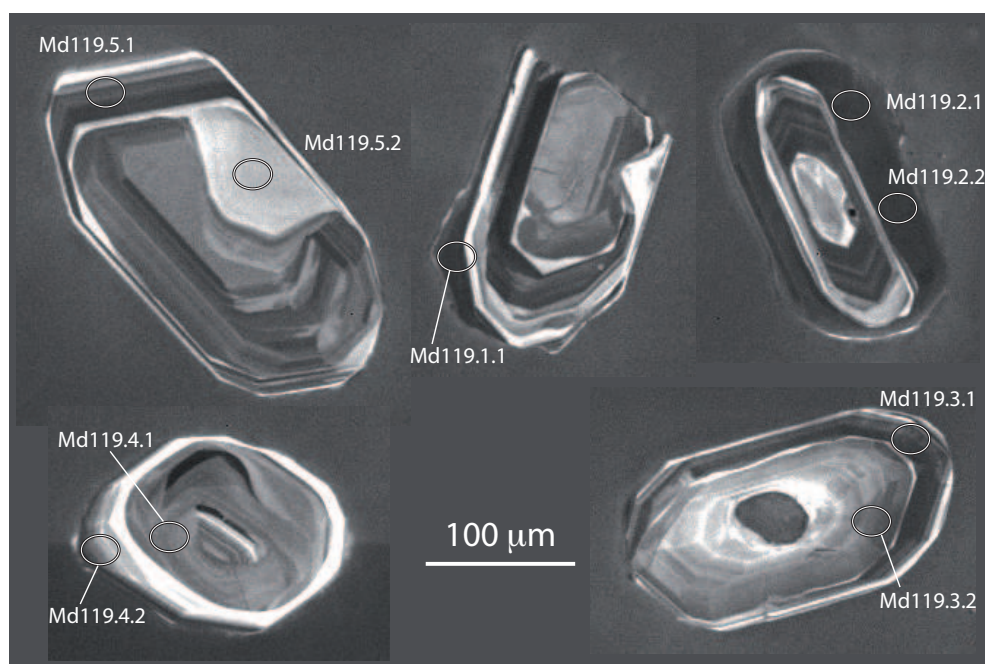


Figure C.5: CL images of zircon from sample Md119-10-04. Data for all measurement spots are given in Table 4.16 (page 102).

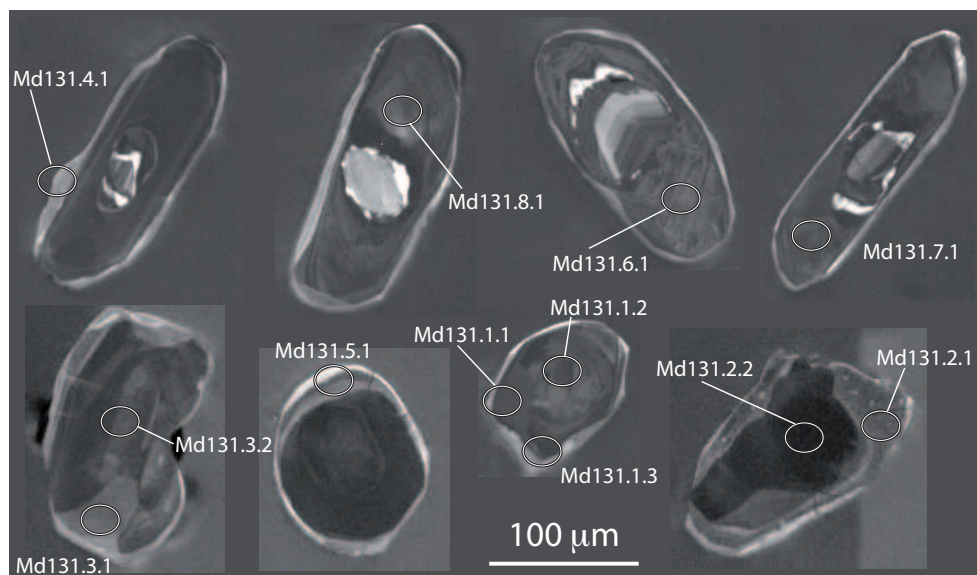


Figure C.6: CL images of zircon from sample Md131-3-04. Data for all measurement spots are given in Table 4.16 (page 103).

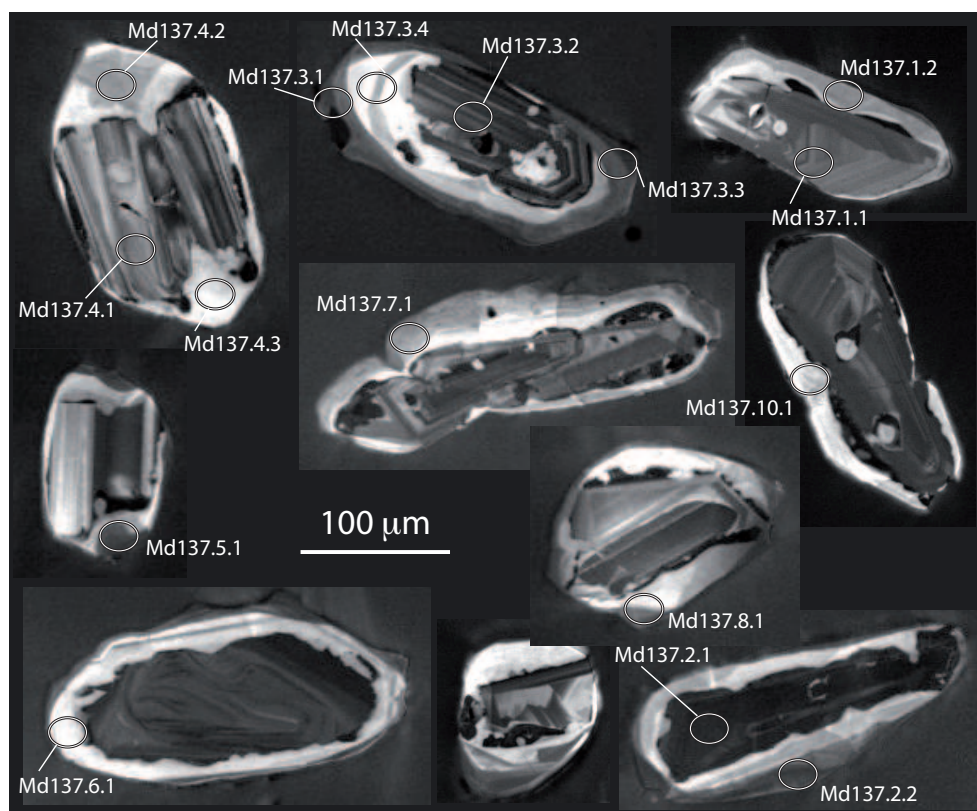


Figure C.7: CL images of zircon from sample Md137-1-04. Data for all measurement spots are given in Table 4.16 (page 103).

Appendix D

Mautia Hill: Mineral analyses used for
thermobarometric calculations

D. Mautia Hill: Mineral analyses for thermobarometry

Table D.1: Microprobe analyses for thermobarometry in metapelitic samples (calculations were done without consideration of ferric iron!). n. c. = not calculated; n. d. = not determined; Fe³⁺ after Droop (1987).

Sample Mineral No.	T27-1-93(1)			T27-1-93(2)			T27-2-93(3)			T27-2-93(4)			T30-2-93(5)			T30-2-93(6)		
	Grt	Pl	Bt	Grt	Pl	Bt	Grt	Pl	Bt	Grt	Pl	Bt	Grt	Pl	Bt	Grt	Pl	Bt
SiO ₂	39.72	59.68	38.62	39.04	59.98	38.39	39.50	59.94	38.15	39.78	59.27	38.07	39.48	61.64	37.98	38.53	61.10	37.97
Al ₂ O ₃	22.33	25.79	17.34	22.26	25.90	17.33	22.41	25.40	17.53	22.43	25.91	17.01	22.25	24.30	17.82	21.99	24.79	17.75
TiO ₂	0.56	0.00	2.39	0.03	0.00	2.43	0.01	0.00	2.22	0.00	0.00	2.22	0.04	0.00	1.96	0.03	0.00	1.98
Cr ₂ O ₃	0.00	0.00	0.03	0.00	0.00	0.02	0.00	0.00	0.04	0.00	0.00	0.01	0.00	0.00	0.05	0.00	0.00	0.03
FeO	24.81	n. c.	12.47	27.32	n. c.	12.08	24.51	n. c.	12.20	25.44	n. c.	12.67	25.84	n. c.	12.91	29.50	n. c.	13.34
Fe ₂ O ₃	0.00	0.01	n. c.	0.26	0.05	n. c.	0.06	0.06	n. c.	0.00	0.05	n. c.	0.18	0.05	n. c.	0.00	0.07	n. c.
MgO	10.28	0.00	16.86	8.53	0.00	16.14	9.85	0.00	16.60	10.25	0.00	16.80	9.89	0.00	16.06	7.24	0.00	15.69
MnO	0.40	0.00	0.02	0.53	0.00	0.03	0.87	0.00	0.02	0.45	0.00	0.02	0.71	0.00	0.01	1.04	0.00	0.04
CaO	2.87	6.79	0.01	2.85	6.87	0.01	3.35	6.51	0.01	2.48	7.10	0.03	2.39	5.34	0.01	2.06	5.71	0.00
Na ₂ O	0.00	7.52	0.69	0.00	7.64	0.67	0.00	7.71	0.65	0.00	7.29	0.52	0.00	8.38	0.57	0.00	8.35	0.53
K ₂ O	0.00	0.00	8.39	0.00	0.01	8.25	0.00	0.06	8.50	0.00	0.03	8.50	0.00	0.08	8.68	0.00	0.07	8.71
BaO	n. d.	0.00	0.18	n. d.	0.00	0.16	n. d.	0.00	0.18	n. d.	0.00	0.18	n. d.	0.00	0.15	n. d.	0.00	0.19
Cl	n. d.	n. d.	0.01	n. d.	n. d.	0.01	n. d.	n. d.	0.01	n. d.	n. d.	0.02	n. d.	n. d.	0.01	n. d.	n. d.	0.02
Total	100.96	99.79	97.01	100.82	100.46	95.52	100.56	99.68	96.11	100.83	99.65	96.04	100.78	99.78	96.21	100.39	100.09	96.24
Si	2.99	2.66	5.55	2.99	2.66	5.58	3.00	2.67	5.53	3.01	2.65	5.54	3.00	2.74	5.52	2.99	2.71	5.53
Al	1.98	1.35	2.93	2.01	1.35	2.97	2.00	1.34	2.99	2.00	1.36	2.92	1.99	1.27	3.05	2.01	1.30	3.05
Ti	0.03	0.00	0.26	0.00	0.00	0.27	0.00	0.00	0.24	0.00	0.00	0.24	0.00	0.00	0.21	0.00	0.00	0.22
Cr	0.00	0.00	0.00	0.00	0.00	0.00	0.00	0.00	0.00	0.00	0.00	0.00	0.00	0.00	0.01	0.00	0.00	0.00
Fe ²⁺	1.56	n. c.	1.50	1.75	n. c.	1.47	1.55	n. c.	1.48	1.61	n. c.	1.54	1.64	n. c.	1.57	1.92	n. c.	1.62
Fe ³⁺	0.00	0.00	n. c.	0.01	0.00	n. c.	0.00	0.00	n. c.	0.00	0.00	n. c.	0.01	0.00	n. c.	0.00	0.00	n. c.
Mg	1.15	0.00	3.61	0.97	0.00	3.50	1.11	0.00	3.59	1.15	0.00	3.64	1.12	0.00	3.48	0.84	0.00	3.41
Mn ²⁺	0.03	0.00	0.00	0.03	0.00	0.00	0.06	0.00	0.00	0.03	0.00	0.00	0.05	0.00	0.00	0.07	0.00	0.00
Ca	0.23	0.32	0.00	0.23	0.33	0.00	0.27	0.31	0.00	0.20	0.34	0.00	0.19	0.25	0.00	0.17	0.27	0.00
Na	0.00	0.65	0.19	0.00	0.66	0.19	0.00	0.67	0.18	0.00	0.63	0.15	0.00	0.72	0.16	0.00	0.72	0.15
K	0.00	0.00	1.54	0.00	0.00	1.53	0.00	0.00	1.57	0.00	0.00	1.58	0.00	0.00	1.61	0.00	0.00	1.62
Ba	n. d.	0.00	0.01	n. d.	0.00	0.01	n. d.	0.00	0.01	n. d.	0.00	0.01	n. d.	0.00	0.01	n. d.	0.00	0.01
Cl	n. d.	n. d.	0.00	n. d.	n. d.	0.00	n. d.	n. d.	0.00	n. d.	n. d.	0.00	n. d.	n. d.	0.00	n. d.	n. d.	0.00
Total	7.98	4.99	15.59	8.00	4.99	15.53	8.00	4.99	15.61	8.00	4.99	15.62	8.00	4.99	15.62	8.00	5.00	15.61
oxygens	12	8	22	12	8	22	12	8	22	12	8	22	12	8	22	12	8	22
X _{Fe}	0.58	—	0.29	0.64	—	0.30	0.58	—	0.29	0.58	—	0.30	0.59	—	0.31	0.70	—	0.32
X _{Prrp}	0.39	—	—	0.33	—	—	0.37	—	—	0.39	—	—	0.37	—	—	0.28	—	—
X _{Alrn}	0.53	—	—	0.58	—	—	0.52	—	—	0.54	—	—	0.55	—	—	0.64	—	—
X _{Sps}	0.01	—	—	0.01	—	—	0.02	—	—	0.02	—	—	0.06	—	—	0.06	—	—
X _{Grs}	0.08	—	—	0.07	—	—	0.09	—	—	0.07	—	—	0.06	—	—	0.06	—	—
X _{And}	0.00	—	—	0.01	—	—	0.00	—	—	0.00	—	—	0.01	—	—	0.00	—	—
X _{An}	—	0.33	—	—	0.33	—	—	0.32	—	—	0.35	—	—	0.26	—	—	0.27	—
X _{Ab}	—	0.67	—	—	0.67	—	—	0.68	—	—	0.65	—	—	0.74	—	—	0.73	—

Table D.2: Microprobe analyses for thermobarometry in metabasic samples (calculations were done without consideration of ferric iron!). n.c. = not calculated; n.d. = not determined; Fe³⁺ after Droop (1987).

Sample Mineral No.	T73-1-93(1)			T73-1-93(2)			T73-8-93(3)				T73-8-93(4)			
	Grt	Pl	Cpx	Grt	Pl	Cpx	Grt	Pl	Cpx	Hbl	Grt	Pl	Cpx	Hbl
	110	279	199	81	262	176	387	440	526	568	381	454	534	566
SiO ₂	38.77	55.71	51.05	37.82	55.17	51.01	38.38	57.39	51.19	44.88	38.50	56.32	51.25	44.48
TiO ₂	0.05	0.00	0.22	0.15	0.00	0.21	0.13	0.00	0.22	1.15	0.01	0.00	0.24	1.03
Al ₂ O ₃	20.88	27.24	2.60	20.66	27.16	2.78	21.61	26.58	2.93	12.60	21.32	27.17	2.96	11.61
Cr ₂ O ₃	0.03	0.00	0.11	0.06	0.00	0.05	0.06	0.00	0.02	0.10	0.10	0.00	0.02	0.13
FeO	21.48	n.c.	10.63	21.78	n.c.	11.01	22.03	n.c.	8.68	15.49	24.83	n.c.	8.91	15.57
Fe ₂ O ₃	0.00	0.06	0.66	0.06	0.00	0.61	0.00	0.01	1.22	0.00	0.00	0.10	1.11	0.00
MgO	3.17	0.00	10.57	2.57	0.00	10.30	3.24	0.00	11.74	10.07	3.03	0.00	11.61	10.56
MnO	0.66	0.00	0.16	0.95	0.00	0.17	1.30	0.00	0.16	0.14	1.56	0.00	0.14	0.14
CaO	14.14	9.71	22.36	14.08	9.77	22.75	13.03	8.62	22.61	11.19	10.85	9.33	22.30	11.46
Na ₂ O	0.00	5.95	0.64	0.00	5.81	0.54	0.00	6.62	0.58	1.54	0.00	6.37	0.69	1.55
K ₂ O	0.00	0.06	0.00	0.00	0.11	0.00	0.00	0.03	0.00	0.23	0.00	0.05	0.00	0.20
BaO	n.d.	0.00	n.d.	n.d.	0.00	n.d.	n.d.	0.00	n.d.	0.03	n.d.	0.00	n.d.	0.00
Cl	n.d.	n.d.	n.d.	n.d.	n.d.	n.d.	n.d.	n.d.	n.d.	0.00	n.d.	n.d.	n.d.	0.00
Total	99.19	98.72	99.01	98.12	98.02	99.42	99.78	99.25	99.34	97.42	100.20	99.34	99.23	96.73
Si	3.04	2.53	1.95	3.02	2.53	1.94	3.00	2.59	1.93	6.63	3.02	2.55	1.94	6.64
Al	1.93	1.46	0.11	1.94	1.47	0.13	1.99	1.41	0.13	2.19	1.97	1.45	0.13	2.04
Ti	0.00	0.00	0.01	0.01	0.00	0.01	0.01	0.00	0.01	0.13	0.00	0.00	0.01	0.12
Cr	0.00	0.00	0.00	0.00	0.00	0.00	0.00	0.00	0.00	0.01	0.01	0.00	0.00	0.02
Fe ²⁺	1.41	n.c.	0.34	1.45	n.c.	0.35	1.44	n.c.	0.27	1.91	1.63	n.c.	0.28	1.94
Fe ³⁺	0.00	0.00	0.02	0.00	0.00	0.02	0.00	0.00	0.03	0.00	0.00	0.00	0.03	0.00
Mg	0.37	0.00	0.60	0.31	0.00	0.58	0.38	0.00	0.66	2.22	0.35	0.00	0.65	2.35
Mn ²⁺	0.04	0.00	0.01	0.06	0.00	0.01	0.09	0.00	0.00	0.02	0.10	0.00	0.00	0.02
Ca	1.19	0.47	0.91	1.20	0.48	0.93	1.09	0.42	0.91	1.77	0.91	0.45	0.90	1.83
Na	0.00	0.52	0.05	0.00	0.52	0.04	0.00	0.58	0.04	0.44	0.00	0.56	0.05	0.45
K	0.00	0.00	0.00	0.00	0.01	0.00	0.00	0.00	0.00	0.04	0.00	0.00	0.00	0.04
Ba	n.d.	0.00	n.d.	n.d.	0.00	n.d.	n.d.	0.00	n.d.	0.00	n.d.	0.00	n.d.	0.00
Cl	n.d.	n.d.	n.d.	n.d.	n.d.	n.d.	n.d.	n.d.	n.d.	0.00	n.d.	n.d.	n.d.	0.00
Total	7.99	5.00	4.00	8.00	5.00	4.00	8.00	5.00	4.00	15.38	7.99	5.01	4.00	15.45
oxygens	12	8	6	12	8	6	12	8	6	23	12	8	6	23
X _{Fe}	0.79	—	0.36	0.83	—	0.37	0.79	—	0.29	0.46	0.82	—	0.30	0.45
X _{Prp}	0.12	—	—	0.10	—	—	0.13	—	—	—	0.12	—	—	—
X _{Alm}	0.47	—	—	0.48	—	—	0.48	—	—	—	0.54	—	—	—
X _{Sps}	0.01	—	—	0.02	—	—	0.29	—	—	—	0.35	—	—	—
X _{Grs}	0.39	—	—	0.40	—	—	0.36	—	—	—	0.30	—	—	—
X _{And}	0.00	—	—	0.00	—	—	0.00	—	—	—	0.00	—	—	—
X _{An}	—	0.47	—	—	0.48	—	—	0.42	—	—	—	0.45	—	—
X _{Ab}	—	0.53	—	—	0.52	—	—	0.58	—	—	—	0.55	—	—
X _{En}	—	—	0.32	—	—	0.31	—	—	0.35	—	—	—	0.35	—
X _{Fs}	—	—	0.19	—	—	0.20	—	—	0.17	—	—	—	0.17	—
X _{Wo}	—	—	0.49	—	—	0.49	—	—	0.48	—	—	—	0.48	—

Publications related to this thesis

Papers

- N. Jöns** & V. Schenk (in review): Relics of the Mozambique Ocean in the central East African Orogen: evidence from the Vohibory Block of southern Madagascar. Submitted to *Geology*.
- N. Jöns** & V. Schenk (to be submitted): The ultra-high temperature granulites of southern Madagascar in a polymetamorphic context: implications for the amalgamation of the Gondwana supercontinent.
- N. Jöns**, V. Schenk, P. Appel & T. Razakamanana (2006): Two-stage metamorphic evolution of the Bemarivo Belt of Northern Madagascar: constraints from reaction textures and in-situ monazite dating. *Journal of metamorphic Geology* **24**, 329-347 (doi: 10.1111/j.1525-1314.2006.00641.x).
- N. Jöns**, V. Schenk, P. Appel & T. Razakamanana (2006): Pan-African polyphase metamorphism in Madagascar: an example from the Bemarivo Belt. In: Schwitzer, C., Brandt, S., Ramilijaona, O., Rakotomalala Razanahoera, M., Ackermann, D., Razakamanana, T., Ganzhorn, J. U. (eds.) *Proceedings of the German-Malagasy Research Cooperation in Life and Earth Sciences*, pp. 29-39, Concept Verlag, Berlin.
- N. Jöns** & V. Schenk (2004): Petrology of whiteschists and associated rocks at Mautia Hill (Tanzania): Fluid infiltration during high-grade metamorphism? *Journal of Petrology* **45**, 1959-1981 (doi: 10.1093/petrology/egh044).

Conference abstracts

- N. Jöns**, V. Schenk & T. Razakamanana (2006): Character and timing of high- and ultrahigh-temperature metamorphism during the Pan-African orogeny: conclusions for the Gondwana assembly from metapelites of southern Madagascar. In: Brown, M. & Piccoli, P. M. (eds.) *Granulites & Granulites 2006, Program and Abstracts*, p. 36.

- N. Jöns**, V. Schenk, P. Appel & T. Razakamanana (2005): P-T evolution of the Bemarivo Belt (northern Madagascar): The final assembly of Gondwana. In: Wingate, M. T. D. & Pisarevsky, S. A. (eds.) *Supercontinents and Earth Evolution Symposium 2005*, Geological Society of Australia Inc. Abstracts **81**, p. 103.
- N. Jöns**, V. Schenk, T. John & T. Razakamanana (2005): Relics of the Mozambique Ocean: Geochemistry of the Vohibory Block (Madagascar). In: Wingate, M. T. D. & Pisarevsky, S. A. (eds.) *Supercontinents and Earth Evolution Symposium 2005*, Geological Society of Australia Inc. Abstracts **81**, p. 133.
- N. Jöns**, V. Schenk, P. Appel & T. Razakamanana (2005): Two-stage metamorphic evolution of the Bemarivo Belt (Northern Madagascar): constraints from reaction textures and in-situ monazite dating. *Geophysical Research Abstracts* **7**, EGU05-A-02044.
- N. Jöns**, V. Schenk & T. Razakamanana (2004): Témoin métamorphique de la croûte archéenne de Madagascar: Orogenèse pan-africaine et collapsus orogénique durant la formation du Gondwana (Metamorphic overprinting of Archean crust in Madagascar: Pan-African orogeny and orogenic collapse during the formation of Gondwana). *Symposium: Madagascar - un jardin d'évolution en danger. Geological, biological and agronomical/forestry aspects for sustainable development (Antananarivo/Madagascar)*, Abstract Volume, p. 37.
- N. Jöns** & V. Schenk (2004): Fluid infiltration during high-grade metamorphism: a petrological study on whiteschists and associated rocks from Mautia Hill, Tanzania. *20th Colloquium of African Geology, Orléans, France*, Abstract Volume, p. 212.

Danksagung

An erster Stelle gebührt mein Dank meinem Doktorvater, Professor Volker Schenk, der durch seine Vorlesungen und Kurse mein Interesse an der metamorphen Petrologie geweckt hat. In jeder Hinsicht stand er mir in den vergangenen Jahren mit Rat und Tat zur Seite, sei es bei der Finanzierung des Forschungsprojektes, der Geländearbeit oder der Auswertung und Interpretation der Labordaten. Somit hat er großen Anteil daran, daß die hier vorliegende Arbeit zustande gekommen ist.

Professor Théodore Razakamanana (Université de Toliara, Madagaskar) war während der drei Geländeaufenthalte in Madagaskar ein unersetzlicher Diskussionspartner und Helfer bei allen organisatorischen Dingen. Dafür danke ich ihm sehr. Misaotra betsaka!

Dr. Peter Appel danke ich dafür, mir mit viel Engagement die Durchführung der chemischen Monazitdatierung beigebracht zu haben. Bei auftretenden Fragen und Problemen mit der Mikrosondenanalytik war er jederzeit ein kompetenter Ansprechpartner.

Dr. Timm John vermittelte mir das Laborwissen über die Durchführung der Druckbombenaufschlüsse. Ferner war er in allen Stadien meiner Arbeit ein hilfreicher Diskussionspartner, wofür ich mich hiermit herzlich bei ihm bedanke.

Die SHRIMP-Zirkondatierungen wurden mit freundlicher Genehmigung von Professor Sergey Sergeev am Centre of Isotopic Research des All-Russian Geological Research Institute (VSEGEI) in Sankt Petersburg (Rußland) durchgeführt. Für ihre Hilfe bei den Messungen und Auswertungen der Daten danke ich Dr. Alexander Larionov, Ilya Paderin, Dr. Sergey Presniakov und Nickolay Rodionov.

Barbara Mader half jederzeit tatkräftig bei der Mikrosondenanalytik mit. Astrid Weinkauff führte die Röntgenfluoreszenzmessungen durch. Andreas Fehler stellte die unzähligen mikroskopischen Präparate her. François Rakoto (Budget, Antananarivo) war während der gesamten Geländearbeit in Madagaskar ein allzeit zuverlässiger und hilfsbereiter Begleiter. Bertha Luzabiko und Amiri Nambunga trugen zum Gelingen der Probenname in Tansania bei. Mit gutem Rat standen mir ferner Dr. Petra Herms sowie Dr. Peter Raase zur Seite. Ihnen allen sei für ihr Unterstützung sehr gedankt.

Dr. Dieter Garbe-Schönberg und seinen Mitarbeiterinnen danke ich für die Hilfe bei der Durchführung der ICP-MS-Analytik.

Sowohl in beruflicher als auch privater Hinsicht waren mir Dr. Wolf-Achim Kahl, Denny Loose, François van der Straaten und Nelson Boniface in den vergangenen Jahren in Kiel stets eine Bereicherung. Dres. Peter Michalik und Nouri-Saïd Rahmoun standen mir bei der T_EXnischen Umsetzung dieser Arbeit zur Seite, wofür ich ihnen danke.

Einen besonderen Dank spreche ich Dr. Christoph Beier aus, der mir seit vielen Jahren ein guter Freund und Kollege ist, auf dessen Hilfe und ehrlichen Rat ich mich immer verlassen konnte.

Auch meinen Eltern und meiner Schwester danke ich dafür, daß sie mir ein verlässlicher Rückhalt während all der Jahre waren.

Diese Arbeit wurde durch ein Promotionsstipendium der Studienstiftung des deutschen Volkes gefördert. Dr. Hans-Ottmar Weyand danke ich herzlichst dafür, an den von ihm organisierten Doktorandenforen teilgenommen haben zu dürfen. Diese Veranstaltungen haben sehr dazu beigetragen, den Blick auf angrenzende Wissenschaftsdisziplinen nicht zu verlieren und fachübergreifende Diskussionsmöglichkeiten aufzutun. Professor Anja Pistor-Hatam sei für ihre Unterstützung „vor Ort“ gedankt.

Weitere Unterstützung erhielt ich durch die Graduiertenförderung des Landes Schleswig-Holstein sowie den Deutschen Akademischen Austausch Dienst. Zudem wurde das Projekt durch die Deutsche Forschungsgemeinschaft gefördert (Sche 256/16-1 & Sche 256/17-1).

Bei all der mir zuteil gewordenen Hilfe bleibt mir schlußendlich nur zu erwähnen, daß ich für eventuell verbliebene Unzulänglichkeiten selbstverständlich ganz allein verantwortlich bin.

Lebenslauf

Persönliche Daten

Name	Niels Jöns
Anschrift	Jungmannstraße 62 24105 Kiel
E-Mail	nj@min.uni-kiel.de
Geburtsdatum	30. April 1977
Geburtsort	Bad Segeberg
Staatsangehörigkeit	deutsch

Ausbildung

Städt. Gymnasium, Bad Segeberg	1996 Abitur
Universität Kiel	1997–2003 Studium der Geologie und Paläontologie 2001–2003 Studium der Mineralogie Abschluß im Januar 2003 als Diplom-Geologe Seit Juli 2003 Promotionsstudium (Mineralogie)

Kiel, im September 2006

Erklärung

Hiermit erkläre ich, Niels Jöns, daß die vorgelegte Abhandlung, abgesehen von der Beratung durch meine akademischen Lehrer, nach Inhalt und Form meine Arbeit ist und ausschließlich unter Verwendung der angegebenen Hilfsmittel entstanden ist. Ferner erkläre ich, daß ich weder diese noch eine ähnliche Arbeit an anderer Stelle im Rahmen eines Prüfungsverfahrens vorgelegt habe.

Kiel, im September 2006

(Niels Jöns)